

**A NEW ITERATIVE APPROACH TO SOLVING THE TRANSPORT  
EQUATION**

A Dissertation

by

ALEXANDER E. MASLOWSKI OLIVARES

Submitted to the Office of Graduate Studies of  
Texas A&M University  
in partial fulfillment of the requirements for the degree of

DOCTOR OF PHILOSOPHY

December 2008

Major Subject: Nuclear Engineering

**A NEW ITERATIVE APPROACH TO SOLVING THE TRANSPORT  
EQUATION**

A Dissertation

by

ALEXANDER E. MASLOWSKI OLIVARES

Submitted to the Office of Graduate Studies of  
Texas A&M University  
in partial fulfillment of the requirements for the degree of

DOCTOR OF PHILOSOPHY

Approved by:

Chair of Committee,	Marvin L. Adams
Committee Members,	Raytcho Lazarov
	Paul Nelson
	Jean C. Ragusa
Head of Department,	Raymond Juzaitis

December 2008

Major Subject: Nuclear Engineering

## ABSTRACT

A New Iterative Approach to Solving the Transport Equation. (December 2008)

Alexander E. Maslowski Olivares, B.S., Texas A&M University

Chair of Advisory Committee: Dr. Marvin L. Adams

We present a new iterative approach to solving neutral-particle transport problems. The scheme divides the transport solution into its particular and homogeneous or “source-free” components. The particular problem is solved directly, while the homogeneous problem is found iteratively. To organize the iterative inversion of the homogeneous components, we exploit the structures of the so called Case-modes that compose it. The asymptotic Case-modes, those that vary slowly in space and angle, are assigned to a diffusion solver. The remaining transient Case-modes, those with large spatial gradients, are assigned to a transport solver. The scheme iterates on the contribution from each solver until the particular plus homogeneous solution converges.

The iterative method is implemented successfully in slab geometry with isotropic scattering and one energy group. The convergence rate of the method is only weakly dependent on the scattering ratio of the problem. Instead, the rate of convergence depends strongly on the material thickness of the slab, with thick slabs converging in few iterations. The transient solution is obtained by applying a One Cell Inversion scheme instead of a Source Iteration based scheme. Thus, the transient unknowns are calculated with little coordination between them. This independence among unknowns makes our scheme ideally suited for transport calculations on parallel architectures.

The slab geometry iterative scheme is adapted to XY geometry. Unfortunately, this attempt to extend the slab geometry iterative scheme to multiple dimensions has not been successful. The exact filtering scheme needed to discriminate asymptotic and transient modes has not been obtained and attempts to approximate this filtering process

resulted in a divergent iterative scheme. However, the development of this iterative scheme yield valuable analysis tools to understand the Case-mode structure of any spatial discretization under arbitrary material properties.

## ACKNOWLEDGEMENTS

I would like to thank Dr. Marvin Adams for the intense, educative and sometimes long hours spent in developing this project and thus, my graduate education. The topic of this research grew from a class assignment to its current form through these long hours of discussion. I would also like to thank Dr. Adams for his patience in reviewing the multiple drafts to this dissertation and supporting research.

I thank Dr. Jean Ragusa, Dr. Raytcho Lazarov and Dr. Paul Nelson for their work in reviewing this dissertation and for their service on my Ph.D. committee. I am especially appreciative to Dr. Nelson for his input on previous Caseology studies, and to Dr. Barry Ganapol and Dr. Ed Larsen for their insightful discussions on slab geometry Caseology and its extension to multiple dimensions.

The final stage of this research was completed at Lawrence Livermore National Laboratory. I thank Dr. Patrick Brantley and AX division for hosting me in the final stages of this research.

I am grateful to have had Dr. Jae Chang, Tim Smith and Gabriel Tanase as colleagues working on the Texas A&M Parallel Deterministic Transport code. Much of the insight they shared on the C++ language became the foundation to my programming style and skills.

Finally, I thank my father, Eugenio, and my mother, Gladys, for their advice and unconditional support. I am especially grateful to have shared the graduate years of my education with my wife, Amy, and thank her for reviewing uncountable number of documents and for sacrificing some of our family time to complete this degree.

This research was performed under appointment to the U.S. Department of Energy Nuclear Engineering and Health Physics Fellowship Program sponsored by the U.S. Department of Energy's Office of Nuclear Energy, Science, and Technology.

## TABLE OF CONTENTS

	Page
ABSTRACT .....	iii
ACKNOWLEDGEMENTS .....	v
TABLE OF CONTENTS .....	vi
LIST OF FIGURES .....	viii
LIST OF TABLES .....	x
I. INTRODUCTION .....	1
I.A. The Transport Equation .....	2
I.B. Parallelization in Space and Angle.....	5
I.C. Background: Source Iteration.....	7
I.D. Background: Cell Inversions.....	10
I.E. Nodal Block Inversions .....	11
I.F. The Iterative Scheme and Organization .....	12
II. THE ANALYTIC TRANSPORT SOLUTION.....	14
II.A. Structure of the Solution Space to the Transport Equation .....	15
II.B. Eigenfunctions and Eigenvalues of the Transport Operator .....	16
II.C. Full-Range and Half-Range Orthogonality.....	18
II.D. Structure of the Asymptotic Solution Space in XY Geometry.....	21
II.E. Structure of the Solution Space to the Discrete Ordinates Approximation .....	24
II.F. Full-Range and Half-Range Discrete Ordinates Orthogonality .....	29
II.G. Summary.....	33
III. THE CONTINUOUS FINITE ELEMENT APPROXIMATION.....	35
III.A. The Continuous Finite Element Family of Methods.....	35
III.B. Case-Mode Analysis of the CFEM Solution .....	37
III.C. Numerical Results.....	41
III.D. Summary of Results .....	56
IV. THE DISCONTINUOUS FINITE ELEMENT APPROXIMATION.....	59
IV.A. The Discontinuous Finite Element Family of Methods .....	59

	Page
IV.B. Case-Mode Analysis of the LD Solution .....	62
IV.C. Numerical Results .....	70
IV.D. Summary of Results .....	74
V. THE ITERATIVE METHOD: SLAB GEOMETRY .....	78
V.A. The Iterative Method .....	78
V.B. Analysis .....	89
V.C. Numerical Results .....	100
V.D. Summary of Results .....	130
VI. THE ITERATIVE METHOD: XY GEOMETRY .....	132
VI.A. Opportunities in Multiple Dimensions .....	132
VI.B. The Iterative Method .....	133
VI.C. Analysis .....	153
VI.D. Numerical Results .....	156
VI.E. Summary of Results .....	161
VII. CONCLUSIONS .....	164
VII.A. Summary of the Dissertation .....	164
VII.B. Suggestion for Future Work .....	166
REFERENCES .....	168
APPENDIX A: DFEM CASE-MODE ANALYSIS EXAMPLE: LINEAR DISCONTINUOUS .....	171
VITA .....	216

## LIST OF FIGURES

	Page
Fig. 1. Sweeping schedule for an $S_2$ problem distributed among five domains. ....	9
Fig. 2. Characteristic direction $\omega$ to an asymptotic mode and its projection to the XY plane $\omega_{xy}$ . ....	24
Fig. 3. Evaluation of the dispersion relation and location of its roots for $c = 0.05$ . ....	26
Fig. 4. One-region $S_2$ CFEM order of convergence test problem .....	42
Fig. 5. Two-region $S_4$ asymptotic and transient CFEM behavior test problem.....	45
Fig. 6. Scalar flux of the two-region $S_4$ problem for the mesh with refined boundary layers. ....	48
Fig. 7. Decaying-transient scalar flux with refined boundary layers.....	49
Fig. 8. Growing-asymptotic scalar flux with refined boundary layers.....	51
Fig. 9. Decaying-asymptotic scalar flux with refined boundary layers.....	52
Fig. 10. Scalar flux of the two-region $S_4$ problem for the mesh without refined boundary layers. ....	53
Fig. 11. Growing-transient scalar flux without refined boundary layers. ....	54
Fig. 12. Absolute value of the transient-growing scalar flux without refined boundary layers. ....	55
Fig. 13. One-region CFEM order of convergence test problem.....	71
Fig. 14. One-region problem with varying scattering ratio.....	101
Fig. 15. Scalar flux of a single-region slab with varying scattering ratio. ....	103
Fig. 16. Transient scalar flux of a single-region slab with varying scattering ratio. ....	104
Fig. 17. $S_8$ relaxation length spectrum change with scattering ratio. ....	106
Fig. 18. One-region problem with varying total cross-section.....	107
Fig. 19. Scalar flux of a single-region slab with varying total cross-section. ....	108
Fig. 20. Transient scalar flux of single-region slab with varying total cross-section. .	109
Fig. 21. Multi-region problem with an increasing number of material regions. ....	110
Fig. 22. Scalar flux of problem with an increasing number of material regions.....	111
Fig. 23. Transient scalar flux of slab with an increasing number of material regions. .	112

	Page
Fig. 24. 16-regions slab with varying scattering ratio.....	113
Fig. 25. Transient scalar flux with varying scattering ratio.....	114
Fig. 26. Scalar flux with varying scattering ratio.....	115
Fig. 27. Two-region heterogeneous problem. ....	117
Fig. 28. Scalar flux to the LD-optimized mesh. ....	122
Fig. 29. Right-boundary zoom of the scalar flux with the LD-optimized mesh. ....	122
Fig. 30. Right-boundary zoom of the transient scalar flux with an LD-optimized mesh. ....	123
Fig. 31. Order of DFEM spatial convergence problem.....	126
Fig. 32. Two-region XY geometry test problem.....	157
Fig. 33. Cell-average scalar flux of the two-region XY geometry test problem.....	159

## LIST OF TABLES

		Page
TABLE I.	Order of Convergence of the CFEM Single-Cell Attenuation Factor of DD, Quadratic and Sixth Order .....	44
TABLE II.	Order of Convergence of the CFEM Angle-Shape Function for DD, Quadratic and Sixth Order.....	46
TABLE III.	Relative Error of the Single-Cell Attenuation Factor, Within-Cell Attenuation Factor and Amplitudes of the LD Solution .....	73
TABLE IV.	Relative Error of the Left and Right Angular Flux of the LD Solution .....	74
TABLE V.	Spectral Radius of the Ideal Method with Multiple Regions in Slab Geometry .....	91
TABLE VI.	Rate of Convergence for an Infinite Homogeneous Problem .....	97
TABLE VII.	Approximate Transient Single-Cell Attenuation Factor for the DD and LD Discretizations.....	98
TABLE VIII.	Number of Iterations to Converge a Single-Region Slab of Increasing Optical Thickness. ....	102
TABLE IX.	Number of Iterations to Converge a Single-Region Slab of Increasing Total Cross-Section .....	107
TABLE X.	Number of Iterations to Converge the Solution of a Slab with an Increasing Number of Material Regions. ....	110
TABLE XI.	Number of Iterations to Converge the Solution of a Multiple-Region Slab with Increasing Discontinuity in Scattering Ratio .....	113
TABLE XII.	Optimal Mesh Configuration for DD .....	118
TABLE XIII.	Optimal Mesh Configuration for LD .....	119
TABLE XIV.	Comparison of the Number of Iterations Among Source Iteration, One Cell Inversion and the Proposed Iterative Scheme .....	120
TABLE XV.	Number of Total Iterations with Varying Number of Maximum Inner Iterations for the LD-Optimized Mesh .....	125
TABLE XVI.	Error and Error Ratio of the DD Solution .....	128
TABLE XVII.	Error and Error Ratio of the LD Solution .....	128

	Page
TABLE XVIII. Number of Iterations to Solve the Different Configurations to the XY Geometry Test Problem.....	160

## I. INTRODUCTION

We present a new iterative scheme to efficiently solve particle transport problems in massively parallel architectures. Particle transport problems are modeled based on the linear Boltzmann Equation for dilute gas interactions with a background medium, which describes radiation particles as they are emitted by a source, stream through a host medium, and are either absorbed by the medium or escape our domain of interest.

Transport calculations are an important contributor to the solution of a wide array of problems. In nuclear engineering, we implement them to design radiation shields, nuclear reactors and radiation detectors, and to assess radiation doses to individuals. In general, we find transport implemented in problems where streaming particles play an important role in the transfer and production of energy. In nuclear reactors neutrons are absorbed by the fuel to produce fission events and are released after the event. In supernovas neutrinos transfer and remove energy from the imploding stars. In laser-induced fusion photons deposit the energy that helps create the high pressures needed for fusion to occur.

The common theme among these particle transport problems is the complexity of a complete calculation. The transport solution commonly resides in multiple spatial dimensions plus time, an energy domain and a domain to describe the streaming directions. To this, we add the influence of the transported particles on the physical properties of the host medium. The result is a coupled multiphysics problem with a large number of unknowns that requires large amounts of memory and a large number of operations to obtain their values. Parallel machines address this need for large computational resources, but their memory and processors alone are not enough. The algorithms to solve these problems must be designed to obtain the correct solution and maximize the use of the computational resources.

To solve for the transport unknowns and construct the particle flux, we build a

---

This dissertation follows the style of *Nuclear Science and Engineering*.

system of partial differential equations and discretize them into a matrix equation. By taking this path, we have addressed the transport problem using a deterministic approach in contrast to a stochastic approach, which utilizes Monte Carlo techniques to solve the system of partial differential equations. At this point, we state that our problems of interest are linear; that is, the matrix to be inverted is independent of the solution, and the problem can be solved by directly or iteratively inverting the matrix that represents the system of equations. Direct solvers invert the matrix through a series of elementary matrix operations. However, this family of methods requires too many operations to compute a solution. The practical choice to invert our system is iterative solvers, which compute the product of the matrix inverse to the source within a predefined tolerance.

Ideally an iterative scheme converges unconditionally towards the correct solution and does so in few iterations. In parallel architectures we add an extra requirement, that our iterative scheme exploit the computational resources efficiently. In other words, if  $m$  times as many processors are use to solve a problem we want the solver to compute the solution  $m$  times faster. The scalability of current algorithms is problem and architecture-dependent. Nevertheless, we aim towards designing a transport algorithm that scales independent of the problem and that can be more easily implemented, while remaining unconditionally stable and rapidly converging.

### *1.A. The Transport Equation*

The solution to the general Boltzmann Equation describes the evolution of particles densities confined to a space-momentum volume in arbitrary geometries, under the influence of force fields and undergoing collisions. We restrict our study to the following neutral-particle transport assumption<sup>1</sup>:

1. Particle to particle interactions are negligible compared to the interactions between particles and the background medium.
2. Particles stream in the absence of any force field. The shortest possible particle trajectory between two points is a straight line.
3. Particles behave like points, and not waves.
4. Collision between particles and atoms in the medium are instantaneous.

Given these assumptions, the transport equation is:

$$\begin{aligned} \frac{1}{v(E)} \frac{\partial \psi}{\partial t} + \hat{\Omega} \cdot \bar{\nabla} \psi(\hat{\Omega}, \bar{r}, t, E) + \sigma_t(\bar{r}, E) \psi(\hat{\Omega}, \bar{r}, t, E) \\ = \int_{4\pi} d\Omega' \int_0^{\infty} dE' \sigma_s(\bar{r}, \hat{\Omega}', \hat{\Omega}, E' \rightarrow E) \psi(\hat{\Omega}', \bar{r}, t, E') + Q(\bar{r}, \hat{\Omega}, E), \end{aligned} \quad (1)$$

where

$\psi(\hat{\Omega}, \bar{r}, E, t)$  = angular flux in direction  $\hat{\Omega}$ ,

$\sigma_t(\bar{r}, E)$  = total macroscopic cross-section,

$\sigma_s(\bar{r}, \hat{\Omega}', \hat{\Omega}, E' \rightarrow E)$  = scattering macroscopic cross-section from direction  $\hat{\Omega}'$

and energy  $E'$  into direction  $\hat{\Omega}$  and energy  $E$ ,

$Q(\bar{r}, \hat{\Omega}, E)$  = extraneous source of particles emitted with direction  $\hat{\Omega}$  at energy  $E$ .

This equation tracks the flux of particles, their density times their speed, in space ( $r$ ), energy ( $E$ ), and direction ( $\hat{\Omega}$ ) as they evolve in time ( $t$ ). By integrating the angular flux over all streaming directions, we compute the energy-dependent “scalar flux”:

$$\phi(r, E, t) = \int_{4\pi} d\Omega \psi(\hat{\Omega}, \bar{r}, E, t). \quad (2)$$

The scalar flux is a sensible unknown because it can be used directly to compute particle reaction rates. The rate of a specific reaction is the product of the total distance traveled by all particles in a volume per unit time (or the scalar flux integrated over a volume) multiplied by the average number of reactions that occur per distance traveled by each particles (or the macroscopic cross-section for specific reaction.)

With the exception of the time derivative, each term models the net entrance or exit of particles into our phase space volume, divided by that volume. To aid in explaining each term, we integrate the equation over a volume, energy range and over all streaming directions, and apply the divergence theorem to the spatial integral of the second term:

$$\begin{aligned}
\frac{\partial N}{\partial t} = & - \oint_{\partial V} dS \int_{\Delta E} dE \int d\Omega \cdot \psi(\hat{\Omega}, \bar{r}, t, E) \hat{\Omega} \cdot \hat{n} \\
& - \int_{\Delta V} dV \int_{\Delta E} dE \int d\Omega \cdot \sigma_t(\bar{r}, E) \psi(\hat{\Omega}, \bar{r}, t, E) \\
& + \int_{\Delta V} dV \int_{\Delta E} dE \int d\Omega \cdot \left[ \begin{aligned} & Q(\bar{r}, \hat{\Omega}, E) \\ & + \int_{4\pi} d\Omega' \int_0^{\infty} dE' \sigma_s(\bar{r}, \hat{\Omega}', \hat{\Omega}, E' \rightarrow E) \psi(\hat{\Omega}', \bar{r}, t, E') \end{aligned} \right], \quad (3)
\end{aligned}$$

where

$\frac{\partial N}{\partial t}$  = total change rate of the particle population in  $\Delta V$  with energy within  $\Delta E$ ,

$\oint_{\partial V} dS \int_{\Delta E} dE \int d\Omega \cdot \psi(\hat{\Omega}, \bar{r}, t, E) \hat{\Omega} \cdot \hat{n}$  = net number of particles with energies in

$\Delta E$  streaming out of  $\Delta V$ ,

$\int_{\Delta V} dV \int_{\Delta E} dE \sigma_t(\bar{r}, E) \psi(\hat{\Omega}, \bar{r}, t, E)$  = number of particles with energies in  $\Delta E$

colliding with the media filling  $\Delta V$ ,

$\int_{\Delta V} dV \int_{4\pi} d\Omega \int_{4\pi} d\Omega' \int_{\Delta E} dE \int_0^{\infty} dE' \sigma_s(\bar{r}, \hat{\Omega}', \hat{\Omega}, E' \rightarrow E) \psi(\hat{\Omega}', \bar{r}, t, E')$  = number of particle

scattering into the energy range  $\Delta E$  from both within  $\Delta E$  and outside this energy range inside  $\Delta V$ ,

$\int_{\Delta V} dV \int_{\Delta E} dEQ(\bar{r}, \hat{\Omega}, E)$  = number of particles emitted by a neutron source in  $\Delta V$

with energies within  $\Delta E$ .

This equation simply states that the change rate of particles in a volume equal the rate of particle gain minus the loss rate. Thus, the transport equation is imply a statement of conservation of particles a six-dimensional phase space (position, energy and direction.)

### I.B. Parallelization in Space and Angle

We focus the design of our scheme on creating concurrent work in the spatial and angular domains of the transport equation, and we seek simplicity of implementation and schedule on parallel architectures. We perform a domain decomposition of the problem in space and angle, and allow the computation of the solution on each domain to be performed by a different processor. To address the parallelization of these two domains only, we consider the static transport equation and integrate over all energies to obtain:

$$\hat{\Omega} \cdot \vec{\nabla} \psi(\hat{\Omega}, \vec{r}) + \sigma_t(\vec{r}) \psi(\hat{\Omega}, \vec{r}) = \int_{4\pi} d\Omega' \sigma_s(\vec{r}, \hat{\Omega}' \cdot \hat{\Omega}) \psi(\hat{\Omega}', \vec{r}) + Q(\vec{r}, \hat{\Omega}). \quad (4)$$

Here:

$$\psi(\hat{\Omega}, \vec{r}) = \int_0^\infty dE \psi(\hat{\Omega}, \vec{r}, E),$$

$$Q(\hat{\Omega}, \vec{r}) = \int_0^\infty dE Q(\hat{\Omega}, \vec{r}, E),$$

$$\sigma_x(\vec{r}) \approx \frac{\int_0^\infty dE \sigma_x(\vec{r}, E) \psi(\hat{\Omega}, \vec{r}, E)}{\int_0^\infty dE \psi(\hat{\Omega}, \vec{r}, E)}.$$

Although this model has few physical applications in itself, it is consistent with the transport equation for a single group belonging to the multi-group discretization (Lewis and Miller.) Thus, an algorithm that is scalable in space an angle could be extended to address problems with concurrent work in the energy domain. Wienke and Hiromoto address the parallelization of problems with concurrent work in energy, with Gauss-Seidel and Jacobi-like algorithms over multiple energy groups. Under their approach, transport algorithms are organized in two levels of tasks:

1. an outer loop that computes the flux distribution for each energy group,
2. an inner loop that solves this single-group static problem.

For the derivation of our scheme, we assume that the single-group solution has been projected into a spatial basis of lower dimension:

$$\psi(\hat{\Omega}, \vec{r}) = \sum_{p=1}^P \psi_p(\hat{\Omega}) b_p(\vec{r}), \quad (5)$$

and that the solution is discretized in angle using the discrete ordinates method<sup>1,2</sup>. The discrete ordinates method approximates the scalar flux by evaluating the angular flux at specific streaming directions and by numerically integrating them:

$$\Phi(\vec{r}) = \int_{4\pi} d\hat{\Omega} \psi(\hat{\Omega}, \vec{r}) \approx \sum_{m=1}^M w_m \psi(\hat{\Omega}_m, \vec{r}). \quad (6)$$

At this point we emphasize that our approach does belong to the discrete ordinate family in that it uses a quadrature to approximate part of the scalar flux. However, in our method we decompose the solution into multiple components, each component differentiated by the magnitude of its eigenvalues, and then we apply the discrete ordinate approximation to the components associated to the largest eigenvalues. The combination of continuous and discrete-ordinate components remains in the discrete ordinates family, but has improved numerical properties and avoids some of the obstacles of parallelizing a full discrete ordinate problem.

Finally, we assume that after a collision particles scatter isotropically. In terms of our scattering source notation this implies:

$$\int_{4\pi} d\Omega' \sigma_s(\vec{r}, \hat{\Omega}' \cdot \hat{\Omega}) \psi(\hat{\Omega}', \vec{r}) = \frac{\sigma_s(\vec{r})}{4\pi} \int_{4\pi} d\Omega \psi(\hat{\Omega}, \vec{r}) \quad (7)$$

Given the assumed simplifications, we present the transport problems in matrix form:

$$L \cdot \Psi(\hat{\Omega}) = S \cdot \Phi + Q(\hat{\Omega}) \quad \text{with} \quad \left[ \Psi(\hat{\Omega}) \right]_p = \psi_p(\hat{\Omega}), \quad (8)$$

where

$L$  = streaming plus total collision matrix,

$S$  = scattering matrix,

$Q(\hat{\Omega})$  = extraneous-source vector.

The scalar flux remains a numerical integration of the angular flux over all streaming directions:

$$\Phi = \sum_{m=1}^M w_m \Psi(\hat{\Omega}_m). \quad (9)$$

### *I.C. Background: Source Iteration*

We consider two schemes classically employed in solving the single-group, static transport equation: Source Iteration and Cell Inversions. Source Iteration inverts the transport problem iteratively by computing the current source of scattered particles, adding this source to the extraneous source, and inverting the leakage plus total-collision operator:

$$L(\hat{\Omega}) \cdot \Psi^{(l+1)}(\hat{\Omega}) = S \cdot \Phi^{(l)} + \tilde{L}(\hat{\Omega}) \cdot \Psi_{inc}^{(l+1)}(\hat{\Omega}) + Q(\hat{\Omega}), \quad (10)$$

with

$$\Phi^{(l+1)} = \int_{4\pi} d\Omega \Psi^{(l+1)}(\hat{\Omega}). \quad (11)$$

These operations are done until the solution is converged to the desired tolerance.

For infinite-medium problems, the rate of convergence of Source Iteration is bounded by the scattering to total cross-section ratio, or scattering ratio, of the host medium. Therefore, in problems where particles scatter many times before either leaking or being absorbed, Source Iteration converges slowly. To accelerate the Source Iteration convergence rate multigrid methods in space<sup>3,4</sup> and in angle<sup>5</sup> have been designed. These multigrid techniques remove error modes of a specific range of frequencies to reduce the convergence rate to a fraction of the scattering ratio. However, these acceleration techniques can be difficult to derive and implement, as in the Diffusion Synthetic Acceleration<sup>5</sup>, or may be divergent, as in the case of Transport Synthetic Acceleration<sup>5</sup>. Acceleration can be increased or instabilities removed by casting the multigrid problem as a preconditioner and applying a method from the Krylov family around the resulting preconditioned Source Iteration<sup>6</sup>. The ability of Krylov-based method to remove instabilities makes preconditioned Source Iteration scheme very tolerant of shortcomings in their preconditioning. Overall, Source Iteration solvers are very effective in calculating the solution in few iterations and are ideal for computations in serial architectures.

The advantage of Source-Iteration-based methods in serial calculations derives from the simplicity of only inverting the collision-leakage operator, a triangular matrix

after discretization, and the robustness of its preconditioned-Krylov iterative schemes. Source Iteration requires that only the scattering source contain old information; thus, we solve the unknowns in a cell when all its interface conditions become available. We refer to this process of solving the unknowns in the order dictated by the streaming direction as a “sweep”. The ordering of the solution is expected if the problem is viewed as a triangular matrix inversion.

In parallel architectures, sweeping the angular flux reduces the number of unknowns that can be solved concurrently. Within a single iteration and in Cartesian coordinates, only angular fluxes belonging to different streaming directions are guaranteed to be fully independent. The unknowns belonging to different streaming directions are only grouped at the end of an iteration to update the scalar flux. On the other hand, dependencies may exist between angular fluxes belonging to separate locations and the same streaming direction. An angular flux depends on all its upstream neighbors that have an equal streaming direction. Naturally, the parallelization of Source Iteration began in the angular phase space of Cartesian geometries<sup>7</sup>. However, the concurrent work available in the angular domain is limited to the number of streaming directions. This level of concurrency is insufficient for massively parallel machines.

Angle-based concurrency was extended to curvilinear geometries<sup>8,9</sup> where the redistribution term of the leakage operator<sup>7,10</sup> introduced dependencies among the angular fluxes belonging to different streaming directions. Here a Block Jacobi approach was forced on the angular domain dependencies to make concurrent work available<sup>8,9</sup>. Under the Block Jacobi approach, domain decomposition is done ignoring the dependencies among sub-domains. Dependencies between sub-domains are broken by employing old information to communicate them. The old information reduces the convergence rate of the iterative process. Thus, as the size of the Jacobi blocks is refined, the convergence rate is degraded, but more concurrent work becomes available.

Similar challenges arise when decomposing the spatial domain. In one dimension, no concurrent work is available unless dependencies are broken through a

Block Jacobi process. In XY geometry concurrent work was found as the sweep progressed away from corners<sup>11</sup>. Fig. 1 presents a hypothetical rectangular problem, with four streaming directions. The cells in Fig. 1 are numbered in the order in which they need to be swept to solve the first streaming direction without breaking the dependencies. Cells with an equal number can be solved concurrently and are said to belong to a *sweeping plane*<sup>11,12,13</sup>. The cells from a single sweeping plane are independent of each other, but this concurrency is limited since dependencies exist between sweeping planes. In general, if sweeping is implemented to solve problems with  $N$  spatial dimensions, sweeping planes of dimension  $N - 1$  appear with concurrent work within them.

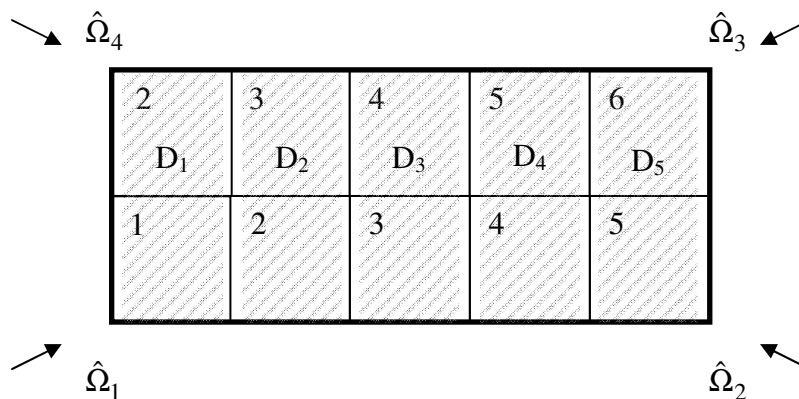


Fig. 1. Sweeping schedule for an  $S_2$  problem distributed among five domains.

An important fraction of current state of the art iterative schemes employ some variation of Source Iteration. However, sweeps challenge all the favorable numerical properties that these schemes offer when implemented in parallel computer architectures. The dependencies that sweep introduce among unknowns reduces the concurrent work available; thus, sweep-based algorithms scale poorly. Several domain decomposition arrangements, performance models and figures of merit have been developed to measure

and maximize the scalability of Source Iteration algorithms<sup>11,12,13</sup>. The domain decomposition techniques aim at minimizing the average idle processor time and reducing the amount of processor coordination needed. As with the Block Jacobi scheme, alternatives to sweep-based iterative methods suffer from poor convergence rate as sub-domains are reduced in size<sup>5</sup>.

#### *I.D. Background: Cell Inversions*

The second approach to solving iteratively the transport equation is to invert the discretized transport operator in a specific region with incoming interface conditions from previous iterations:

$$\left[ I - \int_{4\pi} d\Omega L_i(\hat{\Omega})^{-1} S_i \right] \cdot \Phi_i^{(l+1)} = \int d\Omega L_i(\hat{\Omega})^{-1} \left[ Q_i(\hat{\Omega}) + \tilde{L}(\hat{\Omega}) \cdot \Psi_{i,inc}^{(l)} \right], \quad (12)$$

$$L_i(\hat{\Omega}) \Psi_i^{(i+1)}(\hat{\Omega}) = S_i \cdot \Phi_i^{(i+1)} + Q_i(\hat{\Omega}) + \tilde{L}(\hat{\Omega}) \cdot \Psi_{i,inc}^{(l)}. \quad (13)$$

Here we emphasize that the interface conditions to the region must belong to a previous iteration. Otherwise, this approach would reduce to inverting exactly the transport operator of the entire problem or implementing a direct solver. In parallel calculations, Cell Inversion offers the advantage that no dependencies exist per iteration, since interface conditions are constructed based on an old solution. With the absence of sweeps, task management is greatly simplified and processors have work available at all times.

The challenge to successfully implement Cell Inversion schemes resides, first, in inverting the discretized transport operator exactly in a block and, second, in converging the global problem in few iterations. To address the first challenge most Cell Inversion methods focus in grouping only a few number of cells; classically One Cell or Two-Cell Inversions have been attempted<sup>14,15</sup>. This approach reduces the complexity of the matrix inversion by reducing its dimension. The second challenge has proven more elusive. Because Cell Inversions compute the solution using old information, the convergence rate of this scheme degrades as cell blocks become optically thin. Thus, the convergence rate of Cell Inversions competes with mesh refinement level required to obtain

meaningful results. In other words, highly accurate solutions obtained in highly resolved meshes converge at a lower rate than their coarse counterparts.

The promise of a sweep-less scheme remains seductive for transport calculations in parallel architectures. Nowak, Larsen and Martin designed a scheme that partially implemented Cell Inversions to solve the coarser operator of a multigrid problem. However, the added computational cost of implementing the Cell Inversion made this approach impractical. Kim and Palmer derived a scheme that combines Source Iteration sweep with a Cell Inversion step and accelerates them synthetically. The result was an improvement of the convergence rate in the scheme, but with the penalties of scheduling a sweep.

### *I.E. Nodal Block Inversions*

We make a special remark on the Nodal Block Inversion method used to solve problems discretized with the Spectral Green Function Constant Nodal Scheme (SPG-CN)<sup>16</sup>. This iterative scheme solves the unknowns to a single cell exactly, but employing the most current interface conditions.

For slab geometry, the SPG scheme recasts the transport problem into the space of modes that construct the exact solution, and assigns in each cell the coefficient of the modes as the unknowns. Thus, the SPG scheme requires a description of the solution modes, more precisely of the eigenvalues and eigenfunctions to reconstruct each mode in space and angle. By inverting exactly the transport problem for a single cell, the SPG scheme has the implicit behavior equivalent to the Cell Inversion method. However, in its original implementation, the interface conditions to each cell were given by the most current angular flux solution; thus, the SPG scheme performs sweeps.

In XY geometry, the SPG approach is extended in the form of a Nodal Method with Constant cross-leakage terms (SPG-CN)<sup>17</sup>. The resulting slab-geometry equation for each set of nodes is solved using the SPG approach with the cross-leakage terms assigned to the extraneous source. The extension of the SPG iterative scheme to XY geometries is labeled Nodal Block Inversion, although this block inversion method did contain sweeps.

Our interest on this method lies on its exploitation of the structure to the exact transport solution. The SPG-CN scheme was design to achieve the low-cost and high-accuracy results that have been classically linked to Diffusion Nodal methods. This method achieved these nodal goals, but was not configured with parallel calculations in mind. We present a method that exploits the structure of the transport solution to avoid sweeps while converging Cell Inversion scheme in few iterations. Unlike SPG, our scheme only requires the calculations of the asymptotic eigenvalues, those of magnitude smaller than one, and a description of the respective asymptotic eigenfunctions. That is, the method avoids calculation of transient-mode eigenvalues.

#### *I.F. The Iterative Scheme and Organization*

We have designed a scheme that solves slab geometry transport problems using One Cell Inversions, and thus is intrinsically parallelizable, and that achieves a convergence rate competitive with preconditioned Source Iteration. To do so, we take an approach unlike any scheme previously presented: we assign a fraction of the boundary and interface conditions to a diffusion operator and the remaining fraction to a transport operator. The solutions from each operator are added to produce the final solution.

Our scheme exploits the structure of the transport solution. It is well known that the transport solution in slab geometry is a linear combination of asymptotic and transient modes plus a particular solution. Asymptotic modes vary slowly in space, and are constructed with only two eigenvalues; this makes them ideally diffusive. Transient modes have large gradients in space and angle, and are constructed on a spectrum of eigenvalues, which requires a transport operator to construct their solution accurately. The keystone of our method is the orthogonality relations that allow us to differentiate the asymptotic and transient contribution to the solution at boundary and interfaces; thus, allowing to construct separate diffusion and transient problems in each region.

These slab geometry results suggest that we have designed a Block Jacobi method that converges in few iterations. We consider how the structure of the slab geometry solution extends to multiple-dimension problems, and attempt to extend our

iterative scheme to XY geometries. In XY geometry our scheme offers one more potential advantage that, as we construct the asymptotic solution on a diffusion solver the ray effects of discrete ordinates transport approximations will be mitigated.

We organize this dissertation as follows. In Section II we present a review of the structure of the analytic transport solution, which we follow in Section III and Section IV with a similar analysis of the Continuous and Discontinuous Finite Element approximate transport solutions. In Section V, we apply the knowledge gained from these analyses to design an iterative scheme for slab geometry. We also present numerical results that illustrate the scheme's behavior. In Section VI, we present our attempt to extend the iterative scheme to XY geometry. We end with some concluding remarks and suggestions for future work in Section VII.

## II. THE ANALYTIC TRANSPORT SOLUTION

We present in this section a review of the analytic solution of the transport equation for static problems with isotropic scattering, a single energy group and for axially-symmetric slab geometry. This description was originally presented by Case and Zweifel<sup>18,19</sup> and was an adaptation to particle transport of Davidson's<sup>20,21,22</sup> singular eigenfunctions in slab geometries and Van Kampen<sup>20,21,23</sup> work on plasma oscillations. The rigor of Case and Zweifel's analysis of the transport solution was originally challenged by the mathematical community on several fronts<sup>21,24</sup>. Nevertheless, subsequent work by Larsen and Habetler<sup>21,25</sup>, Hangelbroek<sup>21,26</sup>, and Slawny and Zweifel<sup>21,27</sup>, showed that Case and Zweifel original description was correct.

Soon after Case's<sup>18</sup> analysis was published, his results were reproduced by Abu-Shumays and Bareiss<sup>28</sup>. However, Abu-Shumays and Bareiss employed spherical harmonics in their analysis, which allowed them to extend Case's results to problems in slab geometry without axial symmetry. Abu-Shumays and Bareiss<sup>20</sup> then proceeded to construct a framework to analyze transport problems in arbitrary geometries, and applied this framework to the specific cases of one-dimensional spherical and cylindrical geometries. Abu-Shumays and Bareiss foresaw<sup>20</sup> that their results could be extended to the discrete ordinates transport approximation. Recently, Germogenova<sup>29</sup> presented a description of the Case-mode structure of the discrete ordinates approximation for axially-symmetric slab geometry problems.

Naturally, Case and Zweifel's analysis for axial-symmetric slab geometries was extended to problems with multiple energy groups and anisotropic scattering. We highlight the work of Mika<sup>19,30</sup> in the analysis of problems with anisotropic scattering, and of Bowden, Sancaktar and Zweifel<sup>31,32</sup> in problems with multiple energy groups and isotropic scattering. Ganapol<sup>33</sup> confirmed the results of Bowden et al using Fourier Transforms instead of singular eigenfunctions, but included anisotropic scattering in the analysis of problems with multiple energy groups.

The design of our iterative scheme exploits the structure of the transport solution presented by Case and Zweifel in slab geometry. In this section, we review the analytic transport solution in slab geometry, and present an adaptation of Bareiss and Abu-Shumays's framework to the particular case of XY geometry. We also review the structure of the solution of the discrete ordinates transport approximation.

### II.A. Structure of the Solution Space to the Transport Equation

In 1D Cartesian geometry, the transport equation of interest is given by:

$$\mu \frac{\partial \psi}{\partial x} + \sigma_t(x) \psi(x, \mu) = \sigma_t(x) \frac{c(x)}{2} \phi(x) + Q(x, \mu), \quad (14)$$

$$\phi(x) = \int_{-1}^1 d\mu \psi(x, \mu), \quad (15)$$

with incident boundary conditions specified at the boundaries:

$$\psi(0, \mu) = \psi_{inc}(\mu), \mu > 0, \quad \psi(X, \mu) = \psi_{inc}(\mu), \mu < 0, \quad (16)$$

where

$\psi(x, \mu) \equiv$  angular flux,

$\phi(x) \equiv$  scalar flux,

$$\phi(x) = \int_{-1}^1 d\mu \psi(x, \mu)$$

$\sigma_t(x) \equiv$  total macroscopic cross-section,

$c(x) \equiv$  scattering ratio,

$Q(x, \mu) \equiv$  extraneous source.

We consider a region  $i$ , in which material properties are constant:

$$\mu \frac{\partial \psi_i}{\partial x} + \sigma_{t,i} \psi_i(x, \mu) = \sigma_{t,i} \frac{c_i}{2} \phi_i(x) + Q_i(x, \mu). \quad (17)$$

We divide the transport solution into its particular and homogeneous components:

$$\psi_i(x, \mu) = \psi_i^p(x, \mu) + \psi_i^h(x, \mu). \quad (18)$$

Here, the homogeneous component satisfies the transport equation for the region in the absence of the extraneous source:

$$\mu \frac{\partial \psi_i^h}{\partial x} + \sigma_{t,i} \psi_i^h(x, \mu) = \sigma_{t,i} \frac{c_i}{2} \phi_i^h(x), \quad (19)$$

and the particular solution satisfies the transport equation with the extraneous source included.

We focus on the structure of the homogeneous solution. The homogeneous solution is a linear combination of modes, each mode having the following form:

$$\psi_i(x, \mu, \nu_i) = A(\nu_i) \alpha(\mu, \nu_i) e^{-\sigma_{t,i} x / \nu_i}. \quad (20)$$

Here  $\nu$  is the relaxation length, which scales each mode in space and in angle,  $A$  is the amplitude,  $\alpha_i$  is the angle-shape function. These are the so called Case-modes of the homogeneous solution to the transport equation.

### *II.B. Eigenfunctions and Eigenvalues of the Transport Operator*

Next, we derive an explicit expression for the angle-shape function and a relation to determine the relaxation lengths. We do so by considering the angle-shape function as an eigenfunction to the transport operator. As an eigenfunction, we chose the arbitrary normalization:

$$\int_{-1}^1 d\mu \alpha(\mu, \nu_i) = \frac{2}{c_i}. \quad (21)$$

Next, we replace the angular flux in the homogeneous transport equation by its Case-mode structure:

$$\sigma_{t,i} \left[ -\frac{\mu}{\nu_i} + 1 \right] \alpha(\mu, \nu_i) e^{-\sigma_{t,i} x / \nu_i} = \sigma_{t,i} \frac{c_i}{2} \int_{-1}^1 d\mu \alpha(\mu, \nu_i) e^{-\sigma_{t,i} x / \nu_i}, \quad (22)$$

and apply our arbitrary normalization to the scattering term, and solve for the angle-shape function:

$$\alpha(\mu, \nu_i) = \frac{\nu_i}{\nu_i - \mu}. \quad (23)$$

This expression limits towards infinity as the relaxation length approaches the directional cosine in value. To allow the normalization of the angle shape-function of relaxation lengths with magnitude smaller than one, we insert Cauchy's principal value to the normalization integral and complement it with a Dirac-delta function:

$$\alpha(\mu_i, \nu) = P \frac{\nu_i}{\nu_i - \mu} + \lambda(\nu_i) \delta(\nu_i - \mu), \quad (24)$$

where Cauchy's principal value is defined by:

$$\int_{-1}^1 d\mu P \frac{\nu_i}{\nu_i - \mu} = \lim_{\varepsilon \rightarrow 0} \left[ \int_{-1}^{\nu_i - \varepsilon} d\mu \frac{\nu_i}{\nu_i - \mu} + \int_{\nu_i + \varepsilon}^1 d\mu \frac{\nu_i}{\nu_i - \mu} \right], \quad (25)$$

and the Dirac-delta function is defined by:

$$\delta(\nu_i - \mu) = \begin{cases} 0, & \text{if } \nu_i \neq \mu \\ 1, & \text{if } \nu_i = \mu \end{cases}. \quad (26)$$

Given this expression for the angle-shape function, we assume that the relaxation lengths may have magnitudes greater and smaller than one, and we explore these possible relaxation length ranges separately. For the angle-shape functions with relaxation lengths of magnitudes larger than one, the Cauchy principal value is not required; the normalization of its respective angle-shape function reduces to:

$$\nu_i^a \int_{-1}^1 d\mu \frac{1}{\nu_i^a - \mu} = \nu_i^a \ln \left[ \frac{1 + 1/\nu_i^a}{1 - 1/\nu_i^a} \right] = \frac{2}{c_i}. \quad (27)$$

This expression has only two roots; each with the following properties:

$$\nu_i^a \in \Re \text{ and } |\nu_i^a| > 1, \text{ if } c_i \in \Re \text{ and } 0 < c_i < 1.$$

We refer to the Case-modes belonging to these relaxation lengths as the asymptotic component of the homogeneous solution. These modes have an asymptotic behavior since their large relaxation length magnitude produce a small spatial gradient, and their contribution dominates the homogeneous solution in the region's interior.

The expression that determines the asymptotic relaxation length can also be obtained by inserting the asymptotic Case-mode for our asymptotic modes in the source-free transport equation:

$$\begin{aligned}
& -\mu \frac{\sigma_{t,i}}{v_i} A(v_i) \alpha(\mu, v_i) e^{-\sigma_i x/v_i} + \sigma_{t,i} A(v_i) \alpha(\mu, v_i) e^{-\sigma_i x/v_i} \\
& = \sigma_{t,i} \frac{c_i}{2} A(v_i) e^{-\sigma_i x/v_i} \int_{-1}^1 d\mu \alpha(\mu, v_i), \tag{28}
\end{aligned}$$

isolating the angle-shape function in the left-hand-side, and integrating the equation over the angular domain:

$$\int_{-1}^1 d\mu \alpha(\mu, v_i) = \frac{c_i}{2} \int_{-1}^1 d\mu \alpha(\mu, v_i) \int_{-1}^1 d\mu \frac{1}{1 - \mu/v_i}, \tag{29}$$

$$\int_{-1}^1 d\mu \frac{v_i}{v_i - \mu} = \frac{2}{c_i} \tag{30}$$

We refer to this integral equation as the dispersion relation.

For those relaxation lengths with magnitudes smaller than one, the normalization of the angle-shape function reduces to:

$$v_i P \int_{-1}^1 d\mu \frac{1}{v_i - \mu} + \lambda(v_i) = \frac{2}{c_i}, \tag{31}$$

which results in the following expression for  $\lambda$ :

$$\lambda(v_i) = 1 - v_i c_i \tanh^{-1} v_i, \tag{32}$$

where  $\lambda(v_i) = 0$  for the spectrum of relaxation lengths in the interval  $[-1, 1]$ , if  $0 < c < 1$  and  $c \in \Re$ . We label the case-modes with relaxation lengths belonging to this range as transient, since their small relaxation lengths imply large gradients, strong attenuation in space and a solution mostly localized around the region's interface.

### II.C. Full-range and Half-range Orthogonality

The set of angle-shape functions constitutes a complete basis for solutions constructed on half the spectrum of relaxation lengths (half-range) and for solutions with the full spectrum of relaxation lengths (full-range.) Mathematically we imply that a problem with a half-range solution has the form:

$$\psi_i(x, \mu) = \psi(x, \mu, v_i^{\alpha-}) + \int_{-1}^0 dv \psi(x, \mu, v) \quad \text{if } \mu \in [-1, 0], \tag{33}$$

$$\psi_i(x, \mu) = \psi(x, \mu, v_i^{a+}) + \int_0^1 dv \psi(x, \mu, v) \quad \text{if } \mu \in [0, 1]. \quad (34)$$

Similarly, a full-range solution has the form:

$$\psi_i(x, \mu) = \psi(x, \mu, v_i^{a+}) + \psi(x, \mu, v_i^{a-}) + \int_{-1}^1 dv \psi_i(x, \mu, v) \quad \text{if } \mu \in [-1, 1]. \quad (35)$$

Case and Zweifel offers further detail on the completeness of these angle-shape functions to span half-range and full-range problems.

For full-range problems, we derive the orthogonality relation by inserting our ansatz for the solution modes into the transport equation, and multiplying the resulting equation by angle-shape function from an arbitrary Case-mode:

$$\alpha(\mu, v_i) \alpha(\mu, \tilde{v}_i) \left[ 1 - \frac{\mu}{v} \right] = \frac{c_i}{2} \alpha(\mu, \tilde{v}_i) \int_{-1}^1 d\mu \alpha(\mu, v_i), \quad (36)$$

which implies,

$$\alpha(\mu, v_i) \alpha(\mu, \tilde{v}_i) \left[ 1 - \frac{\mu}{\tilde{v}_i} \right] = \frac{c_i}{2} \alpha(\mu, v_i) \int_{-1}^1 d\mu \alpha(\mu, \tilde{v}_i). \quad (37)$$

Integrating over all directions and subtracting both equations:

$$\left( \frac{1}{v_i} - \frac{1}{\tilde{v}_i} \right) \int_{-1}^1 d\mu \mu \left[ \alpha(\mu, v_i) \alpha(\mu, \tilde{v}_i) \right] = 0, \quad (38)$$

$$\int_{-1}^1 d\mu \mu \left[ \alpha(\mu, v_i) \alpha(\mu, \tilde{v}_i) \right] = \begin{cases} 0 & \text{if } v_i \neq \tilde{v}_i \\ \int_{-1}^1 d\mu \mu \left[ \alpha(\mu, v_i) \right]^2 & \text{otherwise} \end{cases}. \quad (39)$$

This relation, which we define as our full-range filter, discriminates modes of different relaxation length. Given this full-range filter, the contribution to the angular flux from a single mode reduces to:

$$\psi_i(x, \mu, \tilde{v}_i) = \alpha(\mu, \tilde{v}_i) \frac{\int_{-1}^1 d\mu \mu \alpha(\mu, \tilde{v}_i) \psi_i(x, \mu)}{\int_{-1}^1 d\mu \mu \left[ \alpha(\mu, \tilde{v}_i) \right]^2}. \quad (40)$$

Using a similar approach, we can derive a weight function that discriminates modes of different relaxation lengths for problems only specified in half the angular domain. Again, we proceed by inserting the ansatz belonging to a single relaxation

length into the transport equation and multiplying the resulting expression by an angle-shape function and the hypothetical weight function:

$$H(\mu)\alpha(\mu, \nu_i)\alpha(\mu, \tilde{\nu}_i)\left[1 - \frac{\mu}{\nu_i}\right] = \frac{c_i}{2} H(\mu)\alpha(\mu, \tilde{\nu}_i) \int_{-1}^1 d\mu \alpha(\mu, \nu_i), \quad (41)$$

$$H(\mu)\alpha(\mu, \nu_i)\alpha(\mu, \tilde{\nu}_i)\left[1 - \frac{\mu}{\tilde{\nu}_i}\right] = \frac{c_i}{2} H(\mu)\alpha(\mu, \nu_i) \int_{-1}^1 d\mu \alpha_i(\mu, \tilde{\nu}_i). \quad (42)$$

We integrate over half of the angular domain; in this case we chose the range of positive directional cosines:

$$\begin{aligned} & \left[ \frac{1}{\nu_i} - \frac{1}{\tilde{\nu}_i} \right] \int_0^1 d\mu [\mu H(\mu)] [\alpha(\mu, \nu_i)\alpha(\mu, \tilde{\nu}_i)] \\ &= \int_0^1 d\mu H(\mu) [\alpha(\mu, \nu_i) - \alpha(\mu, \tilde{\nu}_i)]. \end{aligned} \quad (43)$$

If an integral weighted by  $H$  normalizes the angle-shape function to a constant that is independent of the relaxation length, then:

$$\int_0^1 d\mu H(\mu) [\alpha(\mu, \nu_i) - \alpha(\mu, \tilde{\nu}_i)] = 0, \quad (44)$$

and

$$\left[ \frac{1}{\nu} - \frac{1}{\tilde{\nu}} \right] \int_0^1 d\mu [\mu H(\mu)] [\alpha(\mu, \nu_i)\alpha(\mu, \tilde{\nu}_i)] = 0. \quad (45)$$

The  $H$  weight that satisfies the normalization condition is:

$$\mu H(\mu) = \gamma(\mu) [\nu_i^{a^+} - \mu]. \quad (46)$$

Here:

$$\gamma(\mu) = \frac{c_i}{2} \mu \frac{X^-(\mu)}{\Lambda^-(\mu)} = \frac{c_i}{2} \mu \frac{X^+(\mu)}{\Lambda^+(\mu)}, \quad (47)$$

$$\Lambda^\pm(\mu) = \lim_{\text{Im}(\mu) \rightarrow 0^\pm} \left[ 1 - \mu \frac{c_i}{2} \ln \left( \frac{1 + 1/\nu_i}{1 - 1/\nu_i} \right) \right], \quad (48)$$

$$X^\pm(\mu) = \lim_{\text{Im}(\mu) \rightarrow 0^\pm} \frac{1}{1 - \mu} \exp \left\{ \frac{1}{2\pi \cdot i} \int_0^1 d \frac{\mu_0}{\mu_0 - \mu} \ln \left[ \frac{\Lambda^+(\mu_0)}{\Lambda^-(\mu_0)} \right] \right\}, \quad (49)$$

with  $\mu \in [-1,1]$ .

Given the definition of the half-range weight function above then the half-range orthogonality relation is:

$$\int_0^1 d\mu [\mu H(\mu)] [\alpha(\mu, \nu_i) \alpha(\mu, \tilde{\nu}_i)] = \begin{cases} 0 & \text{if } \nu \neq \tilde{\nu} \\ \int_0^1 d\mu [\mu H(\mu)] [\alpha(\mu, \nu_i)]^2 & \text{otherwise} \end{cases}, \quad (50)$$

which implies that the contribution to the angular flux by a single mode is:

$$\psi(x, \mu, \nu_i) = \alpha(\mu, \nu_i) \frac{\int_0^1 d\mu \mu H(\mu) \alpha(\mu, \nu_i) \psi(x, \mu)}{\int_0^1 d\mu \mu H(\mu) [\alpha(\mu, \nu_i)]^2}. \quad (51)$$

Here the angular flux is only specified in half the angular domain and is constructed by modes from only half the relaxation lengths:

$$\psi(x, \mu) = \psi(x, \mu, \nu_i^{a+}) + \int_0^1 d\nu \psi(x, \mu, \nu), \quad \mu \in [0,1], \quad (52)$$

where we have arbitrarily chosen an angular flux specified in the range of positive directional cosines. A similar relation can be derived for a solution specified in the range of negative directional cosines.

#### II.D. Structure of the Asymptotic Solution Space in XY Geometry

Based on Bareiss and Abu-Shumays<sup>20</sup> framework to analyze the solution space of transport problems in multiple dimensions, we present an ansatz for the asymptotic component to the transport solution in XY geometry dimensions. Recall the transport equation in XY geometry for a region with homogeneous material conditions:

$$\hat{\Omega} \cdot \bar{\nabla} \psi_i + \sigma_{t,i} \psi_i(\bar{r}, \Omega) = \frac{c}{4\pi} \phi_i(\bar{r}) + Q_i(\bar{r}, \Omega), \quad (53)$$

$$\phi_i(\bar{r}) = \int_{4\pi} d\Omega \psi_i(\bar{r}, \Omega), \quad (54)$$

under the incident flux conditions:

$$\psi(\bar{r}_0, \Omega) = \psi_{inc}(\Omega), \quad \text{with } \hat{\Omega} \cdot \hat{n} < 0, \quad (55)$$

Here, for all  $\vec{r}_0$ ,  $\hat{n}$  is the outward-pointing, unit vector, normal to the boundaries of region  $i$ .

We guess that the asymptotic component to the angular flux is constructed on a combination of modes propagating along a direction  $\hat{w}$ :

$$\psi_i(\vec{r}, \hat{w}, \hat{\Omega}, \nu_i) = A(\hat{w}, \nu_i) \alpha(\hat{w}, \hat{\Omega}, \nu_i) \exp\left[-\frac{\sigma_{t,i}}{\nu_i} (x\hat{e}_x + y\hat{e}_y) \cdot \hat{w}\right]. \quad (56)$$

Here  $\hat{w}$  is a three dimensional vector with components that reside in the XY plane and along the  $z$  - axis. Mathematically:

$$\hat{w} = \cos \theta_0 \hat{w}_{xy} + \sin \theta_0 \hat{e}_z, \quad (57)$$

where

$$\hat{w}_{xy} = \cos \gamma_0 \hat{e}_x + \sin \gamma_0 \hat{e}_y,$$

$$\text{for } \theta_0 = [0, \pi/2] \text{ and } \gamma_0 = [0, 2\pi].$$

We insert our ansatz into the transport equation, to derive an expression for the angle-shape function:

$$-\alpha(\hat{w}, \hat{\Omega}, \nu_i) \cos \theta_0 \frac{\hat{\Omega} \cdot \hat{w}_{xy}}{\nu_i} + \alpha(\hat{w}, \hat{\Omega}, \nu_i) = \frac{c_i}{4\pi} \int_{4\pi} d\Omega \alpha(\hat{w}, \hat{\Omega}, \nu_i), \quad (58)$$

and we define the streaming vector with respect to the coordinate system defined by  $\hat{w}$ :

$$\hat{\Omega} = \cos \theta \hat{w}_{xy} + \sin \theta \left[ \cos \gamma \hat{e}_z + \sin \gamma (\hat{e}_z \times \hat{w}_{xy}) \right], \quad (59)$$

for  $\theta = [0, \pi]$  and  $\gamma = [0, 2\pi]$ .

Next, we normalize the angle-shape function to an arbitrary value, we choose:

$$\int_{4\pi} d\Omega \alpha(\hat{w}, \hat{\Omega}, \nu_i) = \frac{4\pi}{c_i}. \quad (60)$$

and we insert this normalization into Eq.(58). Solving for the angle-shape function, we obtain:

$$\alpha(\hat{w}, \hat{\Omega}, \nu_i) = \frac{\nu_i / \cos \theta_0}{\nu_i / \cos \theta_0 - \cos \theta}, \quad (61)$$

As in the slab geometry analysis, this arbitrary normalization is valid if the angle-shape function is a valid eigenfunction to transport operator.

With an explicit expression to the angle-shape function, we can define a dispersion relation that determines the spectrum of relaxation lengths:

$$\int_{4\pi} d\Omega \frac{v_i / \cos \theta_0}{v_i / \cos \theta_0 - \cos \theta} = \frac{4\pi}{c_i}, \quad (62)$$

we evaluate the integral to obtain:

$$\int_{-1}^1 d\mu \frac{v_i / \cos \theta_0}{v_i / \cos \theta_0 - \mu} = \frac{2}{c_i}. \quad (63)$$

Here  $\cos \theta_0$  is the projection of vector  $\hat{\omega}$  on the XY plane where the transport problem resides. We present in Fig. 2 an illustration of the coordinates defining  $\hat{\omega}$  with respect to the XY plane. We compare Eq.(63) to Eq.(21), and observe that the spectrum of relaxation lengths that satisfies the slab geometry dispersion relation equals the spectrum of  $v_i / \cos \theta_0$  values. We also note that the angle-shape function and spatial attenuation factor in XY geometry are not scaled by the relaxation length, but by  $v_i / \cos \theta_0$ . Thus, we can expect for each direction  $\hat{\omega}$  a spectrum of projected relaxation lengths in the transient range between [-1,1], and two of asymptotic magnitude greater than one. We group the ansatz over the range of directions  $\hat{\omega}$ , and obtain the XY geometry angular flux:

$$\psi_i(\vec{r}, \hat{\Omega}, v_i) = \int_0^\pi d\gamma_0 \int_0^1 d\mu_0 A(\mu_0, \gamma_0, v_i) \cdot \left\{ \frac{v_i / \mu_0}{v_i / \mu_0 - \cos \gamma_0 \mu - \sin \gamma_0 \eta} \cdot \exp \left[ -\frac{\sigma_{t,i}}{v_i / \mu_0} (\cos \gamma_0 x + \sin \gamma_0 y) \right] \right\}. \quad (64)$$

Here:

$$\mu = \hat{\Omega} \cdot \hat{e}_x,$$

$$\eta = \hat{\Omega} \cdot \hat{e}_y.$$

This ansatz is well known to satisfy the transport equation with asymptotic relaxation lengths. We design our iterative scheme for XY geometries with this asymptotic description in mind.

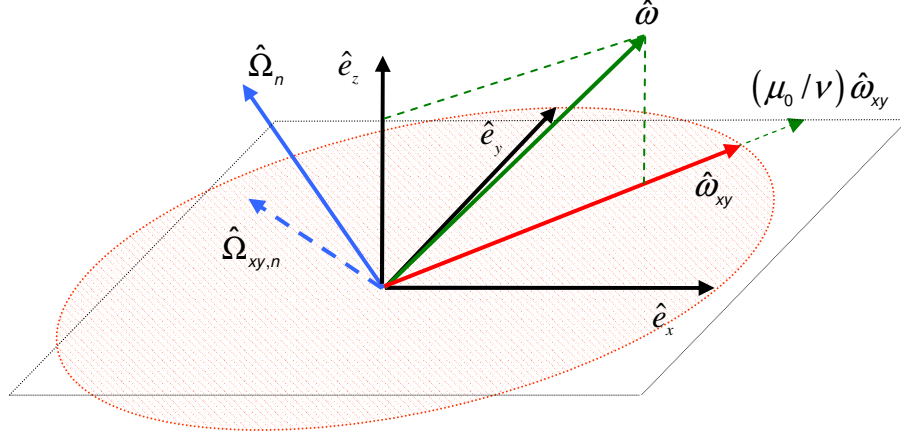


Fig. 2. Characteristic direction  $\hat{\omega}$  to an asymptotic mode and its projection to the XY plane  $\hat{\omega}_{xy}$ .

### II.E. Structure of the Solution Space to the Discrete Ordinates Approximation

The structure of the discrete ordinate solution follows closely that of its analytic counterpart. The discrete ordinate approximate transport equation for our problems of interests is:

$$\hat{\Omega}_n \cdot \vec{\nabla} \psi_{i,n} + \sigma_{t,i} \psi_{i,n}(\vec{r}) = \frac{c}{4\pi} \phi_i(\vec{r}) + Q_{i,n}(\vec{r}), \quad (65)$$

$$\phi_i(\vec{r}) = \sum_{m=1}^M w_m \psi_{i,m}(\vec{r}). \quad (66)$$

Here  $M$  is the number discrete streaming direction, for an  $S_N$  calculation in slab geometry  $M$  equals the number of levels  $N$ , in XY  $M$  equals  $N(N+1)/2$  and in XYZ  $M$  equals  $N(N+1)$ .

For slab geometry, the Case-modes have the form:

$$\psi_{i,n}(x, \nu_i) = A(\nu_i) \alpha(\mu_n, \nu_i) e^{-\sigma_i x / \nu_i}. \quad (67)$$

We insert this ansatz into the slab geometry transport equation to verify that it is a valid guess, and follow the same procedure used for the asymptotic modes in the analytic case to derive the discrete ordinate dispersion relation:

$$\sum_{n=1}^M w_n \frac{\nu_i}{\nu_i - \mu_n} = \frac{2}{c_i}. \quad (68)$$

We compute a common denominator to obtain the following characteristic polynomial:

$$P(\nu_i) = \frac{2}{c_i} \prod_{n=1}^M \nu_i - \mu_n - \nu_i \sum_{n=1}^M w_n \prod_{\substack{n=1 \\ m \neq n}}^M \nu_i - \mu_m. \quad (69)$$

The roots of  $P(\nu)$  are the relaxation lengths of the region. It follows from the order of the characteristic polynomial that the discrete ordinates solution is built on  $M$  relaxation lengths. If the host media is neither non-multiplying ( $c < 1$ ) nor pure-absorbing ( $c > 0$ ), then we obtain two asymptotic modes with magnitudes greater than one, and  $M - 2$  transient relaxation lengths with magnitude bound by discrete directional cosines of the quadrature:

$$\nu^1 < \mu_1 < \nu^2 < \mu_2 < \nu^2 < \dots < \mu_{M-1} < \nu^{M-1} < \mu_M < \nu^M,$$

Furthermore if the quadrature employed is symmetric:

$$\nu^m = -\nu^{M-m+1},$$

that is the relaxation lengths occur in pairs of equal magnitude and opposite sign.

We illustrate the behavior of  $P(\nu)$  in Fig. 3 by evaluating the left hand side of Eq.(68) with a symmetric quadrature set of size  $M = 4$ . In the hypothetical case that  $c_i$  equal 0.05, the roots to  $P(\nu)$  would be located in the figure at the intersection of the red and blue lines. We confirm that for this quadrature set  $P(\nu)$  has four singularity points

that occur when  $\nu$  equals the value of directional cosines in the quadrature. These quadrature points bound the magnitude of the transient relaxation lengths and provide a lower bound to the asymptotic ones. Therefore, as  $c_i$  approaches zero, the asymptotic and transient roots to  $P(\nu)$  equal the four directional cosines in the quadrature. On the other hand, as  $c_i$  approaches one, the asymptotic roots of the  $P(\nu)$  approach infinity.

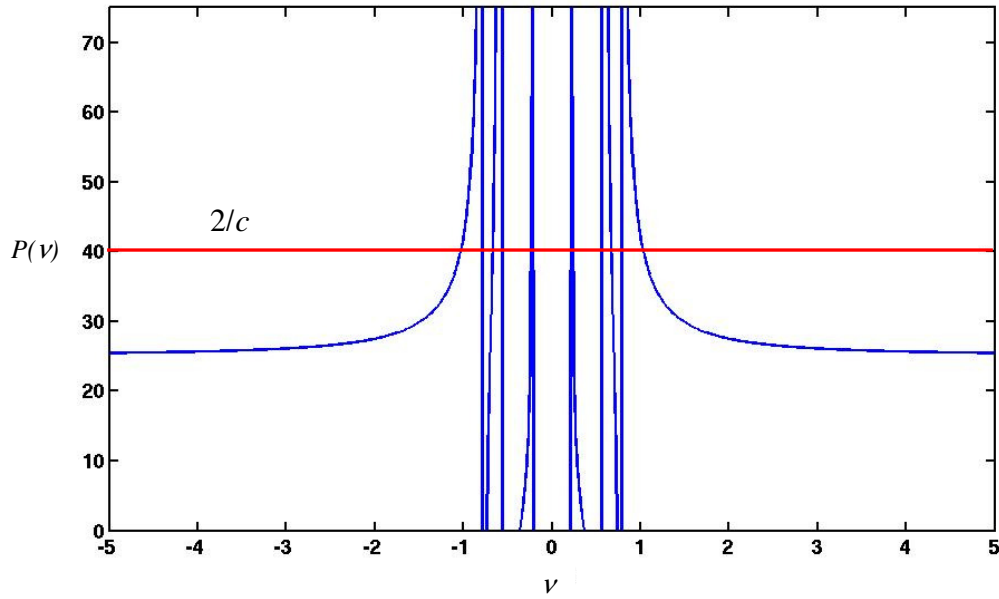


Fig. 3. Evaluation of the dispersion relation and location of its roots for  $c = 0.05$ .

Finally, we can normalize the angle-shape function to an arbitrary value since these functions correspond to the equation's eigenfunctions. We choose the following normalization:

$$\sum_{n=1}^M w_n \alpha_n (\mu_n, \nu_i^k) = \frac{2}{c_i}, \quad (70)$$

which results in the following angle-shape functions:

$$\alpha(\mu_n, \nu_i^k) = \frac{\nu_i^k}{\nu_i^k - \mu_n}. \quad (71)$$

The structure of the discrete ordinate approximate solution does not require the addition of Cauchy's principal value, since the lack of a continuous spectrum of streaming directions avoids the singularity points that exist otherwise. Thus for problems with non-multiplicative media ( $c < 1$ ), we can compute all relaxation lengths with the dispersion relation. While for problems with purely-absorbing media ( $c = 0$ ), the relaxation lengths migrate towards the value of the discrete directional and the angle-shape functions evaluate to zero for every angle except at angles whose directional cosine equal the relaxation length.

For XY geometry, we guess that the discrete ordinates solution is constructed by a linear combination of the following modes:

$$\psi_n^k(\vec{r}) = A_i^k(\hat{\omega}) \alpha(\hat{\omega}, \hat{\Omega}_n, \nu_i^k) \exp\left[-\frac{\sigma_{t,i}}{\nu_i^k} \hat{\omega} \cdot (x\hat{e}_x + y\hat{e}_y)\right], \quad (72)$$

where,

$$\hat{\omega} = \cos \theta_0 \hat{\omega}_{xy} + \sin \theta_0 \hat{e}_z,$$

$$\hat{\Omega}_n = \cos \theta_n \hat{\omega}_{xy} + \sin \theta_n \left[ \cos \gamma_n \hat{e}_z + \sin \gamma_n (\hat{e}_z \times \hat{\omega}_{xy}) \right],$$

$$\hat{\omega}_{xy} = \cos \gamma_0 \hat{e}_x + \sin \gamma_0 \hat{e}_y,$$

$$\text{for } \theta_0 = [0, \pi/2] \text{ and } \gamma_0 = [0, 2\pi].$$

We insert this ansatz into the discrete ordinates transport equation:

$$\alpha(\hat{\omega}, \hat{\Omega}_n, \nu_i^k) \left[ -\frac{\cos \theta_n}{\nu_i^k / \cos \theta_0} + 1 \right] = \frac{c_i}{4\pi} \sum_{n=1}^M w_n \alpha(\hat{\omega}, \hat{\Omega}_n, \nu_i^k), \quad (73)$$

and insert the normalization of the angle-shape function:

$$\sum_{n=1}^M w_n \alpha(\hat{\omega}, \hat{\Omega}_n, \nu_i^k) = \frac{4\pi}{c_i}, \quad (74)$$

to yield the angle-shape function expression:

$$\alpha(\hat{\omega}, \hat{\Omega}_n, v_i^k) = \frac{v_i^k / \cos \theta_0}{v_i^k / \cos \theta_0 - \cos \theta_n} \quad (75)$$

Given this angle-shape function, the dispersion relation is:

$$\sum_{n=1}^M w_n \frac{v_i^k / \cos \theta_0}{v_i^k / \cos \theta_0 - \hat{\Omega}_n \cdot \hat{\omega}_{xy}} = \frac{4\pi}{c_i} \quad (76)$$

We recast our ansatz in terms of the ratio  $v^k / \cos \theta_0$ , to find that this ratio scales the distribution of the ansatz in angle and space:

$$\psi_n^k(\vec{r}) = A_i^k(\hat{\omega}) \left\{ \frac{v_i^k / \cos \theta_0}{v_i^k / \cos \theta_0 - \hat{\Omega}_n \cdot \hat{\omega}_{xy}} \exp \left[ -\frac{\sigma_{i,i}}{v_i^k / \cos \theta_0} \hat{\omega}_{xy} \cdot (x\hat{e}_x + y\hat{e}_y) \right] \right\} \quad (77)$$

In the slab geometry study, we searched the range of relaxation lengths to understand the behavior of the angular flux in space and angle. These relaxation lengths were obtained by calculating the roots to the dispersion relation. In XY geometry the relaxation lengths do not scale the solution; instead, the solution is scaled by the ratio  $v^k / \cos \theta_0$ . Fortunately, these ratio are also the roots to Eq.(76). Slab and XY geometry are both scaled by the roots to the dispersion relation, even if these roots only yield the relaxation lengths in slab geometry. As a side note, this implies that since  $\cos \theta_0$  is a continuous function with a range between [0,1] then, discrete ordinates solution in XY geometry are constructed on an infinite number of relaxation lengths. Therefore, we make the following modification to our notation:

$$\psi_n^k(\vec{r}) = A_i^k(\hat{\omega}) \frac{(v_i / \cos \theta_0)^k}{(v_i / \cos \theta_0)^k - \hat{\Omega}_n \cdot \hat{\omega}_{xy}} \exp \left[ -\frac{\sigma_{i,i}}{(v_i / \cos \theta_0)^k} \hat{\omega}_{xy} \cdot (x\hat{e}_x + y\hat{e}_y) \right], \quad (78)$$

to reflect that the roots to Eq.(76) are discrete values and not the relaxation lengths.

The roots to the XY geometry dispersion relation are a function of the product  $\hat{\Omega}_n \cdot \hat{\omega}_{xy}$ . Similar to slab geometry, the range of this product is between -1 and 1.

Therefore, we can expect  $M - 2$  roots with a magnitude smaller than one, the transient lengths, and 2 roots with a magnitude larger than 1, the asymptotic lengths.

In slab geometry, the roots of the dispersion relation are a function of the directional cosines of the quadrature. This implies that in slab geometry a symmetric quadrature set yields symmetric relaxation lengths. In XY geometry this is no longer the case. Even if a symmetric quadrature is employed, the distribution of  $\hat{\Omega}_n \cdot \hat{\omega}_{xy}$  products may not be symmetric; therefore, neither will be the distribution of the roots to the XY geometry dispersion relation. The lengths scaling the XY geometry Case-modes are not symmetric.

Finally, it is possible that multiple  $\hat{\Omega}_n \cdot \hat{\omega}_{xy}$  products share the same value. In such cases, the multiplicity of some roots to the dispersion relation would be greater than one. This implies that the expression to the angle-shape and attenuation functions would change so that, the solution space to the transport equation could be fully spanned.

With these observations in mind, the angular flux satisfying the discrete ordinate XY geometry transport equation is:

$$\psi_n(x, y) = \sum_{k=1}^M \int_0^1 d\mu_0 \int_0^\pi d\gamma_0 \psi_n^k(\mu_0, \gamma_0, x, y) \quad (79)$$

Here:

$$\mu_n = \hat{\Omega}_n \cdot \hat{e}_x,$$

$$\eta_n = \hat{\Omega}_n \cdot \hat{e}_y,$$

$$\alpha_{n,i}^k(\mu_0, \gamma_0) = \frac{(v_i / \mu_0)^k}{(v_i / \mu_0)^k - \cos \gamma_0 \mu_n - \sin \gamma_0 \eta_n},$$

$$\psi_n^k(\mu_0, \gamma_0, x, y) = A_i^k(\mu_0, \gamma_0) \alpha_{n,i}^k(\mu_0, \gamma_0) \exp \left[ -\frac{\sigma_{t,i}}{(v_i / \mu_0)^k} \hat{\omega} \cdot (x \hat{e}_x + y \hat{e}_y) \right].$$

## II.F. Full-Range and Half-Range Discrete Ordinates Orthogonality

We conclude this chapter with a derivation of the full and half-range orthogonality relations in slab geometry and extend the full-range orthogonality relation to multiple dimensions. For this derivation, we assume that the completeness of the

angle-shape functions as the basis to span the angular flux in the full and half-range remains valid and thus, the angle-shape functions are orthogonal in the angular domain. For the full-range orthogonality in 1D, we insert the ansatz belonging to a relaxation length into slab-geometry the homogeneous transport equation and multiply the resulting relation by the angle-shape function from an arbitrary mode:

$$-\frac{\mu_n}{\nu^k} \alpha_{i,n}^k \alpha_{i,n}^l + \alpha_{i,n}^k \alpha_{i,n}^l = \frac{c_i}{2} \alpha_{i,n}^l \sum_{n=1}^M w_n \alpha_{i,n}^k, \quad (80)$$

Similarly, by inserting the arbitrary Case-mode into the transport equation:

$$-\frac{\mu_n}{\nu^l} \alpha_{i,n}^k \alpha_{i,n}^l + \alpha_{i,n}^k \alpha_{i,n}^l = \frac{c_i}{2} \alpha_{i,n}^k \sum_{n=1}^M w_n \alpha_{i,n}^l. \quad (81)$$

Integrating the above equations over all directions and subtracting them, the result is:

$$\left[ \frac{1}{\nu^l} - \frac{1}{\nu^k} \right] \sum_{n=1}^M w_n \mu_n \alpha_{i,n}^k \alpha_{i,n}^l = 0, \quad (82)$$

which implies:

$$\sum_{n=1}^M w_n \mu_n \alpha_{i,n}^k \alpha_{i,n}^l = \begin{cases} 0, & \text{if } k \neq l \\ \sum_{n=1}^M w_n \mu_n [\alpha_{i,n}^k]^2, & \text{if } k = l. \end{cases} \quad (83)$$

Operating with this orthogonality relation on the angular flux, we obtain the contribution from a single mode to the total solution:

$$\psi_n^k(x) = \alpha_{i,n}^k \frac{\sum_{n=1}^M w_n \mu_n \alpha_{i,n}^k \psi_n(x)}{\sum_{n=1}^M w_n \mu_n \alpha_{i,n}^k \alpha_{i,n}^k}. \quad (84)$$

We built the half-range orthogonality relation by stating the conditions that we aim to satisfy, and constructing from these conditions a system of equations with the half-range orthogonality weight function as the unknown. The conditions that we aim to satisfy are:

$$\sum_{\mu_n < 0} w_n W_{i,n}^k \alpha_{i,n}^k \alpha_{i,n}^l = \begin{cases} 0 & \text{if } l \neq k \\ \sum_{\mu_n < 0} w_n W_{i,n}^k [\alpha_{i,n}^k]^2 & \text{if } l = k \end{cases} \text{ with } \nu^k, \nu^l < 0, \quad (85)$$

$$\sum_{\mu_n > 0} w_n W_{i,n}^k \alpha_{i,n}^k \alpha_{i,n}^l = \begin{cases} 0 & \text{if } l \neq k \\ \sum_{\mu_n > 0} w_n W_{i,n}^k [\alpha_{i,n}^k]^2 & \text{if } l = k \end{cases} \text{ with } \nu^k, \nu^l > 0. \quad (86)$$

For each case-mode, we can construct a system of  $M/2$  equations to solve for the value of the weight function at different quadrature points. Based on the evaluation of these weight functions, if an angular flux is constructed by a linear combination of modes from only half the range of Case-modes, then the contribution from a single mode to the angular flux is:

$$\psi_n^k(x) = \alpha_{i,n}^k \frac{\sum_{\mu_m > 0} w_m W_{i,m}^k \alpha_{i,m}^k \psi_m(x)}{\sum_{\mu_m > 0} w_m W_{i,m}^k \alpha_{i,m}^k \alpha_{i,m}^k}, \quad (87)$$

where:

$$\psi_n(x) = \sum_{\nu^k > 0} A_i^k \alpha_{i,n}^k f^k(x).$$

Similarly:

$$\psi_n^k(x) = \alpha_{i,n}^k \frac{\sum_{\mu_n < 0} w_n W_{i,n}^k \alpha_{i,n}^k \psi_n(x)}{\sum_{\mu_n < 0} w_n W_{i,n}^k \alpha_{i,n}^k \alpha_{i,n}^k}, \quad (88)$$

with

$$\psi_n(x) = \sum_{\nu^k < 0} A_i^k \alpha_{i,n}^k f^k(x).$$

In XY geometry, the filtering of Case-modes is more complex. Case-modes continue to be scaled by multiple relaxation lengths, but are constructed along multiple

directions  $\hat{\omega}$ . We derive an orthogonality relation between Case-modes in multiple dimensions based on our slab geometry approach. We multiply the transport equation as satisfied by a single Case-mode by the angular flux of another arbitrary Case-mode:

$$\psi_n^l \hat{\Omega}_n \cdot \bar{\nabla} \psi_n^k + \sigma_{t,i} \psi_n^l \psi_n^k = \sigma_{t,i} \frac{c_i}{4\pi} \psi_n^l \phi^k, \quad (89)$$

Similarly:

$$\psi_n^k \hat{\Omega}_n \cdot \bar{\nabla} \psi_n^l + \sigma_{t,i} \psi_n^k \psi_n^l = \sigma_{t,i} \frac{c_i}{4\pi} \psi_n^k \phi^l. \quad (90)$$

After numerical integrating the equations above over all streaming directions, and subtracting them, we obtain:

$$\sum_{n=1}^M w_n \psi_n^l \left[ \hat{\Omega}_n \cdot \bar{\nabla} \psi_n^k \right] = \sum_{n=1}^M w_n \psi_n^k \left[ \hat{\Omega}_n \cdot \bar{\nabla} \psi_n^l \right]. \quad (91)$$

This relation can only segregate Case-modes with different relaxation lengths and equal direction  $\hat{\omega}$ . To show that this is the case, we insert our ansatz to the structure of Case-modes in multiple dimensions, Eq.(72), into Eq.(91):

$$\begin{aligned} & \sum_{n=1}^M w_n \alpha_n^l(\mu_0, \gamma_0) \alpha_n^k(\mu_0, \gamma_0) \left[ \frac{\hat{\Omega}_n \cdot \hat{\omega}_{xy}^k}{(\nu / \cos \mu_0)^k} \right] \\ &= \sum_{n=1}^M w_n \alpha_n^l(\mu_0, \gamma_0) \alpha_n^k(\mu_0, \gamma_0) \left[ \frac{\hat{\Omega}_n \cdot \hat{\omega}_{xy}^l}{(\nu / \cos \mu_0)^l} \right], \end{aligned} \quad (92)$$

$$\left( \frac{\hat{\omega}_{xy}^k \cdot}{(\nu / \cos \mu_0)^k} - \frac{\hat{\omega}_{xy}^l \cdot}{(\nu / \cos \mu_0)^l} \right) \cdot \sum_{n=1}^M w_n \hat{\Omega}_n \alpha_n^l(\mu_0, \gamma_0) \alpha_n^k(\mu_0, \gamma_0) = 0. \quad (93)$$

If both modes are aligned, then the orthogonality relation is reduced to its slab geometry form:

$$\sum_{n=1}^M w_n (\hat{\omega}_{xy} \cdot \hat{\Omega}_n) \alpha_{i,n}^k(\mu_0, \gamma_0) \alpha_{i,n}^l(\mu_0, \gamma_0)$$

$$= \begin{cases} 0, & k \neq l \\ \sum_{n=1}^M w_n [\hat{\omega}_{xy} \cdot \hat{\Omega}_n] [\alpha_{i,n}^k(\mu_0, \gamma_0)]^2, & k = l \end{cases} \quad (94)$$

Otherwise, we obtain a relation that does not differentiate between angular-shape functions belonging to different relaxation lengths.

The homogeneous angular flux in multiple dimensions is constructed on a linear combination of Case-modes scaled by multiple relaxation lengths, and propagating along an infinite number of directions  $\hat{\omega}$ . We aim for a filtering relationship that differentiates from a homogeneous angular flux the contribution from those Case-modes scaled by a single relaxation length. From Eq.(93), we found that an orthogonality relation only exists for those Case-modes propagating along the same direction  $\hat{\omega}_{xy}$ . Therefore, a successful filtering scheme requires a reasonable estimate to the residual produced from filtering Case-modes propagating along different directions  $\hat{\omega}_{xy}$ .

We employ the filtering relations in Eqs.(84) in the derivation of the slab geometry iterative scheme. These filtering relations allow us to isolate the contribution to the homogeneous angular flux from Case-modes scaled by a single relaxation length. In doing so, we obtain the freedom to divide the homogeneous transport equation into multiple problems; each satisfied by a group of Case-modes and potentially solved by diverse numerical techniques. For slab geometry the filtering process is straightforward; an orthogonality relation exists that can fully isolate any Case-mode. In XY geometry dimensions the filtering process is uncertain. Filtering is only done accurately if all Case-modes in the angular flux are aligned along the same direction; otherwise, a filtering residual is produced. In the derivation of our iterative scheme in XY geometry dimensions, we keep this uncertainty in mind.

### *II.G. Summary*

In this chapter, we have presented the structure of the analytic solution for problems with isotropic scattering in slab and XY geometry, and for a continuous angular variable and for the discrete ordinates method. Our approach was largely based

on Case and Zweifel's analysis of the slab geometry problem; in that we related the components of the Case-mode structure with the eigenvalues and eigenfunctions of the transport operator. We have derived an implicit relation, the dispersion relation, which determines the eigenvalues to the transport operator that respect the overall equation and label these eigenvalues as relaxation lengths. We have also derived an explicit expression for the respective eigenfunctions, and labeled them as the angle-shape functions. Based on the magnitude of the relaxation length, two groups of modes with solutions under distinct scales arise: those with asymptotic scales, and those with transient scales. We have assumed that the Case-mode structure for our range of problems constitutes the complete homogeneous solution, and exploited this completeness to construct orthogonality relations that segregate the contribution to the homogeneous solution from a specific relaxation length. We proceed with an extension of the Case-mode analysis to problems discretized spatially under the family of Continuous and Discontinuous Finite Element methods in slab geometry. Recall that our goal is to construct an iterative method that can discriminate among Case-mode of different scale and solves each efficiently by exploiting its scaling properties separately.

### III. THE CONTINUOUS FINITE ELEMENT APPROXIMATION

We define the family of Continuous Finite Element Methods (CFEM) to discretize the Discrete-Ordinate transport equation in slab geometry, for one energy group and isotropic scattering. With this family of methods defined, we analyze the Case-mode structure of its solution and present numerical results that suggest that this analysis is correct. The analysis of this family of methods is the first step towards the construction of an efficient transport solving algorithm that exploits the range of scales in the solution.

#### III.A. The Continuous Finite Element Family of Methods

The slab geometry, one group transport equation, with isotropic scattering is:

$$\mu_n \frac{\partial \psi_n}{\partial x} + \sigma_t(x) \psi_n(x) = \sigma_t(x) \frac{c(x)}{2} \phi(x) + Q(x). \quad (95)$$

Here we define the scalar flux as:

$$\phi(x) = \sum_{n=1}^N w_n \psi_n(x) \quad \text{with} \quad \sum_{n=1}^N w_n = 2. \quad (96)$$

We begin our derivation by stating that the angular flux solution is projected to a space of lower dimension, which is spanned by a set of basis functions  $b_r$ :

$$\psi_n(x) = \sum_{r=1}^R \psi_{n,r} b_r(x). \quad (97)$$

We chose these basis functions to be polynomials of order  $P$  and aim at constructing a system of equations that dictates the amplitude of each polynomial basis. For convenience in our analysis, we select the group of Cardinal Functions as our polynomial basis. To define these Cardinal Functions we divide the spatial domain into  $J$  cells, and assign to each cell  $P + 1$  nodes. We designate the location of node  $p$  in cell  $j$  as  $x_{j,p}$ . Given this nomenclature the angular flux approximation is defined as:

$$\psi_n(x) = \sum_{p=1}^{P+1} \psi_{n,j,p} b_{j,p}(x), \quad x \in [x_{j,1}, x_{j,P+1}]. \quad (98)$$

We define the cardinal basis function as the piecewise continuous polynomials of degree  $P$  such that:

$$b_{j,p}(x_{j',p'}) = \delta_{j,j'} \delta_{p,p'}. \quad (99)$$

For CFEMs, we determine the polynomial amplitudes by enforcing the continuity of the angular flux at cell boundaries and integrating the transport equation over the cell's domain weighted by a space of  $P$  functions. The result is a system  $P + 1$  equations for each cell. We chose the weight space to equal the first  $P$  basis functions of the solution space in each cell. The system of equation in cell  $j$  is:

$$\psi_{n,j,1} = \begin{cases} \psi_{n,inc} & \text{if } j = 1 \\ \psi_{n,j-1,P+1} & \text{if } j > 1 \end{cases}, \quad \text{for } \mu_n > 0, \quad (100)$$

$$\psi_{n,j,P+1} = \begin{cases} \psi_{n,inc} & \text{if } j = J \\ \psi_{n,j+1,1} & \text{if } j < J \end{cases}, \quad \text{for } \mu_n < 0, \quad (101)$$

$$\int_{x_{j,1}}^{x_{j,P+1}} dx b_{j,i}(x) \left\{ \sum_{p=1}^{P+1} \psi_{n,j,p} \left[ \mu_n \frac{\partial b_{j,p}}{\partial x} + \sigma_{t,i} b_{j,p}(x) \right] \right\} = \int_{x_{j,1}}^{x_{j,P+1}} dx b_{j,i}(x) \left\{ \sigma_{t,j} \frac{c_j}{2} \sum_{p=1}^{P+1} b_{j,p}(x) [\phi_{j,p} + Q_{j,p}(x)] \right\}, \quad \text{for } i = 1 \dots P. \quad (102)$$

Here we assumed that the material properties are constant inside of cell  $j$ , and we defined the scalar flux and the moments to the extraneous source as:

$$\phi_{j,p} = \sum_{n=1}^N w_n \psi_{n,j,p}, \quad (103)$$

$$Q_{j,p} = \int_{x_{j,1}}^{x_{j,P+1}} dx b_{j,p}(x) Q(x). \quad (104)$$

A widely implemented member of the CFEM family is the Diamond Difference method which corresponds to a linear polynomial basis and weight space,  $P = 1$ . The CFEM family of methods can be solved using Source Iteration sweeps or Block Inversions.

### III.B. Case-Mode Analysis of the CFEM Solution

We analyze the Case-mode structure of the homogeneous solution to the CFEM approximate transport equation. With this analysis our goal is to describe the structure of the modes that are linearly combined to construct the homogeneous solution, and to determine the relaxation lengths that scale each mode. Recall that the homogeneous solution satisfies the transport equation in the absence of an extraneous source, while the particular solution satisfies the transport equation with all its components. Based on the procedures develop in the previous chapter for the analytic transport equation, we guess that the angular has the structure:

$$\psi_{n,j,p}^k = A^k (g^k)^{j-1} \cdot a_n^k \cdot z_p^k, \quad (105)$$

$$\psi_{n,j,p} = \sum_{k=1}^N \psi_{n,j,p}^k, \quad (106)$$

where

$k \equiv$  mode index,

$j \equiv$  cell index,

$p \equiv$  node index,

$A^k \equiv$  amplitude,

$a_n^k \equiv$  angle-shape function,

$g^k \equiv$  single-cell attenuation factor,

$z_p^k \equiv$  left boundary node to node  $p$  attenuation factor.

We define that single-cell attenuation factor that we seek based on the continuity of angular flux conditions as:

$$z_{p+1}^k = z_1^k \cdot g^k. \quad (107)$$

We insert the ansatz into the last  $P$  equations of the CFEM system to obtain:

$$\begin{aligned}
a_n^k \sum_{p=1}^{P+1} z_p^k \int_{x_{j,1}}^{x_{j,P+1}} dx b_{j,i}(x) \left[ \frac{\partial b_{j,p}}{\partial x} + \frac{\sigma_t}{\mu_n} b_{j,p}(x) \right] = \\
\frac{\sigma_t}{\mu_n} \frac{c}{2} \sum_{m=1}^N w_m a_m^k \sum_{p=1}^{P+1} z_p^k \int_{x_{j,1}}^{x_{j,P+1}} dx b_{j,i}(x) b_{j,p}(x), \quad \text{for } i = 1 \dots P. \quad (108)
\end{aligned}$$

To reduce the number of subscripts, we removed the subscript indicating the material property under the assumption that the system of equation belongs to a single-cell and the material properties to this cell are homogeneous. With this simplification in mind, we recast this system of equation in matrix form:

$$a_n^k [\mathbf{L} + \tau_n \mathbf{M}] \bar{z}^k = \tau_n \frac{c}{2} \sum_{m=1}^N w_m a_m^k \mathbf{M} \bar{z}^k. \quad (109)$$

Here  $\mathbf{L}, \mathbf{M} \in \mathbb{R}^{P \times P}$ ,  $\bar{z}^k \in \mathbb{R}^{P \times 1}$ :

$$\tau_n = \frac{\sigma_t \Delta x}{\mu_n},$$

$$[\bar{z}^k]_p = z_p^k, \quad p = 1 \dots P,$$

and

$$[\mathbf{L}]_{i,p} = \int_{x_{j,1}}^{x_{j,P+1}} dx b_{j,i}(x) \frac{db_{j,p}(x)}{dx}, \quad (110)$$

$$[\mathbf{L}]_{i,1} = \int_{x_{j,1}}^{x_{j,P+1}} dx b_{j,i}(x) \frac{db_{j,1}(x)}{dx} + g^k \int_{x_{j,1}}^{x_{j,P+1}} dx b_{j,i}(x) \frac{db_{j,P+1}(x)}{dx}, \quad (111)$$

$$[\mathbf{M}]_{i,p} = \frac{1}{\Delta x} \int_{x_{j,1}}^{x_{j,P+1}} dx b_{j,i}(x) b_{j,p}(x), \quad (112)$$

$$[\mathbf{M}]_{i,1} = \frac{1}{\Delta x} \left[ \int_{x_{j,1}}^{x_{j,P+1}} dx b_{j,i}(x) b_{j,1}(x) + g^k \int_{x_{j,1}}^{x_{j,P+1}} dx b_{j,i}(x) b_{j,P+1}(x) \right]. \quad (113)$$

After some algebra Eq.(109) yields:

$$\bar{z}^k = \tau_n \frac{c}{2} \sum_{n=1}^N w_n [\mathbf{I} + \tau_n \mathbf{L}^{-1} \mathbf{M}]^{-1} \cdot \mathbf{L}^{-1} \mathbf{M} \cdot \bar{z}^k, \quad (114)$$

Based on the structure of the matrix in the eigenvalue problem above, it follows that:

$$\mathbf{L}^{-1} \mathbf{M} \bar{z}^k = \lambda^k \cdot \bar{z}^k. \quad (115)$$

or that  $z$  is a valid eigenvector to both  $\mathbf{L}$  and  $\mathbf{M}$ .

We replace the eigenvalue relationship above into Eq.(109) and add it over all streaming directions:

$$\sum_{n=1}^N w_n a_n^k \vec{z}^k = \frac{c}{2} \sum_{m=1}^N w_m a_m^k \sum_{n=1}^N w_n \frac{\tau_n}{\lambda + \tau_n} \vec{z}^k, \quad (116)$$

and revert  $\tau$  to its original value:

$$\sum_{n=1}^N w_n \frac{\sigma_t \Delta x / \lambda^k}{\sigma_t \Delta x / \lambda^k + \mu_n} = \frac{2}{c}. \quad (117)$$

We compare this result to the dispersion relation presented in the previous chapter:

$$\sum_{n=1}^N w_n \frac{v^k}{v^k - \mu_n} = \frac{2}{c}, \quad (118)$$

and conclude that the eigenvalues of  $\mathbf{L}^{-1}\mathbf{M}$  must equal:

$$\lambda^k = -\frac{\sigma_t \Delta x}{v^k}. \quad (119)$$

The eigenvalues of  $\mathbf{L}^{-1}\mathbf{M}$  scale the optical thickness of each cell to the relaxation length of each mode, similarly to the scaling done to the optical thickness by the directional cosine in  $\tau_n$ . To maintain a consistency of nomenclature, we define relaxation-length-scaled optical thickness as:

$$\tau^k \equiv -\lambda^k = \frac{\sigma_t \Delta x}{v^k}. \quad (120)$$

Next, we observe that multiples of  $z$  are valid eigenvectors of a mode. Thus, we can normalize the angle-shape functions to an arbitrary value while keeping the product  $a_n z$  constant and  $z$  as a valid eigenvector. As in the previous chapter, we chose the normalization:

$$\sum_{n=1}^N w_n a_n^k = \frac{2}{c}. \quad (121)$$

We insert this normalization into Eq.(109), and replace the  $\mathbf{L}^{-1}\mathbf{M}$  by its eigenvalue to obtain the expression for the angle shape function:

$$a_n^k = \alpha_n^k = \frac{\nu^k}{\nu^k - \mu_n}. \quad (122)$$

The angle-shape function is exact with respect to the slab-geometry analytic angle-shape function.

We conclude this analysis with the expression of the single-cell attenuation factor  $g$ , which we defined in Eq.(107) in terms of  $z$ . We recast the eigenvalue problem of  $z$  as:

$$\left(\tilde{\mathbf{M}} + g^k \cdot \mathbf{M}_{P,1}\right) \bar{z}^k = \frac{1}{\lambda} \left(\tilde{\mathbf{L}} + g^k \cdot \mathbf{L}_{P,1}\right) \bar{z}^k, \quad (123)$$

where

$$\mathbf{L} = \tilde{\mathbf{L}} + g^k \mathbf{L}_{P,1}, \text{ with } \mathbf{L}, \tilde{\mathbf{L}}, \mathbf{L}_{P,1} \in \mathbb{R}^{P \times P},$$

$$\left[\mathbf{L}_{P,1}\right]_{i,j} = \delta_{i,P} \delta_{j,1} \left[\mathbf{L}\right]_{1,P},$$

$$\mathbf{M} = \tilde{\mathbf{M}} + g^k \mathbf{M}_{P,1}, \text{ with } \mathbf{M}, \tilde{\mathbf{M}}, \mathbf{M}_{P,1} \in \mathbb{R}^{P \times P}.$$

$$\left[\mathbf{M}_{P,1}\right]_{i,j} = \delta_{i,P} \delta_{j,1} \left[\mathbf{M}\right]_{1,P}.$$

Based on the sparse structure of  $\mathbf{L}_{P,1}$ , we simplify the problem to:

$$\frac{1}{g^k} \not\leftarrow = \left(\tilde{\mathbf{M}} - \frac{1}{\lambda_i^k} \tilde{\mathbf{L}}\right)^{-1} \left(\mathbf{M}_{P,1} + \frac{1}{\lambda_i^k} \mathbf{L}_{P,1}\right) \not\leftarrow. \quad (124)$$

Each element of the  $\tilde{\mathbf{M}} - \frac{1}{\lambda_i^k} \tilde{\mathbf{L}}$  and  $\mathbf{M}_{P,1} + \frac{1}{\lambda_i^k} \mathbf{L}_{P,1}$  matrices is a polynomial of the form  $c_0 + \lambda_i^k c_1$  with  $c_0$  and  $c_1$  determine solely by the basis functions of the CFEM employed. Thus, the single-cell attenuation factor  $g$  is a ratio of polynomials in  $\lambda_i^k$ , which itself depends only on the cell optical thickness and the relaxation length. More specifically, the single-cell attenuation factor is a function of  $\lambda_i^k$  and is not influenced by the directional cosines. This is an important scaling property shared between the analytic single-cell attenuation factor  $\exp(-\lambda_i^k)$  and the CFEM single-cell attenuation factor.

Because these CFEM make no special treatment for right and left-pointing directional cosines, we can deduce the following property for the CFEM single-cell attenuation factor:

$$g(\tau^k) = \frac{1}{g(-\tau^k)}. \quad (125)$$

This property implies that the polynomials in the numerator and denominator of the single-cell attenuation factor have the same order. Furthermore, the coefficient to each power of  $\tau^k$  in the numerator and denominator must be equal, except for the signs of the odd power coefficients. We conclude that the single-cell attenuation factor is a rational polynomial of the form:

$$g(\tau^k) = \frac{d_0 - d_1\tau^k + \dots + d_p(-\tau^k)^p}{d_0 + d_1\tau^k + \dots + d_p(\tau^k)^p}. \quad (126)$$

We have verified that if the weight and basis functions span the polynomial space of degree  $P$ , then  $g^k$  is a  $(P, P)$  Padé approximation of the  $\exp(-\tau^k)$  function. Based on the properties of this family of rational polynomials, we expect that a Taylor expansion of  $g^k$  about  $\tau^k = 0$  yields an accurate result with respect to the exact single-cell attenuation factor of order  $2P$ . For example the single-cell attenuation factor for the linear CFEM is:

$$g(\tau^k) = \frac{2 - \tau^k}{2 + \tau^k}. \quad (127)$$

Even in the case that the weight and basis functions are not polynomials Eq.(126) holds with modified coefficients.

### III.C. Numerical Results

We gathered two sets of numerical datum to support the results from our analysis. First, we performed an order of convergence study on the angle-shape function and single-cell attenuation of the DD ( $P = 1$ ), the quadratic ( $P = 2$ ) and the sixth-order CFEM ( $P = 6$ ) CFEMs. The order of convergence of the angle-shape function and single-cell attenuation factor of these CFEMs were computed with respect to the analytic single-cell attenuation factor and  $(P, P)$  Padé. We performed a second experiment that implemented the discrete ordinates Filtering relations from Section II to segregate the contribution from each mode to the homogeneous solutions. Our goal with this

experiment was to illustrate the role of each CFEM Case-mode in the construction of the total solution.

### Order of Convergence

We solved the one region problem presented in Fig. 4 with an  $S_2$  Gauss-Legendre quadrature set and three CFEMs: DD (linear), quadratic and sixth-order. The thickness of the slab was kept constant to 3 cm, and the problem was solved with nine homogeneous meshes of cell thickness  $\Delta x = 3^{1-J}$ , with  $J = [1,9]$ .

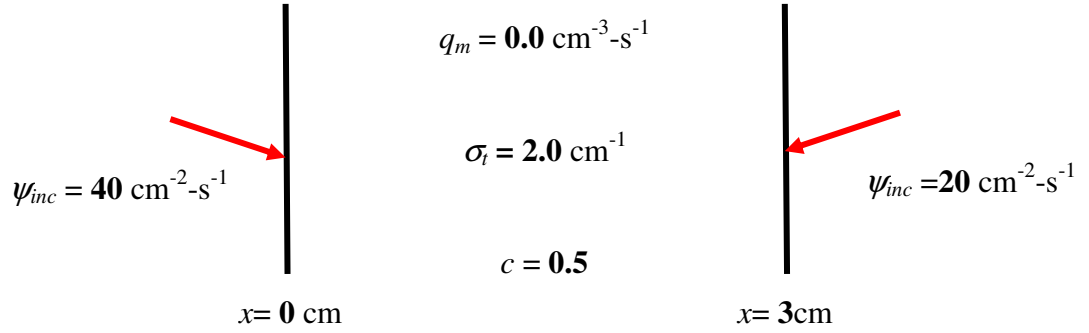


Fig. 4. One-region  $S_2$  CFEM order of convergence test problem.

This material configuration and quadrature set produce a solution built on two modes of equal relaxation length in magnitude but with opposite sign. Based on the Case-mode structure of angular flux presented in Eq.(105), the angular flux solution of the Left and Right node of cell  $j$  is:

$$\psi_{m,j,L} \equiv \psi_{m,j,1} = A^1 a_m^1 (g^1)^{j-1} + A^2 a_m^2 (g^2)^{j-1}, \quad (128)$$

$$\psi_{m,j,R} \equiv \psi_{m,j,P+1} = A^1 a_m^1 (g^1)^{j-1} z_{P+1}^1 + A^2 a_m^2 (g^2)^{j-1} z_{P+1}^2. \quad (129)$$

Since the relaxation length have equal magnitude and opposite sign their single-cell attenuation factors are equal to the inverse of the other, Eq.(125). Inserting the

definition of the single-cell attenuation factor, Eq.(105), and with  $z_1 = 1$ , then the Case-mode structure of the angular flux at the left and right edge simplify to:

$$\psi_{m,j,L} = A^1 a_m^1 (g^1)^{j-1} + A^2 a_m^2 \left( \frac{1}{g^1} \right)^{j-1}, \quad (130)$$

$$\psi_{m,j,R} = A^1 a_m^1 (g^1)^j + A^2 a_m^2 \left( \frac{1}{g^1} \right)^j. \quad (131)$$

We sum these angular fluxes over all direction and apply the angular-shape normalization, Eq.(121):

$$\phi_{j,L} = \frac{2}{c} \left[ A^1 (g^1)^{j-1} + A^2 \left( \frac{1}{g^1} \right)^{j-1} \right], \quad (132)$$

$$\phi_{j,R} = \frac{2}{c} \left[ A^1 (g^1)^j + A^2 \left( \frac{1}{g^1} \right)^j \right]. \quad (133)$$

We manipulate Eqs.(132) and (133) for cells 1,  $(J + 1) / 2$ , and  $J$  to obtain the quadratic equations of  $g^{(J-1)/2}$ :

$$g^{J-1} - \frac{\phi_{1,L} + \phi_{J,L}}{\phi_{(J+1)/2,L}} \cdot g^{\frac{J-1}{2}} + 1 = 0. \quad (134)$$

With the single-cell attenuation factor  $g$  computed, we solve for the angle-shape functions  $a_m$ :

$$a_m^1 = \frac{2}{c} \frac{\psi_{m,1,L} - \psi_{m,K,L} \cdot g^{J-1}}{\phi_{1,L} - \phi_{K,L} \cdot g^{J-1}}, \quad (135)$$

$$a_m^2 = \frac{2}{c} \frac{\psi_{m,K,L} - \psi_{m,1,L} g^{J-1}}{\phi_{K,L} - \phi_{1,L} g^{J-1}}. \quad (136)$$

We define the relative errors for the order of convergence calculations as:

$$E_J(g) = \left| \frac{g - Pade(P+1, P+1)}{Pade(P+1, P+1)} \right|, \quad (137)$$

$$E_J(a) = \max_{l,m} \left| \frac{\alpha_m^l - a_m^l}{\alpha_m^l} \right|. \quad (138)$$

If our analysis is correct, we expect the relative error to be a numerical zero or  $O 10^{-15}$  to  $O 10^{-16}$  given our 64-bit arithmetic and convergence tolerance. We present our numerical results in Table I for the single-cell attenuation factor and in Table II for the angle-shape function.

TABLE I

Order of Convergence of the CFEM Single-Cell Attenuation Factor of DD ( $P = 1$ ), Quadratic ( $P = 2$ ) and Sixth Order ( $P = 6$ ).

$J$	$\epsilon^k$	$E_J(g)$		
		<b>DD</b>	<b>Quadratic</b>	<b>Sixth-Order</b>
1	2.45E+00	3.98E-15	4.81E-15	7.72E-15
2	8.16E-01	3.30E-15	6.28E-16	1.00E-15
3	2.72E-01	6.56E-15	0.00E+00	2.19E-15
4	9.07E-02	8.51E-16	1.46E-15	1.34E-15
5	3.02E-02	2.28E-16	5.72E-16	6.87E-16
6	1.01E-02	0.00E+00	0.00E+00	0.00E+00
7	3.36E-03	1.11E-16	0.00E+00	1.11E-16
8	1.12E-03	1.11E-16	0.00E+00	1.11E-16
9	3.73E-04	0.00E+00	1.11E-16	1.11E-16

### Asymptotic and Transient Mode Behaviors

We solve a second problem with two material regions with an  $S_4$  Gauss-Legendre quadrature set to test the filtering scheme develop in Section II for discrete

ordinates solution with analytic angle-shape functions. The material properties of the regions, incident boundary conditions and slab configuration are presented in Fig. 5. The problem was solved with two different mesh configurations. The first mesh divided each region into three boundary layers between (0 cm, 1.3 cm) with 10 cells, (1.3 cm, 8.7 cm) with 10 cells, (8.7 cm, 10 cm) with 10 cells, (10 cm, 12 cm) with 10 cells, (12 cm, 18 cm) with 4 cells, and (18 cm, 20 cm) with 10 cells. The second mesh was a homogeneous mesh with 15 cells in the left region and 5 cells in the right region. Three CFEMs were used to solve the problem DD, quadratic, and sixth order, which we converged to a tolerance of  $10^{-6}$ .

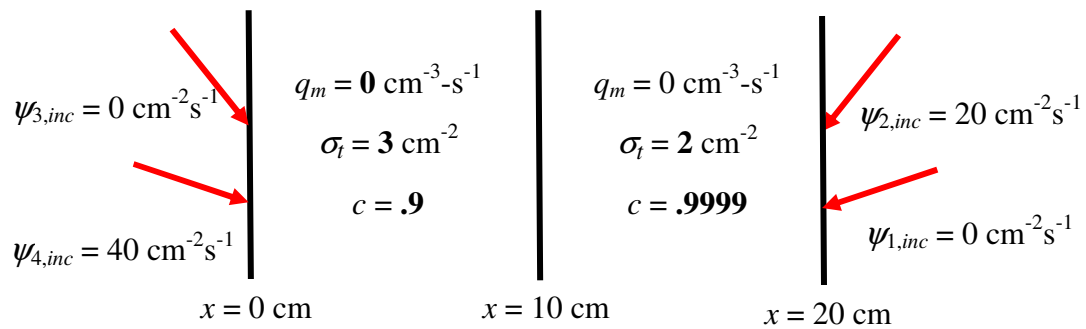


Fig. 5. Two-region  $S_4$  asymptotic and transient CFEM behavior test problem.

TABLE II

Order of Convergence of the CFEM Angle-Shape Function for DD ( $P = 1$ ), Quadratic ( $P = 2$ ) and Sixth Order ( $P = 6$ ).

$J$	$t^k$	$E_J(a)$		
		DD	Quadratic	High-Order
1	2.45E+00	2.99E-14	1.86E-14	2.99E-15
2	8.16E-01	4.36E-15	4029E-15	4.55E-15
3	2.72E-01	2.84E-15	2.47E-15	1.71E-15
4	9.07E-02	2.34E-15	3.64E-15	4.29E-15
5	3.02E-02	3.77E-15	1.33E-15	1.33E-15
6	1.01E-02	4.55E-15	1.56E-15	2.84E-15
7	3.36E-03	2.08E-14	1.65E-14	8.72E-15
8	1.12E-03	2.46E-14	1.55E-14	1.29E-14
9	3.73E-04	5.82E-14	2.82E-14	5.50E-15

Based on the quadrature set chosen we expect four modes in the solution: an asymptotic mode of magnitude increasing with  $x$ , an asymptotic one decreasing in  $x$ , a transient one increasing in  $x$ , and a transient one decreasing in  $x$ . To illustrate the role of each mode in the construction of the angular and scalar flux, we decompose these solutions into their single mode components:

$$\psi_{m,j,L}(x) = A_{j,L}^{a+}(x)a_{j,m}^{a+} + A_{j,L}^{a-}(x)a_{j,m}^{a-} + A_{j,L}^{t+}(x)a_{j,m}^{t+} + A_{j,L}^{t-}(x)a_{j,m}^{t-}, \quad (139)$$

$$\psi_{m,j,R}(x) = A_{j,R}^{a+}(x)a_{j,m}^{a+} + A_{j,R}^{a-}(x)a_{j,m}^{a-} + A_{j,R}^{t+}(x)a_{j,m}^{t+} + A_{j,R}^{t-}(x)a_{j,m}^{t-}, \quad (140)$$

$$\phi_{j,L}(x) = \frac{2}{c_j} \left[ A_{j,L}^{a+}(x) + A_{j,L}^{a-}(x) + A_{j,L}^{t+}(x) + A_{j,L}^{t-}(x) \right], \quad (141)$$

$$\phi_{j,R}(x) = \frac{2}{c_j} \left[ A_{j,R}^{a+}(x) + A_{j,R}^{a-}(x) + A_{j,R}^{t+}(x) + A_{j,R}^{t-}(x) \right]. \quad (142)$$

Here we have labeled asymptotic and transient modes as  $a$  and  $t$  respectively, and those decaying with  $x$  as  $-$  growing with  $x$  as  $+$ . With respect to the Case-mode structure presented in Eq.(105), we lumped the mode amplitude, single-cell attenuation factor and within-cell attenuation factor into a single effective amplitude  $A$ . If the angle-shape functions are known, then we can use them to map the angular flux to the scalar flux contribution from each mode:

$$\begin{pmatrix} \phi_{j,i}^{a+} \\ \phi_{j,i}^{t+} \\ \phi_{j,i}^{t-} \\ \phi_{j,i}^{a-} \end{pmatrix} = \frac{2}{c_j} \begin{bmatrix} a_1^{a+} & a_1^{t+} & a_1^{t-} & a_1^{a-} \\ a_2^{a+} & a_2^{t+} & a_2^{t-} & a_2^{a-} \\ a_3^{a+} & a_3^{t+} & a_3^{t-} & a_3^{a-} \\ a_4^{a+} & a_4^{t+} & a_4^{t-} & a_4^{a-} \end{bmatrix}^{-1} \begin{pmatrix} \psi_{1,j,i} \\ \psi_{2,j,i} \\ \psi_{3,j,i} \\ \psi_{4,j,i} \end{pmatrix}. \quad (143)$$

We compute the angle shape function for each mode in each region by solving the discrete ordinates dispersion relation, Eq.(118), for each relaxation length and by implementing the resulting relaxation lengths into the CFEM angle-shape expression, Eq.(122). We compare this single-mode scalar flux contribution to that computed by implementing the full-range filtering relation to the angular flux:

$$\phi_{j,i}^k = \frac{2}{c_j} \frac{\sum_{n=1}^N w_n \mu_n a_{n,j}^k \psi_{n,j,i}}{\sum_{n=1}^N w_n \mu_n (a_{n,j}^k)^2}. \quad (144)$$

The single-mode scalar fluxes from both approaches agree to the convergence tolerance specified for the problem. We present in Fig. 6 the scalar flux for the mesh configuration with resolved boundary layers, and in Fig. 7 through Fig. 9 its single-mode components.

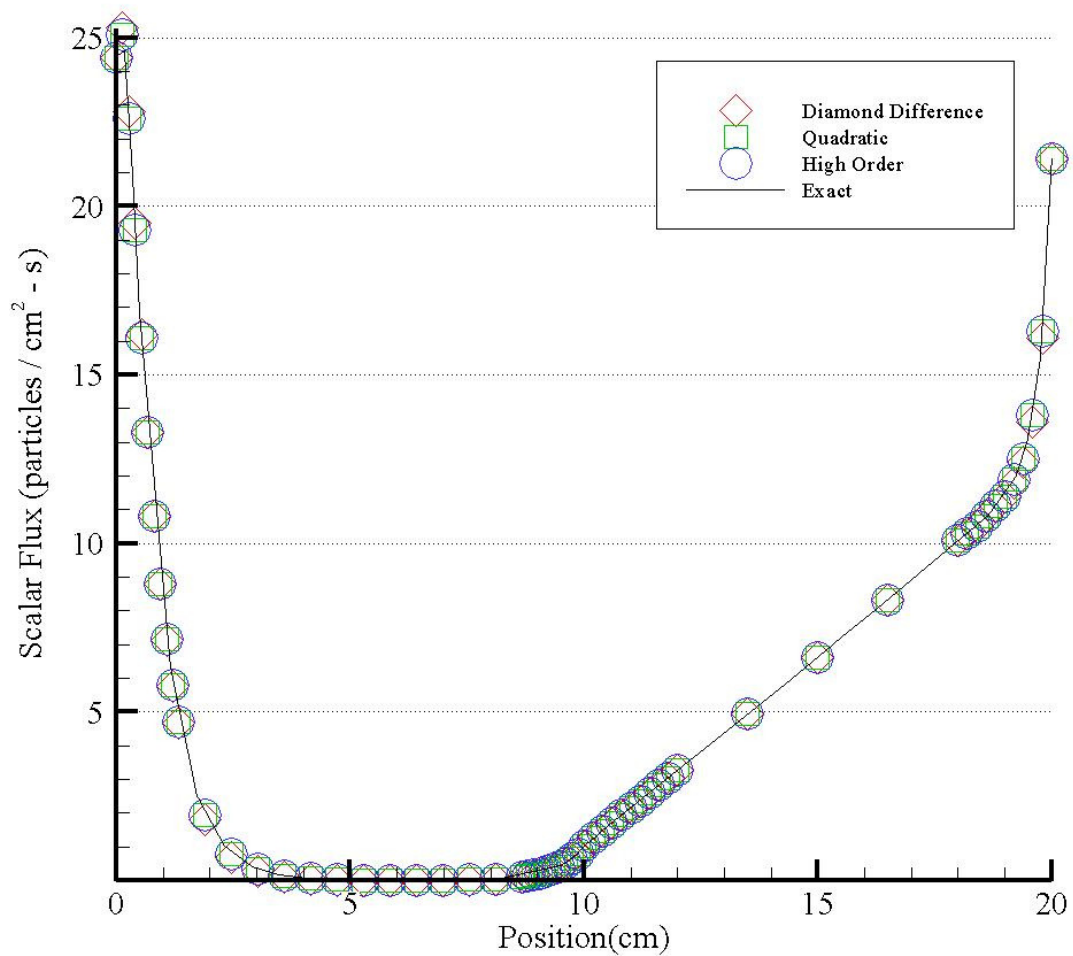


Fig. 6. Scalar flux of the two-region  $S_4$  problem for the mesh with refined boundary layers.

Fig. 6 presents the exact scalar flux (solid line) as well as the DD, quadratic and sixth order CFEM solutions. The solution in this figure was computed using the heterogeneous mesh with refined cells at the boundary layers. This grid allowed the CFEMs to accurately attenuate the transient modes at the boundaries without affecting the solution in the region's interiors. In the interior fewer cells were sufficient to compute an accurate solution since at this location the main contribution to the scalar

flux comes from asymptotic modes. As a result of the grid configuration, all three CFEMs produced accurate total scalar and angular flux. We present the transient and asymptotic component to the solution of Fig. 6, on Fig. 7 through Fig. 9.

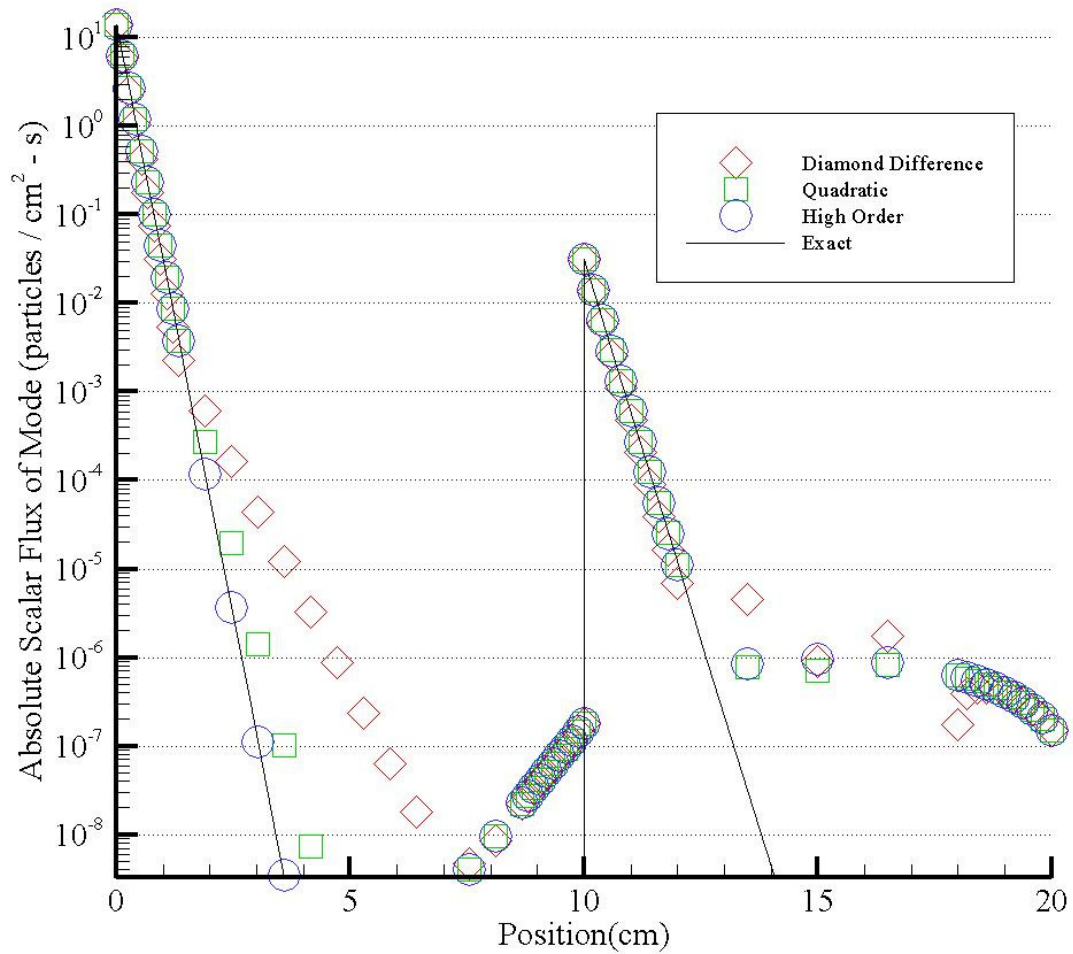


Fig. 7. Decaying-transient scalar flux with refined boundary layers.

In Fig. 7 we present the decaying-transient scalar flux for the exact and CFEM solutions. In a region of constant material properties and constant cell thickness, the scalar flux magnitude decreases by a constant magnitude, hence the scalar flux lies on a straight line of a semi-log plot. In the first 1.3 cm of the left region, all three CFEMs lie accurately over the exact solution. In this region the decaying-transient solution is attenuated four orders of magnitude. However in the 7.4 cm, the interior mesh region, the CFEMs do not share the same spatial distribution. This does not significantly affect the accuracy of total scalar flux since at this location the solution is dominated by the asymptotic modes, which we confirmed with the accurate distribution of all three methods in Fig. 6. In the region interior's even DD can get by with a low order Padé (1,1) since the asymptotic  $t^{\pm}$  is small enough. Similar comments hold for the right-side region. We remark that in the remainder of the left-side region the solution begins to grow for this transient-decaying scalar flux and recall that the scalar flux was converged to a tolerance of  $10^{-6}$ . Below a magnitude of  $10^{-6}$ , the scattering source is not fully converged and an iterative error creeps into the decaying-transient solution. This iterative error is spanned by the decaying-transient angle-shape function since the filter tallies it to this mode. Spatially however, this iterative error is distributed by the incorrect eigenvalue thus the positive slope.

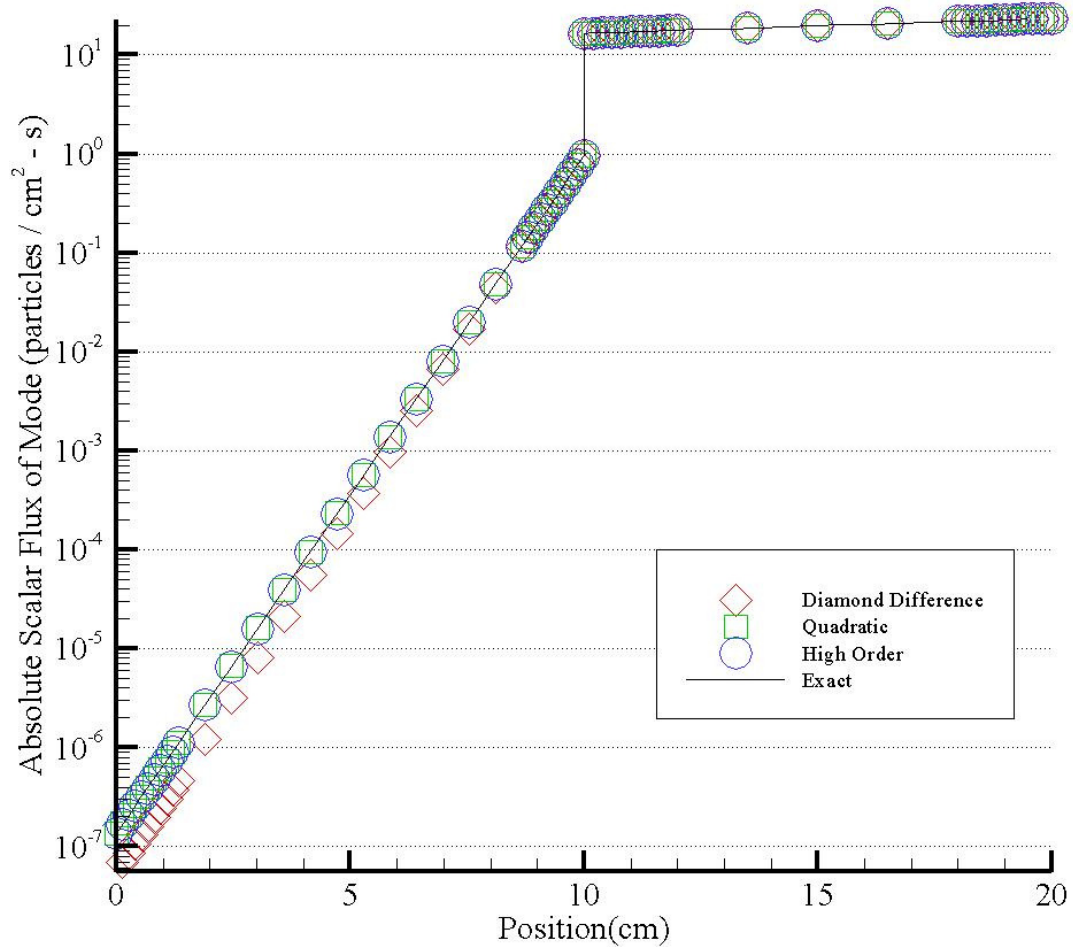


Fig. 8. Growing-asymptotic scalar flux with refined boundary layers.

In Fig. 8 and Fig. 9, we present the asymptotic scalar flux to this problem with resolved boundary layers. For these modes the asymptotic eigenvalues are small enough that all three modes capture accurately their spatial attenuation. The asymptotic solution of the exact, quadratic and sixth-order CFEM lies on the same curve, while the DD scalar flux deviates from this curve when the asymptotic scalar flux is small.

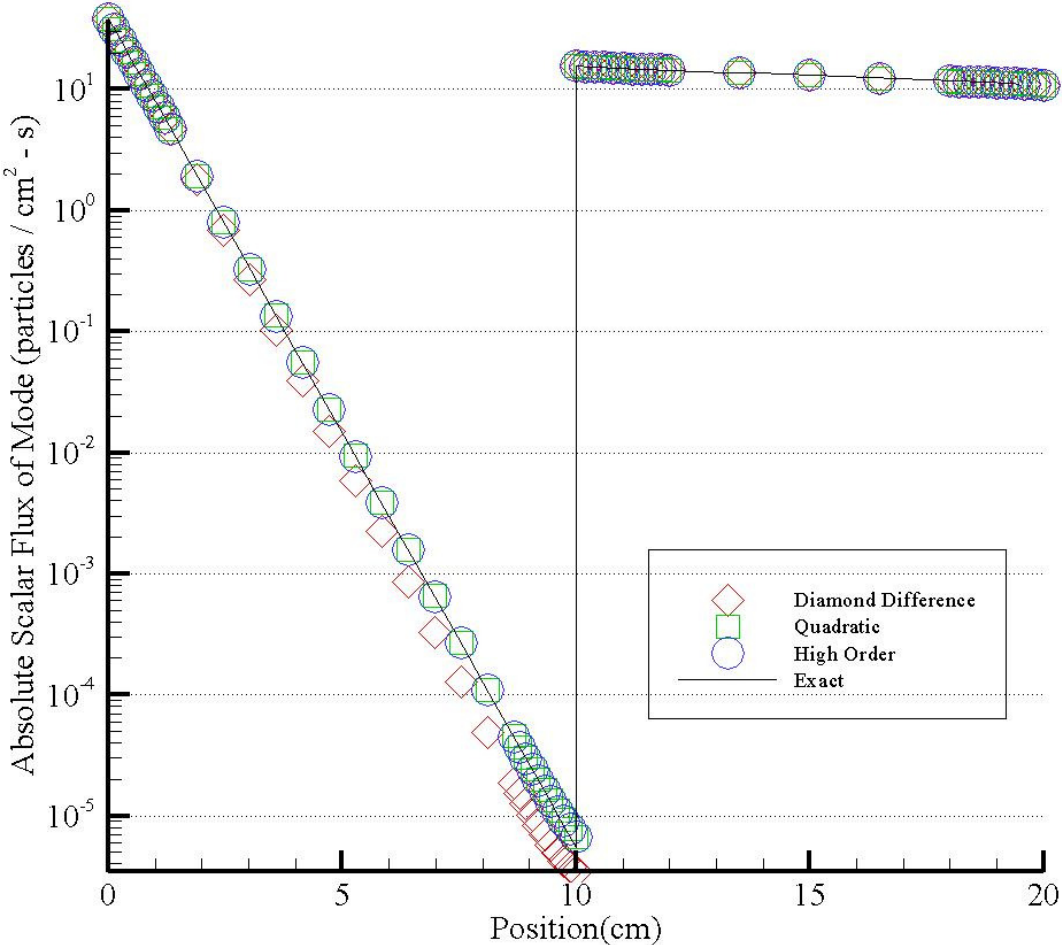


Fig. 9. Decaying-asymptotic scalar flux with refined boundary layers.

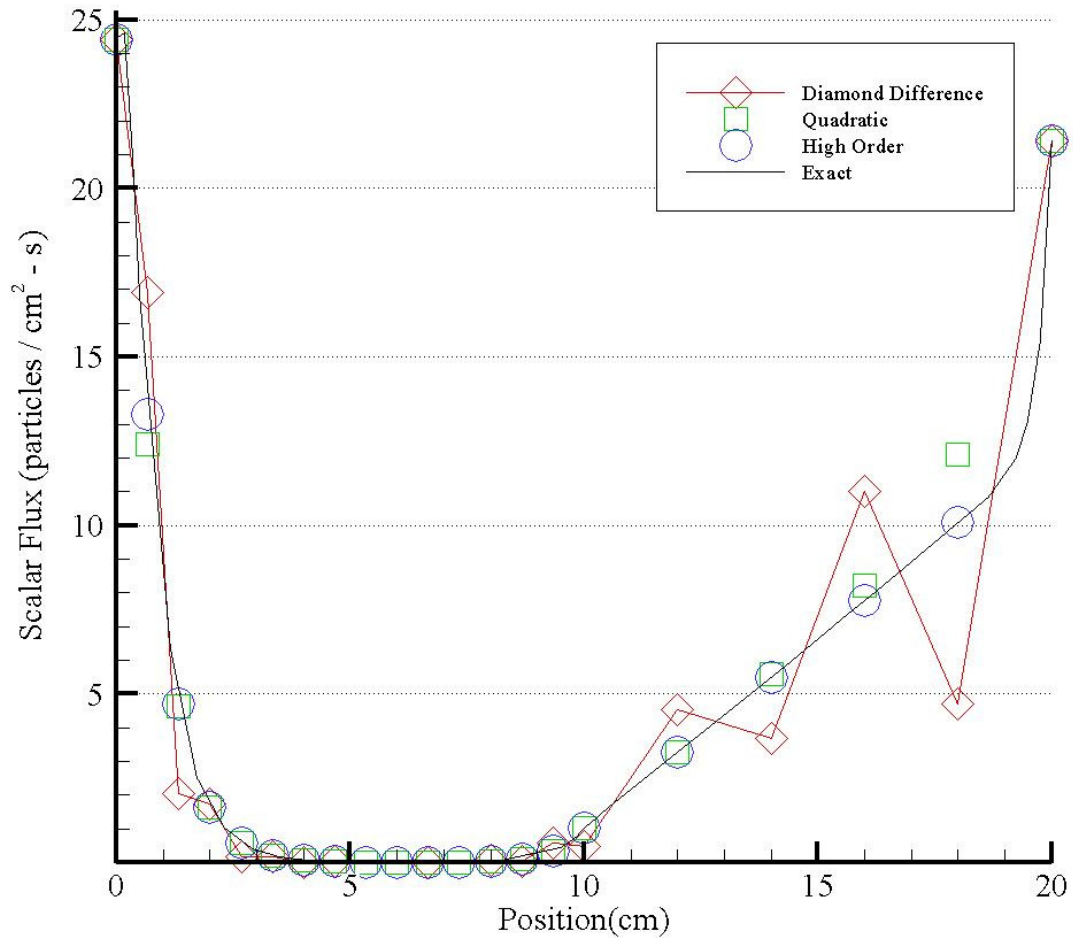


Fig. 10. Scalar flux of the two-region  $S_4$  problem for the mesh without refined boundary layers.

The spatial distribution of the scalar flux for the problem solved without resolving boundary layers is presented in Fig. 10. This grid placed 15 cells in the first 10 cm and 5 cells in the second 10 cm. In this case, only the sixth-order CFEM provide an accurate attenuation of all four modes; therefore, its scalar flux lies on the exact solution. The DD solution oscillates around the exact solution, while the quadratic CFEM consistently under-attenuates its solution. These DD oscillations are well known

and our analysis explains them based on accuracy of the attenuation of the transient modes.

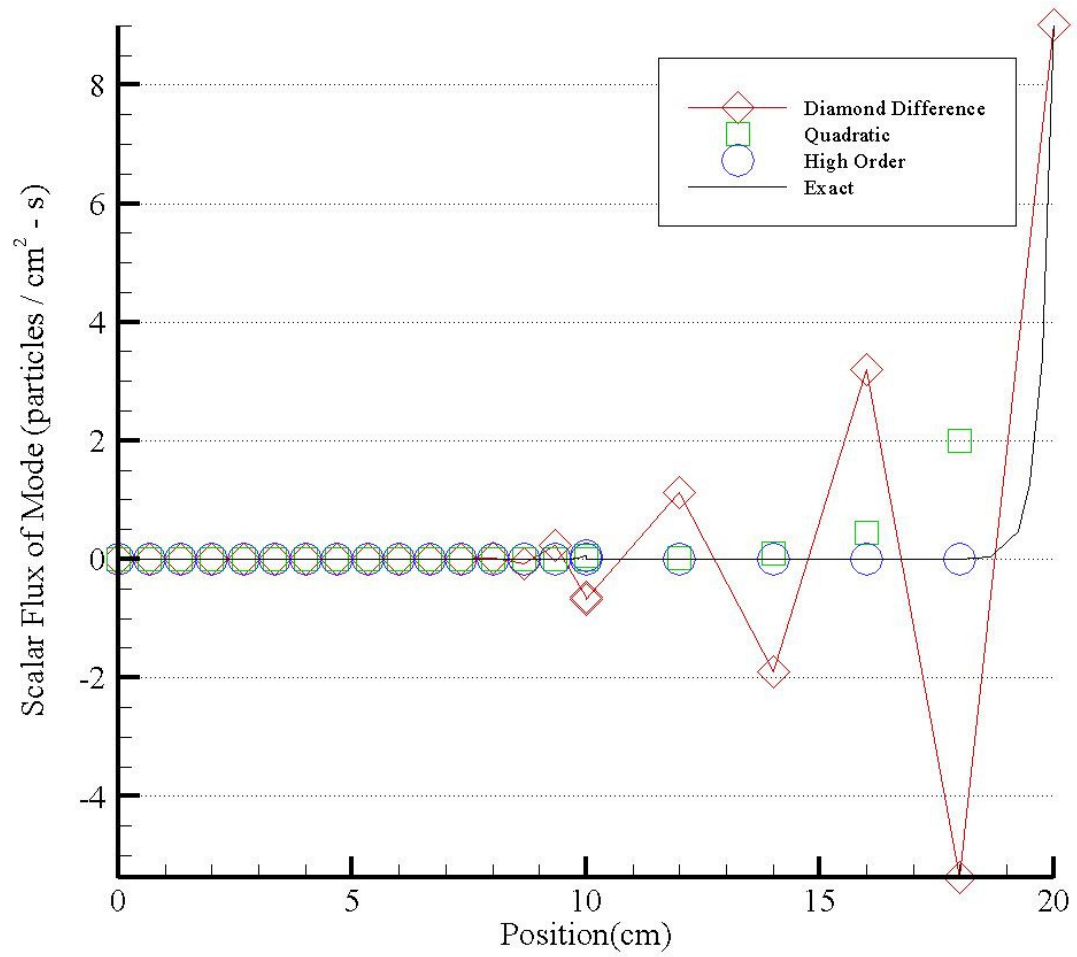


Fig. 11. Growing-transient scalar flux without refined boundary layers.

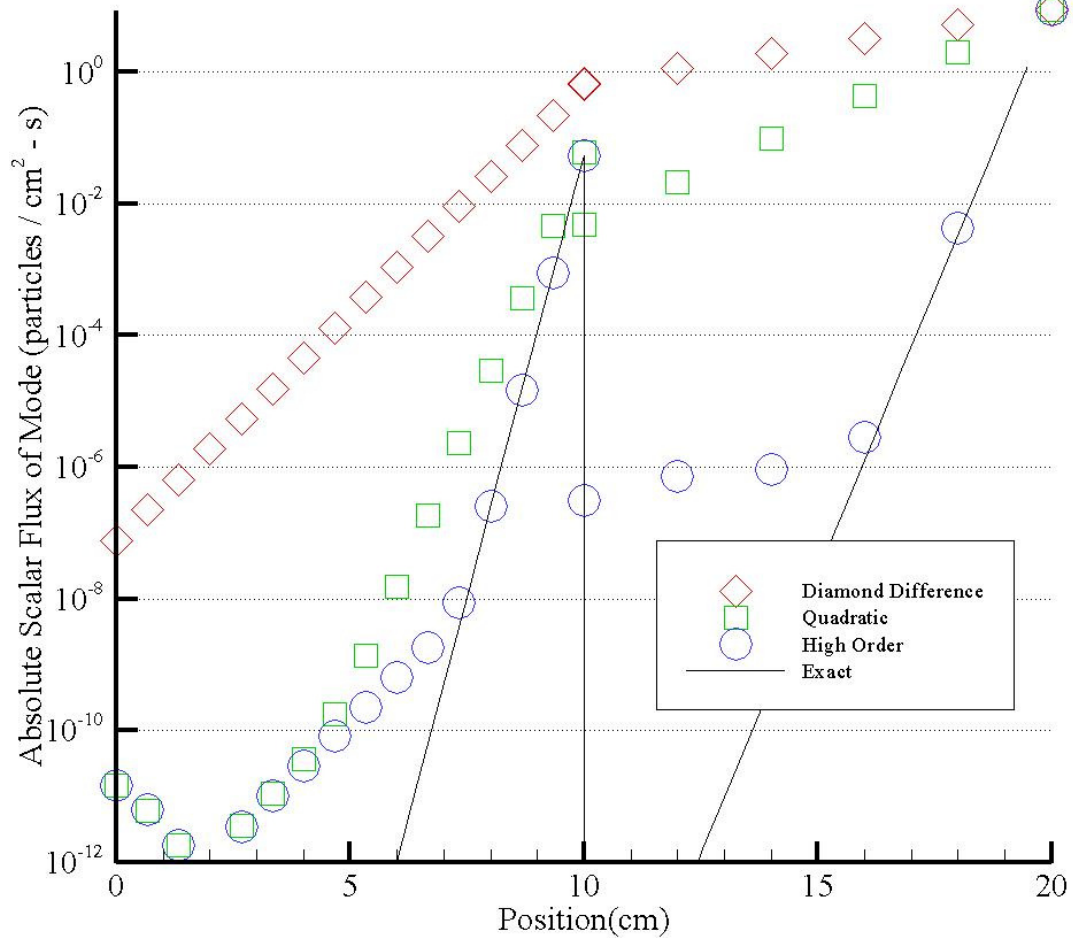


Fig. 12. Absolute value of the transient-growing scalar flux without refined boundary layers.

In Fig. 11 we present the growing-transient distribution of the all three CFEMs. In Fig. 12 we present the distribution in absolute value for the same scalar flux using a semilog scale. We focus on the right boundary of the problem. At this boundary the growing transient mode has a non-trivial contribution for all methods and this contribution increases in magnitude per cell by a constant magnitude. The Padé (1,1) exponential approximation for his mode is roughly  $-0.6$ , which is roughly the factor by

which DD increases from cell to cell. The negative value of this exponential approximation explains the oscillation in the decaying-transient scalar flux and total scalar flux. The quadrature single-cell attenuation factor, a Padé (2,2), is positive but not strong enough to accurately attenuate within the boundary layers. The sixth-order CFEM attenuates the transient-decaying scalar flux remarkably well to within the scalar flux tolerance with 2 cm cells. All of this is in exact accordance with the results presented in our analysis.

### III.D. Summary of Results

We have extended Case and Zweifel's analysis of the structure to the exact slab geometry solution to the family of Continuous Finite Element Methods. From this analysis, we have found that:

1. The structure of the CFEM homogeneous solution mimics exactly that of the analytic homogeneous solution, that is they both are linear combination of mode of the form:

$$\psi_{n,j}(x_{j,1}) = \sum_{k=1}^N A^k a_n^k (g^k)^{j-1}, \quad (145)$$

$$\psi_{n,j}(x_{j,P+1}) = \sum_{k=1}^N A^k a_n^k (g^k)^j. \quad (146)$$

Here  $a_n$  is the angle-shape function,  $g$  is the single-cell attenuation factor and  $A$  the amplitude.

2. Each mode is scaled to the exact discrete-ordinates relaxation length. In other words, the eigenvalues to the streaming and to CFEM approximation to this operator are scaled by the correct set of relaxation lengths. In the set of Discrete Ordinate Problems, these relaxation lengths are determined by the dispersion relation:

$$\frac{2}{c} = \sum_{n=1}^N \frac{v^k}{v^k - \mu_n}. \quad (147)$$

The CFEM homogeneous solution is a linear combination of two asymptotic modes and  $N - 2$  transient modes.

3. CFEMs obtain the exact angle-shape function. Thus, the homogeneous angular flux of CFEMs is spanned by the correct orthogonal angular basis. We can apply the Discrete Ordinate filtering relations presented in Section II to determine the contribution from a single mode to the scalar and angular flux.
4. The single-cell attenuation factor of CFEMs is determined by the rational function:

$$g^k = \frac{\sum_{n=1}^{P+1} d_n^k (-\tau^k)^{n-1}}{\sum_{n=1}^{P+1} d_n^k (\tau^k)^{n-1}}, \quad \tau^k = \frac{\Delta x \sigma_t}{\nu^k}. \quad (148)$$

Here  $P + 1$  is the dimension of the space of weight and basis function chosen.

From Eq.(148), this analysis shows that CFEMs approach the incorrect single-cell attenuation limit of  $\pm 1$  as cells becomes infinitely thick for each mode ( $\tau^k \rightarrow \infty$ ); CFEMs are not robust. This analysis also implies that it is futile to search for a basis and weight space that avoids this thick cell limit.

This implies that as we coarsen a fine grid, we can expect to progressively find oscillations in the angular flux. First transient modes, those with the largest  $\tau^k$  and smallest  $\nu^k$ , find that the grid scaled by their relaxation length is too coarse to produce a meaningful result. At this refinement level, the angular flux will oscillate around the asymptotic solution. As we continue to coarsen the grid, the cells will be too optically thick for the asymptotic modes, those with smallest  $\tau^k$  and largest  $\nu^k$ , and the angular flux as a whole oscillates.

This also explains how CFEMs obtain the correct asymptotic limit if the boundary layers are resolved correctly and the interior is left coarse. Boundary layers are needed to accurately attenuate transient modes where the contribution to the angular flux solution is important. The slab interior does not require a fine mesh because here asymptotic modes are the main contributors to the angular flux and their solution is scaled to large relaxation lengths.

5. If polynomial functions are chosen as the basis and weight functions then the single-cell attenuation factor the single-cell attenuation factor is a Padé ( $P, P$ )

approximation of the exponential function. For a small  $\tau^k$  (which could occur with thin cells and large relaxation lengths) the truncation error to the single-cell attenuation factor of this subset of CFEMs is determined by:

$$g^k = \exp(\tau^k) + O \cdot (\tau^k)^{2P+1}. \quad (149)$$

6. The results highlighted in the first two conclusions are ideal properties of a spatial discretization. The only length scales in the CFEM solution are relaxation lengths  $\nu^k$  and not mean-free-paths. CFEMs are scaled by the exact discrete ordinates Relaxation lengths, and their angular fluxes are spanned by the correct angle-shape functions.

7. The understanding of the CFEM Case-structure allows us to predict the accuracy of an angular and scalar flux given the specifications of a mesh. At this point this prediction is restricted to slab geometry, single energy group, isotropic scattering problems. In Section V, we implement our understanding of CFEMs to construct a grid that achieves the targeted accuracy and minimizes number of cells.

## IV. THE DISCONTINUOUS FINITE ELEMENT APPROXIMATION

We present a derivation of the family of Discontinuous Finite Element Methods (DFEM), and apply this general approach to derive the Linear Discontinuous (LD) member of this family. The solution space of the LD method is then analyzed into its Case-mode structure with one caveat: only a power series expansion of the Case-mode components is derived. Nevertheless, the analysis remains useful to understanding the scaling of each Case-mode, and provides the insight we aim for in the design of our iterative scheme. Our Case-mode analysis is not limited to the LD method; it can be expanded to any discretization of the transport equation. We provide detail algebra of the analysis in Appendix A.

### IV.A. The Discontinuous Finite Element Family of Methods

Recall the slab geometry, one group transport equation, with isotropic scattering:

$$\mu_n \frac{\partial \psi_n}{\partial x} + \sigma_t(x) \psi_n(x) = \sigma_t(x) \frac{c(x)}{2} \phi(x) + Q(x), \quad (150)$$

with the scalar flux defined as:

$$\phi(x) = \sum_{n=1}^N w_n \psi_n(x) \text{ with } \sum_{n=1}^N w_n = 2. \quad (151)$$

Similar to the CFEM derivation, we project the transport solution into a polynomial space spanned by a set of polynomial basis functions  $b_r$ :

$$\psi_n(x) = \sum_{r=1}^{P+1} \psi_{n,r} b_r(x), \quad (152)$$

We discretize the problem spatially with a grid of  $J$  cells, and  $P+1$  nodes in each cell. We choose the set of cardinal functions as our polynomial basis, and define these cardinal functions with respect to each node:

$$b_{j,p}(x_{j',p'}) = \delta_{j,j'} \delta_{p,p'}, \quad (153)$$

where  $b_{j,p}$  is the basis function centered around node  $p$  of cell  $j$ , and  $x_{j,p}$  is the spatial coordinate of that node.

We determine the amplitudes to each basis function by testing the transport equation against a space of functions of equal dimension. For a single streaming direction, the result is a system of  $P+1$  equations with the same number of angular flux unknowns. The system of equations for the unknowns belonging to a single direction is:

$$\int_{x_{j,1}}^{x_{j,P+1}} dx b_{j,i}(x) \left\{ \sum_{p=1}^{P+1} \psi_{n,j,p} \left[ \mu_n \frac{\partial b_{j,p}}{\partial x} + \sigma_{t,j} b_{j,p}(x) \right] \right\} = \int_{x_{j,1}}^{x_{j,P+1}} dx b_{j,i}(x) \left\{ \sigma_{t,j} \frac{c_j}{2} \sum_{p=1}^{P+1} b_{j,p}(x) [\phi_{j,p} + Q_{j,p}] \right\}, \text{ for } i = 1 \dots P+1. \quad (154)$$

Here we have assumed that the total and scattering cross-sections are constant in space per cell, and we define:

$$\phi_{j,p} = \sum_{n=1}^N w_n \psi_{n,j,p}, \quad (155)$$

$$Q_{j,p} = \int_{x_{j,1}}^{x_{j,P+1}} dx b_{j,p}(x) Q(x). \quad (156)$$

In contrast to the CFEM approximation, we do not dedicate a single equation to enforce the continuity of the angular flux. Instead, to communicate interface conditions, we evaluate the leakage at the cell edge and assign to it the upstream angular flux. To evaluate the leakage at cell edges, we integrate by parts the streaming term:

$$\int_{x_{j,1}}^{x_{j,P+1}} dx b_{j,i}(x) \frac{\partial b_{j,p}}{\partial x} = [b_{j,i}(x) b_{j,p}(x)]_{x_{j,1}}^{x_{j,P+1}} - \int_{x_{j,1}}^{x_{j,P+1}} dx \frac{\partial b_{j,i}}{\partial x} b_{j,p}(x), \quad (157)$$

$$\begin{aligned} \mu_n \left[ \sum_{p=1}^{P+1} \psi_{n,j,p} b_{j,i}(x) b_{j,p}(x) \right]_{x_{j,1}}^{x_{j,P+1}} + \sum_{p=1}^{P+1} \psi_{n,j,p} \left\{ \begin{array}{l} -\mu_n \int_{x_{j,1}}^{x_{j,P+1}} dx \frac{\partial b_{j,i}}{\partial x} b_{j,p}(x) \\ + \sigma_{t,j} \int_{x_{j,1}}^{x_{j,P+1}} dx b_{j,i}(x) b_{j,p}(x) \end{array} \right\} \\ = \int_{x_{j,1}}^{x_{j,P+1}} dx b_{j,i}(x) \left\{ \sigma_{t,j} \frac{c_j}{2} \sum_{p=1}^{P+1} b_{j,p}(x) [\phi_{j,p} + Q_{j,p}] \right\} \text{ for } i = 1 \dots P+1. \quad (158) \end{aligned}$$

Then, we evaluate the first term at the left and right cell edges, and assign the upstream value to the angular flux:

$$\left[ \psi_{n,j,1} b_{j,1}(x) b_{j,1}(x) \right]_{x_{j,1}} \equiv \psi_{n,j,surf,L} = \begin{cases} \psi_{n,j-1,P+1} & \text{if } \mu_n > 0 \\ \psi_{n,inc} & \text{if } \mu_n > 0 \text{ and } j = 1, \\ \psi_{n,j,1} & \text{if } \mu_n < 0 \text{ and } j > 1 \end{cases} \quad (159)$$

$$\left[ \psi_{n,j,P+1} b_{j,P+1}(x) b_{j,P+1}(x) \right]_{x_{j,P+1}} \equiv \psi_{n,j,surf,R} = \begin{cases} \psi_{n,j+1,1} & \text{if } \mu_n < 0 \\ \psi_{n,inc} & \text{if } \mu_n < 0 \text{ and } j = J. \\ \psi_{n,j,P+1} & \text{if } \mu_n > 0 \text{ and } j < I \end{cases} \quad (160)$$

The resulting DFEM system of equations is:

$$\begin{aligned} \mu_n \left\{ \begin{array}{l} \psi_{n,j,surf,R} \delta_{i,P+1} \delta_{p,P+1} \\ -\psi_{n,j,surf,L} \delta_{i,1} \delta_{p,1} \end{array} \right\} + \sum_{p=1}^{P+1} \psi_{n,j,p} \left\{ \begin{array}{l} -\mu_n \int_{x_{j,1}}^{x_{j,P+1}} dx \frac{\partial b_{j,i}}{\partial x} b_{j,p}(x) \\ +\sigma_{t,j} \int_{x_{j,1}}^{x_{j,P+1}} dx b_{j,i}(x) b_{j,p}(x) \end{array} \right\} \\ = \int_{x_{j,1}}^{x_{j,P+1}} dx b_{j,i}(x) \left\{ \sigma_{t,j} \frac{c_j}{2} \sum_{p=1}^{P+1} b_{j,p}(x) [\phi_{j,p} + \mathcal{Q}_{j,p}] \right\} \text{ for } i = 1 \dots P+1. \end{aligned} \quad (161)$$

From this family of methods, LD is specified by the system of equations:

$$\begin{aligned} \mu_n \left\{ \begin{array}{l} \psi_{n,j,surf,R} \\ -\psi_{n,j,surf,L} \end{array} \right\} + \Delta x_j \sigma_{t,j} \left\{ \begin{array}{l} \psi_{n,j,L} \\ \psi_{n,j,R} \end{array} \right\} \\ = \Delta x_j \sigma_{t,j} \frac{c_j}{2} \left\{ \begin{array}{l} \phi_{j,L} \\ \phi_{j,R} \end{array} \right\} + \Delta x_j \left\{ \begin{array}{l} \mathcal{Q}_{j,L} \\ \mathcal{Q}_{j,R} \end{array} \right\}, \end{aligned} \quad (162)$$

$$\begin{aligned} \mu_n \left\{ \begin{array}{l} \psi_{n,j,surf,R} \\ -\psi_{n,j,surf,L} \end{array} \right\} + \Delta x_j \sigma_{t,j} \left\{ \begin{array}{l} \psi_{n,j,L} \\ \psi_{n,j,R} \end{array} \right\} \\ = \Delta x_j \sigma_{t,j} \frac{c_j}{2} \left\{ \begin{array}{l} \phi_{j,L} \\ \phi_{j,R} \end{array} \right\} + \Delta x_j \left\{ \begin{array}{l} \mathcal{Q}_{j,L} \\ \mathcal{Q}_{j,R} \end{array} \right\}, \end{aligned} \quad (163)$$

where we have relabeled the first and second nodes of the cell respectively as left and right:

$$\psi_{n,j} = \psi_{n,j,L} b_{j,1}(x) + \psi_{n,j,R} b_{j,2}(x), \quad (164)$$

$$\psi_{n,j,L} \equiv \psi_{n,j,1}, \quad (165)$$

$$\psi_{n,j,R} \equiv \psi_{n,j,2}. \quad (166)$$

#### IV.B. Case-Mode Analysis of the LD Solution

##### Case-Mode Solution Components

We analyze the homogeneous solution from the LD method based on Case and Zweifel's approach to the analysis of its analytic counterpart. First, we decompose the homogeneous angular flux into a linear combination of modes. Then, each mode is separated into a product of three functions that describes the mode's distribution in space within the cell, in space from cell to cell, and in angle. Finally, we decompose each Case-mode component into a power series with respect to the cell thickness, and assume that the cell thickness is thin enough for these series to be convergent. We truncate the power series of each Case-mode component and solve for the coefficients. The LD left and right cell-edge angular fluxes are constructed on linear combination of Case-modes, which we label:

$$\psi_{n,j,L} = \sum_{k=1}^N \psi_{n,j,L}^k, \quad (167)$$

$$\psi_{n,j,R} = \sum_{k=1}^N \psi_{n,j,R}^k, \quad (168)$$

$$\psi_{n,j,L}^k = A^k b_n^k (g^k)^{j-1}, \quad (169)$$

$$\psi_{n,j,R}^k = A^k d_n^k (g^k)^{j-1} z^k. \quad (170)$$

Here:

$k \equiv$  mode index,

$j \equiv$  cell index,

$A^k \equiv$  amplitude,

$b_n^k \equiv$  angle-shape function of the left node,

$d_n^k \equiv$  angle-shape function of the right node,

$g^k \equiv$  single-cell attenuation factor,

$z^k \equiv$  within-cell node attenuation factor.

We have intentionally not specified the left angle-shape function as equal to the right angle-shape function, and the within-cell attenuation factor as equal to the single-cell attenuation factor. This was done so that the Case structure had enough freedom to capture correctly the discontinuity in the angular flux. Next, we recast the LD transport equation in matrix form:

$$[\mathbf{L} + \tau_n \mathbf{M}] \bar{\Psi}_n^k = \frac{c}{2} \tau_n \bar{\Phi}^k + \bar{\Psi}_{n,surf} \quad \text{for } \mu_n > 0, \quad (171)$$

$$[\mathbf{P}\mathbf{L}\mathbf{P} + \tau_n \mathbf{M}] \bar{\Psi}_n^k = \frac{c}{2} \tau_n \bar{\Phi}^k + \bar{\Psi}_{n,surf} \quad \text{for } \mu_n < 0, \quad (172)$$

where:

$$\tau_n = \frac{\Delta x_j \sigma_{t,j}}{|\mu_n|},$$

$$\bar{\Psi}_n^k = \begin{pmatrix} \psi_{n,j,L}^k \\ \psi_{n,j,R}^k \end{pmatrix}, \quad \bar{\Phi}^k = \sum_{n=1}^N w_n \bar{\Psi}_n^k,$$

$$\mathbf{L} = \begin{bmatrix} 1 & 1 \\ -1 & 1 \end{bmatrix}, \quad \mathbf{M} = \frac{1}{6} \begin{bmatrix} 2 & 1 \\ 1 & 2 \end{bmatrix}, \quad \mathbf{P} = \begin{bmatrix} 0 & 1 \\ 1 & 0 \end{bmatrix}.$$

For simplicity, we assumed that the slab has homogeneous material properties, and we no longer continue to track the cell index.

The surface angular flux vector is defined by its upstream value:

$$\bar{\Psi}_{n,surf} = \begin{pmatrix} \psi_{n,j-1,R} \\ 0 \end{pmatrix} \quad \text{for } \mu_n > 0, \quad (173)$$

$$\bar{\Psi}_{n,surf} = \begin{pmatrix} 0 \\ \psi_{n,j+1,L} \end{pmatrix} \quad \text{for } \mu_n < 0. \quad (174)$$

We insert a single Case-mode into the LD transport equation and replace the mode by its angle-shape and spatial distribution components:

$$\begin{aligned} & [\mathbf{L} + \tau_n \mathbf{M}] \begin{pmatrix} b_n^k \\ d_n^k z^k \end{pmatrix} (g^k)^{j-1} \\ & = \frac{c}{2} \tau_n \sum_{m=1}^N \begin{pmatrix} b_m^k \\ d_m^k z^k \end{pmatrix} (g^k)^{j-1} + \begin{pmatrix} d_n^k z^k \\ 0 \end{pmatrix} (g^k)^{j-2} \quad \text{for } \mu_n > 0, \end{aligned} \quad (175)$$

$$\begin{aligned}
[\mathbf{PLP} + \tau_n \mathbf{M}] \begin{pmatrix} b_n^k \\ d_n^k z^k \end{pmatrix} (g^k)^{j-1} \\
= \frac{c}{2} \tau_n \sum_{m=1}^N \begin{pmatrix} b_m^k \\ d_m^k z^k \end{pmatrix} (g^k)^{j-1} + \begin{pmatrix} 0 \\ b_n^k \end{pmatrix} (g^k)^j \text{ for } \mu_n < 0.
\end{aligned} \tag{176}$$

We assume that the cell thickness is fine enough so that we can decompose the components to each Case-mode into a power series with respect to the cell thickness:

$$g = \sum_{i=1}^{\infty} \gamma^{(i)} \Delta x^i, \quad z = \sum_{i=1}^{\infty} \zeta^{(i)} \Delta x^i, \quad d_n = \sum_{i=1}^{\infty} \delta_n^{(i)} \Delta x^i, \quad b_n = \sum_{i=1}^{\infty} \gamma_n^{(i)} \Delta x^i. \tag{177}$$

We insert these power series into Eqs.(171) and (172), and we solve for coefficients of equal power. The resulting equations for the coefficients of order  $i$  are:

$$\begin{aligned}
[\mathbf{L} + \tau_n \mathbf{M}] \begin{pmatrix} \sum_{e+f=i} \beta_n^{k,(e)} g^{k,(f)} \\ \sum_{e+f+h=i} d_n^{k,(e)} z^{k,(f)} g^{k,(h)} \end{pmatrix} = \frac{c}{2} \tau_n \sum_{m=1}^N \begin{pmatrix} \sum_{e+f=i} \beta_m^{k,(e)} \gamma^{k,(f)} \\ \sum_{e+f+k=i} \delta_m^{k,(e)} \zeta^{k,(f)} \gamma^{k,(h)} \end{pmatrix} \\
+ \begin{pmatrix} \sum_{e+f=i} \delta_n^{k,(e)} \zeta^{k,(f)} \\ 0 \end{pmatrix} \text{ for } \mu_n > 0,
\end{aligned} \tag{178}$$

$$\begin{aligned}
[\mathbf{PLP} + \tau_n \mathbf{M}] \begin{pmatrix} \beta_n^{k,(i)} \\ \sum_{e+f=i} \delta_n^{k,(e)} \zeta^{k,(f)} \end{pmatrix} = \frac{c}{2} \tau_n \sum_{m=1}^N \begin{pmatrix} \beta_m^{k,(i)} \\ \sum_{e+f=i} \delta_m^{k,(e)} \zeta^{k,(f)} \end{pmatrix} \\
+ \begin{pmatrix} 0 \\ \sum_{e+f=i} \beta_n^{k,(e)} \gamma^{k,(f)} \end{pmatrix} \text{ for } \mu_n < 0.
\end{aligned} \tag{179}$$

For each mode there are  $2N + 2$  unknowns and Eqs. (178) and (179) provide only  $2N$  equations. To close the system of equations we recall the angle-shape function normalization or dispersion relation:

$$\sum_{n=1}^N w_n d_n^k = \frac{2}{c}, \quad \sum_{n=1}^N w_n \delta_n^{k,(i)} = \begin{cases} 2/c, & \text{if } i = 0 \\ 0, & \text{if } i > 0 \end{cases}, \tag{180}$$

$$\sum_{n=1}^N w_n b_n^k = \frac{2}{c}, \quad \sum_{n=1}^N w_n \beta_n^{k,(i)} = \begin{cases} 2/c, & \text{if } i = 0 \\ 0, & \text{if } i > 0 \end{cases}. \quad (181)$$

We solve for each coefficient and relate them to their exact counterparts. From this term by term comparison, we obtain:

$$d_n^k = \alpha_n^k \left[ 1 - \frac{c}{2} \frac{1}{6} \sum_{\mu_n < 0} w_n \alpha_n^k (\tau^k)^2 \right] + O_n(\tau^k)^3 = \alpha_n^k + \tilde{O}_n(\tau^k)^3, \mu_n > 0, \quad (182)$$

$$d_n^k = \alpha_n^k \left[ 1 + \frac{c}{2} \frac{1}{6} \sum_{\mu_n > 0} w_n \alpha_n^k (\tau^k)^2 \right] + O_n(\tau^k)^3 = \alpha_n^k + \tilde{O}_n(\tau^k)^3, \mu_n < 0, \quad (183)$$

$$b_n^k = \alpha_n^k \left[ 1 + \frac{c}{2} \frac{1}{6} \sum_{\mu_n < 0} w_n \alpha_n^k (\tau^k)^2 \right] + O_n(\tau^k)^3 = \alpha_n^k + \tilde{O}_n(\tau^k)^3, \mu_n > 0, \quad (184)$$

$$b_n^k = \alpha_n^k \left[ 1 - \frac{c}{2} \frac{1}{6} \sum_{\mu_n > 0} w_n \alpha_n^k (\tau^k)^2 \right] + O_n(\tau^k)^3 = \alpha_n^k + \tilde{O}_n(\tau^k)^3, \mu_n < 0, \quad (185)$$

$$\begin{aligned} z^k &= 1 - \tau^k + \frac{1}{2} \left[ 1 + \frac{c}{2} \frac{1}{3} \left( \sum_{\mu_n > 0} w_n \alpha_n^k - \sum_{\mu_n < 0} w_n \alpha_n^k \right) \right] (\tau^k)^2 + O(\tau^k)^3 \\ &= g^{k,\text{exact}} + \tilde{O}(\tau^k)^3, \end{aligned} \quad (186)$$

$$g^k = 1 - \tau^k + \frac{1}{2} (\tau^k)^2 - \frac{1}{6} (\tau^k)^3 + O(\tau^k)^4 = g^{k,\text{exact}} + \tilde{O}(\tau^k)^4. \quad (187)$$

Here  $g^{k,\text{exact}}$  is the exact single-cell attenuation factor and  $\alpha_n^k$  is the exact angle shape function. From Section II, these functions are equal to:

$$g^{k,\text{exact}} = \exp(-\tau^k), \quad (188)$$

$$\alpha_n^k = \frac{\nu^k}{\nu^k - \mu_n}. \quad (189)$$

The LD single-cell attenuation factor is accurate to a third order. Such a high-order approximation is delivered impressively by a linear polynomial-based discretization. It is obtained with a cost, the Case-modes are constructed on angles-shape functions that are different from node to node and, therefore, are an approximation of the analytic ones. The LD Case-modes can not be exactly filtered with the analytic

orthogonality relations derived in Section II, and at this points, a derivation of LD orthogonality relations is not evident.

From the expansions in Eqs.(182) through (187), LD Case-modes scale the optical thickness of each cell by the exact discrete ordinates relaxation lengths,  $\nu$ . For any spatial discretization, this is a desirable characteristic. It implies that the LD Case-modes play the same roles as the analytic ones in constructing the homogeneous angular flux: 2 modes are asymptotic with a global influence on the solution, and  $N - 2$  transient modes are transient with an important role in capturing localized gradients (here  $N$  is the number of quadrature levels.)

We continue this analysis of the LD homogeneous solution with a look at the effect of the LD approximation of the angular-shape functions on the amplitudes of each Case-mode.

### Case-Mode Amplitudes

By imposing incident boundary conditions on a problem, we specify the Case-modes that need to be excited to correctly span the conditions at both boundaries. An exact set of amplitudes requires that the homogeneous solution is built on the correct angle-shape functions, and that each mode is attenuated exactly to the opposing boundary edge. With this section of our LD analysis, we look at the effect on the Case-mode amplitudes of the angle-shape function approximations. To do so, we assume that the problem has homogeneous material properties and that incident boundary conditions are specified on both boundary edges. With no discontinuity in the scattering ratio and no particular solution, these assumptions imply that the homogeneous solution is spanned by a single set of angle-shape functions at each cell edge. Similar to the previous analysis sections, our final product is a power series expansion of the LD and analytic Case-mode amplitudes, and a comparison of the coefficients in these series.

We begin the amplitude analysis by constructing the incident boundary conditions in terms of the analytic Case-mode components:

$$\psi_{n,inc} = \sum_{k=1}^N A^{k,exact} \alpha_n^k, \text{ for } \mu_n > 0, \quad (190)$$

$$\psi_{n,inc} = \sum_{k=1}^N A^{k,exact} \alpha_n^k \left( g^{k,exact} \right)^J, \text{ for } \mu_n < 0. \quad (191)$$

These exact boundary conditions are spanned by the analytic Case-modes as well as the LD Case-modes. Based on the LD Case-mode structure, the boundary conditions are equal to:

$$\psi_{n,inc} = \sum_{k=1}^N A^{k,LD} d_n^k \frac{z^k}{g^k}, \text{ for } \mu_n > 0, \quad (192)$$

$$\psi_{n,inc} = \sum_{k=1}^N A^{k,LD} b_n^k \left( g^k \right)^J, \text{ for } \mu_n < 0. \quad (193)$$

We expand the Case-mode components of the boundary conditions above into the power series presented in the previous section, Eqs.(182) through (187):

$$\begin{aligned} \psi_{n,inc} &= \sum_{k=1}^N A^{k,LD} \alpha_n^k \left[ 1 + \frac{c}{12} \sum_{\mu_n > 0} w_n \alpha_n^k \left( \tau^k \right)^2 + O_n^k \left( \tau^k \right)^3 \right] \\ &= \sum_{k=1}^N A^{k,exact} \alpha_n^k, \text{ for } \mu_n > 0, \end{aligned} \quad (194)$$

$$\begin{aligned} \psi_{n,inc} &= \sum_{k=1}^N A^{k,LD} \alpha_n^k \left( g^{k,exact} \right)^J \left[ 1 - \frac{c}{12} \sum_{\mu_n > 0} w_n \alpha_n^k \left( \tau^k \right)^2 + O_n^k \left( \tau^k \right)^3 \right] = \\ &= \sum_{k=1}^N A^{k,exact} \alpha_n^k \left( g^{k,exact} \right)^J, \text{ for } \mu_n < 0. \end{aligned} \quad (195)$$

We expand the analytic and exact Case-mode amplitudes into power series of  $\tau$

$$A^{k,exact} = \sum_{i=1}^{\infty} A^{k,exact,(i)} \left( \tau^k \right)^i, \quad (196)$$

$$A^{k,LD} = \sum_{i=1}^{\infty} A^{k,LD,(i)} \left( \tau^k \right)^i. \quad (197)$$

We insert these expansions into Eqs.(194) and (195), and we compare coefficients of similar power. In terms of the exact Case-mode amplitude coefficients, the LD amplitude is:

$$A^{k,LD} = A^{k,\text{exact},(0)} + A^{k,\text{exact},(1)}\tau^k + \left[ A^{k,\text{exact},(2)} - A^{k,\text{exact},(0)} \frac{c}{12} \sum_{\mu_n > 0} w_n \alpha_n^k \right] (\tau^k)^2 +$$

$$O^k (\tau^k)^3 = A^{k,\text{exact}} + O^k (\tau^k)^3. \quad (198)$$

The LD Case-modes are built on amplitudes that have a second order error. Previous convergence studies<sup>34</sup> concluded that the LD cell-exiting angular flux and the cell-average scalar flux have third order errors. For our Case-mode expansion of the amplitude, angular-shape functions and within-cell attenuation factor to be consistent with the results from these studies, we expect that the interaction of these components will yield a more accurate error.

### Spatial Convergence of the Cell-Edge and Cell-Average Angular Flux

To conclude our analysis of the LD Case-mode space, we combine the expansions to the LD Case-mode components to reconstruct the left-edge, right-edge, and cell-average angular flux. We insert the Case-mode components in their power series expansion forms, Eqs.(182) through (187) and Eq.(198), into the left-edge angular flux, Eq.(169):

$$\psi_{n,j,L} = \sum_{k=1}^N A^{LD} b_n^k (g^k)^{j-1} = \sum_{k=1}^N \alpha_n^k (g^{k,\text{exact}})^{j-1} \left[ \begin{array}{l} A^{k,\text{exact},(0)} + A^{k,\text{exact},(1)}\tau^k \\ -\frac{1}{6} A^{k,\text{exact},(0)} (\tau^k)^2 + O_n^k (\tau^k)^3 \end{array} \right] =$$

$$\psi_{n,j,L}^{\text{exact}} + \tilde{O}_n \Delta x^2, \quad \text{for } \mu_n > 0, \quad (199)$$

$$\psi_{n,j,L} = \sum_{k=1}^N A^{LD} b_n^k (g^k)^{j-1} = \sum_{k=1}^N \alpha_n^k (g^{k,\text{exact}})^{j-1} \left[ A^{k,\text{exact}} + O_n^k (\tau^k)^3 \right] =$$

$$\psi_{n,j,L}^{\text{exact}} + \tilde{O}_n \Delta x^3, \quad \text{for } \mu_n < 0. \quad (200)$$

Similarly for the right node of the same cell:

$$\psi_{n,j,R} = \sum_{k=1}^N A^{LD} d_n^k (g^k)^{j-1} z^k = \sum_{k=1}^N \alpha_n^k (g^{k,\text{exact}})^j \left[ A^{k,\text{exact}} + O_m^k (\tau^k)^3 \right] =$$

$$\psi_{n,j,R}^{\text{exact}} + \tilde{O}_n \Delta x^3, \quad \text{for } \mu_n > 0, \quad (201)$$

$$\psi_{n,j,R} = \sum_{k=1}^N A^{LD} d_n^k (g^k)^{j-1} z^k = \sum_{k=1}^N \alpha_n^k (g^{k,\text{exact}})^{j-1} \left[ A^{k,\text{exact},(0)} + A^{k,\text{exact},(1)} \tau^k - \frac{1}{6} A^{k,\text{exact},(0)} (\tau^k)^2 + O_n^k (\tau^k)^3 \right] = \psi_{n,j,R}^{\text{exact}} + \tilde{O}_n \Delta x^2, \text{ for } \mu_n < 0. \quad (202)$$

As suggested by the convergence studies<sup>34</sup>, the cell-exiting angular flux converges at a higher rate, third order, than its cell-entering counter parts, second order. We explain this spatial super-convergence by noting that the cell-exiting angular fluxes, Eqs.(200) and (201), have the same structure than that used to span the boundary conditions, Eqs.(173) and (174). Particularly they share the same product of the amplitude times the angle-shape function at the left cell edge and the amplitude times the angle-shape function and a ratio of within-cell and cell-to-cell attenuation factors on the right cell edge. To construct the boundary conditions, this product is multiplied by the single-cell attenuation factor, which has a third order global error. Therefore, the boundary conditions are constructed on a third order quantity that is extended to the cell-exiting angular flux by an attenuation factor of similar order. The amplitude is approximated to a second order to compensate for the low order approximation of the angle-shape function. That is the amplitude error is such that its product with the rest of the Case-mode components remained third order; even though, the amplitude by itself is second order accurate. The order of convergence of the cell-exiting angular flux is limited by the global error generated from the compounding of the single-cell attenuation factor error from cell to cell. We explain the second order convergence of the cell-entering angular flux by noting that within the cell the cell-exiting angular flux is traced back to the entering edge under a second order approximation of the attenuation factor.

We combine the results for the left-edge and right-edge angular flux to obtain the cell-average angular flux expansion:

$$\begin{aligned} \psi_{n,j} &= \sum_{k=1}^N \alpha_n^k (g^{k,\text{exact}})^{j-1} \left[ \begin{aligned} &\left( A^{k,\text{exact},(0)} + A^{k,\text{exact},(1)} \tau^k \right) \frac{1+g^k}{2} \\ &-\frac{1}{6} A^{k,\text{exact},(0)} (\tau^k)^3 + O_n^k (\tau^k)^3 \end{aligned} \right] = \\ &\sum_{k=1}^N \alpha_n^k (g^{k,\text{exact}})^{j-1} \left[ A^{k,\text{exact}} \frac{1+g^{k,\text{exact}}}{\tau^k} + O_n^l (\tau^k)^3 \right] = \psi_{n,j}^{\text{exact}} + \tilde{O}_n \Delta x^3. \end{aligned} \quad (203)$$

Finally, we add the cell-average angular flux over all directions to obtain the expansion of the cell-averaged scalar flux:

$$\phi_j = \sum_{k=1}^N (g^{k,\text{exact}})^{j-1} \left[ A^{k,\text{exact}} \frac{1+g^{k,\text{exact}}}{\tau^k} + O_n^l (\tau^k)^3 \right] = \phi_j^{\text{exact}} + \tilde{O}_n \Delta x^3. \quad (204)$$

With the expansion of the angular and scalar flux, we complete our analysis of the LD Case-mode space. The analysis agrees with previous numerical evidence that suggested that the linear polynomial basis function of the LD method can render a third order transport approximation. To our knowledge, this is the first analysis to derive the order of convergence of the LD angular fluxes without any simplifying assumptions on the materials properties. By decomposing the LD homogeneous transport solution into its Case-modes and by expanding the Case-mode components into power series of the cell thickness, this analysis illustrate how the LD linear polynomial basis super-converges in space.

#### IV.C. Numerical Results

We confirm the findings from our analysis by comparing the Case-mode components of the LD and the analytic solution to a homogeneous problem. We computed the LD solution to the problem with material properties and boundary conditions specified in Fig. 13. The problem was solved with an  $S_2$  Gauss-Legendre quadrature set, to a relative tolerance of  $10^{-14}$ . To calculate the orders of convergence, we computed the solution with nine different grids of progressively higher refinement levels:  $\Delta x = 3^{1-n}$  for  $n = [1,9]$ .

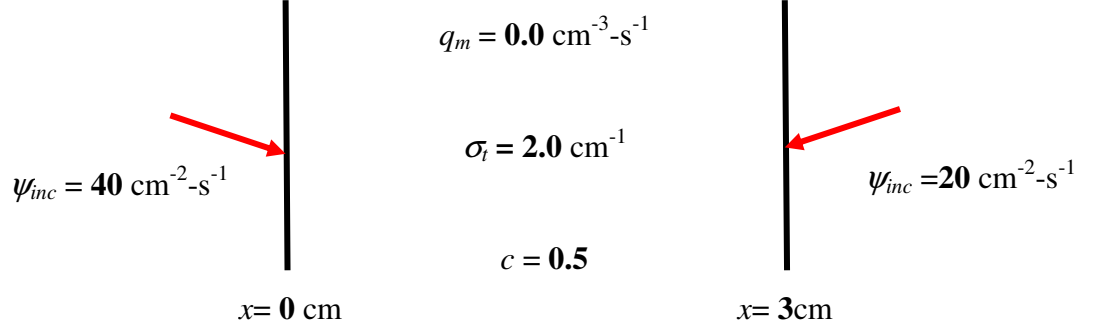


Fig. 13. One-region CFEM order of convergence test problem.

Based on the problem's configuration, we expect the total solution to be equal to the homogeneous solution, and the homogeneous solution to be composed of two Case-modes of relaxation lengths equal in magnitude but opposite in sign. The angular flux of the left and right edge of cell  $j$  is specified by:

$$\psi_{m,j,L} = A^1 d_m^1 g^{j-1} + A^2 d_m^2 g^{J-j+1}, \quad (205)$$

$$\psi_{m,j,R} = A^1 b_m^1 g^{j-1} z + A^2 b_m^2 \frac{g^{J-j+1}}{z}. \quad (206)$$

Applying the dispersion relation to the angle-shape functions, we obtain the following expression of the scalar flux:

$$\phi_{j,L} = \frac{2}{c} \left[ A^1 g^{j-1} + A^2 g^{J-j+1} \right], \quad (207)$$

$$\phi_{j,R} = \frac{2}{c} \left[ A^1 g^{j-1} z + A^2 \frac{g^{J-j+1}}{z} \right]. \quad (208)$$

By applying Eq.(207) to the first, last, and middle cell, we obtain the following expression for the single-cell attenuation factor and Case-mode amplitudes:

$$G^2 - \frac{\phi_{1,L} + \phi_{J,L}}{\phi_{(J+1)/2,L}} \cdot G + 1 = 0, \quad (209)$$

$$A^1 = \frac{c}{2} \frac{\phi_{1,L} - \phi_{J,L} G}{1 - G^2}, \quad (210)$$

$$A^1 = \frac{c}{2} \frac{1}{g} \frac{\phi_{J,L} - \phi_{1,L} G}{1 - G^2}. \quad (211)$$

where  $G = g^{\frac{J-1}{2}}$ .

With the single-cell attenuation factor and the amplitudes determined, the within-cell attenuation factor, left and right angular-shape functions are:

$$A^1 z^2 - \frac{c}{2} \phi_{(J+1)/2,R} \frac{z}{G} + A^2 g = 0, \quad (212)$$

$$d_m^1 = \frac{2}{c} \frac{\psi_{m,1,L} - \psi_{m,J,L} G^2}{\phi_{1,L} - \phi_{J,L} G^2}, d_m^2 = \frac{2}{c} \frac{\psi_{m,J,L} - \psi_{m,1,L} G^2}{\phi_{J,L} - \phi_{1,L} G^2}, \quad (213)$$

$$b_m^1 = \frac{1}{z} \frac{2}{c} \frac{\psi_{m,1,R} - \psi_{m,J,R} G^2}{\phi_{1,L} - \phi_{J,L} G^2}, b_m^2 = z \frac{2}{c} \frac{\psi_{m,J,R} - \psi_{m,1,R} G^2}{\phi_{J,L} - \phi_{1,L} G^2}. \quad (214)$$

For each grid configuration we computed the value of the Case-mode components of the LD and analytic solution using Eqs.(209) through (214). We define the relative error between the LD and analytic results as:

$$E_n(g) = \left| \frac{g - e^{-\tau}}{e^{-\tau}} \right|, \quad (215)$$

$$E_n(z) = \left| \frac{z - e^{-\tau}}{e^{-\tau}} \right|, \quad (216)$$

$$E_n(d) = \max_{k,m} \left| \frac{\alpha_m^k - d_m^k}{\alpha_m^k} \right|, \quad (217)$$

$$E_n(b) = \max_{k,m} \left| \frac{\alpha_m^k - b_m^k}{\alpha_m^k} \right|, \quad (218)$$

$$E_n(A^1, A^2) = \max_k \left| \frac{A^{k,\text{exact}} - A^k}{A^{k,\text{exact}}} \right|. \quad (219)$$

Here  $\tau = \frac{\sigma_i \Delta x}{|\nu|}$ .

The order of convergence results are listed in Table III and Table IV. The tables present the relative error for each grid calculation and the ratio between errors of

consecutive calculations. Since the grid is refined by a factor of three between consecutive calculations, we expect a linear order of convergence to yield a ratio of three, a quadratic order of convergence yield a ratio of nine, and a cubic order of convergence yield a ratio of 81.

The results confirm the prediction from our analysis. The angle-shape functions, amplitudes and within-cell attenuation factor exhibit a quadratic order of convergence, while the single-cell attenuation factor exhibits a cubic order of convergence.

TABLE III

Relative Error of the Single-Cell Attenuation Factor, Within-Cell Attenuation Factor and Amplitudes of the LD Solution.

$n$	$\tau$	$G$		$z$		$A$	
		$E_n$	$R_n$	$E_n$	$R_n$	$E_n$	$R_n$
1	2.45E+00	4.33E+02	—	5.53E-01	—	4.08E-01	—
2	8.16E-01	5.47E-03	78.2	3.64E-02	15.2	5.74E-02	7.10
3	2.72E-01	7.52E-05	72.8	6.96E-03	5.23	8.82E-03	6.51
4	9.07E-02	9.73E-07	77.3	9.00E-04	7.74	1.10E-03	8.00
5	3.02E-02	1.22E-08	79.6	1.05E-04	8.56	1.27E-04	8.65
6	1.01E-02	1.52E-10	80.5	1.19E-05	8.85	1.44E-05	8.88
7	3.36E-03	1.88E-12	80.8	1.33E-06	8.95	1.60E-06	8.96
8	1.12E-03	2.31E-14	81.1	1.48E-07	8.98	1.78E-07	8.99
9	3.73E-04	2.22E-16	104.	1.64E-08	8.99	1.98E-08	9.00

TABLE IV

Relative Error of the Left and Right Angular Flux of the LD Solution.

$n$	$\tau_\nu$	$D$		$b$	
		$E_n$	$R_n$	$E_n$	$R_n$
1	2.45E+00	4.01E+00	—	4.01E+00	—
2	8.16E-01	1.05E-01	38.1	1.30E+00	3.09
3	2.72E-01	1.08E-02	9.77	1.08E-02	121.
4	9.07E-02	1.18E-03	9.14	1.18E-03	9.14
5	3.02E-02	1.30E-04	9.04	1.30E-04	9.04
6	1.01E-02	1.45E-05	9.01	1.45E-05	9.01
7	3.36E-03	1.61E-06	9.00	1.61E-06	9.00
8	1.12E-03	1.78E-07	9.00	1.78E-07	9.00
9	3.73E-04	1.98E-08	9.00	1.98E-08	9.00

#### IV.D. Summary of Results

We have presented a general derivation of the family of Discontinuous Finite Element Methods, and applied this derivation to the linear polynomial member of this family. The homogeneous or source-free solution of the linear DFEM was analyzed into its Case-mode to produce a power series expansion of each Case-mode component. This analysis approach is not limited to the LD discretization; it is applicable to any slab geometry spatial discretization with one energy group. From the LD analysis, we draw the following conclusions:

1. The LD solution is constructed on a linear combination of Case-modes; each Case-mode is the product of an amplitude, an angle-shape function, and a within-cell and a cell-to-cell attenuation factor. Because the angular flux is discontinuous at cell edges, the left and right edge angular flux have the following non-equal structures:

$$\psi_{n,j,L}^k = A^k b_n^k (g^k)^{j-1}, \quad (220)$$

$$\psi_{n,j,R}^k = A^k d_n^k (g^k)^{j-1} z^k. \quad (221)$$

Where  $d_m$  and  $b_m$  are the node-dependent angle-shape functions.  $g$  and  $z$  are both attenuation factors with the distinction that  $g$  represents the spatial variation from one cell to the next, and  $z$  represents the spatial variation from one node to the next within a cell.

2. By assigning an extra degree of freedom to capturing the transport equation and not to enforce the continuity of the angular flux, the LD method obtains a third-order accuracy of the spatial attenuation from cell to cell. This is a desired and surprising property for a method derived from a linear polynomial basis. The power series expansion of the LD single-cell attenuation factor yield:

$$g^k = 1 - \tau^k + \frac{1}{2}(\tau^k)^2 - \frac{1}{6}(\tau^k)^3 + O(\tau^k)^4 = g^{k,\text{exact}} + \tilde{O}(\tau^k)^4. \quad (222)$$

Within the cell, Case-modes are attenuated to a first-order accuracy. For optically thin cells, the within-cell attenuation factor is:

$$\begin{aligned} z^k &= 1 - \tau^k + \frac{1}{2} \left[ 1 + \frac{c}{2} \frac{1}{3} \left( \sum_{\mu_n > 0} w_n \alpha_n^k - \sum_{\mu_n < 0} w_n \alpha_n^k \right) \right] (\tau^k)^2 + O(\tau^k)^3 \\ &= g^{k,\text{exact}} + \tilde{O}(\tau^k)^3. \end{aligned} \quad (223)$$

This discrepancy suggests that boundary conditions are transported from cell to cell with a third order error, and within the cell they are transported with a second order error. Therefore, from this result alone we expect that angular fluxes belonging to different nodes will converge at different rates.

3. The gains achieved in the accuracy of the single-cell attenuation factor are countered by inexact angle-shape functions. Furthermore, the angle-shape functions of the angular fluxes belonging to different cell nodes are not equal. An expansion of these functions with respect to the mode-scaled optical thickness yield:

$$d_n^k = \alpha_n^k \left[ 1 - \frac{c}{2} \frac{1}{6} \sum_{\mu_n < 0} w_n \alpha_n^k (\tau^k)^2 \right] + O_n(\tau^k)^3 = \alpha_n^k + \tilde{O}_n(\tau^k)^3, \mu_n > 0, \quad (224)$$

$$d_n^k = \alpha_n^k \left[ 1 + \frac{c}{2} \frac{1}{6} \sum_{\mu_n > 0} w_n \alpha_n^k (\tau^k)^2 \right] + O_n(\tau^k)^3 = \alpha_n^k + \tilde{O}_n(\tau^k)^3, \mu_n < 0, \quad (225)$$

$$b_n^k = \alpha_n^k \left[ 1 + \frac{c}{2} \frac{1}{6} \sum_{\mu_n < 0} w_n \alpha_n^k (\tau^k)^2 \right] + O_n(\tau^k)^3 = \alpha_n^k + \tilde{O}_n(\tau^k)^3, \mu_n > 0, \quad (226)$$

$$b_n^k = \alpha_n^k \left[ 1 - \frac{c}{2} \frac{1}{6} \sum_{\mu_n > 0} w_n \alpha_n^k (\tau^k)^2 \right] + O_n(\tau^k)^3 = \alpha_n^k + \tilde{O}_n(\tau^k)^3, \mu_n < 0. \quad (227)$$

Each LD angle-shape function is a multiple of the exact angle-shape function. However, the multiplying factor is dependent of the node location and the hemisphere to which the streaming direction belongs to. Thus, the Case-mode analysis used for CFEMs can not be used with DFEMs and at this point, we must settle for power expansions of the Case-mode components.

4. The amplitudes to each LD Case-modes are approximated with respect to the exact amplitudes with a second order error:

$$A^{k,LD} = A^{k,\text{exact},(0)} + A^{k,\text{exact},(1)} \tau^k + \left[ A^{k,\text{exact},(2)} - A^{k,\text{exact},(0)} \frac{c}{12} \sum_{\mu_n > 0} w_n \alpha_n^k \right] (\tau^k)^2 + O(\tau^k)^3. \quad (228)$$

From 3, this is initially surprising, since each Case-mode is transported from cell to cell with a third order global error. However, the second order error in the amplitudes complements the error of the angle-shape and within-cell attenuation factors such that their product yields boundary conditions for the LD problem approximated with a third order error.

5. The expansions of the LD Case-mode components were initially posed as power series with respect to the cell's optical thickness. However, the expansion results showed that these Case-mode components are functions of the optical thickness scaled to the exact Discrete Ordinate relaxation length. As a results, a problem discretized with

the LD method and solved with  $N$  quadrature points, has 2 asymptotic Case-modes and  $N - 2$  transient Case-modes.

6. Given all the component expansions, this analysis provides the convergence rate of the error for a single Case-mode to the angular flux at different locations. This analysis does not assume any particular material properties; it only assumes that the ratio of the mode's relaxation length to the cell's optical thickness is small enough for the expansion to converge. The product of the angular-shape functions, attenuation factors and mode amplitudes yields the following convergence rate for the cell-entering, cell-exiting and cell-average angular fluxes:

$$\psi_{n,j,\text{ent}} = \sum_{k=1}^N \alpha_n^k (g^{k,\text{exact}})^{j-1} \left[ \begin{array}{l} A^{k,\text{exact},(0)} + A^{k,\text{exact},(1)} \tau^k \\ -\frac{1}{6} A^{k,\text{exact},(0)} (\tau^k)^2 + O_n^k (\tau^k)^3 \end{array} \right] = \psi_{n,j,\text{ent}}^{\text{exact}} + \tilde{O}_n \Delta x^2, \quad (229)$$

$$\psi_{n,j,\text{ext}} = \sum_{k=1}^N \alpha_n^k (g^{k,\text{exact}})^{j-1} \left[ A^{k,\text{exact}} + O_n^k (\tau^k)^3 \right] = \psi_{n,j,\text{ext}}^{\text{exact}} + \tilde{O}_n \Delta x^3, \quad (230)$$

$$\psi_{n,j} = \sum_{k=1}^N \alpha_n^k (g^{k,\text{exact}})^{j-1} \left[ A^{k,\text{exact}} \frac{1 + g^{k,\text{exact}}}{\tau^k} + O_n^k (\tau^k)^3 \right] = \psi_{n,j}^{\text{exact}} + \tilde{O}_n \Delta x^3. \quad (231)$$

## V. THE ITERATIVE METHOD: SLAB GEOMETRY

We configure a scheme that combines diffusion and transport solvers to construct iteratively a transport solution in few iterations and with no domain-wide transport sweeps. The scheme is ideal for parallel calculations where sweeps add scheduling and communication penalties. The iterative scheme exploits the Case-mode structure of the homogeneous transport solution to decide how to partition the work among solvers. Asymptotic modes, those with slow varying solutions in space and angle, are assigned to the diffusion solver. The remaining transient modes are assigned to the transport operator to correctly capture the strong spatial and angular gradients that appear around material interfaces. As a result, transport sweeps across the entire domain are not needed, and the parallelization challenge is reduced to the parallelization of a diffusion problem. This method is unlike any iterative or acceleration schemes previously explored; the diffusion solver does not assist the transport solver by operating on its iterative error. Our scheme constructs simultaneously a diffusion and transport solution and combines them.

We divide this chapter as follows. First, we present an organization of the iterative scheme with a mathematical description for slab geometry problems. Then, we present preliminary results on the convergence of the scheme if analytic diffusion and transport solvers are used. We replace the analytic transport solver by a discretized one from the Continuous and Discontinuous Finite Element Families, and we apply a Fourier Analysis to predict the convergence rate of the scheme. Finally, we implement the iterative scheme with both transport discretizations and present numerical results. The chapter is closed with a conclusion section.

### *V.A. The Iterative Method*

We organize the iterative scheme into five tasks. Overall the scheme coordinates the contribution from the diffusion, transport and, for problems with extraneous sources, computes the particular solution. In what follows, we assume that the particular solution

is known, since it can be easily computed to an accuracy consistent with the spatial discretization.

We organize the iterative in five steps as follows:

0. Make an initial guess for the transient and asymptotic solution, in most cases zero for both components.
1. Compute incident-current boundary and interface conditions for the asymptotic solver by subtracting the homogeneous angular flux from the transient one.
2. Compute the asymptotic solution with the diffusion solver. This is a global calculation across regions.
3. Compute the transient boundary conditions by updating homogeneous solution and filtering from it the asymptotic components.
4. Compute the transient solution using the transport solver. This is a local calculation.
5. Update the total scalar flux and test if it has converged.

Based on these steps, in the first iteration the diffusion solver will be excited by the correct asymptotic amplitudes and contaminated with a transient fraction. On the other hand, the transport boundary conditions will be incomplete; they will be missing a fraction partly due to the contamination of the asymptotic problem. However, as we iterate and filter on the homogeneous solution, the contamination fraction is reduced and the transport problem is correctly excited by the complete transient spectrum. We envisioned that this approach would place the burden of the global calculation on the diffusion solver by minimally exposing the transport solver to global asymptotic modes. The transport solver is assigned to only solve the transient solutions localized around material interfaces. We reinforce this advantage by converging the total scalar flux instead of converging each component separately. This avoids wasting iterations converging the transient solution in the interior of the slab where their relative importance is minimal.

For the mathematical description of the iterative scheme, we recall the slab-geometry, isotropic scattering, and single energy group transport equation for region  $i$ :

$$\mu_n \frac{\partial \psi_n}{\partial x} + \sigma_{t,i} \psi_n(x) = \sigma_{t,i} \frac{c_i}{2} \phi(x) + Q_i(x). \quad (232)$$

Here we assumed that the scattering ratio and total cross-section are constant through the region. Detail description to the structure of the transport solution is presented in Section II through IV.

### The Asymptotic Component (Step 1 and 2)

We construct the asymptotic solution by calculating the difference between the current homogeneous and transient solution at the region's boundaries, computing the resulting incident currents, and solving for the asymptotic distribution inside the region. From the continuity of angular flux at the boundary interfaces, the incident asymptotic angular flux is:

$$\psi_{n,i}^A(x) \Big|_{x_{i-1/2}} = \psi_{n,i-1}^H(x) \Big|_{x_{i-1/2}} - \psi_{n,i,inc}^T, \quad \mu_n > 0, \quad (233)$$

$$\psi_{n,i}^A(x) \Big|_{x_{i+1/2}} = \psi_{n,i+1}^H(x) \Big|_{x_{i+1/2}} - \psi_{n,i,inc}^T, \quad \mu_n < 0, \quad (234)$$

where,

$x_{i-1/2} \equiv$  spatial location of the left interface of region  $i$ ,

$x_{i+1/2} \equiv$  spatial location of the right interface of region  $i$ ,

$\psi_{n,i}^H(x) \equiv$  homogeneous angular flux of angle  $n$  and region  $i$ ,

$\psi_{n,i}^A(x) \equiv$  asymptotic angular flux of angle  $n$  and region  $i$ ,

$\psi_{n,i,inc}^T \equiv$  incident transient angular flux on region  $i$ .

We have made special emphasis on labeling the transient variable as incident with the DFEM transport approximations in mind. As described in Section IV, DFEMs produce a discontinuous solution with edge-incident angular fluxes being more accurate than edge-exiting angular fluxes. With the goal of preserving the high accuracy of DFEMs, we are careful to employ edge-incident angular fluxes in every step of our scheme.

Based on the structure of the asymptotic space, the left and right asymptotic incident angular fluxes are related to the asymptotic amplitudes by:

$$\begin{aligned} \psi_{n,i}^A(x) = & \alpha_{i,n}^{a+} A_i^{a+} \exp\left(-\sigma_{t,i}(x - x_{i-1/2})/\nu^{a+}\right) \\ & + \alpha_{i,n}^{a-} A_i^{a-} \exp\left(-\sigma_{t,i}(x_{i+1/2} - x)/\nu^{a-}\right). \end{aligned} \quad (235)$$

Here  $a+$  is the Case-mode with the positive relaxation length,  $a-$  is the Case-mode of negative asymptotic relaxation length,  $\nu^{a+}$  is the positive asymptotic relaxation length and  $\alpha_{i,n}$  is the respective angle-shape function in the streaming direction  $n$ .

Adding Eqs.(233) and (234), over all incident directions and inserting Eq.(235) into the resulting half-range sum, we obtain:

$$\begin{aligned} A_i^{a+} \sum_{\mu_n > 0} w_n \alpha_{i,n}^{a+} + A_i^{a-} \exp\left(-\sigma_{t,i}(x_{i+1/2} - x_{i-1/2})/\nu^{a-}\right) \sum_{\mu_n > 0} w_n \alpha_{i,n}^{a-} \\ = \sum_{\mu_n > 0} w_n \left[ \psi_{n,i-1}^H(x) \Big|_{x_{i-1/2}} - \psi_{n,i,inc}^T \right], \end{aligned} \quad (236)$$

$$\begin{aligned} A_i^{a+} \exp\left(-\sigma_{t,i}(x_{i+1/2} - x_{i-1/2})/\nu^{a+}\right) \sum_{\mu_n < 0} w_n \alpha_{i,n}^{a+} + A_i^{a-} \sum_{\mu_n < 0} w_n \alpha_{i,n}^{a-} \\ = \sum_{\mu_n < 0} w_n \left[ \psi_{n,i+1}^H(x) \Big|_{x_{i+1/2}} - \psi_{n,i,inc}^T \right]. \end{aligned} \quad (237)$$

For problems with multiple material regions, we link the asymptotic amplitudes between material regions by reverting the incident homogeneous solution into its asymptotic and transient components. Thus, the system of equation that determines the asymptotic amplitudes after  $l$  iterative steps is:

$$\begin{aligned} \left[ \begin{array}{l} A_i^{a+, (l)} \sum_{\mu_n > 0} w_n \alpha_{i,n}^{a+} + A_i^{a-, (l)} \exp\left(-\sigma_{t,i}(x_{i+1/2} - x_{i-1/2})/\nu_i^{a-}\right) \sum_{\mu_n > 0} w_n \alpha_{i,n}^{a-} \\ -A_{i-1}^{a+, (l)} \exp\left(-\sigma_{t,i-1}(x_{i-1/2} - x_{i-3/2})/\nu_{i-1}^{a+}\right) \sum_{\mu_n > 0} w_n \alpha_{i-1,n}^{a+} + A_{i-1}^{a-, (l)} \sum_{\mu_n > 0} w_n \alpha_{i-1,n}^{a-} \end{array} \right] \\ = \sum_{\mu_n > 0} w_n \left[ \psi_{n,i-1}^{T, (l)}(x) \Big|_{x_{i-1/2}} - \psi_{n,i,inc}^{T, (l)} \right], \end{aligned} \quad (238)$$

$$\begin{aligned}
& \left[ \begin{aligned} & A_i^{a+, (l)} \exp(-\sigma_{t,i} (x_{i+1/2} - x_{i-1/2}) / v_i^{a+}) \sum_{\mu_n < 0} w_n \alpha_{i,n}^{a+} + A_i^{a-, (l)} \sum_{\mu_n < 0} w_n \alpha_{i,n}^{a-} \\ & -A_{i+1}^{a+, (l)} \sum_{\mu_n < 0} w_n \alpha_{i+1,n}^{a+} + A_{i+1}^{a-, (l)} \exp(-\sigma_{t,i+1} (x_{i+3/2} - x_{i+1/2}) / |v_i^{a-}|) \sum_{\mu_n < 0} w_n \alpha_{i+1,n}^{a-} \end{aligned} \right] \\
& = \sum_{\mu_n < 0} w_n \left[ \psi_{n,i+1}^{T,(l)}(x) \Big|_{x_{i+1/2}} - \psi_{n,i,inc}^{T,(l)} \right]. \quad (239)
\end{aligned}$$

If the region lies on the problem's left boundary, then Eq.(239) remains unchanged while Eq.(238) is:

$$\begin{aligned}
& \left[ \begin{aligned} & A_i^{a+, (l)} \sum_{\mu_n > 0} w_n \alpha_{i,n}^{a+} + A_i^{a-, (l)} \exp(-\sigma_{t,i} (x_{i+1/2} - x_{i-1/2}) / |v_i^{a-}|) \sum_{\mu_n > 0} w_n \alpha_{i,n}^{a-} \end{aligned} \right] \\
& = \sum_{\mu_n > 0} w_n \left[ \psi_{n,inc} - \psi_{n,i,inc}^{T,(l)} \right]. \quad (240)
\end{aligned}$$

Here:

$\psi_{n,inc} \equiv$  left boundary conditions.

In the case the region lies on the right boundary, then Eq.(239) becomes:

$$\begin{aligned}
& \left[ \begin{aligned} & A_i^{a+, (l)} \exp(-\sigma_{t,i} (x_{i+1/2} - x_{i-1/2}) / v_i^{a+}) \sum_{\mu_n < 0} w_n \alpha_{i,n}^{a+} + A_i^{a-, (l)} \sum_{\mu_n < 0} w_n \alpha_{i,n}^{a-} \end{aligned} \right] \\
& = \sum_{\mu_n < 0} w_n \left[ \psi_{n,inc} - \psi_{n,i,inc}^{T,(l)} \right]. \quad (241)
\end{aligned}$$

The asymptotic problem consists on  $2I$  unknown amplitudes with the same number of equations, where  $I$  is the total number of regions. The asymptotic relaxations are obtained from the dispersion relation, and used to compute the angle-shape function:

$$\sum_{n=1}^N w_n \frac{v^k}{v^k - \mu_n} = \frac{2}{c}, \quad (242)$$

$$\alpha_n^{a\pm} = \frac{v^{a\pm}}{v^{a\pm} - \mu_n}, \quad (243)$$

where  $v^{a+} = \max[v^k]$ ,  $v^{a-} = \min[v^k]$ .

### The Transient Component (Steps 3 and 4)

We solve the remaining Case-modes of the homogeneous transport solution in this step. We group these modes into a single variable that satisfies the homogeneous transport equation:

$$\mu_n \frac{\partial \psi_{n,i}^T}{\partial x} + \sigma_{t,i} \psi_{n,i}^T(x) = \sigma_{t,i} \frac{c_i}{2} \phi_i^T(x). \quad (244)$$

Here we label the solution as belonging to region  $i$ , to account for the discontinuity of the transient angular flux across regions.

We calculate the incident angular flux to the transient problem by reconstructing the asymptotic angular flux exiting from each region, updating the homogeneous angular flux and filtering from the homogeneous angular flux the asymptotic component. The asymptotic angular flux is:

$$\psi_{n,i,i+1/2}^{A,(l)} = \alpha_{i,n}^{a+} A_i^{a+,(l)} \exp(-\sigma_t(x_{i+1/2} - x_{i-1/2})/v_i^{a+}) + \alpha_{i,n}^{a-} A_i^{a-,(l)}, \quad (245)$$

$$\psi_{n,i,i-1/2}^{A,(l)} = \alpha_{i,n}^{a+} A_i^{a+,(l)} + \alpha_{i,n}^{a-} A_i^{a-,(l)} \exp(-\sigma_{t,i}(x_{i-1/2} - x_{i+1/2})/|v_i^{a-}|). \quad (246)$$

At the left and right edge of region  $i$ , the resulting homogeneous angular flux is:

$$\psi_{n,i,i-1/2}^{H,(l+1/2)} = \psi_{n,i,i-1/2}^{A,(l)} + \psi_{n,i,inc}^{T,(l)}, \quad \mu_n > 0, \quad (247)$$

$$\psi_{n,i,i-1/2}^{H,(l+1/2)} = \psi_{n,i,i-1/2}^{A,(l)} + \psi_{n,i}^{T,(l)}(x) \Big|_{x_{i-1/2}}, \quad \mu_n < 0, \quad (248)$$

$$\psi_{n,i,i+1/2}^{H,(l+1/2)} = \psi_{n,i,i+1/2}^{A,(l)} + \psi_{n,i}^{T,(l)}(x) \Big|_{x_{i+1/2}}, \quad \mu_n > 0, \quad (249)$$

$$\psi_{n,i,i+1/2}^{H,(l+1/2)} = \psi_{n,i,i+1/2}^{A,(l)} + \psi_{n,i,inc}^{T,(l)}, \quad \mu_n < 0. \quad (250)$$

Again, we have only employed edge-incident transient angular fluxes when calculating the homogeneous angular flux. By doing so, we compute the homogeneous angular flux with the most accurate information available in the special case that a DFEM discretizes the transient problem.

We filter the asymptotic components and subtract them from the homogeneous solution to obtain the current transient incident angular flux on region  $i$ :

$$\psi_{n,i,inc}^{T,(l+1)} = \psi_{n,i-1/2}^{H,(l+1/2)} - \alpha_{n,i}^{a+} \frac{\langle \psi_{i,i-1/2}^{H,(l+1/2)}, \alpha_i^{a+} \rangle}{\langle \alpha_i^{a+}, \alpha_i^{a+} \rangle} - \alpha_{n,i}^{a-} \frac{\langle \psi_{i,i-1/2}^{H,(l+1/2)}, \alpha_i^{a-} \rangle}{\langle \alpha_i^{a-}, \alpha_i^{a-} \rangle}, \quad \mu_n > 0, \quad (251)$$

$$\psi_{n,i,inc}^{T,(l+1)} = \psi_{n,i+1/2}^{H,(l+1/2)} - \alpha_{n,i}^{a+} \frac{\langle \psi_{i,i+1/2}^{H,(l+1/2)}, \alpha_i^{a+} \rangle}{\langle \alpha_i^{a+}, \alpha_i^{a+} \rangle} - \alpha_{n,i}^{a-} \frac{\langle \psi_{i,i+1/2}^{H,(l+1/2)}, \alpha_i^{a-} \rangle}{\langle \alpha_i^{a-}, \alpha_i^{a-} \rangle}, \quad \mu_n < 0, \quad (252)$$

where we define the Case-mode inner product as:

$$\langle \alpha^k, \alpha^l \rangle = \sum_{n=1}^N w_n \mu_n \alpha_n^k \alpha_n^l = \delta_{l,k} \sum_{n=1}^N w_n \mu_n [\alpha_n^k]^2. \quad (253)$$

With the transient boundary conditions defined, we invert the transport problem in each region and obtain the transient angular flux. For slab geometry problems; both analytic and discretized transport solvers are available to describe the transient spatial distribution. However, if our goal is to address problems in multiple dimensions, then the analytic option is no longer available. Also a disadvantage is that an analytic approach requires a full description of the relaxation lengths, transient and asymptotic, so that the angle-shape and attenuation factors may be calculated. For the first step in our analysis, we solve the transient distribution using an analytic solver to confirm that we are on the right track in the configuration of the iterative scheme. Beyond this analysis, we implement a discretized transport solver. The equations describing the analytic transient problem in region  $i$  are:

$$\sum_{\nu^t > 0} \alpha_{n,i}^t A_i^{t,(l+1)} + \sum_{0 > \nu^t > -1} \alpha_{n,i}^t A_i^{t,(l+1)} \exp\left(-\sigma_{t,i}(x_{i+1/2} - x_{i-1/2})/|\nu_i^t|\right) = \psi_{n,i,inc}^{T,(l+1)}, \quad \mu_n > 0, \quad (254)$$

$$\sum_{\nu^t > 0} \alpha_{n,i}^t A_i^{t,(l+1)} \exp\left(-\sigma_{t,i}(x_{i+1/2} - x_{i-1/2})/\nu_i^t\right) + \sum_{\nu^t < 0} \alpha_{n,i}^t A_i^{t,(l+1)} = \psi_{n,i,inc}^{T,(l+1)}, \quad \mu_n < 0. \quad (255)$$

The solution to these equations is the amplitude of each Case-mode, from which we reconstruct the angular flux based on the angle shape functions  $\alpha^l$  and the single cell attenuation factor. These transient equations allow for an asymptotic presence in the transport calculation. However, as the problem converges towards the correct solution, the asymptotic contamination is removed from the transient incident conditions. The

asymptotic Case-modes are progressively excited less until the solution to their amplitudes is zero.

We tested the performance of the iterative scheme with a CFEM and DFEM transport discretization, more specifically with Diamond Difference (DD), a linear CFEM, and Linear Discontinuous (LD), a linear DFEM. We allow the transport problem to be inverted with either Source Iterations (SI) or One Cell Inversions (OCI). However, if the goal of the iterative scheme is to improve the parallelization of the transport problem, then OCI is the advantageous choice. OCI inverts exactly the transport problem of a single cell on the incident angular flux from a previous iteration. By using old incident conditions, the cell inversions do not need to be scheduled in a specific order, which avoids the use of SI sweeps and improves the local parallelization of the algorithm. OCI is an ideal scheme for parallel computation; however, if implemented by itself, it tends to converge slowly. It propagates boundary conditions on a region towards its interior one cell per iteration. We expect that by removing the asymptotic component from the OCI calculation, the number of iteration will be greatly reduced. Without asymptotic modes, the solution will penetrate fewer cells into the slab and fewer iterations will be needed to resolve the interior solution.

To define our discretized transport problem, we divide region  $i$  into  $J$  cells with 2 nodes per cell. We label the left edge of cell  $j$  as  $x_{i,j,L}$  and the right edge as  $x_{i,j,R}$ . Based on this notation, the OCI equations for the DD problem are:

$$\mu_n \frac{\psi_{n,i,j,R}^{T,(\tilde{l}+1)} - \psi_{n,i,j,L}^{T,(l^*)}}{\Delta x_{i,j}} + \sigma_{t,i} \psi_{n,i,j}^{T,(\tilde{l}+1)} = \sigma_{t,i} \frac{C_i}{2} \sum_{m=1}^N w_m \psi_{m,i,j}^{T,(\tilde{l}+1)}, \quad \mu_n > 0, \quad (256)$$

$$\psi_{n,i,j}^{T,(\tilde{l}+1)} = \frac{1}{2} \left[ \psi_{n,i,j,R}^{T,(\tilde{l}+1)} + \psi_{n,i,j,L}^{T,(l^*)} \right], \quad \mu_n > 0, \quad (257)$$

$$\mu_n \frac{\psi_{n,i,j,R}^{T,(l^*)} - \psi_{n,i,j,L}^{T,(\tilde{l}+1)}}{\Delta x_{i,j}} + \sigma_{t,i} \psi_{n,i,j}^{T,(\tilde{l}+1)} = \sigma_{t,i} \frac{C_i}{2} \sum_{m=1}^N w_m \psi_{m,i,j}^{T,(\tilde{l}+1)}, \quad \mu_n < 0, \quad (258)$$

$$\psi_{n,i,j}^{T,(\tilde{l}+1)} = \frac{1}{2} \left[ \psi_{n,i,j,R}^{T,(l^*)} + \psi_{n,i,j,L}^{T,(\tilde{l}+1)} \right], \quad \mu_n > 0, \quad (259)$$

where:

$\tilde{l} \equiv$  inner iteration index,

$$\psi_{n,i,j,R}^{(l^*)} = \begin{cases} \psi_{n,i,inc}^{(l+1)} & \text{if } j = J \\ \psi_{n,i,j-1,L}^{(\tilde{l})} & \text{otherwise} \end{cases},$$

$$\psi_{n,i,j,L}^{(l^*)} = \begin{cases} \psi_{n,i,inc}^{(l+1)} & \text{if } j = 1 \\ \psi_{n,i,j+1,R}^{(\tilde{l})} & \text{otherwise} \end{cases}.$$

In inverting our transient problem, we have several convergence options. We may invert the local transient solution to the global tolerance of the problem. However, this could waste inner iterations since the regional interface conditions are not necessarily converged. We may also converge the transient solution to an arbitrary lower tolerance, but setting such an arbitrary tolerance also risks wasting inner iterations. Since each outer iteration involves an expensive inversion of the global diffusion problem, a balance must be found between the number of inner and outer iteration. The scheme iterates until the boundary conditions to each component are sufficiently accurate so that the spatial distribution of the homogeneous solution meets the convergence tolerance. We recognize that OCI propagates angular fluxes one cell per iteration or that OCI requires at least one inner iteration for every cell in the transient region to transport boundary angular fluxes to the opposite interface. Thus to avoid wasting outer iterations, the number of inner iterations should at least equal the number of cells in the region. We explore these transient convergence possibilities in the Numerical Results section.

The SI system of equations for DD is:

$$\mu_n \frac{\psi_{n,i,j,R}^{T,(\tilde{l}+1)} - \psi_{n,i,j,L}^{T,(l^*)}}{\Delta x_{i,j}} + \sigma_{t,i} \psi_{n,i,j}^{T,(\tilde{l}+1)} = \sigma_{t,i} \frac{c_i}{2} \sum_{m=1}^N w_m \psi_{m,i,j}^{T,(\tilde{l})}, \quad \mu_n > 0, \quad (260)$$

$$\psi_{n,i,j}^{T,(\tilde{l}+1)} = \frac{1}{2} \left[ \psi_{n,i,j,R}^{T,(\tilde{l}+1)} + \psi_{n,i,j,L}^{T,(l^*)} \right], \quad \mu_n > 0, \quad (261)$$

$$\mu_n \frac{\psi_{n,i,j,R}^{T,(l^*)} - \psi_{n,i,j,L}^{T,(\tilde{l}+1)}}{\Delta x_{i,j}} + \sigma_{t,i} \psi_{n,i,j}^{T,(\tilde{l}+1)} = \sigma_{t,i} \frac{c_i}{2} \sum_{m=1}^N w_m \psi_{m,i,j}^{T,(\tilde{l})}, \quad \mu_n < 0, \quad (262)$$

$$\psi_{n,i,j}^{T,(\tilde{l}+1)} = \frac{1}{2} \left[ \psi_{n,i,j,R}^{T,(l^*)} + \psi_{n,i,j,L}^{T,(\tilde{l}+1)} \right], \quad \mu_n < 0, \quad (263)$$

where:

$$\psi_{n,i,j,R}^{(l^*)} = \begin{cases} \psi_{n,i,inc}^{(l+1)} & \text{if } j = J \\ \psi_{n,i,j-1,L}^{(\tilde{l}+1)} & \text{otherwise} \end{cases},$$

$$\psi_{n,i,j,L}^{(l^*)} = \begin{cases} \psi_{n,i,inc}^{(l+1)} & \text{if } j = 1 \\ \psi_{n,i,j+1,R}^{(\tilde{l}+1)} & \text{otherwise} \end{cases}.$$

Based on the DD schemes, the LD-OCI iterative scheme is defined by:

$$\mu_n \begin{bmatrix} \frac{\psi_{n,i,j,L}^{T,(\tilde{l}+1)} + \psi_{n,i,j,R}^{T,(\tilde{l}+1)}}{2} \\ -\psi_{n,i,j,L,surf}^T \end{bmatrix} + \Delta x_{i,j} \sigma_{t,i,j} \begin{bmatrix} \frac{\psi_{n,i,j,L}^{T,(\tilde{l}+1)}}{3} \\ + \frac{\psi_{n,i,j,R}^{T,(\tilde{l}+1)}}{6} \end{bmatrix} = \Delta x_{i,j} \sigma_{t,i,j} \frac{c_i}{2} \sum_{m=1}^N w_m \begin{bmatrix} \frac{\psi_{m,i,j,L}^{T,(\tilde{l}+1)}}{3} \\ + \frac{\psi_{m,i,j,R}^{T,(\tilde{l}+1)}}{6} \end{bmatrix}, \quad (264)$$

$$\mu_n \begin{bmatrix} \frac{\psi_{n,i,j,L}^{T,(\tilde{l}+1)} + \psi_{n,i,j,R}^{T,(\tilde{l}+1)}}{2} \\ + \psi_{n,i,j,R,surf}^T \end{bmatrix} + \Delta x_{i,j} \sigma_{t,i,j} \begin{bmatrix} \frac{\psi_{n,i,j,L}^{T,(\tilde{l}+1)}}{6} \\ + \frac{\psi_{n,i,j,R}^{T,(\tilde{l}+1)}}{3} \end{bmatrix}$$

$$= \Delta x_{i,j} \sigma_{t,i,j} \frac{c_i}{2} \sum_{m=1}^N w_m \begin{bmatrix} \frac{\psi_{m,i,j,L}^{T,(\tilde{l}+1)}}{6} \\ + \frac{\psi_{m,i,j,R}^{T,(\tilde{l}+1)}}{3} \end{bmatrix}, \quad (265)$$

$$\psi_{n,i,j,L,surf}^T = \begin{cases} \psi_{n,i,j,L}^{T,(l^*)} & \text{if } \mu_n > 0 \\ \psi_{n,i,j,L}^{T,(\tilde{l}+1)} & \text{otherwise} \end{cases}, \quad (266)$$

$$\psi_{n,i,j,R,surf}^T = \begin{cases} \psi_{n,i,j,R}^{T,(l^*)} & \text{if } \mu_n < 0 \\ \psi_{n,i,j,R}^{T,(\tilde{l}+1)} & \text{otherwise} \end{cases}. \quad (267)$$

Similarly, the LD-SI scheme is:

$$\mu_n \left[ \frac{\psi_{n,i,j,L}^{T,(\tilde{l}+1)} + \psi_{n,i,j,R}^{T,(\tilde{l}+1)}}{2} \right] + \Delta x_{i,j} \sigma_{t,i,j} \left[ \frac{\psi_{n,i,j,L}^{T,(\tilde{l}+1)}}{3} \right. \\ \left. + \frac{\psi_{n,i,j,R}^{T,(\tilde{l}+1)}}{6} \right] = \Delta x_{i,j} \sigma_{t,i,j} \frac{c_i}{2} \sum_{m=1}^N w_m \left[ \frac{\psi_{m,i,j,L}^{T,(\tilde{l})}}{3} \right. \\ \left. + \frac{\psi_{m,i,j,R}^{T,(\tilde{l})}}{6} \right], \quad (268)$$

$$\mu_n \left[ \frac{\psi_{n,i,j,L}^{T,(\tilde{l}+1)} + \psi_{n,i,j,R}^{T,(\tilde{l}+1)}}{2} \right] + \Delta x_{i,j} \sigma_{t,i,j} \left[ \frac{\psi_{n,i,j,L}^{T,(\tilde{l}+1)}}{6} \right. \\ \left. + \frac{\psi_{n,i,j,R}^{T,(\tilde{l}+1)}}{3} \right] \\ = \Delta x_{i,j} \sigma_{t,i,j} \frac{c_i}{2} \sum_{m=1}^N w_m \left[ \frac{\psi_{m,i,j,L}^{T,(\tilde{l})}}{6} \right. \\ \left. + \frac{\psi_{m,i,j,R}^{T,(\tilde{l})}}{3} \right], \quad (269)$$

$$\psi_{n,i,j,L,surf}^T = \begin{cases} \psi_{n,i,j,L}^{T,(l^*)} & \text{if } \mu_n > 0 \\ \psi_{n,i,j,L}^{T,(\tilde{l}+1)} & \text{otherwise} \end{cases}, \quad (270)$$

$$\psi_{n,i,j,R,surf}^T = \begin{cases} \psi_{n,i,j,R}^{T,(l^*)} & \text{if } \mu_n < 0 \\ \psi_{n,i,j,R}^{T,(\tilde{l}+1)} & \text{otherwise} \end{cases}. \quad (271)$$

### Update the Total Scalar Flux and Test for Convergence (Step 5)

In the final step of our scheme, we take the most current asymptotic amplitudes, transient angular flux and particular solution and combined them into a single angular flux:

$$\psi_{n,i}^{(l+1)}(x) = \psi_{n,i}^{H,(l+1)}(x) + \psi_{n,i}^P(x), \quad (272)$$

$$\psi_{n,i}^{H,(l+1)}(x) = \psi_{n,i}^{T,(l+1)}(x) + \alpha_{n,i}^{a+} A_i^{a+} \exp(-\sigma_{t,i}(x - x_{i-1/2})/v_i^{a+}) \\ + \alpha_{n,i}^{a-} A_i^{a-} \exp(-\sigma_{t,i}(x_{i+1/2} - x)/|v_i^{a-}|). \quad (273)$$

We compute the scalar flux, and test it against the value from a previous iterate. When the relative difference between the two is smaller than a user defined tolerance,

we declare the solution converged and stop iterating. The scalar flux at the end of iteration  $l + 1$  is:

$$\phi_i(x) = \sum_{n=1}^N w_n \psi_{n,i}^{(l+1)}(x). \quad (274)$$

### *V.B. Analysis*

#### **Ideal Method**

To assess if the design of the iterative scheme was heading in the right track, and if so, to predict its convergence properties, we performed two analyses. In the first analysis, we modified the scheme described in the previous five steps so that the best possible convergence could be achieved, even if these modifications were not necessarily practical. The modified five steps were:

1. Compute the integrals of asymptotic angular fluxes over the range of incident angles to each region. We weighted the integrals using the half-range Case-mode filter.
2. Compute the asymptotic flux analytically.
3. Filter the asymptotic contribution to the homogeneous angular flux and compute the incident transient angular flux. Compute  $N - 2$  incident currents by applying the half-range filter to the incident transient angular flux.
4. Solve each transient mode analytically and assuming that no asymptotic contamination has occurred. The transient problem of dimension  $N - 2$  was inverted exactly.
5. Update and test the scalar flux.

We developed a program that assembles the resulting iterative matrix of the scheme and computes the spectral radius of the iterative matrix. Given the spectral radius of the iterative matrix, we can estimate the asymptotic convergence rate of the iteration that appears after a few iterations. The program allowed for an arbitrary number of material regions, and was implemented with a Gauss-Legendre quadrature set.

The first set of results was obtained from homogeneous problems of varying scattering ratio and varying optical thickness. While the search was not exhaustive, we did not find a problem with a spectral radius larger than 0.1. Hence, after one iteration the resulting error is reduced by at least a factor of 10. The behavior of the spectral radius with changes in material properties agree with our expectation:

- the spectral radius increased as the region thickness decreased, yet it asymptoted,
- the spectral radius weakly increased with an increased in the scattering ratio, yet it also asymptoted.

These spectral radius trends were not surprising. They confirmed that the convergence of the problem depends on the coupling between Case-modes belonging to different regions. The coupling between transient and asymptotic modes occurs at the region boundaries; thus, heavily absorbing regions imply a weak coupling between the angular fluxes of opposite boundaries. Increasing the total cross-section or reducing the scattering ratio increases the attenuation of each Case-mode, which reduces the dependence between boundaries. However, a change in the total cross-section translates into a linear change of the optical thickness of the region, while the relationship between the scattering and the optical thickness as scaled by each Case-mode is non-linear. Hence, as the scattering ratio approaches the limit of 1, its effects on the attenuation of each Case-mode asymptote.

A problem of 0.1 mean-free paths in thickness and a scattering ratio of 0.9999 converged with a spectral radius of 0.059 for an  $S_4$  quadrature and 0.043 for a  $S_{16}$  quadrature set. Every problem tested that was at least 10 mean free paths in thickness produced a spectral radius smaller than  $10^{-6}$ .

TABLE V  
Spectral Radius of the Ideal Method with Multiple Regions in Slab Geometry.

Material Properties						Quadrature Order	
Region 1		Region 2		Region 3		$S_4$	$S_{16}$
$\sigma_r \Delta x$	$c$	$\sigma_r \Delta x$	$c$	$\sigma_r \Delta x$	$c$		
1	0.9	0.01	0.9999	1	0.9	0.0170	0.0175
1	0.9	0.1	0.9999	1	0.9	0.0173	0.0177
1	0.9	1.0	0.9999	1	0.9	0.0183	0.0189
1	0.9	10	0.9999	1	0.9	0.0189	0.0193
1	0.9	0.01	0.5	1	0.9	0.0537	0.0963
1	0.9	0.1	0.5	1	0.9	0.0496	0.0895
1	0.9	1.0	0.5	1	0.9	0.0319	0.0555
1	0.9	10	0.5	1	0.9	0.0294	0.0410

We turned next to the calculation of the convergence rate of multi-region problems. We tested the logic to our software by replicating the one-region results with single-material problems configured as multi-region problems. By inserting discontinuities in the scattering ratio, the homogeneous solution is spanned by different angle-shape functions in each region. The spectral radius deteriorates since the scheme must converge transient and asymptotic discontinuous solutions at each material interface. We present the convergence rate results for three regions problem and  $S_4$ ,  $S_6$  quadrature set in Table V. The method remained fast convergent, with a weak dependence between the convergence rate and the discontinuity in scattering ratio. This dependence was amplified by thin regions, in accordance with the single-region findings. The largest spectral radius (0.2) was obtained with a problem of significant scattering ratio discontinuity and very thin middle region.

The results in this section of the analysis confirm that a transport solution can be calculated by iterating between a diffusion and transport solver, or that our iterative approach is promising. The spectral radius calculations establish an upper limit on how fast a more practical method, one with a single and discretized solver for all transient modes, might converge. From this ideal scheme, we can expect our practical method to be strongly sensitive to the optical thickness of each region, and weakly sensitive to the scattering ratio.

### Practical Method

We turn to an infinite-medium Fourier analysis of the iterative method specified in section V.A. As with the Ideal Method analysis, our goal is to estimate the convergence rate of the scheme and understand its behavior with respect to varying material properties. In this analysis, we compute the convergence rate of the scheme by recasting it in terms of the iterative error, decomposing the iterative error into Fourier modes and determine the attenuation factor of the Fourier modes per iteration<sup>6</sup>. We configure the infinite-medium Fourier analysis as follows:

1. We chose each cell to be its own Case-mode region. We couple the asymptotic and transient Case-modes at each cell-edge, and iterate between Case-modes at these locations. For simplicity, we drop the region index from our unknowns, and label the location to the left and right edge of each region as  $x_{j,L}$  and  $x_{j,R}$ .
2. We define the iterative error to each unknown as a linear combination of Fourier modes and assume that the converged solution to each unknown is bound at every point of the infinite spatial domain. In terms of the Fourier expansions, the iterative error to each of the unknowns in our scheme is:

$$A^{a+,(\infty)} - A^{a+,(l)} = \int_{-\infty}^{\infty} d\lambda \Gamma^{a+,(l)}(\lambda) \exp(i\lambda\sigma_t x_{j,L}), \quad (275)$$

$$A^{a-,(\infty)} - A^{a-,(l)} = \int_{-\infty}^{\infty} d\lambda \Gamma^{a-,(l)}(\lambda) \exp(i\lambda\sigma_t x_{j,R}), \quad (276)$$

$$\psi_{n,j,L}^{H,(\infty)} - \psi_{n,j,L}^{H,(l+1/2)} = \int_{-\infty}^{\infty} d\lambda \beta_n^{(l)}(\lambda) \exp(i\lambda\sigma_t x_{j,L}), \quad \mu_m > 0, \quad (277)$$

$$\psi_{n,j,R}^{H,(\infty)} - \psi_{n,j,R}^{H,(l+1/2)} = \int_{-\infty}^{\infty} d\lambda \beta_n^{(l)}(\lambda) \exp(i\lambda \sigma_t x_{j,R}), \quad \mu_m < 0, \quad (278)$$

$$\psi_{n,j-1,R}^{H,(\infty)} - \psi_{n,j-1,R}^{H,(l+1/2)} = \int_{-\infty}^{\infty} d\lambda \gamma_n^{(l)}(\lambda) \exp(i\lambda \sigma_t x_{j,L}), \quad \mu_m > 0, \quad (279)$$

$$\psi_{n,j+1,L}^{H,(\infty)} - \psi_{n,j+1,L}^{H,(l+1/2)} = \int_{-\infty}^{\infty} d\lambda \gamma_n^{(l)}(\lambda) \exp(i\lambda \sigma_t x_{j,R}), \quad \mu_m < 0, \quad (280)$$

$$\psi_{n,j,inc}^{T,(\infty)} - \psi_{n,j,inc}^{T,(l)} = \int_{-\infty}^{\infty} d\lambda \varphi_n^{(l)}(\lambda) \exp(i\lambda \sigma_t x_{j,L}), \quad \mu_m > 0, \quad (281)$$

$$\psi_{n,j,inc}^{T,(\infty)} - \psi_{n,j,inc}^{T,(l)} = \int_{-\infty}^{\infty} d\lambda \varphi_n^{(l)}(\lambda) \exp(i\lambda \sigma_t x_{j,R}), \quad \mu_m < 0, \quad (282)$$

$$\psi_{n,j-1,R}^{T,(\infty)} - \psi_{n,j-1,R}^{T,(l)} = \int_{-\infty}^{\infty} d\lambda w_n^{(l)}(\lambda) \exp(i\lambda \sigma_t x_{j,R}), \quad \mu_m > 0, \quad (283)$$

$$\psi_{n,j+1,L}^{T,(\infty)} - \psi_{n,j+1,L}^{T,(l)} = \int_{-\infty}^{\infty} d\lambda w_n^{(l)}(\lambda) \exp(i\lambda \sigma_t x_{j,L}), \quad \mu_m < 0, \quad (284)$$

$$\phi_j^{T,(\infty)} - \phi_j^{T,(l)} = \int_{-\infty}^{\infty} d\lambda \vartheta^{(l)}(\lambda) \exp(i\lambda \sigma_t (x_{j,L} + x_{j,R})/2). \quad (285)$$

Here  $\iota = \sqrt{-1}$ .

3. We configure a system of equations that relates the Fourier mode amplitudes belonging to two consecutive iterates. We construct the system of equation by noting that Fourier modes are orthogonal; therefore, the amplitudes to each unknown satisfy the system of equations individually. In terms of the Fourier unknowns above, step 1 is:

$$\begin{aligned} \Gamma^{a+, (l)} \left[ 1 - e^{-i\lambda \sigma_t \Delta x} e^{-\frac{\sigma \Delta x}{\nu^{a+}}} \right] \sum_{\mu_n > 0} w_n \mu_n \alpha_n^{a+} - \Gamma^{a-, (l)} \left[ 1 - e^{-\frac{\sigma \Delta x}{\nu^{a+}}} e^{i\lambda \sigma \Delta x} \right] \sum_{\mu_n > 0} w_n \mu_n \alpha_n^{a-} \\ = \sum_{\mu_n > 0} w_n \mu_n \left[ v_n^{(l)} - \varphi_n^{(l)} \right], \end{aligned} \quad (286)$$

$$\begin{aligned} -\Gamma^{a+, (l)} \left[ 1 - e^{-i\lambda \sigma_t \Delta x} e^{-\frac{\sigma \Delta x}{\nu^{a+}}} \right] \sum_{\mu_n < 0} w_n \mu_n \alpha_n^{a+} + \Gamma^{a-, (l)} \left[ 1 - e^{-\frac{\sigma \Delta x}{\nu^{a+}}} e^{i\lambda \sigma \Delta x} \right] \sum_{\mu_n < 0} w_n \mu_n \alpha_n^{a-} \\ = \sum_{\mu_n < 0} w_n \mu_n \left[ v_n^{(l)} - \varphi_n^{(l)} \right]. \end{aligned} \quad (287)$$

In matrix form:

$$D \cdot \Phi^{a+, (l)} = B \cdot \left[ \Psi_{exit}^{T, (l)} - \Psi_{inc}^{T, (l)} \right], \quad (288)$$

where:

$$\Phi^{a+, (l)} = \begin{pmatrix} \Gamma^{a+, (l)} \\ \Gamma^{a-, (l)} \end{pmatrix},$$

$$\left[ \Psi_{exit}^{T, (l)} \right]_n = v_n^{(l)},$$

$$\left[ \Psi_{inc}^{T, (l)} \right]_n = \varphi_n^{(l)}.$$

Step 2:

$$\beta_n^{(l)} = \alpha_n^{a+} \Gamma^{a+, (l)} \exp(-i\lambda\sigma_t \Delta x) \exp\left(-\frac{\sigma_t \Delta x}{v^{a+}}\right) + \alpha_n^{a-} \Gamma^{a-, (l)} + v_n^{(l)}, \mu_n > 0, \quad (289)$$

$$\beta_n^{(l)} = \alpha_n^{a+} \Gamma^{a+, (l)} + \alpha_n^{a-} \Gamma^{a-, (l)} \exp(i\lambda\sigma_t \Delta x) \exp\left(-\frac{\sigma_t \Delta x}{v^{a+}}\right) + v_n^{(l)}, \mu_n < 0, \quad (290)$$

$$\gamma_n^{(l)} = \alpha_n^{a+} \Gamma^{a+, (l)} + \alpha_n^{a-} \Gamma^{a-, (l)} \exp(i\lambda\sigma_t \Delta x) \exp\left(-\frac{\sigma_t \Delta x}{v^{a+}}\right) + \varphi_n^{(l)}, \mu_n > 0, \quad (291)$$

$$\gamma_n^{(l)} = \alpha_n^{a+} \Gamma^{a+, (l)} \exp(-i\lambda\sigma_t \Delta x) \exp\left(-\frac{\sigma_t \Delta x}{v^{a+}}\right) + \alpha_n^{a-} \Gamma^{a-, (l)} + \varphi_n^{(l)}, \mu_n < 0, \quad (292)$$

$$v_n^{(l+1)} = \beta_n^{(l)} - \alpha_n^{a+} \frac{\sum_{\mu_n > 0} w_n \mu_n \alpha_n^{a+} \beta_n^{(l)} + \sum_{\mu_n < 0} w_n \mu_n \alpha_n^{a+} \gamma_n^{(l)}}{\langle \alpha_n^{a+}, \alpha_n^{a+} \rangle} - \alpha_n^{a-} \frac{\sum_{\mu_n > 0} w_n \mu_n \alpha_n^{a-} \beta_n^{(l)} + \sum_{\mu_n < 0} w_n \mu_n \alpha_n^{a-} \gamma_n^{(l)}}{\langle \alpha_n^{a-}, \alpha_n^{a-} \rangle}, \mu_n > 0, \quad (293)$$

$$v_n^{(l+1)} = \beta_n^{(l)} - \alpha_n^{a+} \frac{\sum_{\mu_n > 0} w_n \mu_n \alpha_n^{a+} \gamma_n^{(l)} + \sum_{\mu_n < 0} w_n \mu_n \alpha_n^{a+} \beta_n^{(l)}}{\langle \alpha_n^{a+}, \alpha_n^{a+} \rangle} - \alpha_n^{a-} \frac{\sum_{\mu_n > 0} w_n \mu_n \alpha_n^{a-} \gamma_n^{(l)} + \sum_{\mu_n < 0} w_n \mu_n \alpha_n^{a-} \beta_n^{(l)}}{\langle \alpha_n^{a-}, \alpha_n^{a-} \rangle}, \mu_n < 0, \quad (294)$$

$$\Psi_{exit}^{H, (l+1/2)} = A_1 \cdot \Phi^{A, (l)} + \Psi_{exit}^{T, (l)}, \quad (295)$$

$$\Psi_{inc}^{H,(l+1/2)} = A_2 \cdot \Phi^{A,(l)} + \Psi_{inc}^{T,(l)}, \quad (296)$$

$$\Psi_{inc}^{T,(l+1)} = \Psi_{inc}^{H,(l+1/2)} - F_1 \Psi_{exit}^{H,(l+1/2)} - F_2 \Psi_{inc}^{H,(l+1/2)}. \quad (297)$$

Here:

$$\left[ \Psi_{exit}^{H,(l+1/2)} \right]_n = \beta_n^{(l)},$$

$$\left[ \Psi_{inc}^{H,(l+1/2)} \right]_n = \gamma_n^{(l)}.$$

We present step 4 directly in matrix form to represent simultaneously the DD and LD problem. Step 4 implemented with OCI in matrix form is:

$$O \cdot \Phi^{T,(l+1)} = P \cdot \Psi_{inc}^{T,(l+1)}, \quad (298)$$

$$Q \cdot \Psi_{exit}^{T,(l+1)} = R \cdot \Psi_{inc}^{T,(l+1)} + S \cdot \Phi^{T,(l+1)}. \quad (299)$$

Here:

$$\Phi^{T,(l+1)} = \vartheta^{(l+1)}.$$

4. Given the system of equation representing the five steps of our iterative scheme, we compute the iterative matrix. For simplicity, we derive the iterative matrix with respect to the incident transient angular flux variable:

$$\Psi_{inc}^{T,(l+1)} = G \cdot \Psi_{inc}^{T,(l)}, \quad (300)$$

$$G = I - F_2 - M \cdot (I - T) - F_1 \cdot T, \quad (301)$$

$$T = Q^{-1} \cdot [R + S \cdot O^{-1} \cdot P], \quad (302)$$

$$M = [(I - F_2) A_2 + F_1 A_1] D^{-1} \cdot B. \quad (303)$$

We aim for that rate at which the iterate error is increasing or decreasing in our calculation. From the equations above, we obtained an expression linking the error of the incident transient angular from two consecutive iterations. We assume that enough iterations have passed such that the product of the iterative matrix times the transient vector is equal to the product of the transient vector and the largest iterative eigenvalue:

$$\Psi_{inc}^{T,(l+1)} = \omega \cdot \Psi_{inc}^{T,(l)} \quad \text{as } l \rightarrow \infty, \quad (304)$$

$$\rho(G) = \omega. \quad (305)$$

We have chosen to construct the iterative matrix around the incident transient angular flux. However, had we chosen to construct the iterative matrix around any other set of unknowns, the result would be a matrix that shared the same spectral radius.

The spectral radius from this Fourier analysis was verified against the convergence rate of our scheme as implemented around a DD-OCI and LD-OCI transport solvers. In this implementation, the convergence rate was approximated by:

$$\rho(G) \approx \frac{\left\| \phi_j^{(l+1)} - \phi_j^{(l)} \right\|_{\infty}}{\left\| \phi_j^{(l)} - \phi_j^{(l-1)} \right\|_{\infty}}. \quad (306)$$

In the routines, the problem was configured to produce a zero no solution, but the initial guess was set to one for all variables. This initial configuration implies that scalar flux solution after each iteration is equal to its iterate error. The result to the exact Fourier analysis convergence rate and the approximate convergence rate are presented in Table VI.

We compare the results from both sets of results and note that they agree quite well, adding to our confidence that the scheme and analysis were implemented correctly. We also note that the convergence rate is noticeably slower than with the idealized method, Table III. More specifically we notice that the convergence rate degrades significantly as the cells become optically thin for both DD-OCI and LD-OCI, and as the cells become thick for DD-OCI. In contrast to most iterative method, the convergence rate is marginally sensitive to changes in the scattering ratio. The optical thickness of the cells has a much stronger influence on the convergence rate.

TABLE VI  
Rate of Convergence for an Infinite Homogeneous Problem.

Material Properties		Spectral Radius (DD)		Spectral Radius (LD)	
$\sigma_l \Delta x$	$c$	F. Analysis	Numerical	F. Analysis	Numerical
0.001	0.5	0.998	0.998	0.998	0.998
0.001	0.99999	0.998	0.998	0.998	0.998
0.01	0.5	0.978	0.976	0.978	0.976
0.01	0.99999	0.982	0.979	0.982	0.979
0.5	0.5	0.284	0.260	0.331	0.304
1	0.9	0.102	0.101	0.154	0.150
10	0.999	0.835	0.835	0.094	0.093
100	0.99999	0.982	0.983	0.015	0.015

We explain the behavior of the iterative method with cells of varying thickness by observing the interaction of OCI with the spatial discretizations. As mentioned in the Iterative Method section, OCI are configured such that new information is propagated across a single cell per iteration. Each OCI reduces the iterate error by a factor equal to the single-cell attenuation factor. For thin cells, both DD and LD produce very little attenuation per cell. For thick cells, the analysis in Section III suggests that DD approaches a single-cell attenuation value of  $-1$ ; DD propagates error with little attenuation per iteration. For thick cell, the LD attenuation value approaches zero, and OCI converges quickly. In the Idealized Method analysis the transient Case-mode were solved analytically and the DD thick-cell shortfall was avoided. However, the analytic method is impractical. Nevertheless, this ideal analytic behavior can be mimicked with the LD discretization.

A simply calculation can be done to support this observation. We calculate an approximation to the transient single-cell attenuation factor and compare it to the convergence rate results of Table VI. From Section III, the DD single-cell attenuation for a single mode equals to:

$$g^{DD,k} = \frac{2 - \tau^k}{2 + \tau^k}, \quad (307)$$

where  $\tau^k = \sigma_t \Delta x / \nu^k$  with  $0 < \tau^k < 1$ .

In the LD case not such explicit expression exists if scattering exists. Instead, we approximate the single-cell attenuation factor by the LD expression in purely-absorbing materials:

$$g^{LD,k} = \frac{6 - 2\tau_m}{6 + 4\tau_m + \tau_m^2}, \quad (308)$$

where  $\tau_m = \sigma_t \Delta x / \mu_m$ , but we approximate it by  $\tau_m \approx \sigma_t \Delta x / \nu^k$ . Since the transient relaxation lengths reside in the range between zero and one, we approximate our average relaxation length by  $\nu^k \approx 0.5$ . We present in Table VII the results from our approximation to the LD and DD transient single-cell attenuation factor.

TABLE VII  
Approximate Transient Single-Cell Attenuation Factor for the DD and LD Discretizations.

Optical Thickness (mfps)	DD SCAF	LD SCAF
0.01	0.980	0.990
0.1	0.818	0.905
1.0	0	0.364
10	-0.818	-0.096

Comparison between Table VI and Table VII show similar trends:

1. optically thin cells result little attenuation regardless of the type of discretization employed,
2. optically thick cells results in little attenuation if DD is implemented,
3. at around 1 mfp the DD has a stronger attenuation per cell than LD.

These results support our conjecture that OCI is the weak link in the performance of the iterative scheme. The results from both analyses give us confidence that we understand the factor influencing the scheme.

If this understanding is correct, we can predict the behavior of the scheme and improve it. First, we expect that if the cell thickness results in a large transient single-cell attenuation factors then the method will converge quickly. For DD, thick and thin cells produce little transient attenuation; thus, slow convergence. For LD, only thin cells produce little transient attenuation. When designing a mesh for LD-discretized problems, the sought accuracy must be balanced with the convergence rate. For DD thick cells penalize both the accuracy of the result and the convergence rate. Overall, with our proposed iterative scheme the performance of classic OCI was improved considerably by removing asymptotic modes, therefore avoiding the slow convergence produced by their small attenuation factors.

Second, OCI can only communicate boundary information one cell per iteration. Hence, the minimum number of iterations required to communicate information across a domain equals the number of cells in the domain. For most problems of interest, information must be communicated between boundaries multiple times before convergence is achieved. Therefore, regardless of the spatial discretization, the mesh design must balance the iterative cost of mesh over-refining with its benefits on the calculation accuracy. Too many cells and OCI will need many iterations to transmit boundary information towards the interior and back. Too few cells and the calculation will be inaccurate.

Finally, by removing the asymptotic modes from the OCI solver, we have reduced the OCI domain to the boundary layers. Transient modes significantly

contribute to the solution only in regions surrounding the problem boundaries and material interfaces. In the region's interior, the strong attenuation of the transient Case-modes minimizes the importance of their solution with respect to that from asymptotic modes. We emphasize the relative difference in importance of the asymptotic and transient modes by converging the scalar flux solution as a whole, asymptotic plus transient and plus particular, instead of converging each one of its components. The ideal OCI mesh for our scheme will refine correctly the boundary layer region, but use few cells in the region's interior. If the boundary layers are correctly refined, the transient solution exiting them will be smaller than our convergence tolerance. At the interior, the residual transient modes will be either transmitted with DD, or promptly decayed with LD. By not over-refining the slab's interior, we reduce the number of cells and the number of OCI iterations.

#### *V.C. Numerical Results*

We compiled a collection of test problems to assess the performance of the iterative scheme under different material configurations. To measure the performance of the method, we tally the number of outer and inner iterations needed to converge each problem. In our results, we define an outer iteration as the number of times the five steps of our scheme are performed, and an inner iteration as the total number of iterations done to invert the transient problem, step 4. If OCI is used to invert the transient problem, then one inner iteration equates to inverting each cell at least once. If SI is used, one inner iteration equates to sweeping the domain once. Inner iterations are local to each transport sub-domain without updating the interface conditions, step 3. Unless specified otherwise, we invert each transient sub-domain with OCI and set the maximum number of inner iterations per outer iteration to equal the number of cells in the sub-domain. This limit in the number of outer iterations should be sufficient to transport Case-modes between opposing domain edges without wasting operations on inverting exactly a transient problem with inexact interface conditions. The tasks in one OCI are easily parallelizable, which makes it our default choice to invert the transient problem.

We organize these results as follows. Problems 1 through 4 address the effects of the material configuration on the number of outer iterations. Problems 5 and 6 addresses the effects of the material and mesh configuration on the number of inner iterations. In this problem, we compare also the number of inner iterations to the number of classic SIs and OCIs needed to converge the same problem. In the final problem, we measure the order of spatial convergence of LD and DD under our proposed scheme and compare it to their rate with SI an OCI.

### Test Problem 1: Outer Iterations and Scattering Ratio

We compared the number of outer iterations to converge a single region problem of increasing scattering ratio. The scattering ratio was equal to  $1.0 - 0.1^n$  for  $n = [1, 6]$ , or ranging from  $c = 0.9$  to  $c = 0.999999$ . The problem was solved with an  $S_8$  Gauss-Legendre quadrature set to a tolerance of  $1.0E-12$ . The slab was divided into 16 cells. Fig. 14 illustrates the configuration to this problem.

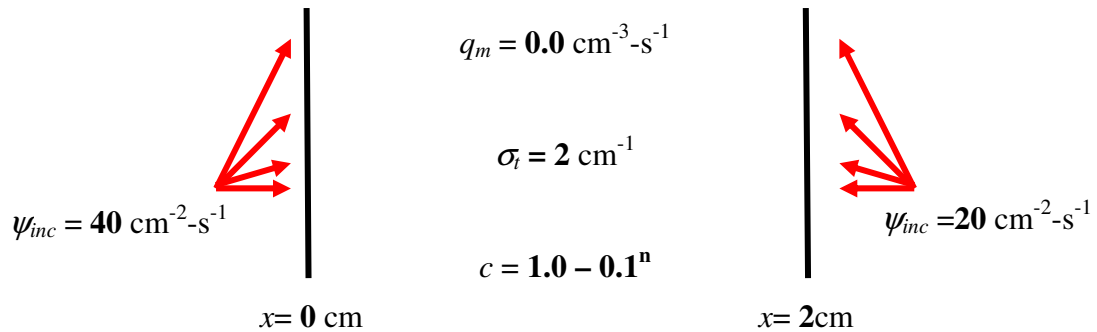


Fig. 14. One-region problem with varying scattering ratio.

The number of outer iterations done to solve each material configuration is presented in Table VIII. By measuring the number of outer iterations, we focus on the effects of the material properties on the diffusion-transport coupling, which in single

region problems only occurs at the boundaries. Asymptotic boundary conditions are constructed solely with incident homogeneous and transient angular fluxes. On the other hand, transient boundary conditions use incident and exiting angular fluxes to filter out the asymptotic contribution. We expect that if the mode-scaled optical thickness of the slab is increased then, the transient boundary conditions will be constructed on local information and the total number of outer iterations reduced. In this first problem, we decrease the mode-scaled optical thickness of the slab by increasing the scattering ratio and therefore, increasing the relaxation length that scales each Case-mode.

TABLE VIII

Number of Iterations to Converge a Single-Region Slab of Increasing Optical Thickness.

n	C	Outer Iterations	
		DD	LD
1	0.9	18	18
2	0.99	20	20
3	0.999	21	21
4	0.9999	21	21
5	0.99999	21	21
6	0.999999	21	21

The number of outer iterations decreased as the scattering ratio was increased. Based on our attenuation argument this was expected. Physically, as the scattering ratio increases the probability that a particle will be absorbed after a collision decreases, and particles travel on average deeper into the slab. We plot the homogeneous scalar flux distribution in Fig. 15, and confirm that with a larger scattering ratio the scalar flux is larger in magnitude in the slab interior. From our Case-mode analysis, the increase in

scattering ratio should affect the attenuation of all Case-modes. We present in Fig. 16 the collection of transient modes in a single scalar flux. The attenuation of transient Case-modes is reduced by the increase in scattering ratio, although this reduction in attenuation is mild with respect to the asymptotic one. By increasing the scattering ratio, we reduced the attenuation of each Case-mode, increased the communication between boundaries and increased the number of iterations.

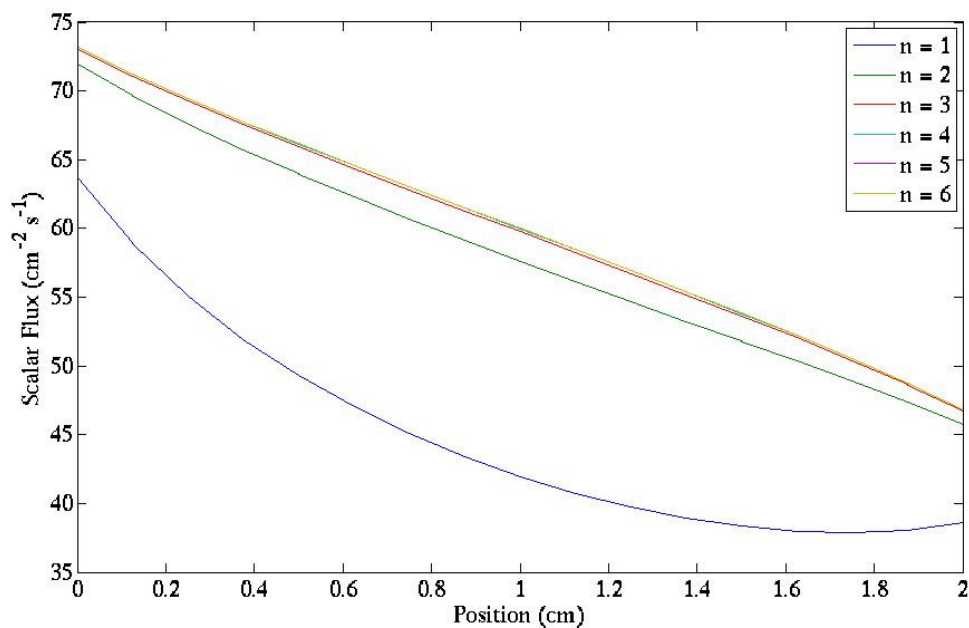


Fig. 15. Scalar flux of a single-region slab with varying scattering ratio.

The increase in outer iterations stabilized beyond a scattering ratio of 0.9999. Above this scattering ratio, we find from Fig. 15 and Fig. 16 that the scalar flux is increasingly dominated by the contribution from the asymptotic Case-modes. In Fig. 16 the amplitude of the transient scalar flux decreases with an increase in scattering ratio while the amplitude of the homogeneous scalar flux in Fig. 15 increases. With the transport problem progressively dominated by the asymptotic component, the transient-

asymptotic coupling is weakened and the scheme finds it easier to assign the boundary conditions to each component. This effect mitigates the reduced Case-mode attenuation produced by the increase in the scattering ratio, and the number of outer iterations stabilizes.

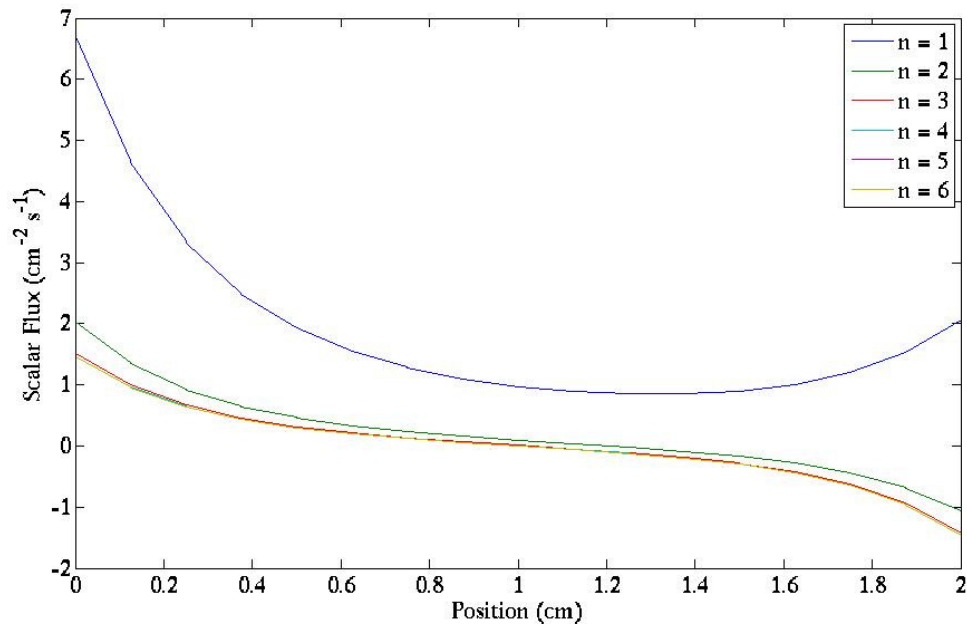


Fig. 16. Transient scalar flux of a single-region slab with varying scattering ratio.

To explain the transition to an asymptotic-dominated solution, we present in Fig. 17 the distribution of relaxation length for each problem. From this figure, a change in scattering ratio does not affect evenly the relaxation length of asymptotic and transient

Case-modes. Based on the dispersion relation, each transient relaxation length is bound by the directional cosines of the quadrature. On the other hand, the asymptotic roots limit towards infinity as the scattering ratio approaches unity. Thus, an increase in scattering ratio produces a larger increase in the asymptotic relaxation lengths than on any transient relaxation length. The asymptotic attenuation is weakened by the increase in scattering ratio at a faster rate than the transient attenuation. The homogeneous solution becomes diffusive; it is constructed mainly on two Case-modes with large relaxation lengths.

The scattering ratio affects negatively the performance of our scheme by increasing the communication between the boundaries, where the transient and asymptotic modes are coupled. However, as the scattering ratio approaches unity this effect is mitigated by the diffusiveness of the solution. The homogeneous solution is dominated by the asymptotic component and it is easier for the scheme to assign the boundary conditions between asymptotic and transient Case-modes.

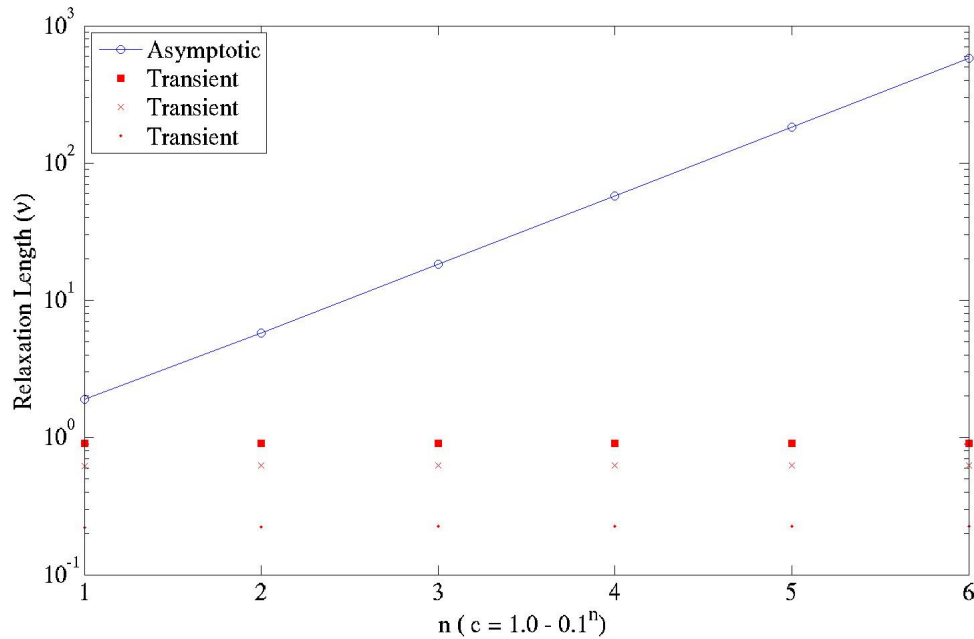


Fig. 17.  $S_8$  relaxation length spectrum change with scattering ratio.

### Test Problem 2: Outer Iterations and Optical Thickness

In this problem, we observe the influence of the optical thickness of the slab on the number of outer iterations. The total cross-section was set to  $2^n$  for  $n = [1,6]$ . The optical thickness of each cell was kept constant to  $0.25 \text{ mfp}$ , or to  $2^{-(n+2)} \text{ cm}$  by changing the total number of cells to solve each case. Each problem was solved with and  $S_8$  quadrature set, and converged to a tolerance of  $1\text{E-}12$ . Fig. 18 presents the material, and boundary configuration to the problem.

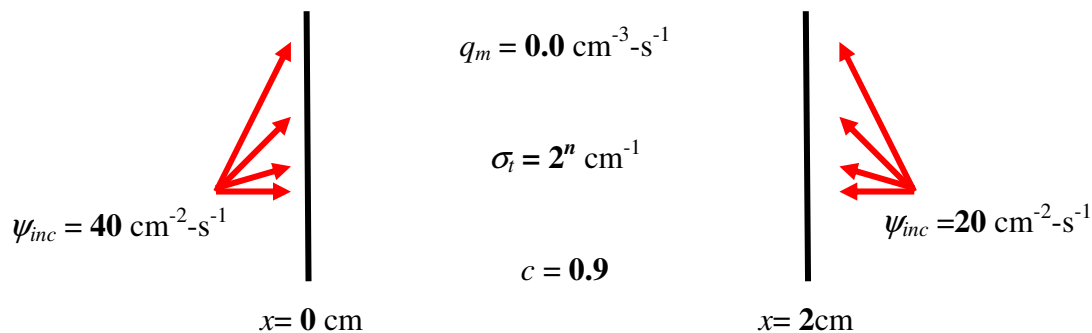


Fig. 18. One-region problem with varying total cross-section.

TABLE IX

Number of Iterations to Converge a Single-Region Slab of Increasing Total Cross-Section.

$n$	$\sigma_t$	Outer Iterations	
		DD	LD
1	2	18	18
2	4	14	14
3	8	11	11
4	16	8	8
5	32	7	7
6	64	6	6

The number of outer iterations for each case is presented in Table IX. The total number of outer iterations decreases considerably as the optical thickness of the slab is increased. A slab with total cross-section of  $64 \text{ cm}^{-1}$  attenuates the scalar flux quickly as illustrated by Fig. 19. In such an optically thick slab, transient and asymptotic boundary conditions can be computed with information local to the slab edges. The number of iterations is small since little coordination is needed between boundaries. Furthermore, for  $n$  greater than 3 the transient solution is negligible in the slab's interior as illustrated by Fig. 20. Because the iterative scheme only tests the scalar flux for

convergence, iterations are not wasted on converging the transient Case-modes in the slab interiors.

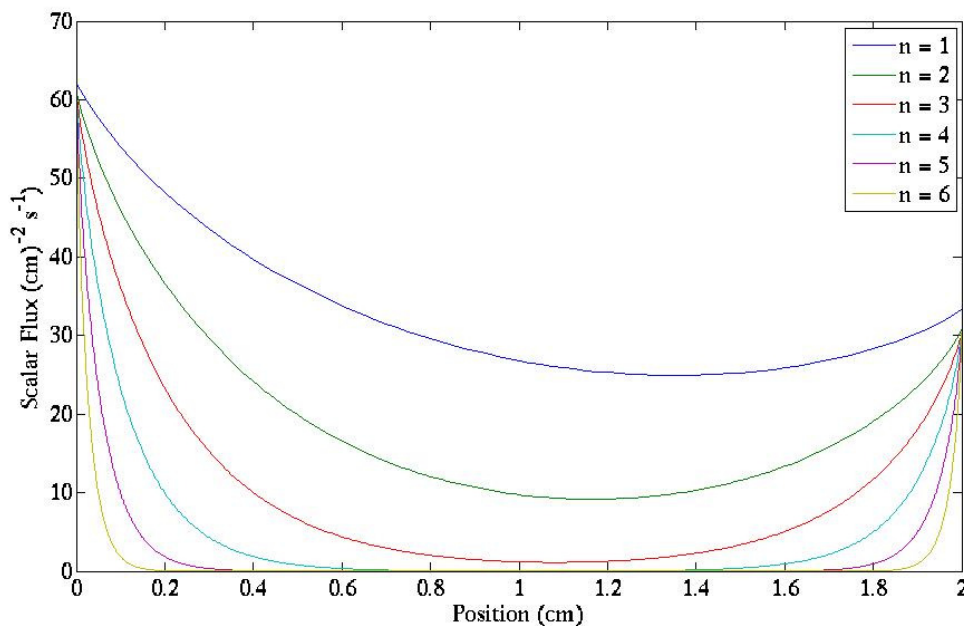


Fig. 19. Scalar flux of a single-region slab with varying total cross-section.

Our iterative scheme iterates on the boundary conditions until its transient and asymptotic components are correctly assigned. These boundary conditions are constructed on angular fluxes exiting and entering the slab. By increasing the attenuation in the slab, we isolate each boundary and reduce the number of outer iterations. For single-region problems, the asymptotic-transient coupling occurs only at the boundaries. We follow these numerical results with multi-region problems that consider the influence of material properties on interface conditions between regions.

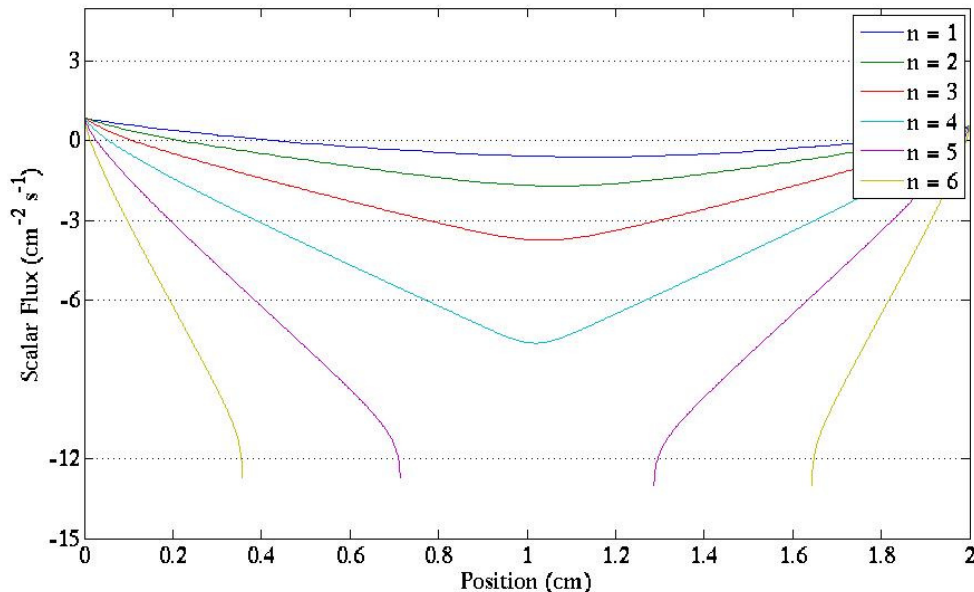


Fig. 20. Transient scalar flux of single-region slab with varying total cross-section.

### Test Problem 3: Outer Iterations and Number of Material Regions

In slabs with a single material regions, asymptotic and transient modes are coupled at the boundaries, and from the previous results this coupling is weakened by increased absorption in the slab. For slabs with multiple material regions, new coupling locations are added at material interfaces. We begin our suite of multi-region problems by testing the effects of adding multiple material interfaces on the total number of iterations. We configured a set of problems with  $2^n$  regions for  $n = [1,5]$ . Fig. 21 represents the boundary conditions and geometry specification of the problem. The total number of cells was set to 16 with total cross-section of  $2 \text{ cm}^{-1}$ . The scattering ratio was set to alternate between  $c_I = 0.5$  and  $c_{II} = 0.999999$ . The problems were solved with an  $S_8$  Gauss-Legendre quadrature set to a relative tolerance of  $1.0\text{E-}12$ .

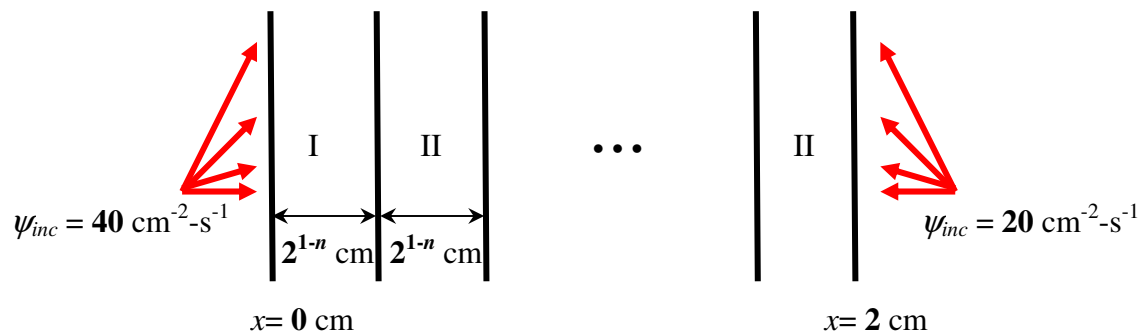


Fig. 21. Multi-region problem with an increasing number of material regions.

TABLE X.

Number of Iterations to Converge the Solution of a Slab with an Increasing Number of Material Regions.

$n$	Total Regions	Outer Iterations
1	2	19
2	4	21
3	8	32
4	16	52

We present the number of iterations per region configuration in Table X. The number of outer iterations increased as the number of interfaces was increased. We remark that in each case tested, half the slab had a scattering ratio of 0.5 and half the slab had a scattering ratio of 0.999999. Thus, we can not explain the increase of outer iterations based on a change in scattering ratio as shown in the first test problem. From case to case, we reshuffled the location of the regions with differing scattering ratio and an increased number of material interfaces.

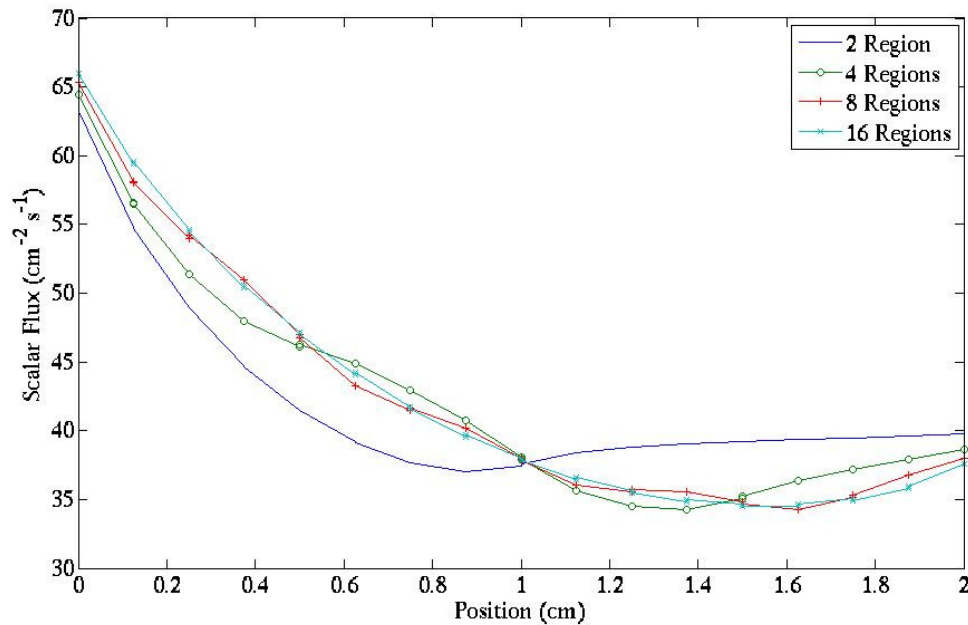


Fig. 22. Scalar flux of problem with an increasing number of material regions.

In Fig. 22, we present the homogeneous scalar flux to the test cases and note how the solutions oscillate as the number of interfaces increases. We explain this increase in oscillation based on the transient Case-mode discontinuities illustrate with Fig. 23. By comparing Fig. 22 and Fig. 23, we conclude that the transient oscillation from negative to positive values created oscillations of the homogeneous solution about the asymptotic Case-modes. These oscillations increase the complexity of the Case-mode separation in our scheme (reflected in the number of outer iterations) by introducing transient sources in the slab interior. Whereas in thick homogeneous slabs transient Case-modes contribute to the solution only at the boundary layers, in these multi-regions problems boundary layers are introduced every few cells. Thus, more outer iterations are spent on converging the transient problem in the slab interior to correctly filter asymptotic modes at the material interfaces and to obtain an accurate homogeneous solution. The number of outer iterations is dependent on the number of material interfaces since in the boundary layers around the interfaces both asymptotic

and transient Case-modes must be satisfactorily converged. This observation is valid for problem with discontinuity in the scattering ratio or with discontinuities in the extraneous source. Either case implies a discontinuity in the asymptotic and transient angular fluxes.

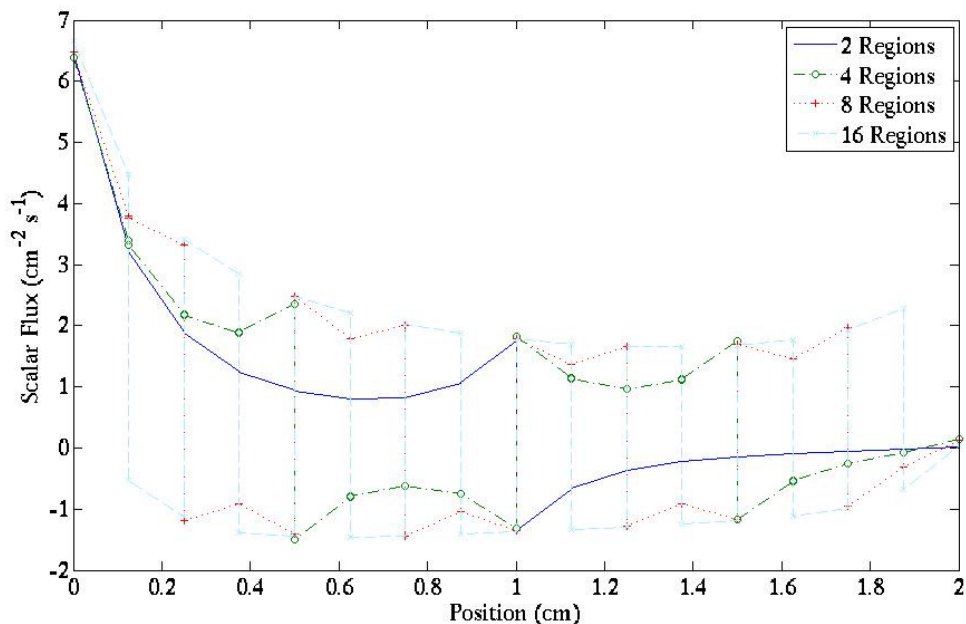


Fig. 23. Transient scalar flux of slab with an increasing number of material regions.

#### Test Problem 4: Outer Iterations and Scattering Ratio Discontinuity

We explore the effects of the scattering ratio discontinuity on the outer iterations. A discontinuity in the scattering ratio indicates that the homogeneous solution is spanned by a different set of angle-shapes functions. With these problems we observe the change in the number of outer iterations as the scheme converges multiple sets of Case-modes. We divided the slab presented in Fig. 24 into 16 regions, and assigned to each region a

different scattering ratio:  $c_I = 0.5$  and  $c_{II} = 1.0 - 0.9^n$  for  $n = [1,5]$ . The transport solution was approximated with an  $S_8$  quadrature set to a relative tolerance of  $1.0E-12$ .

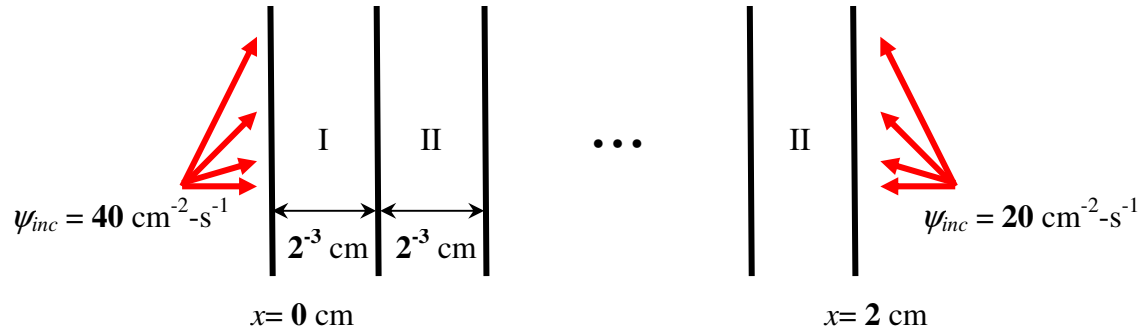


Fig. 24. 16-regions slab with varying scattering ratio.

TABLE XI

Number of Iterations to Converge the Solution of a Multiple-Region Slab with Increasing Discontinuity in Scattering Ratio.

$n$	Region I		Region II		Outer Iterations
	$c$	$\nu^{a+}$	$C$	$\nu^{a+}$	
1	0.9	1.0932	0.9	1.0932	49
2	0.9	1.0932	0.99	5.7967	52
3	0.9	1.0932	0.999	18.2647	52
4	0.9	1.0932	0.9999	57.7373	52
5	0.9	1.0932	0.999999	182.5749	52

The number of outer iterations remained constant with an increase in the scattering ratio discontinuity as presented in Table XI. The only exception was the test case where multiple transient regions were defined but the scattering ratio was

continuous ( $n = 1$ ). However, with respect to the total number of outer iteration the difference between this homogeneous scattering ratio case and the rest of the case is small, only three iterations.

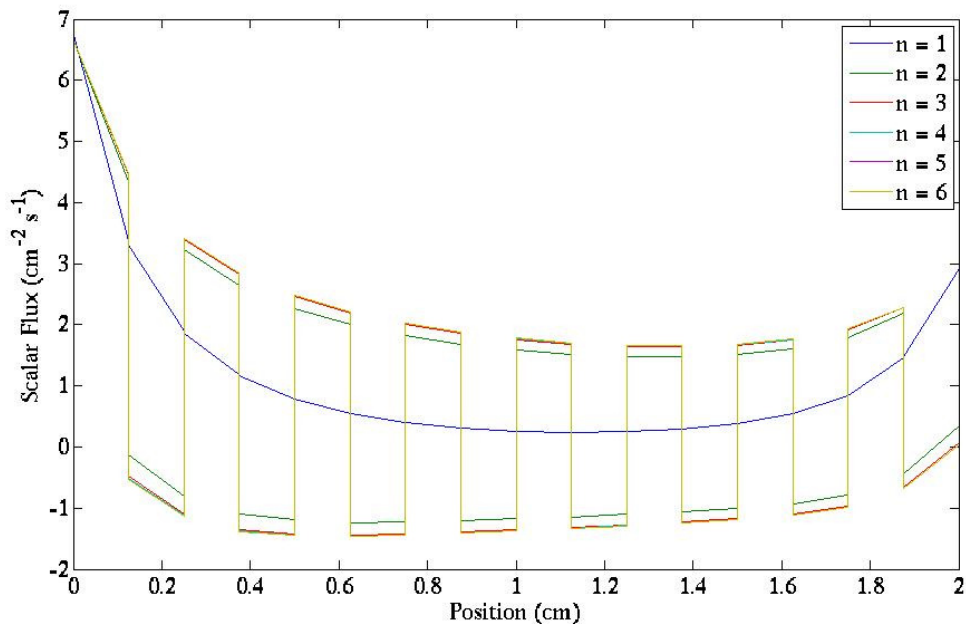


Fig. 25. Transient scalar flux with varying scattering ratio.

From the analysis of the Ideal method presented in this chapter, we expected that inserting scattering ratio discontinuities would degrade the convergence rate of our scheme. As expected the transient scalar flux is discontinuous as shown in Fig. 25, as it is spanned by different angle-shape functions in each material region. From this figure, the discontinuity of the transient scalar flux quickly asymptotes. Furthermore, it did not affect the outer iteration count. In Fig. 26 we present the homogeneous scalar flux. The continuity of the scalar flux points to a correct distribution of the boundary conditions between asymptotic and transient modes by our scheme. The Case-mode filters

correctly removed the asymptotic contribution from the homogeneous angular flux to construct the transient interface conditions.

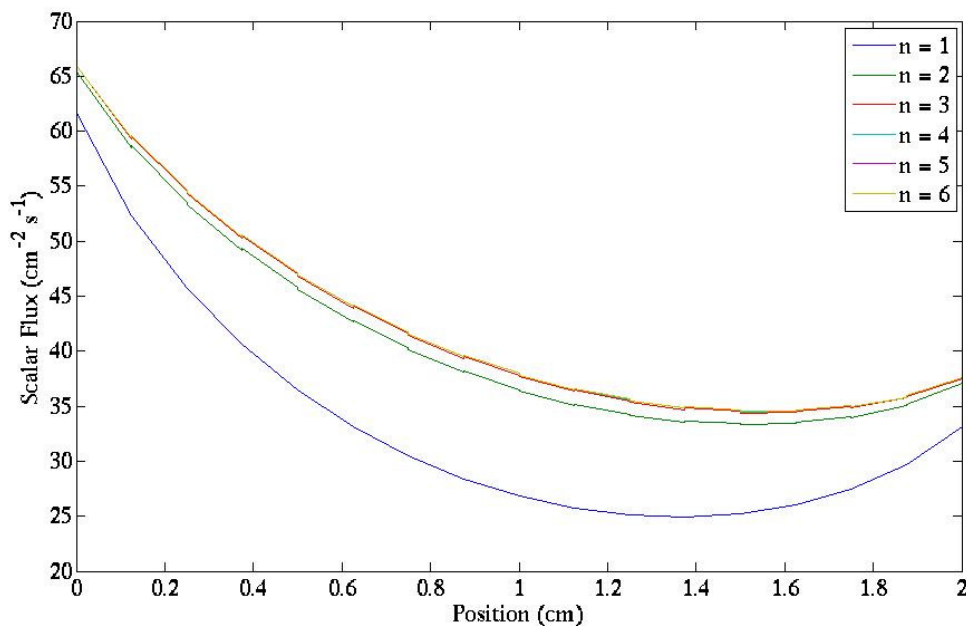


Fig. 26. Scalar flux with varying scattering ratio.

As a side note, the material configuration of the first test case of this problem and that of problem 1 are identical. However to solve this test problem, we configured the scheme such that the transient and asymptotic conditions were calculated at each cell interface. The solution to the first test problem was obtained in less outer iterations than the solution to this problem. If we take into account the number of inner iteration (one inner iteration for each cell in the transient domain) then the total number of iterations to solve problem 1 increases to 288 compared to 48 total iterations for this problem. Increasing reduces the number of OCI but it is not penalty-free. It increases the number of outer iterations; hence, it increases:

- the dimension of analytic diffusion matrix for asymptotic modes,

- the number of times the asymptotic problem is inverted exactly,
- the number of interfaces where the transient interface conditions are calculated,
- the number of times the transient boundary conditions are recalculated.

Our scheme is more effective than OCI in inverting the solution to each cell. Our scheme is much more computationally intensive than OCI. We also note that by defining each cell as its own transient region, the transient solution in each cell converges after one OCI. OCI inverts exactly each cell exactly given its current boundary conditions. Since the region's interface conditions are coordinated by the iterative scheme, then having more than one inner iterations per outer iterations would be computationally wasteful.

For each one of the preceding test problems we did not tally the number of inner iterations, nor did we study the effects of the mesh refinement on the outer iteration count. From the Fourier analysis, we found that the mesh refinement has an effect on the convergence rate of the scheme with OCI. In test problem 5, we explore these effects plus we consider the advantages of OCI versus SI to invert the transient problem.

### **Test Problem 5: Inner Iteration and Mesh Configuration**

We aim for an iterative scheme designed for parallel computing architectures. Per outer iteration, the scheme divides the problem into regional transport blocks and connects each block through a global diffusion problem. In this test case, we study the performance of One Cell Inversions and Source Iteration as the iterative scheme to invert the local transport problems. We tally the total number of OCI or SI iterations, and compare these to their classic implementations in the absence of our Case-mode separation scheme. Based on the lessons learned from the Fourier analysis, we show that the number of inner iterations can be greatly reduced if the mesh is refined just enough to produce an accurate solution with strong attenuation per cell.

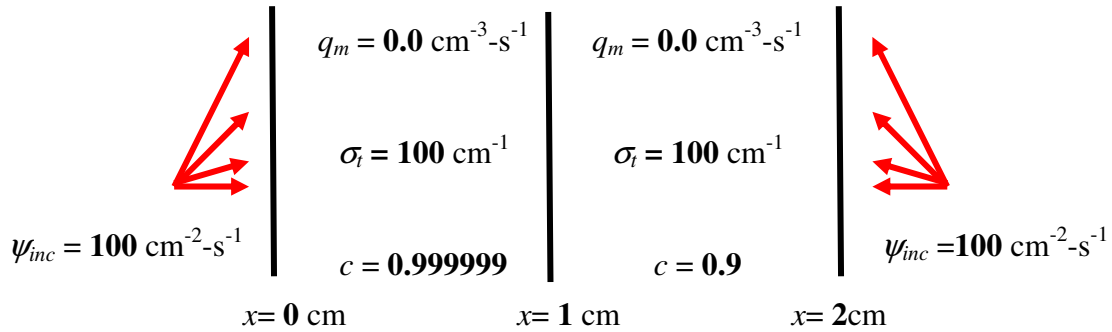


Fig. 27. Two-region heterogeneous problem.

We studied a two region problem with optically thick regions. The regions optical thickness is ideal for our scheme such that the transient Case-modes do not communicate between interfaces. The material and geometry configuration, as well as the boundary conditions are shown in Fig. 27. We computed the solution using an “overkill” mesh of 256 total cells in the slab. Then, we solved the problem with an “optimum” mesh for DD and LD spatial discretizations. The scalar flux solution was computed with an  $S_8$  Gauss-Legendre quadrature and converged to a relative tolerance of 1E-9.

We configured the optimized meshes with the performance of OCI in mind. From the Fourier analysis, we found that OCI converges quickly if the single cell attenuation value per cell is large. We also learned that OCI communicates information towards the opposing edge of a region one cell per inner iterations. Based on these two principles, an optimal OCI mesh has few cells and each cell is as thick as possible discretization error target allows. From the structure of the transient Case space, cells adjacent to the region’s edge should be the finest, since all transient Case-modes are present here. As the transient Case-mode with the steepest gradients decay below the convergence tolerance, cells are coarsen until the last transient Case-mode decays. Then, a single cell can be used to solve the analytic asymptotic solution. No such optimization measure could be deduced for SI with Case-mode separation. Furthermore, from a

parallel computing perspective, OCI is more attractive, which makes its efficient insertion into our algorithm a priority.

The DD optimal mesh was configured in four zones. Each zone addressed the accurate attenuation of a Case-mode. We determine the cell thickness of each zone from the truncation error of Eq.(307). We assigned the maximum value of the truncation error to be equal to the relative error of the overkill mesh. From this expression, we solved for the cell thickness of the transient Case-mode with a magnitude above the relative tolerance and with the shortest relaxation length. The DD optimal mesh configuration is presented in Table XII.

TABLE XII  
Optimal Mesh Configuration for DD.

	Region Width (mfp)	Number of Cells
Region I	11	15
Region II	3	11
Region III	6	2
Interior	60	1
Total	200	114

TABLE XIII  
Optimal Mesh Configuration for LD.

	Region Width (mfp)	Number of Cells
Boundary	9	3
Interior	82	1
Total	200	14

The LD optimal mesh was configured less rigorously than the DD one. Since the LD single-cell attenuation factor approaches zero in the cell-thick limit, we expected that not all LD transient Case-modes needed to be accurately attenuated to arrive to our target discretization error. Those transient Case-modes that found the boundary cells too thick would be quickly attenuated. This is not the case for DD. If each DD transient Case-mode is not correctly discretized, then its single-cell attenuation factor approaches -1, and the OCI convergence rate degrades. To configure the LD mesh, we began from the DD optimal mesh and calculated the solution with thicker boundary cells. We progressively thickened cells closer to the boundary until the relative error fell above our target. This process was done until all cells in the boundary layer were tested. The resulting LD optimal mesh configuration is presented in Table XIII.

We present the number of iterations and the respective maximum relative error in Table XIV. For these results, we defined one inner iteration as the number of times each solver inverted the spatial domain once. For SI this implies a sweep of the domain with old scattering information, but continually transmitting the most current boundary information towards the interior. For OCI, this implies communicating boundary information by a single cell per iteration, but with the most current scattering source.

TABLE XIV

Comparison of the Number of Iterations Among Source Iteration, One Cell Inversion and the Proposed Iterative Scheme.

Transport Configuration	with Mode Separation	Mesh Configuration	Number of Iterations	Relative Error
SI + LD	No	256	24614	3.43E-2
SI + DD	No	256	29400	3.22E-1
OCI + LD	No	256	36206	3.43E-2
OCI + DD	No	256	33672	3.22E-1
SI + LD	Yes	256	1728	8.02E-3
SI + DD	Yes	256	1727	3.96E-2
OCI + LD	Yes	256	31488	8.02E-3
SI + DD	Yes	256	31488	3.96E-2
SI + DD	Yes	114 Optimal	1568	3.55E-2
OCI + DD	Yes	114 Optimal	7980	3.55E-2
OCI + LD	Yes	114 Optimal	7980	7.17E-3
OCI + LD	No	14 Optimal	644	2.13E+0
OCI + DD	Yes	14 Optimal	798	1.66E+2
SI + LD	Yes	14 Optimal	1663	5.88E-2
OCI + LD	Yes	14 Optimal	644	5.88E-2

From the results in Table XIV, we can state the following properties about our method:

1. It is more than an iterative method. The solution was decomposed into sets of Case-modes with distinct scales; each set solved with different numerical techniques. In these results, we solved the asymptotic modes analytically and used a spatial discretization only for transient modes. Thus, our method provides more accurate

solutions. In the overkill problems (256 cells) when the mode decomposition was implemented the relative error was reduced by an order of magnitude. We obtain these reductions of relative errors by assigning the asymptotic modes to an analytic diffusion solver as opposed to Finite Element transport solver.

2. Mesh optimization results in a large reduction of the number of inner iterations. A mesh that is too fine results in too many OCIs to invert the transient domains. A mesh that is too coarse results in an oscillating solution for DD, a small attenuation factors and many OCI inner iterations. For LD, a coarse mesh implies that not enough transient Case-mode will be presented in the solution to produce the target accuracy. However unlike DD, the LD solution will converge in few inner iteration since the large attenuation factors imply a fast convergence rate with OCI.

3. LD requires less OCIs to converge the problem than DD. LD can produce more accurate results with fewer cells than DD for two reasons. First, the LD single cell attenuation factor converges spatially towards the exact attenuation factor at a higher rate. Second as the cell thickness approaches the thick-cell limit, the LD approaches the correct attenuation limit of zero, while DD approaches -1. Therefore, an LD optimized mesh consists of fewer and thicker cells. With OCI, such an optimized mesh implies fewer inner iterations to converge the problem.

4. SI is largely insensitive to mesh optimization. The number of SI inner iterations remained relatively unchanged between the overkill mesh, and the optimized meshes. Nevertheless, adding Case-mode separation to SI reduced the number of inner iterations by a factor of 20. In the absence of asymptotic Case-modes in the transient problem, the effective scattering ratio of the SI scheme was reduced. Since the SI convergence rate is bound by the scattering ratio, SI converged in fewer iterations with Case-mode separation.

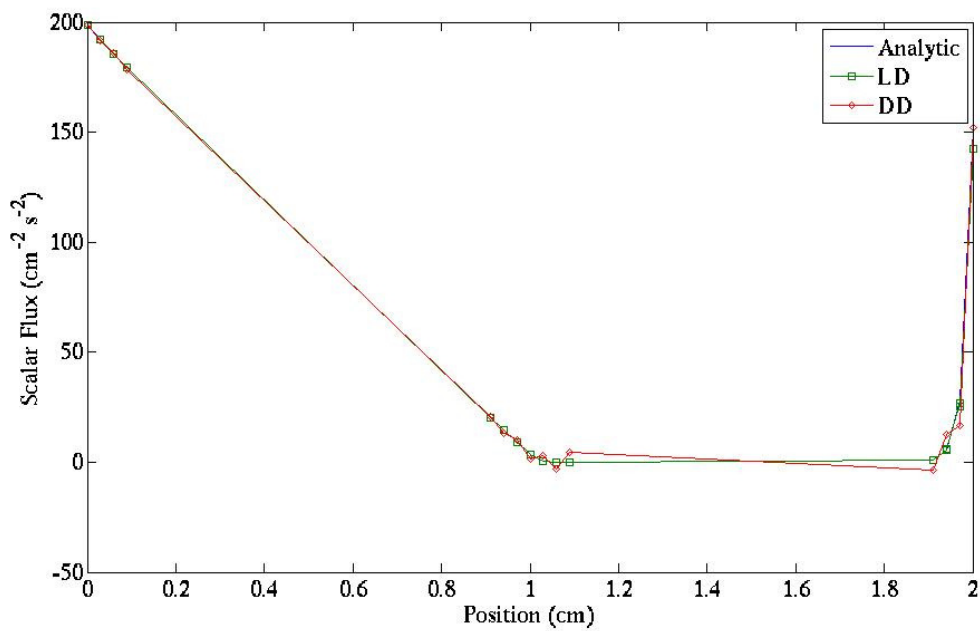


Fig. 28. Scalar flux to the LD-optimized mesh.

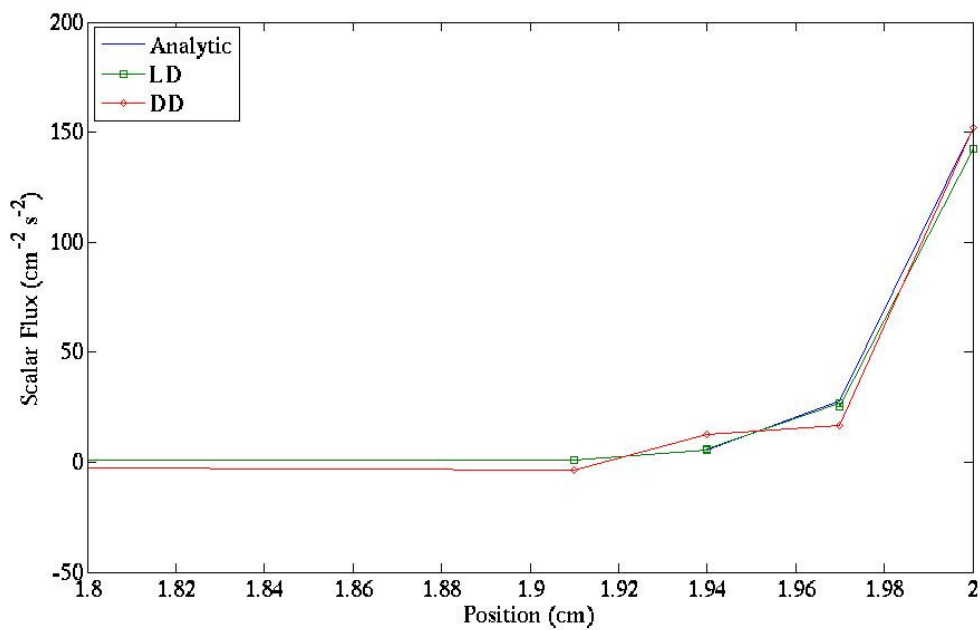


Fig. 29. Right-boundary zoom of the scalar flux with the LD-optimized mesh.

To illustrate the shortcomings of the DD attenuation factor, we contrast the LD and DD solution to the LD-optimized mesh against the analytic solution in Fig. 28 and Fig. 29. With the LD mesh, the DD solution visibly oscillates at the boundary layers of the right region. On the other hand, the LD solution does not oscillate and follows more closely the analytic solution. In Fig. 30, we present the transient solutions to this problem zoomed at the right boundary layer. The DD oscillations are much more pronounced; all DD transient Case-modes oscillate about a scalar flux of zero. There is little transient attenuation with DD, and the coarse mesh produces negative attenuation values for all transient DD Case-modes. This solution is obviously non-physical, and results in a large discretization error. With only 14 total cells, OCI solved the problem in few iterations with DD and LD; but only LD produced an accurate solution.

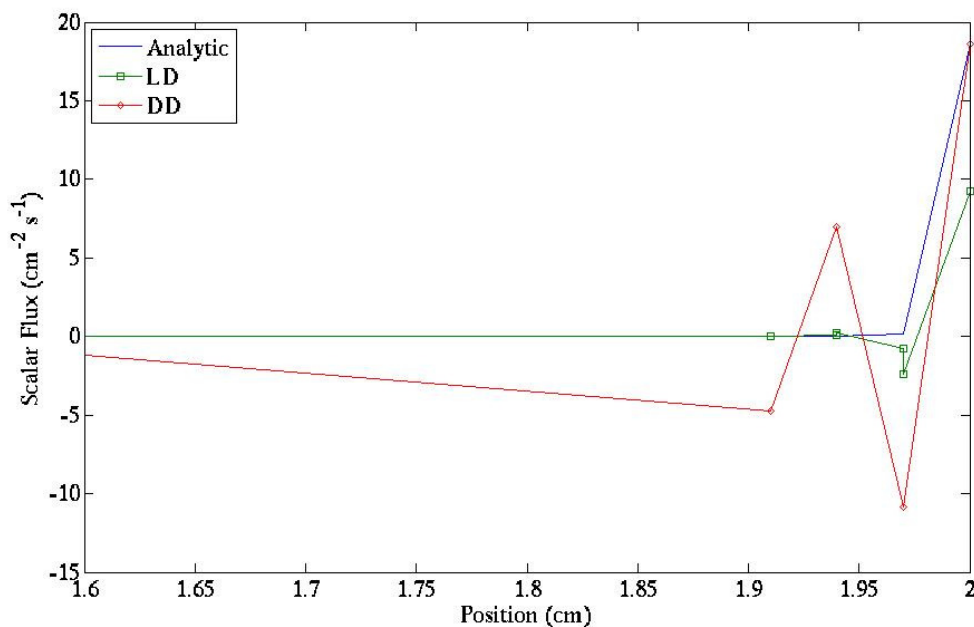


Fig. 30. Right-boundary zoom of the transient scalar flux with an LD-optimized mesh.

For the results in, the number of OCIs per outer iterations were fixed to equal the number of cell. This ensured that all cells in the domain were inverted at least once per outer iterations. Hence, all information from one problem boundary was communicated to the other, but not fully converged. In Table XV, we present results for the LD optimized problem solved under different number of maximum inner iterations. For these results, we also constricted the local transport solver to stop iterating if the transient solution converged to a tolerance of  $1.0E-3$  under its current local interface conditions. Recall that after each outer iteration, we update the boundary conditions to the local transport solver, but we do not do so after each inner iteration. One inner iteration per outer iteration implies that after every OCI the asymptotic solution and transient boundary conditions are recalculated. Three inner iterations imply that three cells are inverted before recalculating the global problem, and so forth. Since the LD-optimized mesh constructed the solution with seven cells per region, at least seven inner iterations are needed to communicate transient information from one interface to the next without updating the global problem.

The total iteration count favored updating asymptotic and transient boundary conditions after every inner iteration. Although this approach used few total iterations, it involved inverting the asymptotic global matrix after each OCI. When the inner iterations maximum was set to 140, the total number of iteration was doubled, but the asymptotic problem was only solved 17 times. We favor such a configuration since the total number of operations is reduced, and from a parallel computing perspective, the problem is divided into a coarse grain parallel transport problem.

TABLE XV

Number of Total Iterations with Varying Number of Maximum Inner Iterations for the LD-Optimized Mesh.

Total Outer Iterations	Maximum Inner Iterations	Total Iterations
305	1	305
102	3	517
46	7	422
50	14	428
43	28	443
17	140	642
34	1000	780

The second configuration (three inner iterations) inverted at least one boundary per outer iteration. Although, this was not the slowest of cases to converge, this option was remarkably slower than the first option (one inner iteration) or the third option (seven inner iteration). We suspect that this option did not spent sufficient inner iterations communicating transient information between the edges of a region. Instead it wasted inner iterations only inverting the boundary layers with little improvement on the region-exiting angular flux. In the seven inner iterations configuration, enough inner iterations were allowed so that changes in the transient boundary conditions were transported to the region-exiting transient angular flux. The resulting region-exiting angular fluxes were not locally converged but they sufficed to improve the boundary conditions of the asymptotic problem and reduce the number of outer iterations. The 1000 inner iterations case, wasted inner iterations by converging the local transient problem to the 1E-3 local tolerance with transient boundary conditions not yet converged.

Overall with this problem case, we have shown that an accurate solution can be obtained with our scheme in very few iterations. Our proposed scheme is organized in multiple independent tasks and improves the parallelization of current discrete ordinates transport algorithms. Parallelization of the transport solution could be done in two levels: a top level with work available in each independent transient region, and a low level with the efficient OCI inversion of the transient domains. The parallelization of the transport problem is reduced to inverting the global diffusion problem to solve the asymptotic problem.

### Test Problem 6: Spatial Convergence

In the derivation of the five steps in our scheme, we made special emphasis in applying angular fluxes to the interface conditions and asymptotic boundaries such that the spatial super-convergence of DFEM discretizations was preserved. In this final test problem we test if our efforts were successful. We calculated the solution to the problem configuration presented in Fig. 31 with six different meshes, and from these results, we computed the spatial convergence rate of DD and LD. We assigned purposefully two material regions to this homogeneous slab, so that the iterative scheme was tested with at least one boundary and one interfaces. All components in our scheme were tested for possible sources of low order information with this problem.

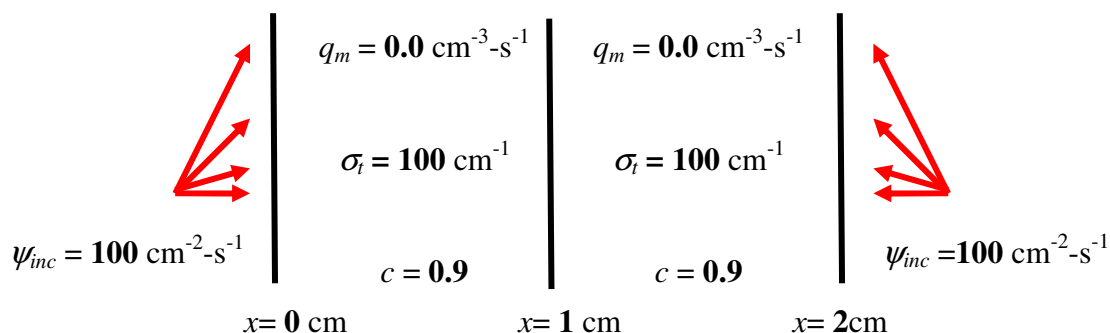


Fig. 31. Order of DFEM spatial convergence problem.

The problem was solved with  $2^n$  cells with  $n = [1,6]$ . The scalar flux was approximated with an  $S_8$  Gauss-Legendre quadrature set, and converged to a relative tolerance of  $1E-12$ .

The analytic solution to the homogeneous and transient scalar flux was computed at cell edges to determine the relative error of the DD and LD calculations. Since the LD solution is discontinuous at cell edges and cell exiting angular fluxes are more accurate than those entering a cell, we defined the LD edge angular fluxes by the cell-exiting angular flux:

$$\psi_{m,i,j+1/2} = \begin{cases} \psi_{m,i,R} & \text{if } \mu_m > 0 \\ \psi_{m,i+1,L} & \text{if } \mu_m < 0 \end{cases} \quad (309)$$

For DD the definition of the angular flux at cell edges is not an issue because the solution is continuous. To determine the order of spatial convergence, we calculate the ratio of error between consecutive iterations. With cell reduced by half between test cases, a ratio of eight implies a third order convergence rate, while a ratio of four implies a second order convergence rate. Table XVI and Table XVII present the relative error and ratio of relative errors for the homogeneous and transient solution of the DD and LD discretization respectively.

The scheme did not degrade the convergence rate of either discretization. For DD this is close to a trivial result. The DD angular flux is continuous at cell interfaces; hence, the angular flux converges with the same rate at cell-exiting and cell-entering locations. When we compute the asymptotic interface sources or when we filter-out asymptotic Case-modes, there are no sources of low-order information. The continuity of the DD angular flux makes it a less troublesome discretization to implement; however, this simplicity is overshadowed by the higher accuracy of the LD discretization and its advantages illustrated in the previous problem.

TABLE XVI  
Error and Error Ratio of DD Solution.

Cell With (mfp)	Transient Relative Error	Transient Error Ratio	Total Relative Error	Total Error Ratio
1	2.26E+0	—	5.35E-2	—
0.5	3.21E-1	7.04	1.04E-2	5.17
0.25	5.61E-2	5.73	2.55E-3	4.06
0.125	1.34E-2	4.17	5.73E-4	4.45
0.625	3.35E-3	4.01	1.04E-4	4.09
0.03125	8.34E-4	4.01	3.48E-5	4.02
0.015625	2.08E-4	4.00	8.69E-6	4.01
0.0078125	5.21E-5	4.00	2.17E-6	4.00

TABLE XVII  
Error and Error Ratio of LD Solution.

Cell With (mfp)	Transient Relative Error	Transient Error Ratio	Total Relative Error	Total Error Ratio
1	4.63E-3	—	1.06E-2	—
0.5	6.27E-2	7.50	1.95E-3	5.42
0.25	7.90E-3	7.81	3.52E-4	5.53
0.125	1.11E-4	7.11	4.77E-5	7.39
0.625	1.48E-4	7.54	6.32E-6	7.54
0.03125	1.91E-5	7.72	8.20E-7	7.71
0.015625	2.43E-6	7.85	1.05E-7	7.84
0.0078125	3.09E-7	7.89	1.33E-8	7.87

Results from this experiment confirm that when LD was implemented the correct source of angular fluxes was selected. At each cell edge, the LD angular fluxes incident on a cell edge are third order accurate while those departing from the cell edge are only second order accurate. The asymptotic interface sources and the asymptotic filter were calculated on cell-exiting homogeneous fluxes only. This was not an evident task because the transient angular flux incident on a region but exiting from a cell was not available from the transient angular flux. A new transient region-incident angular flux was defined and calculated as part of the iteration process. From these results the region-incident transient angular flux was defined correctly such that the scheme preserves the LD third-order spatial convergence for transient angular fluxes.

These results confirm that the LD transient angular flux reflects only the contribution from transient Case-modes. To a third order, there is not asymptotic contamination in the transient angular flux. The LD transient angular flux was compared against the analytic transient angular fluxes to compute the relative error; therefore, any asymptotic contamination would have degraded the transient order of convergence but possibly not degraded the homogeneous relative error. Both homogeneous and transient angular fluxes converged at the same third order rate for LD. We confirm that upon convergence there was no asymptotic contamination in the transient angular flux from the results in the previous test problem. If there had been asymptotic contamination in that problem, then a single interior cell would have been insufficient to accurately compute the solution. If our scheme allowed some low-order asymptotic contamination then the number of interior cells would have increased and the single-cell attenuation factor would have decreased, which would deteriorate the OCI performance. We have correctly addressed the challenges of implement our scheme with the LD discretization, and we can take advantage of the high accuracy that this discretization has to offer.

### *V.D. Summary of Results*

The discrete ordinates homogeneous solution is constructed on a set of Case-modes of distinct scales. We have configured an iterative scheme that is unlike any other scheme previously developed. It exploits the distribution of scales in the Discrete Ordinate solution to make transport calculations more easily parallelizable. The asymptotic subset of discrete ordinates Case-modes varies little in space and angle, and in slab geometry is comprised of only two modes. The remaining Case-modes are transient; they vary in space and angle quickly, which allows them to capture the strong local gradients that differentiate a transport solution from a diffusion one. Naturally, in our scheme, we assign the asymptotic Case-modes to a diffusion solver and the transient Case-modes to a transport solver. We organized our scheme into five steps:

1. Construct the asymptotic boundary and interface conditions.
2. Solve exactly the current global asymptotic solution with a diffusion solver.
3. Filter the asymptotic contribution from the homogeneous solution and construct the transient boundary and interface conditions.
4. Solve the transient solution locally to each material region.
5. Test for convergence the total solution.

Any particular solution to the problem that could arise from extraneous sources was assumed to be known prior to step 1 and approximated by a polynomial function. For our initial guess, we assumed that the homogeneous solution is equal to the asymptotic solution and assign an arbitrary value to it.

We implemented this scheme to solve discrete ordinates problems in slab geometry, with a single energy group and isotropic scattering. We performed a series of analysis and test problems to this implementation to observe the behavior of the scheme under different material configurations. We found that the general performance of the scheme depends on the difficulty to converge the interface conditions to each local transient problem. The scheme converges the scalar flux in few iterations if there are few material interfaces, and the transient solution between interfaces is isolated. Unlike

iterative schemes based on Source Iteration, our iterative method is marginally sensitive to the scattering ratio.

The scheme can utilize any existing transport solver to construct the local transient solution. We emphasized in our design that no specific characteristic to the transient problem are needed other than its interface and boundary conditions. In our study of the scheme, we explored the performance of One Cell Inversions and Source Iterations to iteratively solve the transient domain. Wrapping our scheme around a Source Iteration or One Cell Inversion transport solver greatly improves their performance. However, from a parallel computing perspective our interest was focused on One Cell Inversions. By removing the asymptotic Case-modes from the transport solver, the number of cells needed to attain a target calculation error is reduced and the attenuation per cell is increased. These changes effectively reduced the importance of particle streaming in the problem assigned to the transport solver, and configured it to be ideally suited for One Cell Inversions. Our iterative scheme can be wrapped around current transport solvers and improve their performance.

We have designed a true block-Jacobi scheme that converges in few iterations. It divides the transport problem into regional blocks and communicates each block with the solution from a previous iterate. Only the diffusion calculation for asymptotic Case-modes must be coordinated globally. Each regional block is inverted iteratively using One Cell Inversions, another block-Jacobi scheme. By separating Case-modes based on their relaxation length, our scheme reduces the burden of parallelizing transport problem to the parallelization of a diffusion solver.

## VI. THE ITERATIVE METHOD: XY GEOMETRY

In Section V, we presented an iterative scheme that solves individually the particular, asymptotic and transient components of angular flux. The scheme is ideally suited for transport calculations in parallel architectures. It builds the angular flux by solving a global diffusion problem and then adding to it the solution from a series of local transport problems. Each local transport problem is solved concurrently and the burden of constructing a global solution falls on the diffusion solver. By doing so, the iterative scheme avoids domain-wide sweeps. Furthermore, the scheme converges the solution in few iterations at a rate that is weakly dependent on the scattering ratio. These numerical properties make our iterative scheme a more compelling candidate for parallel calculations than methods based on Source Iteration.

The scheme addresses a narrow subset of transport problems: those with isotropic scattering, a single energy group, and slab geometry. In this chapter, we attempt the extension of the iterative scheme into multiple spatial dimensions. This is a complicated and at this point unsuccessful task. The analytic description of the transport space used to derive the slab geometry scheme is not available for problems in XY geometry. To our knowledge no description of the homogeneous component of the angular flux exists in terms of a set of orthogonal basis functions. This description is critical to the construction of the filtering techniques that decompose the driving terms into the asymptotic and transient components.

We begin this chapter by discussing the potential benefits of applying our scheme in multiple dimensions. Then, we describe the scheme as currently implemented in XY geometry. Finally, we analyze the challenges that our scheme faces in multiple dimensions, with supporting numerical data.

### *VI.A. Opportunities in Multiple Dimensions*

In slab geometry the iterative scheme was not only advantageous with respect to parallel computing. It also allowed for the asymptotic and transient angular fluxes to be

constructed with different numerical techniques. The asymptotic problem was not discretized; instead, it was solved analytically. On the other hand, a discretization of the transport equation was used to construct the transient angular flux. Our scheme produced more accurate results for slab geometry than solving both asymptotic and transient Case-modes under the same transport discretization.

Similarly in XY geometry, the iterative scheme should allow us to use different asymptotic and transient discretization methods to our advantage. The emphasis of our calculation could be placed on obtaining an accurate global asymptotic solution with a cruder treatment of the local transient problems. This would have a significant computational advantage given the cost and complexity of transport calculations against diffusion ones. We also note that a successful extension of this approach to multiple dimensions would have a tremendous benefit: the asymptotic component, which persists far away from its source, would have no ray effects.

### VI.B. The Iterative Method

We expand the five steps of our slab geometry iterative scheme for XY geometry. We recall the transport equation for XY geometry with isotropic scattering and one energy group that we aim to solve:

$$\mu_n \frac{\partial \psi_n}{\partial x} + \eta_n \frac{\partial \psi_n}{\partial y} + \sigma_{t,i} \psi_n(x, y) = \sigma_{t,i} \frac{c_i}{4\pi} \phi(x, y) + Q_i(x, y), \quad (310)$$

$$\phi(x, y) = \sum_{n=1}^N w_n \psi_n(x, y). \quad (311)$$

Here  $i$  is the subscript indexing the material region in the 2D domain.

Similar to the slab geometry case, the iterative scheme aims at solving the homogeneous angular flux iteratively. The homogeneous angular flux respects the transport equation in the absence of an extraneous source:

$$\mu_n \frac{\partial \psi_{n,i}^H}{\partial x} + \eta_{n,i} \frac{\partial \psi_{n,i}^H}{\partial y} + \sigma_{t,i} \psi_{n,i}^H(x, y) = \sigma_{t,i} \frac{c_i}{4\pi} \phi_i^H(x, y), \quad (312)$$

Here we have labeled the homogeneous angular flux with the regional subscript  $i$  since it can be discontinuous across material interfaces. To complete the angular flux we add

the particular solution to the problem, which for our iterative scheme we assume is known. Based on the definitions presented in Section II and for the purpose of our iterative scheme, we define the asymptotic and transient components to the homogeneous angular flux by:

$$\psi_{n,i}^A(\vec{r}) = \int_0^1 d\mu_0 \int_0^\pi d\gamma_0 \left[ \begin{array}{l} A_i^{a+}(\mu_0, \gamma_0) \alpha_n^{a+}(\mu_0, \gamma_0) \exp\left(-\sigma_{t,i} \frac{\vec{r} \cdot \hat{\omega}_{xy}}{(\nu/\mu_0)^{a+}}\right) + \\ A_i^{a-}(\mu_0, \gamma_0) \alpha_n^{a-}(\mu_0, \gamma_0) \exp\left(-\sigma_{t,i} \frac{\vec{r} \cdot \hat{\omega}_{xy}}{(\nu/\mu_0)^{a-}}\right) \end{array} \right], \quad (313)$$

$$\psi_{n,i}^T(\vec{r}) = \psi_{n,i}^H(\vec{r}) - \psi_{n,i}^A(\vec{r}). \quad (314)$$

where  $(\nu/\mu_0)^{a\pm}$  are the two roots of the dispersion relation with magnitudes greater than one.

The particular solution can be calculated easily if the extraneous source is projected into a polynomial space. We bound the order of the polynomial particular solution by the order of convergence of the homogeneous discretizations.

For XY geometry the five steps of scheme are:

1. Compute the asymptotic boundary and interface conditions.
2. Compute the asymptotic scalar flux: a global diffusion calculation computed numerically with the interface conditions assigned as boundary sources.
3. Filter the asymptotic Case-modes from the angular flux and impose the remaining transient angular fluxes as interface conditions to each region.
4. Compute the transient angular flux: a set of independent local transport calculations on each sub-domain.
5. Update the total scalar flux (homogeneous plus particular) and test it for convergence.

These five steps are the same as in slab geometry with one exception: in slab geometry incident-current boundary and interface conditions were assigned to the asymptotic problem. Here we apply net current and scalar flux boundary conditions, which we describe below.

In the following section we present the mathematical configuration of these five steps as we implemented and tested them. However, we have failed to generate a satisfactory filtering scheme for step 3 that would result in a unconditionally convergent method. We discuss this challenge in the last section of this chapter.

### The Asymptotic-Equivalent Diffusion Problem

The asymptotic distribution in each region was solved numerically by discretizing conservation of particles statement, combined with Fick's Law:

$$\vec{\nabla} \cdot \vec{J}_i^A(\vec{r}) + [1 - c_i] \sigma_{t,i} \phi_i^A(\vec{r}) = 0, \quad (315)$$

$$\vec{J}_i^A(\vec{r}) = -D_i \vec{\nabla} \phi_i^A(\vec{r}), \quad (316)$$

with boundary conditions that we describe below.

We implement this system of differential equations to solve the homogeneous asymptotic component of the angular flux; thus, no extraneous source was assigned. This Diffusion Equation system shares with its slab geometry counterpart that its solution space is spanned by functions scaled by a single relaxation length. Thus as in the slab geometry case, we can implement this Diffusion Equation to solve the spatial distribution of Case-modes that share a relaxation length in magnitude. We determine which subset of Case-modes to satisfy with the Diffusion Equation based on their relaxation lengths. For asymptotic Case-modes, we showed in II that their spatial and angular distribution is given by:

$$\psi_{n,i}^A(\vec{r}) = \int_0^1 d\mu_0 \int_0^\pi d\gamma_0 \left[ \begin{array}{l} A_i^{a+}(\mu_0, \gamma_0) \alpha_n^{a+}(\mu_0, \gamma_0) \exp\left(-\sigma_{t,i} \frac{\vec{r} \cdot \hat{\omega}_{xy}}{(v/\mu_0)^{a+}}\right) + \\ A_i^{a-}(\mu_0, \gamma_0) \alpha_n^{a-}(\mu_0, \gamma_0) \exp\left(-\sigma_{t,i} \frac{\vec{r} \cdot \hat{\omega}_{xy}}{(v/\mu_0)^{a-}}\right) \end{array} \right], \quad (317)$$

$$\alpha_n^{a\pm}(\mu_0, \gamma_0) = \frac{(v/\mu_0)^{a\pm}}{(v/\mu_0)^{a\pm} - \hat{\omega}_{xy} \cdot \hat{\Omega}_n}, \quad (318)$$

where we normalize the angle-shape function to obtain the dispersion relation:

$$\sum_{n=1}^N w_n \frac{(\nu/\mu_0)^{a^\pm}}{(\nu/\mu_0)^{a^\pm} - \hat{\omega}_{xy} \cdot \hat{\Omega}_n} = \frac{4\pi}{c_i}, \quad (319)$$

$$\phi_i^A(\vec{r}) = \frac{4\pi}{c_i} \int_0^1 d\mu_0 \int_0^\pi d\gamma_0 \left[ \begin{array}{l} A_i^{a^+}(\mu_0, \gamma_0) \exp\left(-\sigma_{t,i} \frac{\vec{r} \cdot \hat{\omega}_{xy}}{(\nu/\mu_0)^{a^+}}\right) + \\ A_i^{a^-}(\mu_0, \gamma_0) \exp\left(-\sigma_{t,i} \frac{\vec{r} \cdot \hat{\omega}_{xy}}{(\nu/\mu_0)^{a^-}}\right) \end{array} \right]. \quad (320)$$

To derive the asymptotic-equivalent diffusion length, we insert the asymptotic scalar flux of Eq.(320) into the Diffusion Equations, Eqs.(315) and (316), and solve for a relation between the diffusion length and the asymptotic relaxation length:

$$D_i = \left[ (\nu/\mu_0)^{a^+} \right]^2 \frac{1-c_i}{\sigma_{t,i}}. \quad (321)$$

With the diffusion length defined and an asymptotic-equivalent Diffusion Equation determined, we discretize the asymptotic scalar flux problem. We chose the Local Discontinuous Galerkin Finite Element Method (LDG) to discretize the asymptotic problem. To define the LDG system of equations and its approximate scalar flux, we divide the problem's domain into  $O \cdot P$  rectangular cells. Cell  $j$  is bound by a left, right, back and front edge, which we defined with the orthogonal lines:  $(x_{o-1/2}, y)$ ,  $(x_{o+1/2}, y)$ ,  $(x, y_{p-1/2})$  and  $(x, y_{p+1/2})$ . Furthermore, we order cells first by row and then by column. In other words, the left neighbor of cell  $j$  is cell  $j-1$ , and its back neighbor is cell  $j-O$ .

We define the LDG approximation of the scalar flux and current vector based on the orthogonal linear polynomial functions:

$$\phi_j^A(x, y) = \phi_{j,0}^A + \phi_{j,1}^A \left[ 2 \frac{x-x_j}{\Delta x_j} \right] + \phi_{j,2}^A \left[ 2 \frac{y-y_j}{\Delta y_j} \right], \quad (322)$$

$$J_j^{x,A}(x, y) = J_{j,0}^{x,A} + J_{j,1}^{x,A} \left[ 2 \frac{x-x_j}{\Delta x_j} \right] + J_{j,2}^{x,A} \left[ 2 \frac{y-y_j}{\Delta y_j} \right], \quad (323)$$

$$J_j^{y,A}(x, y) = J_{j,0}^{y,A} + J_{j,1}^{y,A} \left[ 2 \frac{x - x_j}{\Delta x_j} \right] + J_{j,2}^{y,A} \left[ 2 \frac{y - y_j}{\Delta y_j} \right]. \quad (324)$$

Here the  $J^x$  is the  $x$  component of the current vector and  $J^y$  its  $y$  component. Also, we defined the volume of the rectangular cells as  $\Delta x_j \cdot \Delta y_j$  with its center located at  $(x_j, y_j)$ .

To derive the system of LDG equations, we test the Diffusion Equation and Fick's Law against the same polynomial space that spans the scalar flux and current vector components:

$$\frac{J_j^{x,A} \Big|_{x_{o+1/2}} - J_j^{x,A} \Big|_{x_{o-1/2}}}{\Delta x_j} + \frac{J_j^{y,A} \Big|_{y_{p+1/2}} - J_j^{y,A} \Big|_{y_{p-1/2}}}{\Delta y_j} + [1 - c_j] \sigma_{j,t} \phi_{j,0}^A = 0, \quad (325)$$

$$3 \frac{J_j^{x,A} \Big|_{x_{o+1/2}} + J_j^{x,A} \Big|_{x_{o-1/2}}}{\Delta x_j} + \frac{J_{j,1}^{y,A} \Big|_{y_{p+1/2}} - J_{j,1}^{y,A} \Big|_{y_{p-1/2}}}{\Delta y_j} - 6 \frac{J_{j,0}^{x,A}}{\Delta y_j} + [1 - c_j] \sigma_{j,t} \phi_{j,1}^A = 0, \quad (326)$$

$$\frac{J_{j,2}^{x,A} \Big|_{x_{o+1/2}} - J_{j,2}^{x,A} \Big|_{x_{o-1/2}}}{\Delta x_j} + 3 \frac{J_j^{y,A} \Big|_{y_{p+1/2}} + J_j^{y,A} \Big|_{y_{p-1/2}}}{\Delta y_j} - 6 \frac{J_{j,0}^{y,A}}{\Delta y_j} + [1 - c_j] \sigma_{j,t} \phi_{j,2}^A = 0, \quad (327)$$

$$J_{j,0}^{x,A} = -D_j \frac{\phi_j^A \Big|_{x_{o+1/2}} - \phi_j^A \Big|_{x_{o-1/2}}}{\Delta x_j}, \quad (328)$$

$$J_{j,0}^{y,A} = -D_j \frac{\phi_j^A \Big|_{y_{p+1/2}} - \phi_j^A \Big|_{y_{p-1/2}}}{\Delta y_j}, \quad (329)$$

$$J_{j,1}^{y,A} = -3D_j \left[ \frac{\phi_j^A \Big|_{x_{p+1/2}} + \phi_j^A \Big|_{x_{p-1/2}}}{\Delta x_j} - 2 \frac{\phi_{j,0}^A}{\Delta x_j} \right], \quad (330)$$

$$J_{j,1}^{y,A} = -D_j \frac{\phi_{j,1}^A \Big|_{y_{p+1/2}} - \phi_{j,1}^A \Big|_{y_{p-1/2}}}{\Delta y_j}, \quad (331)$$

$$J_{j,2}^{x,A} = -D_j \frac{\phi_{j,2}^A \Big|_{x_{p+1/2}} - \phi_{j,2}^A \Big|_{x_{p-1/2}}}{\Delta x_j}, \quad (332)$$

$$J_{j,2}^{y,A} = -3D_j \left[ \frac{\phi_j^A|_{y_{p+1/2}} - \phi_j^A|_{y_{p-1/2}}}{\Delta y_j} - 2 \frac{\phi_{j,2}^A}{\Delta y_j} \right]. \quad (333)$$

Here, we highlight the terms that belong to the cell edges. These edge terms result from the evaluation of the integrals containing current and scalar flux gradients. They are equivalent to the edge terms that appeared in the derivation of the LD transport method in Section IV. Similar to the LD method, the resulting solution is discontinuous; a numerical artifice produced by not enforcing directly the continuity of the scalar flux and current vector. However, unlike the LD method we do not apply upwinding to communicate boundary conditions on each cell. Instead we apply a linear average of quantities that are physically continuous. To add a level of complexity to the configuration of the asymptotic boundary conditions, the exact asymptotic scalar flux is not necessarily continuous across cell edges. The exact asymptotic scalar flux can be discontinuous if across cell interfaces there exist a discontinuity in the extraneous source or in the scattering ratio. To address the configuration of the asymptotic interface conditions on each cell, we begin by defining the exact asymptotic discontinuity factors.

The asymptotic quantities defined at the cell edges can be either continuous or discontinuous depending on whether they are located at a material interface or not. From our slab geometry experience, Case-modes are born at interfaces separating discontinuities of the scattering ratio or discontinuities of the extraneous source. We configure these discontinuity factors based on the physical continuity of the complete scalar flux, particular plus homogeneous. At the material interface separating cell  $j$  and  $j - 1$ , the total scalar fluxes are defined by:

$$\phi_j|_{x_{o-1/2}} \equiv \frac{\int_{y_{p-1/2}}^{y_{p+1/2}} dy \cdot \phi(x_{o-1/2}, y)}{\Delta y_j} = \phi_j^A(x_{o-1/2}, y_j) + \phi_j^{T+P}|_{x_{o-1/2}}, \quad (334)$$

$$\phi_{j-1}|_{x_{o-1/2}} \equiv \frac{\int_{y_{p-1/2}}^{y_{p+1/2}} dy \cdot \phi(x_{o-1/2}, y)}{\Delta y_{j-1}} = \phi_{j-1}^A(x_{o-1/2}, y_j) + \phi_{j-1}^{T+P}|_{x_{o-1/2}}. \quad (335)$$

where the superscript  $T + P$  identifies the transient plus particular component of the scalar flux. Since the total scalar flux is continuous across material interfaces, we can calculate the discontinuity between asymptotic scalar fluxes:

$$\phi_j^A(x_{o-1/2}, y_j) = \phi_{j-1}^A(x_{o-1/2}, y_j) + \phi_{j-1}^{T+P} \Big|_{x_{o-1/2}} - \phi_j^{T+P} \Big|_{x_{o-1/2}}. \quad (336)$$

We do not directly enforce a continuity statement on the asymptotic interface scalar flux. Instead at the left interface of cell  $j$ , we apply a linear average of the interface condition presented in Eq.(336):

$$\phi_j^A \Big|_{x_{o-1/2}} = \frac{\phi_j^A(x_{o-1/2}, y_j) + \phi_{j-1}^A(x_{o-1/2}, y_j)}{2} - \frac{\Delta\phi_{o-1/2,p}^{T+P}}{2}, \quad (337)$$

$$\Delta\phi_{o-1/2,p}^{T+P} \equiv \phi_j^{T+P} \Big|_{x_{o-1/2}} - \phi_{j-1}^{T+P} \Big|_{x_{o-1/2}}. \quad (338)$$

Similarly for a material interface located at the right edge of a cell:

$$\phi_j^A \Big|_{x_{o+1/2}} = \frac{\phi_j^A(x_{o+1/2}, y_j) + \phi_{j+1}^A(x_{o+1/2}, y_j)}{2} + \frac{\Delta\phi_{o+1/2,p}^{T+P}}{2}, \quad (339)$$

$$\Delta\phi_{o+1/2,p}^{T+P} \equiv \phi_{j+1}^{T+P} \Big|_{x_{o+1/2}} - \phi_j^{T+P} \Big|_{x_{o+1/2}}. \quad (340)$$

Based on this treatment of the asymptotic scalar flux at material interfaces, the remaining asymptotic scalar flux quantities defined at cell edges are defined by:

$$\phi_j^A \Big|_{y_{p-1/2}} = \frac{\phi_{j,0}^A - \phi_{j,2}^A}{2} + \frac{\phi_{j-1,0}^A + \phi_{j-1,2}^A}{2} - \frac{\Delta\phi_{o,p-1/2}^{T+P}}{2}, \quad (341)$$

$$\phi_j^A \Big|_{y_{p+1/2}} = \frac{\phi_{j,0}^A + \phi_{j,2}^A}{2} + \frac{\phi_{j+1,0}^A - \phi_{j+1,2}^A}{2} + \frac{\Delta\phi_{o,p+1/2}^{T+P}}{2}, \quad (342)$$

$$\phi_{j,2}^A \Big|_{x_{o-1/2}} = \frac{\phi_{j,2}^A + \phi_{j-1,2}^A}{2} - \frac{\Delta\phi_{2,o-1/2,p}^{T+P}}{2}, \quad (343)$$

$$\phi_{j,2}^A \Big|_{x_{o+1/2}} = \frac{\phi_{j,2}^A + \phi_{j-1,2}^A}{2} + \frac{\Delta\phi_{2,o+1/2,p}^{T+P}}{2}, \quad (344)$$

$$\phi_{j,1}^A \Big|_{y_{o-1/2}} = \frac{\phi_{j,1}^A + \phi_{j-1,1}^A}{2} - \frac{\Delta\phi_{1,o,p-1/2}^{T+P}}{2}, \quad (345)$$

$$\phi_{j,1}^A \Big|_{x_{p+1/2}} = \frac{\phi_{j,1}^A + \phi_{j-1,1}^A}{2} + \frac{\Delta\phi_{1,\phi,p+1/2}^{T+P}}{2}. \quad (346)$$

The cell interface conditions for the  $x$  and  $y$  components of the current vector are defined similarly to those for the scalar flux defined above. Note that if there is no material or source discontinuity between cell  $j$  and its corresponding neighbor then, the asymptotic interface source equals zero. Mathematically, for the left edge of cell  $j$  this implies that the asymptotic boundary source is defined as:

$$\frac{\Delta\phi_{o-1/2,p}^{T+P}}{2} = \begin{cases} 0, & \text{if } c_j = c_{j-1} \text{ and } Q_j = Q_{j-1} \\ \phi_j^{T+P} \Big|_{x_{o-1/2}} - \phi_{j-1}^{T+P} \Big|_{x_{o-1/2}}, & \text{otherwise} \end{cases}. \quad (347)$$

We define the asymptotic source only at material interfaces so that as we discretize the transient problem, the asymptotic problem is not excited by numerical discontinuities in the transient solution.

Finally, we define the scalar flux and current unknowns at the problem boundaries. We replicate the approach used to derive the scalar flux continuity statement across material interface, except that we replace the unknowns from the previous cell by the boundary conditions. At the left boundary of the problem, the boundary scalar flux is equal to:

$$\phi_j \Big|_{x_{1/2}} \equiv \frac{\int_{y_{p-1/2}}^{y_{p+1/2}} dy \cdot g_L(y)}{\Delta y_j} = \phi_j^A(0, y_j) + \phi_j^{T+P} \Big|_{x_{1/2}}, \quad (348)$$

$$\phi_j \Big|_{x_{1/2}} - \phi_j^{T+P} \Big|_{x_{1/2}} = \phi_{j,0}^A - \phi_{j,1}^A. \quad (349)$$

Here  $g_L$  is the function specifying the scalar flux on the left domain boundary. This equates the asymptotic scalar flux evaluated at a left boundary cell edge to:

$$\phi_j^A \Big|_{x_{1/2}} = \frac{\phi_{j,0}^A - \phi_{j,1}^A}{2} - \frac{\Delta\phi_{1/2,j}^{T+P}}{2}, \quad (350)$$

$$\Delta\phi_{1/2,p}^{T+P} = \phi_j^{T+P} \Big|_{x_{1/2}} - \phi_j \Big|_{x_{1/2}}. \quad (351)$$

Here we have only defined the scalar flux boundary conditions and discontinuity factors. An equal treatment is given to define the net current normal component and its discontinuity sources at the boundaries.

We insert all the edge unknowns defined, into the discretized Diffusion Equation, Eqs.(325) through (333), and obtain:

$$\begin{aligned} & \frac{J_{j+1,0}^{x,A} - J_{j+1,1}^{x,A}}{2\Delta x_j} (1 - \delta_{o,o}) - \frac{J_{j-1,0}^{x,A} + J_{j-1,1}^{x,A}}{2\Delta x_j} (1 - \delta_{o,1}) + \frac{J_{j+1,0}^{y,A} - J_{j+1,2}^{y,A}}{2\Delta y_j} (1 - \delta_{p,p}) \\ & - \frac{J_{j-1,0}^{y,A} + J_{j-1,2}^{y,A}}{2\Delta y_j} (1 - \delta_{p,1}) + \frac{J_{j,1}^{x,A}}{\Delta x_j} + \frac{J_{j,2}^{y,A}}{\Delta y_j} + [1 - c_j] \sigma_{t,j} \phi_{j,0}^A = S_{j,0}^{T+P}, \end{aligned} \quad (352)$$

$$\begin{aligned} & 3 \frac{J_{j+1,0}^{x,A} - J_{j+1,1}^{x,A}}{2\Delta x_j} (1 - \delta_{o,o}) + 3 \frac{J_{j-1,0}^{x,A} + J_{j-1,1}^{x,A}}{2\Delta x_j} (1 - \delta_{o,1}) + \frac{J_{j+1,1}^{y,A}}{2\Delta y_j} (1 - \delta_{p,p}) \\ & - \frac{J_{j-1,1}^{y,A}}{2\Delta y_j} (1 - \delta_{p,1}) - 3 \frac{J_{j,0}^{x,A}}{\Delta x_j} + [1 - c_j] \sigma_{t,j} \phi_{j,1}^A = S_{j,1}^{T+P}, \end{aligned} \quad (353)$$

$$\begin{aligned} & \frac{J_{j+1,2}^{x,A}}{2\Delta x_j} (1 - \delta_{o,o}) - \frac{J_{j-1,2}^{x,A}}{2\Delta x_j} (1 - \delta_{o,1}) + 3 \frac{J_{j+K,0}^{x,A} - J_{j+K,1}^{x,A}}{2\Delta x_j} (1 - \delta_{p,p}) \\ & + 3 \frac{J_{j-K,0}^{x,A} - J_{j-K,1}^{x,A}}{2\Delta x_j} (1 - \delta_{p,1}) - 3 \frac{J_{j,0}^{y,A}}{\Delta y_j} + [1 - c_j] \sigma_{t,j} \phi_{j,2}^A = S_{j,2}^{T+P}, \end{aligned} \quad (354)$$

$$J_{j,0}^{x,A} = -D_j \left[ \frac{\phi_{j+1,0}^A - \phi_{j+1,1}^A}{2\Delta x_j} (1 - \delta_{o,o}) - \frac{\phi_{j-1,0}^A + \phi_{j-1,1}^A}{2\Delta x_j} (1 - \delta_{o,1}) + \frac{\phi_{j,1}^A}{\Delta x_j} \right] + \vartheta_{j,0}^{x,T+P}, \quad (355)$$

$$J_{j,1}^{x,A} = -3D_j \left[ \frac{\phi_{j+1,0}^A - \phi_{j+1,1}^A}{2\Delta x_j} (1 - \delta_{o,o}) + \frac{\phi_{j-1,0}^A + \phi_{j-1,1}^A}{2\Delta x_j} (1 - \delta_{o,1}) - \frac{\phi_{j,0}^A}{\Delta x_j} \right] + \vartheta_{j,0}^{x,T+P}, \quad (356)$$

$$J_{j,2}^{x,A} = -D_j \left[ \frac{\phi_{j+1,2}^A}{2\Delta x_j} (1 - \delta_{o,o}) - \frac{\phi_{j-1,2}^A}{2\Delta x_j} (1 - \delta_{o,1}) \right] + \vartheta_{j,0}^{x,T+P}, \quad (357)$$

$$J_{j,0}^{y,A} = -D_j \left[ \frac{\phi_{j+K,0}^A - \phi_{j+K,2}^A}{2\Delta y_j} (1 - \delta_{p,p}) - \frac{\phi_{j-K,0}^A + \phi_{j-K,2}^A}{2\Delta y_j} (1 - \delta_{p,p}) + \frac{\phi_{j,2}^A}{\Delta y_j} \right] + \vartheta_{j,0}^{y,T+P}, \quad (358)$$

$$J_{j,1}^{y,A} = -D_j \left[ \frac{\phi_{j+K,1}^A}{2\Delta y_j} (1 - \delta_{p,p}) - \frac{\phi_{j-1,1}^A}{2\Delta y_j} (1 - \delta_{p,1}) \right] + \vartheta_{j,1}^{y,T+P}, \quad (359)$$

$$J_{j,2}^{y,A} = -3D_j \left[ \frac{\phi_{j+K,0}^A - \phi_{j+K,2}^A}{2\Delta y_j} (1 - \delta_{p,p}) + \frac{\phi_{j-K,0}^A + \phi_{j-K,2}^A}{2\Delta y_j} (1 - \delta_{p,p}) - \frac{\phi_{j,0}^A}{\Delta y_j} \right] + \vartheta_{j,2}^{y,T+P}, \quad (360)$$

where the discontinuity sources and boundary conditions are defined by:

$$S_{j,0}^{T+P} = -\frac{\Delta J_{k+1/2,l}^{x,T+P}}{2\Delta x_j} - \frac{\Delta J_{k-1/2,l}^{x,T+P}}{2\Delta x_j} - \frac{\Delta J_{k,l+1/2}^{x,T+P}}{2\Delta y_j} - \frac{\Delta J_{k,l-1/2}^{x,T+P}}{2\Delta y_j}, \quad (361)$$

$$S_{j,1}^{T+P} = -3\frac{\Delta J_{o+1/2,p}^{x,T+P}}{2\Delta x_j} + 3\frac{\Delta J_{o-1/2,p}^{x,T+P}}{2\Delta x_j} - \frac{\Delta J_{1,o,p+1/2}^{x,T+P}}{2\Delta y_j} - \frac{\Delta J_{1,o,p-1/2}^{x,T+P}}{2\Delta y_j}, \quad (362)$$

$$S_{j,2}^{T+P} = -\frac{\Delta J_{2,o+1/2,p}^{x,T+P}}{2\Delta x_j} - \frac{\Delta J_{2,o-1/2,p}^{x,T+P}}{2\Delta x_j} - 3\frac{\Delta J_{o,p+1/2}^{x,T+P}}{2\Delta y_j} + 3\frac{\Delta J_{o,p-1/2}^{x,T+P}}{2\Delta y_j}, \quad (363)$$

$$\vartheta_{j,0}^{x,T+P} = -D_j \frac{\Delta \phi_{o+1/2,p}^{T+P}}{2\Delta x_j} - D_j \frac{\Delta \phi_{o-1/2,p}^{T+P}}{2\Delta x_j}, \quad (364)$$

$$\vartheta_{j,1}^{x,T+P} = -3D_j \frac{\Delta \phi_{o+1/2,p}^{T+P}}{2\Delta x_j} + 3D_j \frac{\Delta \phi_{o-1/2,p}^{T+P}}{2\Delta x_j}, \quad (365)$$

$$\vartheta_{j,2}^{x,T+P} = -D_j \frac{\Delta \phi_{2,o+1/2,p}^{T+P}}{2\Delta x_j} - D_j \frac{\Delta \phi_{2,o-1/2,p}^{T+P}}{2\Delta x_j}, \quad (366)$$

$$\vartheta_{j,0}^{y,T+P} = -D_j \frac{\Delta \phi_{o,p+1/2}^{T+P}}{2\Delta x_j} - D_j \frac{\Delta \phi_{o,p-1/2}^{T+P}}{2\Delta x_j}, \quad (367)$$

$$\vartheta_{j,1}^{y,T+P} = -D_j \frac{\Delta \phi_{1,o,p+1/2}^{T+P}}{2\Delta y_j} - D_j \frac{\Delta \phi_{1,o,p-1/2}^{T+P}}{2\Delta y_j}, \quad (368)$$

$$\vartheta_{j,2}^{y,T+P} = -3D_j \frac{\Delta \phi_{o,p+1/2}^{T+P}}{2\Delta y_j} + 3D_j \frac{\Delta \phi_{o,p-1/2}^{T+P}}{2\Delta y_j}. \quad (369)$$

Here the prescribed boundary quantities are contained in the transient plus asymptotic discontinuity source, as defined by Eq.(351).

The system of equations above is recasted in matrix form is:

$$\mathbf{D} \cdot \Phi^A = \mathbf{M} \cdot (\Phi^T + \Phi^P) + \mathbf{B} \cdot (\Phi_{inc}). \quad (370)$$

Here:

$\mathbf{D} \equiv$  asymptotic-equivalent diffusion matrix,

$\Phi^A \equiv$  asymptotic scalar flux and current,

$\mathbf{M} \cdot (\Phi^T + \Phi^P) \equiv$  asymptotic interface discontinuity source,

$\mathbf{B} \cdot \Phi_{inc} \equiv$  asymptotic boundary source,

$\Phi^T \equiv$  transient scalar flux and current,

$\Phi^P \equiv$  particular scalar flux and current.

### Asymptotic Angular Flux Reconstruction

The diffusion problem defined in the previous section produces the scalar flux of the asymptotic Case-modes. Although the scheme's final product is the combined scalar flux from the asymptotic, transient and particular components; the asymptotic angular flux is still needed to define step 1 and step 3. To construct the asymptotic angular flux from its scalar flux, we exploit the properties of the LDG scalar flux approximation and combine them with our description of the asymptotic solution space.

We assume that the grid resolves asymptotic scalar fluxes such that their distribution in space can be accurately described by a linear polynomial function:

$$\begin{aligned} \phi^{a\pm}(\mu_0, \gamma_0, \vec{r}) &= \frac{4\pi}{c} A^{a\pm}(\mu_0, \gamma_0) \exp\left(-\sigma_t \frac{\hat{\omega}_{xy} \cdot (\vec{r} - \vec{r}_j)}{(v/\mu_0)^{a\pm}}\right) \\ &\approx \frac{4\pi}{c} A^{a\pm}(\mu_0, \gamma_0) \left[1 - \sigma_t \frac{\hat{\omega}_{xy} \cdot (\vec{r} - \vec{r}_j)}{(v/\mu_0)^{a\pm}}\right], \end{aligned} \quad (371)$$

$$\phi^A(\vec{r}) \approx \frac{4\pi}{c} \int_0^1 d\mu_0 \int_0^\pi d\gamma_0 \left\{ \begin{array}{l} A^{a^+}(\mu_0, \gamma_0) \left[ 1 - \sigma_t \frac{\hat{\omega}_{xy} \cdot (\vec{r} - \vec{r}_j)}{(\nu/\mu_0)^{a^+}} \right] \\ + A^{a^-}(\mu_0, \gamma_0) \left[ 1 - \sigma_t \frac{\hat{\omega}_{xy} \cdot (\vec{r} - \vec{r}_j)}{(\nu/\mu_0)^{a^-}} \right] \end{array} \right\}. \quad (372)$$

Here we assume that the quadrature employed was symmetric and the asymptotic relaxation lengths have equal magnitude but opposite signs.

The approximation in Eq.(372) implies that in each cell the asymptotic solution has a constant gradient. We simplify the asymptotic space by rotating the coordinate system in each cell such that one of the coordinate axes is aligned with the gradient vector. This rotation produces a scalar that only varies along the characteristic line; the asymptotic scalar flux is one dimensional. With such a change of basis, the asymptotic Case-modes in XY-geometry are reduced to their asymptotic structure of slab geometry, which simplifies the scalar flux into:

$$\phi_j^A(\vec{r}) = \frac{4\pi}{c_j} \left\{ \begin{array}{l} A_j^{a^+} \left[ 1 - \sigma_{j,t} \frac{\hat{\omega}_{xy} \cdot (\vec{r} - \vec{r}_j)}{(\nu/\mu_0)^{a^+}} \right] \\ + A_j^{a^-} \left[ 1 - \sigma_{t,j} \frac{\hat{\omega}_{xy} \cdot (\vec{r} - \vec{r}_j)}{(\nu/\mu_0)^{a^-}} \right] \end{array} \right\}, \quad (373)$$

$$\hat{\omega}_{xy} = \frac{\vec{\nabla} \phi_j^A}{\|\vec{\nabla} \phi_j^A\|}, \quad (374)$$

$$\|\vec{\nabla} \phi_j^A\| = \frac{4\pi}{c_j} \sigma_{j,t} \left[ -\frac{A^{a^+}}{(\nu/\mu_0)_j^{a^+}} - \frac{A^{a^-}}{(\nu/\mu_0)_j^{a^-}} \right]. \quad (375)$$

Similarly, the asymptotic angular flux simplifies to its slab geometry counterpart:

$$\psi_{j,n}^A = \left\{ \begin{array}{l} \frac{(\nu/\mu_0)_j^{a+}}{(\nu/\mu_0)_j^{a+} - \hat{\Omega}_n \cdot \hat{\omega}_{xy}} A_j^{a+} \left[ 1 - \sigma_{t,j} \frac{\hat{\omega}_{xy} \cdot (\bar{r} - \bar{r}_j)}{(\nu/\mu_0)_j^{a+}} \right] \\ + \frac{(\nu/\mu_0)_j^{a-}}{(\nu/\mu_0)_j^{a-} - \hat{\Omega}_n \cdot \hat{\omega}_{xy}} A_j^{a-} \left[ 1 - \sigma_{t,j} \frac{\hat{\omega}_{xy} \cdot (\bar{r} - \bar{r}_j)}{(\nu/\mu_0)_j^{a-}} \right] \end{array} \right\}. \quad (376)$$

Therefore, if the positive and negative asymptotic relaxation length, scalar flux, and its gradient are known, we can reconstruct the angular flux by a rotation of the coordinate system.

We highlight that the gradient of the scalar flux may vary from cell to cell. Thus, the Case-mode direction  $\hat{\omega}$ , may vary from cell to cell as well. Furthermore, from our observation in Section II, the value of the asymptotic relaxation lengths is a function of the mode direction  $\hat{\omega}$ . Shifts in the direction of the gradient perturb the direction of  $\hat{\omega}$  and thus, perturb the magnitude of the asymptotic relaxation lengths. The asymptotic roots to the dispersion relation must be recomputed for each cell after each iteration, which implies a non-linear step. However, as the asymptotic roots to the dispersion relation become much larger than one their sensitivity to perturbation in the Case mode direction diminishes. The sensitive also diminishes as the quadrature set is refined. A constant asymptotic relaxation length is a reasonable assumption for problem with large scattering ratios or refined quadrature set; we make this assumption in our implementation.

We summarize this discussion with the four steps to calculate the asymptotic angular flux, if the linear approximation of the asymptotic scalar flux and its gradient are known:

1. Compute the single asymptotic Case-mode direction  $\hat{\omega}^A$ , Eq.(374).
2. Compute the asymptotic roots to the dispersion relation:

$$\sum_{n=1}^N w_n \frac{(\nu/\mu_0)^{a\pm}}{(\nu/\mu_0)^{a\pm} - \hat{\omega}_{xy} \cdot \hat{\Omega}_n} = \frac{4\pi}{c_i} \quad (377)$$

3. Compute the asymptotic amplitudes:

$$A_j^{a-} = \frac{c_j}{4\pi} \frac{1}{\sigma_t} \frac{\frac{\sigma_t}{(\nu/\mu_0)_j^{a+}} \phi_j^A(x_j, y_j) - \|\bar{\nabla} \phi_j^A\|}{(\mu_0/\nu)_j^{a+} - (\mu_0/\nu)_j^{a-}}, \quad (378)$$

$$A_j^{a+} = \frac{c_j}{4\pi} \frac{1}{\sigma_t} \frac{-\frac{\sigma_t}{(\nu/\mu_0)_j^{a-}} \phi_j^A(x_j, y_j) + \|\bar{\nabla} \phi_j^A\|}{(\mu_0/\nu)_j^{a+} - (\mu_0/\nu)_j^{a-}}. \quad (379)$$

Here for convenience the asymptotic scalar flux was evaluated at cell-center.

4. Compute the asymptotic angular flux, Eq.(376).

We symbolize these three steps in matrix form as:

$$\Psi^A = \mathbf{C}(\Phi) \cdot \Phi^A, \quad (380)$$

where  $\mathbf{C}(\Phi)$  is the matrix that maps the approximate LDG asymptotic Case-space of the scalar flux to the angular flux. We note that  $\mathbf{C}$  depends on  $\phi$ ; thus Eq.(380) represents a nonlinear operation.

### The Asymptotic Component (Step 1 and 2)

We begin our iterative scheme by defining the diffusion problem that determines the asymptotic distribution of the angular flux. With the asymptotic-equivalent diffusion problem defined in the previous section, only the asymptotic driving terms remain to be configured with respect to the overall scheme. There are two sources of asymptotic Case-modes in a domain. The first source defined from the material discontinuities between cells, and a second source from the asymptotic component of the boundary conditions. The first source is straightforward to define. It is calculated based Eq.(347) using the particular solution, which we assume to know, and the transient angular flux, which we approximate to its value from the previous iterate. With respect to our iterative scheme, this implies that the asymptotic problem, Eq. (370), reduces to:

$$\mathbf{D} \cdot \Phi^{A,(l)} = \mathbf{M} \cdot [\Phi^{T,(l)} + \Phi^P] + \mathbf{B} \cdot (\Phi_{inc}). \quad (381)$$

Here  $l$  distinguishes the value of an unknown after  $l$  iterations.

The asymptotic diffusion problem was configured as having specified boundary values for the scalar flux and current. However, the transport problem that our scheme addresses only specifies incident angular fluxes at the domain's boundaries. Therefore, to completely determine the asymptotic boundary conditions an estimate of the angular flux exiting each boundary edge is needed.

To calculate the asymptotic boundary scalar flux and current, we reconstruct the asymptotic domain-exiting angular flux and add it to the asymptotic component of the incident angular flux boundary conditions. Thus, the boundary conditions to the asymptotic diffusion problem are partially constructed on the asymptotic scalar flux. To break this cycle, we construct the asymptotic boundary conditions on the asymptotic scalar flux from a previous iterate and allow for multiple inner iterations of the asymptotic problem:

$$\mathbf{D} \cdot \Phi^{A,(l^{*+1})} = \mathbf{M} \cdot [\Phi^{T,(l)} + \Phi^P] + \mathbf{B} \cdot \mathbf{W} (\Psi_{inc} + \Psi_{exit}^P + \Psi_{exit}^{T,(l)} + \Psi_{exit}^{A,(l^*)}). \quad (382)$$

Here  $l^*$  is the inner asymptotic iteration counter if multiple asymptotic inner iterations are done. Also here, we assumed that the quadrature is symmetric such that each incident angular flux shares a quadrature weight with and exiting angular flux. With respect to the asymptotic angular flux reconstruction matrix presented in Eq.(380), the asymptotic problem of Eq.(381) reduces to:

$$\mathbf{D} \cdot \Phi^{A,(l^{*+1})} = \left\{ \begin{array}{l} \mathbf{M} \cdot [\Phi^{T,(l)} + \Phi^P] \\ +\mathbf{B} \cdot \mathbf{W} (\Psi_{inc} + \Psi_{exit}^P + \Psi_{exit}^{T,(l)}) + \mathbf{B} \cdot \mathbf{W} \cdot \mathbf{C}(\Phi^{A,(l^*)}) \cdot \Phi^{A,(l^*)} \end{array} \right\}, \quad (383)$$

where  $\mathbf{C}(\Phi^A)$  is a non-linear operator.

The maximum number of inner iterations could be set to an arbitrary maximum or the asymptotic scalar flux could be converged to specified tolerance. In the derivation of the slab geometry scheme, we found that if the asymptotic problem was inverted iteratively then the solution must be converged exactly in each outer iteration for the overall scheme to be unconditionally stable. Based on this observation, we speculate that the asymptotic boundary conditions will need to be converged also for the overall

scheme to remain stable. Regardless of the criteria chosen to determine the number of inner iterations, we link the asymptotic inner unknowns to those of overall scheme by:

$$\Phi^{A,(l^*)} = \begin{cases} \Phi^{A,(l-1)}, & \text{if } l^* = 1 \\ \Phi^{A,(l^*)}, & \text{if } 1 < l^* < l^*_{\max} \\ \Phi^{A,(l)}, & \text{if } l^* = l^*_{\max} \end{cases} . \quad (384)$$

### The Transient Interface Conditions (Step 3)

We solve the remaining Case-modes by configuring a transport problem that only excites those modes with transient relaxation lengths. As with the asymptotic Case-modes, the transient sources reside at the problem's boundaries and at interfaces separating scattering ratio and extraneous source discontinuities. We configure the transport problem to the transient Case-modes by filtering the asymptotic contribution from the homogeneous angular flux at each material interface and boundary, and assigning the resulting transient angular fluxes as incident angular flux conditions to each region. In step 3, we configure the interface and boundary conditions to each local transient problem.

From our description of the transport space in multiple dimensions, the angular fluxes from Case-modes with different relaxation length are related by:

$$\sum_{n=1}^N w_n \psi_n^k \hat{\Omega}_n \cdot \vec{\nabla} \psi_n^l = \sum_{n=1}^N w_n \psi_n^l \hat{\Omega}_n \cdot \vec{\nabla} \psi_n^k . \quad (385)$$

Here  $\psi_n^k$  is the angular flux of Case-mode  $k$  at angle  $n$ .

We assume that all Case-modes, transient and asymptotic, have angular fluxes constructed on the structure presented for asymptotic angular fluxes, Eq.(317), which simplifies Eq.(385) to:

$$\left( \frac{\hat{\omega}_{xy}^k}{(\nu / \mu_0^k)^k} - \frac{\hat{\omega}_{xy}^l}{(\nu / \mu_0^l)^l} \right) \cdot \sum_{n=1}^N \hat{\Omega}_n w_n \alpha_n^k (\mu_0^k, \gamma_0^k) \alpha_n^l (\mu_0^l, \gamma_0^l) = 0 . \quad (386)$$

Here modes  $k$  and  $l$  are distributed in space and angle with respect to vector  $\hat{\omega}^k$  and  $\hat{\omega}^l$ , with:

$$\begin{aligned}\mu_0^k &= \hat{\omega}^k \cdot \hat{\omega}_{xy}^k, \\ \mu_0^l &= \hat{\omega}^l \cdot \hat{\omega}_{xy}^l.\end{aligned}$$

Therefore, unless all Case-modes lie on the same direction  $\hat{\omega}$  (as with slab geometry) the filtering relation that we employed in slab geometry to isolate asymptotic modes will not do so in XY geometry; it will leave behind a transient residual. With this limitation in mind, the filtering of asymptotic Case-modes takes the form:

$$\begin{aligned}\sum_{n=1}^N w_n \left[ \omega^{a\pm} \cdot \hat{\Omega}_n \right] \psi_n^H \alpha_n^{a\pm} = \\ A^{a\pm} \sum_{n=1}^N w_n \left[ \hat{\omega}^{a\pm} \cdot \hat{\Omega}_n \right] \alpha_n^{a\pm} \alpha_n^{a\pm} + \sum_{n=1}^N w_n \left[ \hat{\omega}^{a\pm} \cdot \hat{\Omega}_n \right] \psi_n^T \alpha_n^{a\pm},\end{aligned}\quad (387)$$

With respect to our iterative scheme, we define an intermediate homogeneous angular flux constructed on the most current asymptotic and transient angular fluxes. We define this homogeneous angular flux at the boundary edges to each region based on incident and exiting angular fluxes. The homogeneous angular flux for a boundary cell on the left interface of the region is:

$$\psi_{n,j}^{H,(l+1/2)} \Big|_{x_{o-1/2}} = \begin{cases} \psi_{n,inc} - \psi_{n,j}^P \Big|_{x_{o-1/2}}, & \text{if } x_{o-1/2} = 0 \\ \left( \begin{array}{l} \psi_{n,j-1}^{A,(l)} \Big|_{x_{o-1/2}} + \psi_{n,j-1}^{T,(l)} \Big|_{x_{o-1/2}} \\ + \psi_{n,j-1}^P \Big|_{x_{o-1/2}} - \psi_{n,j}^P \Big|_{x_{o-1/2}} \end{array} \right), & \text{otherwise} \end{cases}, \quad (388)$$

with  $\hat{e}_x \cdot \hat{\Omega}_n > 0$ . Here  $(x_{o-1/2}, y_j)$  is the coordinates of the left edge of cell  $j$  and this edge is on the left material interface of region  $i$ . Similar definitions can be extended for the right, bottom and top interface of region  $i$ .

We filter the asymptotic components of this intermediate angular flux, and update the incident transient angular flux on cell  $j$  located on an interface of region  $i$ :

$$\begin{aligned} \psi_{n,inc,o-1/2,p}^{T,(l+1)} &= \psi_{n,j}^{H,(l+1/2)} \Big|_{x_{o-1/2}} \\ &= \left\{ \begin{aligned} &\alpha_{n,j}^{a+} \left[ \sum_{n=1}^N w_n \left[ \omega^{a+} \cdot \hat{\Omega}_n \right] \left( \psi_{n,j}^{H,(l+1/2)} - \psi_{n,j}^{T,(l)} \right) \alpha_n^{a+} \right]_{x_{o-1/2}} \\ &+ \alpha_{n,j}^{a-} \left[ \sum_{n=1}^N w_n \left[ \omega^{a-} \cdot \hat{\Omega}_n \right] \left( \psi_{n,j}^{H,(l+1/2)} - \psi_{n,j}^{T,(l)} \right) \alpha_n^{a-} \right]_{x_{o-1/2}} \end{aligned} \right\} \end{aligned} \quad (389)$$

Here:

$$\psi_{n,inc,o-1/2,p}^{T,(l+1)} \equiv \text{the incident transient angular flux at the boundary edge } (x_{o-1/2}, y_p).$$

With the transient boundary conditions defined, we conclude step 3.

#### The Transient Component (Step 4)

We construct the transient solution with a Linear Discontinuous (LD) discretization of the transport equation. We define the LD angular flux by projecting the exact solution into a linear polynomial space, in this case defined to contain only transient Case-modes:

$$\psi_{n,j}^T(x, y) = \psi_{n,j,0}^T + \psi_{n,j,1}^T \left[ 2 \frac{x - x_j}{\Delta x_j} \right] + \psi_{n,j,2}^T \left[ 2 \frac{y - y_j}{\Delta y_j} \right]. \quad (390)$$

We build the system of equation to solve these angular flux amplitudes by testing the transport equation into the space of basis functions used to span the LD solution. Using the same trial and weight spaces is convenient since the polynomial functions of the trial space are orthogonal, which simplifies the integral evaluation. After projecting the transport equation into the polynomial space, we obtain the following equation system for cell  $j$ :

$$\begin{aligned} \frac{\mu_n}{\Delta x_j} \left[ \psi_n^T \Big|_{x_{o+1/2}} - \psi_n^T \Big|_{x_{o-1/2}} \right] + \frac{\eta_n}{\Delta y_j} \left[ \psi_n^T \Big|_{y_{p+1/2}} - \psi_n^T \Big|_{y_{p-1/2}} \right] + \sigma_{t,j} \psi_{n,j,0}^T \\ = \sigma_{t,j} \frac{c_j}{4\pi} \sum_{m=1}^N w_m \psi_{m,j,0}^T, \end{aligned} \quad (391)$$

$$\begin{aligned} \frac{\mu_n}{\Delta x_j} \left[ \psi_{n,1}^T \Big|_{x_{o+1/2}} - \psi_{n,1}^T \Big|_{x_{o-1/2}} \right] + 3 \frac{\eta_n}{\Delta y_j} \left[ \psi_n^T \Big|_{y_{p+1/2}} + \psi_n^T \Big|_{y_{p-1/2}} - 2\psi_{n,j,0}^T \right] + \sigma_{t,j} \psi_{n,j,1}^T \\ = \sigma_{t,j} \frac{C_j}{4\pi} \sum_{m=1}^N w_m \psi_{m,j,1}^T, \end{aligned} \quad (392)$$

$$\begin{aligned} 3 \frac{\mu_n}{\Delta x_j} \left[ \psi_n^T \Big|_{y_{p+1/2}} + \psi_n^T \Big|_{y_{p-1/2}} - 2\psi_{n,j,0}^T \right] + \frac{\eta_n}{\Delta y_j} \left[ \psi_{n,1}^T \Big|_{x_{o+1/2}} - \psi_{n,1}^T \Big|_{x_{o-1/2}} \right] + \sigma_{t,j} \psi_{n,j,2}^T \\ = \sigma_{t,j} \frac{C_j}{4\pi} \sum_{m=1}^N w_m \psi_{m,j,2}^T. \end{aligned} \quad (393)$$

Here,

$$\mu_n \equiv \hat{\Omega}_n \cdot \hat{e}_x,$$

$$\eta_n \equiv \hat{\Omega}_n \cdot \hat{e}_y.$$

Also, we have defined some angular fluxes and angular flux unknowns as evaluated at the cell surface. These edge unknowns communicate boundary information into the system of equation in cell  $j$ . We assign to each edge-evaluated angular flux unknown its upstream value as follows:

$$\psi_n^T \Big|_{x_{o-1/2}} = \begin{cases} \psi_{n,j-1,0}^T + \psi_{n,j-1,1}^T, & \text{if } \mu_n > 0 \\ \psi_{n,j,0}^T - \psi_{n,j,1}^T, & \text{if } \mu_n < 0 \end{cases}, \quad (394)$$

$$\psi_n^T \Big|_{x_{p+1/2}} = \begin{cases} \psi_{n,j-1,0}^T + \psi_{n,j-1,2}^T, & \text{if } \eta_n > 0 \\ \psi_{n,j,0}^T - \psi_{n,j,2}^T, & \text{if } \eta_n < 0 \end{cases}, \quad (395)$$

$$\psi_{n,2}^T \Big|_{x_{o-1/2}} = \begin{cases} \psi_{n,j-1,2}^T, & \text{if } \mu_n > 0 \\ \psi_{n,j,2}^T, & \text{if } \mu_n < 0 \end{cases}, \quad (396)$$

$$\psi_{n,1}^T \Big|_{y_{p-1/2}} = \begin{cases} \psi_{n,j-1,1}^T, & \text{if } \eta_n > 0 \\ \psi_{n,j,1}^T, & \text{if } \eta_n < 0 \end{cases}. \quad (397)$$

In matrix form, we group the system of equations for all the cells in region  $i$  as:

$$\mathbf{Q} \cdot \Psi^T = \mathbf{R}_1 \cdot \Psi^T + \mathbf{R}_2 \cdot \Psi_{inc \rightarrow i}^T + \mathbf{S} \cdot \Phi^T, \quad (398)$$

$$\mathbf{O} \cdot \Phi^T = \mathbf{P} \cdot \Psi^T. \quad (399)$$

Here,  $\Psi_{inc \rightarrow i}^T$  is the vector of incident transient angular fluxes on the region, which we calculate based on Eq.(389) of step 3.

We solve iteratively the transient system of equations with either One Cell Inversions (OCI) or Source Iterations (SI). In the case of OCI, the iterative system to invert each regional transient transport problem is:

$$\mathbf{Q} \cdot \Psi^{T,(l^{*+1})} = \mathbf{S} \cdot \Phi^{T,(l^{*+1})} + \mathbf{R}_1 \cdot \Psi^{T,(l^*)} + \mathbf{R}_2 \cdot \Psi_{inc \rightarrow i}^{T,(l+1)}, \quad (400)$$

$$\mathbf{O} \cdot \Phi^{T,(l^{*+1})} = \mathbf{P} \cdot \Psi^{T,(l^*)}, \quad (401)$$

where  $l^*$  is the iteration index to the OCI iterative inversion, and  $l$  is the iteration index to overall iterative scheme. Also, the matrix  $\mathbf{P}$  is configured such that it operates only on angular fluxes incident to each cell.

The OCI iterative inversion is done until a predetermined maximum number of OCIs is reached or the local transient solution satisfies a convergence criteria. After each transient region is inverted, the transient angular fluxes are collected and the global transient solution updated. In terms of our inner and outer iteration indexes this implies:

$$\Psi^{T,(l+1)} = \Psi^{T,(l^*)} \quad \text{if } l^* > l^*_{\max} \quad \text{or } \Psi^{T,(l^*)} \text{ of region } j \text{ converged.} \quad (402)$$

A similar iterative inversion of the local transient problem can be configured for SI, with the appropriate modifications to local transient iterative matrix:

$$[\mathbf{Q} - \mathbf{R}_1] \cdot \Psi^{T,(l^{*+1})} = \mathbf{S} \cdot \Phi^{T,(l^*)} + \mathbf{R}_2 \cdot \Psi_{inc \rightarrow i}^{T,(l+1)}, \quad (403)$$

$$\mathbf{O} \cdot \Phi^{T,(l^*)} = \mathbf{P} \cdot \Psi^{T,(l^*)}. \quad (404)$$

### Convergence Test (Step 5)

With the global asymptotic scalar flux and the local transient angular fluxes updated, the total solution is tested for convergence:

$$\Phi^{(l+1)} = \Phi^{A,(l)} + \Phi^{T,(l+1)} + \Phi^P. \quad (405)$$

As in slab geometry, we test convergence on the total scalar flux to avoid wasting iterations on over-converging either the asymptotic or the transient problem. This convergence criterion is especially advantageous with the transient component of the calculation. It allows for a loose convergence of the transient angular flux away from

the boundary layers of each transient region. In the interior of material regions the solution is dominated by the asymptotic and by the particular solution, making the transient contribution at this location is negligible. The transient domain is effectively reduced, which reduces the number of inner iterations if OCI is used to invert the transient problem in each sub-domain.

### VI.C. Analysis

We implemented the scheme described in the previous section and found that the scheme is not unconditionally stable for XY geometry problems. We identified the source of instabilities as the filtering scheme used to construct the transient boundary conditions. We make this identification by comparing the XY scheme with its slab geometry counterpart. These two schemes differed at two points in their design. First, the XY geometry scheme iterates on the asymptotic problem until the scalar flux and current at the problem's boundaries converges. In slab geometry, we configure incident current conditions to the asymptotic problem, which we calculate with available transient and homogeneous angular fluxes. Hence, in slab geometry no asymptotic inner iterations are required.

The second difference is in the asymptotic filtering process. In XY geometry, the Case-mode filter can not isolate those contributors to the homogeneous angular flux that share a common relaxation length. The XY geometry filter can only distinguish among Case-modes with different relaxation length if they share the same direction  $\hat{\omega}$ . Therefore, if the homogeneous angular flux contains contributions from transient Case-modes in directions other than the asymptotic one,  $\hat{\omega}^{a+}$ , then each filtering step produces a transient-contaminated asymptotic amplitude:

$$A^{a\pm} = \frac{\left[ \sum_{n=1}^N w_n \left[ \hat{\omega}^{a\pm} \cdot \hat{\Omega}_n \right] \psi_n^H \alpha_n^{a\pm} - \sum_{n=1}^N w_n \left[ \omega^{a\pm} \cdot \hat{\Omega}_n \right] \tilde{\psi}_n^T \alpha_n^{a\pm} \right]}{\sum_{n=1}^N w_n \left[ \omega^{a\pm} \cdot \hat{\Omega}_n \right] \alpha_n^{a\pm} \alpha_n^{a\pm}} \quad (406)$$

Here:

$$\tilde{\psi}_n^T = \int_0^1 \mu_0 \int_0^{2\pi} d\gamma_0 \psi_n^T(\mu_0, \gamma_0) \left[ 1 - \delta(\gamma_0 - \gamma_0^{a\pm}) \right],$$

or the set of transient angular fluxes that propagate in direction non-parallel to the direction of asymptotic Case-modes.

To overcome this transient residual, we attempted to approximate it with the transient angular flux from a previous iteration:

$$A^{a\pm, (l+1/2)} = \frac{\left[ \sum_{n=1}^N w_n \left[ \hat{\omega}^{a\pm} \cdot \hat{\Omega}_n \right] \psi_n^{H, (l+1/2)} \alpha_n^{a\pm} - \sum_{n=1}^N w_n \left[ \omega^{a\pm} \cdot \hat{\Omega}_n \right] \psi_n^{T, (l)} \alpha_n^{a\pm} \right]}{\sum_{n=1}^N w_n \left[ \omega^{a\pm} \cdot \hat{\Omega}_n \right] \alpha_n^{a\pm} \alpha_n^{a\pm}}. \quad (407)$$

If the exact transient residual was known, then, the filter above would be suitable. Instead in Eq.(407), we have configured a system which tries to solve the asymptotic amplitudes and the transient residual simultaneously. We argue that this configuration is equivalent to constructing a filtering system of equations that is singular. Consider the ideal scenario where the exact homogeneous angular flux is available in all streaming direction. This scenario is equivalent to applying our filtering scheme on an optically transparent single-cell problem, and to assume that on each edge the exiting angular flux equals the boundary conditions on the opposite edge. Our filtering scheme aims at computing from the exact incident homogeneous angular flux the asymptotic amplitudes and the transient filtering residual. Given this scenario, at one of the four cell boundary edges the filtering system of equation is:

$$A^{a\pm, (l)} = \frac{\left[ \sum_{n=1}^N w_n \left[ \hat{\omega}^{a\pm} \cdot \hat{\Omega}_n \right] \psi_{n, inc} \alpha_n^{a\pm} - \sum_{n=1}^N w_n \left[ \omega^{a\pm} \cdot \hat{\Omega}_n \right] \psi_n^{T, (l-1)} \alpha_n^{a\pm} \right]}{\sum_{n=1}^N w_n \left[ \omega^{a\pm} \cdot \hat{\Omega}_n \right] \alpha_n^{a\pm} \alpha_n^{a\pm}}, \quad (408)$$

$$\psi_n^{T, (l)} = \psi_{n, inc} - \alpha_n^{a+} A^{a+, (l)} - \alpha_n^{a-} A^{a-, (l)}. \quad (409)$$

In matrix form:

$$\begin{aligned}
& \begin{bmatrix} \sum_{n=1}^N w_n [\hat{\omega}^{a+} \cdot \hat{\Omega}_n] \alpha_n^{a+} \alpha_n^{a+} & 0 & 0 & \cdots & 0 \\ 0 & \sum_{n=1}^N w_n [\hat{\omega}^{a+} \cdot \hat{\Omega}_n] \alpha_n^{a+} \alpha_n^{a+} & 0 & \cdots & 0 \\ \alpha_1^{a+} & \alpha_1^{a-} & 1 & \cdots & 0 \\ \vdots & \vdots & \vdots & \ddots & \vdots \\ \alpha_N^{a+} & \alpha_N^{a-} & 0 & \cdots & 1 \end{bmatrix} \begin{pmatrix} A^{a+} \\ A^{a-} \\ \psi_1^T \\ \vdots \\ \psi_N^T \end{pmatrix}^{(l)} \\
& = - \begin{pmatrix} \sum_{n=1}^N w_n [\hat{\omega}^{a+} \cdot \hat{\Omega}_n] \alpha_n^{a+} \psi_n^T \\ \sum_{n=1}^N w_n [\hat{\omega}^{a-} \cdot \hat{\Omega}_n] \alpha_n^{a-} \psi_n^T \\ 0 \\ \vdots \\ 0 \end{pmatrix}^{(l-1)} + \begin{pmatrix} \sum_{n=1}^N w_n [\hat{\omega}^{a+} \cdot \hat{\Omega}_n] \alpha_n^{a+} \psi_{n,inc} \\ \sum_{n=1}^N w_n [\hat{\omega}^{a-} \cdot \hat{\Omega}_n] \alpha_n^{a-} \psi_{n,inc} \\ \psi_{1,inc} \\ \vdots \\ \psi_{N,inc} \end{pmatrix} \quad (410)
\end{aligned}$$

This iterative system attempts to solve the linear system:

$$\begin{aligned}
& \begin{bmatrix} \sum_{n=1}^N w_n \mu_n^{a+} \alpha_n^{a+} \alpha_n^{a+} & 0 & w_1 \mu_1^{a+} \alpha_1^{a+} & \cdots & w_N \mu_N^{a+} \alpha_N^{a+} \\ 0 & \sum_{n=1}^N w_n \mu_n^{a-} \alpha_n^{a-} \alpha_n^{a-} & w_1 \mu_1^{a+} \alpha_1^{a-} & \cdots & w_N \mu_N^{a+} \alpha_N^{a-} \\ \alpha_1^{a+} & \alpha_1^{a-} & 1 & \cdots & 0 \\ \vdots & \vdots & \vdots & \ddots & \vdots \\ \alpha_N^{a+} & \alpha_N^{a-} & 0 & \cdots & 1 \end{bmatrix} \begin{pmatrix} A^{a+} \\ A^{a-} \\ \psi_1^T \\ \vdots \\ \psi_N^T \end{pmatrix} \\
& = \begin{pmatrix} \sum_{n=1}^N w_n \mu_n^{a+} \alpha_n^{a+} \psi_{n,inc} \\ \sum_{n=1}^N w_n \mu_n^{a-} \alpha_n^{a-} \psi_{n,inc} \\ \psi_{1,inc} \\ \vdots \\ \psi_{N,inc} \end{pmatrix}, \quad (411)
\end{aligned}$$

where:

$$\mu_n^{a+} \equiv \hat{\omega}^{a+} \cdot \hat{\Omega}_n.$$

The first two rows in our filtering matrix are a linear combination of the last  $N$  rows. We obtain the first row by multiplying each one of the last  $N$  rows by the appropriate filtering weight  $w_n \mu_n^{a+} \alpha_n^{a+}$  and adding the resulting products. We obtain the second row similarly by changing the filtering weight to the negative asymptotic counterpart:  $w_n \mu_n^{a+} \alpha_n^{a-}$ . Since the filtering matrix is singular, any iterative scheme will be ill-conditioned regardless of how the iterative matrix splits the filtering system. By adding more cells and in optically thicker problem, the filtering scheme is more complex; it must discern the asymptotic and transient fractions of approximate homogeneous angular fluxes.

We highlight that the slab geometry filtering matrix is equal to the one in XY geometry. However, in the slab geometry case the transient angular flux is the null space to the top right corner block. Thus, when the iterative filtering process is configured as shown in Eq.(411), we can neglect the vector of transient residuals. The slab geometry filtering scheme is equivalent to inverting the matrix:

$$\begin{bmatrix} \langle \alpha^{a+}, \alpha^{a+} \rangle & 0 & 0 & \cdots & 0 \\ 0 & \langle \alpha^{a-}, \alpha^{a-} \rangle & 0 & \cdots & 0 \\ \alpha_1^{a+} & \alpha_1^{a-} & 1 & \cdots & 0 \\ \vdots & \vdots & \vdots & \ddots & \vdots \\ \alpha_N^{a+} & \alpha_N^{a-} & 0 & \cdots & 1 \end{bmatrix} \begin{pmatrix} A^{a+} \\ A^{a-} \\ \psi_1^T \\ \vdots \\ \psi_N^T \end{pmatrix} = \begin{pmatrix} \langle \alpha^{a+}, \psi_{inc} \rangle \\ \langle \alpha^{a-}, \psi_{inc} \rangle \\ \psi_{1,inc} \\ \vdots \\ \psi_{N,inc} \end{pmatrix}, \quad (412)$$

where

$$\langle \alpha^k, \alpha^l \rangle \equiv \sum w_n \mu_n \alpha_n^k \alpha_n^l.$$

This filtering matrix is invertible; the resulting iterative filtering scheme is stable.

#### VI.D. Numerical Results

To confirm that our analysis is correct, we designed a test problem with a one-dimensional solution and modified it, so that two dimensional Case-modes were progressively present. The test problem consisted of two regions with differing scattering ratio and extraneous sources, and a single cell per region. Thus, the angular

fluxes in each cell are spanned by different set of Case-modes. The material specifications to the problem are presented in Fig. 32. The left region was discretized with ten rectangular cells, while one cell was used to discretize the right region. The problem was solved with an  $S_4$  Level-Symmetric quadrature set, and the scalar flux was converged to a relative tolerance of 1.0E-3. Vacuum boundary conditions were assigned at all four edges.

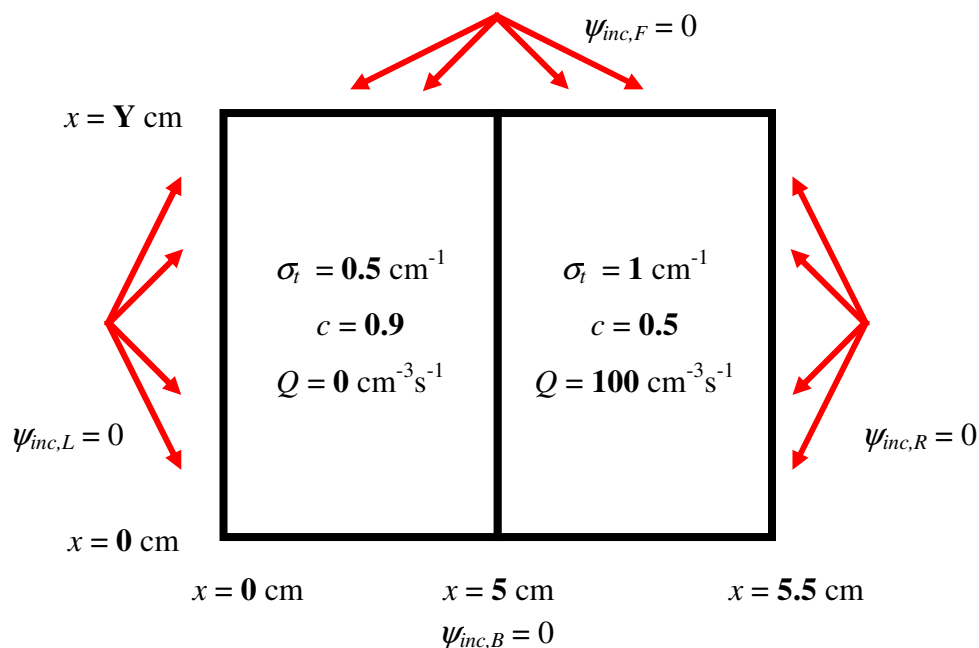


Fig. 32. Two-region XY geometry test problem.

We chose vacuum boundary conditions to minimize the number of inner iterations needed to invert the asymptotic problem per outer iteration. Recall from our description of step 1, that the asymptotic solver iterates internally until it converges the asymptotic angular flux exiting the plane. The asymptotic exiting angular flux is used to compute a scalar flux and current vector at the problem edges, which are reassigned to

the solver as boundary conditions. With vacuum conditions, we aimed at simplifying the asymptotic iterative problem and focus our attention on the transient one where the filtering process is done.

We divided the testing of our software into two levels. The first level tested the asymptotic, transient and particular solvers in our scheme individually. To do so, we manufactured diffusion and transport problems with linear polynomial sources and boundary conditions. Since we implemented linear approximations to the diffusion, transport and particular solvers, then their solution to the manufactured problems should be exact. We found this to be the case for all problems we tested.

The second level tested the coupling among the three components of the angular flux. Again, we applied a transport manufactured solution with linear polynomial distribution in space and angle. Such an angular flux only contains a particular component given our description of the homogeneous Case-space. Hence, if the scheme was implemented correctly the asymptotic and transient solution should be numerical zeros. Again, we found this to be the case for all problems tested.

Finally, we tested the transient-particular coupling. This was done by assigning a transport problem to the coupled transient-particular solver and assigning it to the transient solver only. The solutions from either option should be exactly equal in the absence of an asymptotic component. We chose the problem illustrated in Fig. 32 to perform this test. Both solution options produced the correct result.

To confirm the findings of our analysis, the solution to the problem in Fig. 32 was solved for an very large vertical dimension,  $Y$ , which we progressively reduced. For a very large  $Y$  the solution approaches the one-dimensional (slab) solution and the Case-mode structure of the homogeneous solution is one-dimensional. In reducing the depth of  $Y$ , we aim to progressively introduce XY geometry Case-mode to the solution. By controlling the dimension of the cells we aim to control the dimensionality of the set of Case-modes that are assigned to the filtering scheme.

We began the series of test problems by solving with our XY scheme the plane of 1000 cm in depth. The scalar and angular flux to this problem were essentially one

dimensional. To further test the logic in our software, we used a one-dimensional Case-mode filter with our XY scheme. If the software was configured correctly then the solution to the problem should converge in few iterations. The solution converged in 5 iterations to a tolerance of  $1\text{E-}12$ . We present the asymptotic, transient and particular scalar flux in Fig. 33. Consistent with the results from the previous chapter, the solution in the interior was dominated by the asymptotic component and the transient component only contributed significantly at the material interfaces. Unlike the problems in the previous chapter that were entirely driven by boundary conditions, in this problem particles are born from the extraneous source. In other words, Case-modes were driven by the discontinuity of the particular solution at the material interface. With this problem, we further verified that our scheme was implemented correctly and that the angular flux to the problem was spanned by one-dimensional Case-modes.

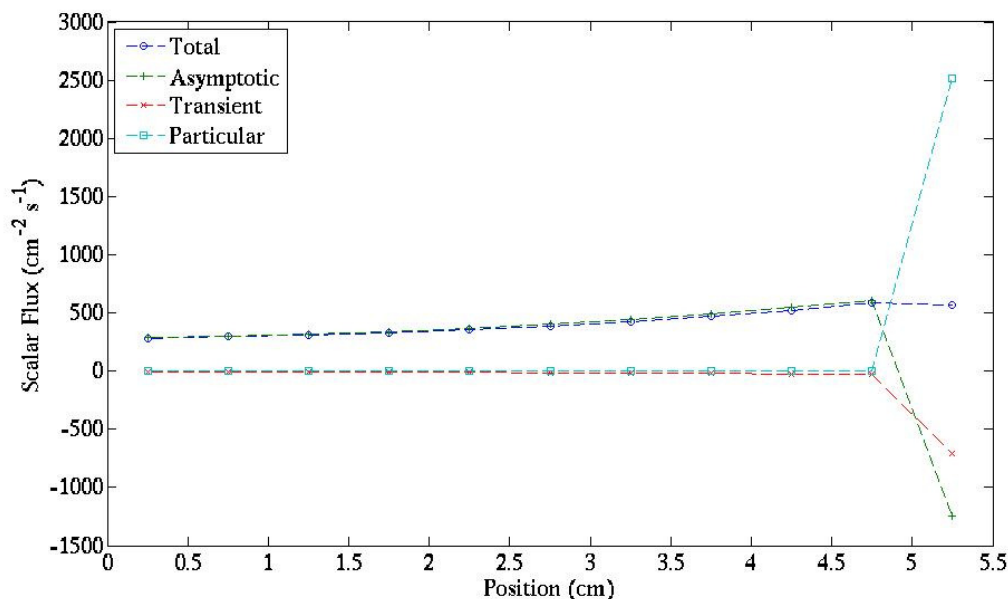


Fig. 33. Cell-average scalar flux of the two-region XY geometry test problem.

TABLE XVIII

Number of Iterations to Solve the Different Configurations to the XY Geometry Test Problem.

Vertical Thickness Y (cm)	Number of iterations
1000	5
100	6
10	8
1	9
0.1	86*
0.01	24*
0.1 (with XY filtering)	86*

\*Code overflows.

We decreased the depth of the problem to a minimum depth of 0.01 cm. With a two-dimensional Case-mode present, the one-dimensional filter failed to discriminate correctly between transient and asymptotic Case-modes. Hence, the scheme failed to converge the scalar flux. Similarly, at 0.01 cm the scheme diverged and the scalar flux exploded to an overflow value within 24 iterations. We present the iteration count to the remaining test problems in Table XVIII. Problems thicker than 0.1 cm did converge. However, the iteration count increased progressively from 5 to 9 iterations. In the thinner problems, two-dimensional Case-modes were present with enough importance as to produce a significant transient residual in the filtering. The resulting transient-contaminated asymptotic amplitudes produced inaccurate transient interface conditions that lead to the divergence of the iterative scheme and the overflow of the solvers. Based on these results, we conclude that as two-dimensional Case-modes are added to

the solution space, the one-dimensional filter fails to discriminate between asymptotic and transient Case-mode, transient interface conditions are miscalculated and the iterative scheme diverges.

We attempted to address the two-dimensional Case-modes with the two-dimensional filtering scheme of Eq.(389). As predicted by our analysis the iterative scheme diverged without a reasonable estimate to the transient residual to the asymptotic filtering. For this test and configuration, the solution overflow in 86 iterations. An estimate of the spectral radius, Eq.(306), yield a value of 100. In other words, the iterative error was 100 times larger than its value in the previous iteration. At this point, we have not found the appropriate weighted inner product that can discriminate among Case-modes scaled by different relaxation lengths and propagating along different Case-mode directions,  $\hat{\omega}$ . Such an inner product would translates mathematically into:

$$\langle \alpha^k(\omega^k), \alpha^l(\omega^l) \rangle = \delta_{k,l} \cdot C_0. \quad (413)$$

Here  $\alpha^k$  and  $\alpha^l$  are the angle-shape functions of modes  $k$  and  $l$ , and  $C_0$  is a constant. This inner product is the key to producing an invertible filtering system. In the absence of such an inner product, our analysis and experience suggest that the transient-asymptotic coupling will cause divergence of the overall iteration scheme.

We discuss suggestions for future studies in Section VII.

#### *VI.E. Summary of Results*

We have designed and implemented an XY extension to our iteration scheme, but the scheme was not unconditionally convergent. The scheme divides the angular flux into its particular, asymptotic and transient components and solves each with numerically different techniques. Asymptotic Case-modes are solved with a Locally Discontinuous Galerkin diffusion discretization, and transient Case-mode with Linear Discontinuous Finite Element method. The particular solution was approximated to a linear polynomial that satisfied the particular component of the transport equation to a linear order. All three components are combined into a single scalar flux, and convergence is tested.

The diffusion equation is satisfied by any set of transport Case-modes that shares a common relaxation length. The degree of freedom that allows for these two operators to share a set of solution modes resides in the magnitude of the diffusion length. We chose to assign in our iterative scheme asymptotic Case-modes to a diffusion solver. To drive this diffusion problem, we configured asymptotic boundary and interface conditions. Asymptotic boundary conditions were computed by removing the transient and particular component of the total incident angular fluxes. The interface conditions were computed by estimating from a previous iterate the discontinuity in the particular and transient solution across material interface. Since the angular flux is continuous across material interface, the discontinuity jump in the non-asymptotic components equals that of the asymptotic component. With an asymptotic equivalent diffusion length, and boundary and interface conditions assigned, the diffusion problem was fully determined. We inverted this diffusion problem exactly as the first step in the iterative process of our scheme.

We derive a procedure to reconstruct an asymptotic angular flux from its scalar flux. The asymptotic angular fluxes were needed to couple the asymptotic problem with the remaining components in the transport calculation. This reconstruction was also needed to translate incident angular flux boundary conditions into the appropriate diffusion boundary conditions without approximation. The ansatz that we used to describe the asymptotic Case-modes suggested that infinite number of Case-modes shared a common asymptotic relaxation length. Each one of these Case-modes propagated itself along a distinct direction,  $\hat{\omega}$ . By projecting the diffusion solution into the LDG polynomial space; we found that the infinite set of asymptotic Case-modes is reduced to a single Case-mode propagated along the direction of the scalar flux gradient. In other words, we can rotate the coordinate system so that the resulting LDG scalar flux is one-dimensional. A one-dimensional scalar flux is constructed on a single direction  $\hat{\omega}$ , in contrast to a multi-dimensional scalar flux constructed on an infinite number of directions. We rotated the coordinate system in each cell to reduce the asymptotic scalar

flux to a one-dimensional form, and reconstruct from it the asymptotic angular flux. The asymptotic angular flux is then remapped to the standard coordinate system.

Transient Case-modes were solved using the homogeneous transport equation without any modification. However, to produce a true transient distribution, the correct transient boundary and interface conditions were needed. These were configured by calculating an interface homogeneous angular flux and discerning its asymptotic component. The asymptotic component was then removed from all incident angular fluxes to obtain the incident transient angular flux. An orthogonality relation that discriminates among Case-modes was necessary to discern the asymptotic component. We could not find such an orthogonality relation that produced the correct asymptotic incident fraction. This was the source of the instabilities in our scheme. A one-dimensional orthogonality scheme does exist, and can be applied in XY geometry to filter Case-modes constructed along a single direction  $\hat{\omega}$ . However, if the filter is applied to an angular flux constructed on multiple directions  $\hat{\omega}$  then, the filtering process produces our desired amplitude plus a residual. The resulting transient interface conditions are numerically contaminated by this residual and the transient and homogeneous solutions are inaccurate. Over many iterations the filtering residual can accumulate to produce an diverging iterative system.

## VII. CONCLUSIONS

### *VII.A. Summary of the Dissertation*

We have designed an iterative method to solve discrete ordinates particle transport calculations with parallel computing in mind. The iterative scheme divides the Linear Boltzmann transport equation into its particular and homogeneous components. The particular component addresses the contribution of particles by extraneous sources to the system. The homogeneous component satisfies the transport equation in the absence of the extraneous source term, and is constructed as a linear combination of Case-modes. Each Case-mode is characterized by a relaxation length that scales the variation of the Case-modes in space and in particle streaming direction. Our iterative scheme assigns those Case-modes that vary slowly, the asymptotic Case-modes, to a diffusion solver that can accurately capture them at lower computational cost. Fast-changing Case-modes, the transient ones, are assigned to a transport solver so that regional details can be captured accurately and consistently with a classic transport calculation. The particular problem is configured and inverted directly prior to starting the iterative process. In this dissertation, we presented an iterative scheme that constructs a transport solution by coordinating the computational efforts of a diffusion and transport solver.

In assigning different operators to solve the asymptotic and transient components, our iterative scheme can potentially simplify the configuration of a parallel transport algorithm. The transient problem is divided into a series of local problems that have little or no communication between them. Each transient region can be solved concurrently with little dependency between regions. The solution to these local transient problems is added to the asymptotic one, which has a global influence; but we discretize and invert with a diffusion solver. Therefore, our iterative scheme reduces the complexity of parallelizing transport problems to the parallelization of diffusion ones.

We have shown that in slab geometry this method is stable and it can invert problems in few iterations. On top of the scheme's parallelization advantages, it

presented some interesting numerical properties. Mainly, the convergence rate of the scheme depends weakly on the scattering ratio of the transport media. A more important factor on the convergence rate was the optical thickness of each region. Problems with optically thick media isolated each transient region and reduced the global character of the asymptotic Case-modes. Hence, the scheme's ability to coordinate the asymptotic and transient problems is accentuated.

Unfortunately, we were unsuccessful in extending our scheme from slab geometry problems to those in multiple dimensions. The derivation of our scheme was heavily supported by the description of the transport Case-space in previous literature. A complete Case-mode expansion analysis of transport problems in XY geometries is not available. We were successful in defining and organizing separate transient and asymptotic problems. However at this point, we are unable to formulate orthogonality relations that discriminate among Case-modes scaled to different relaxation lengths. We employ such an orthogonality relation to coordinate the construction of the transient boundary conditions.

In the process of designing our iterative scheme, we have developed a new analysis technique that applies to any spatial discretization of the slab geometry transport equation. The analysis provides a description of the Case-mode space of the discretization method. Its final product is a Taylor expansion of each Case-mode component with respect to the mesh refinement as scaled by each relaxation length. Hence, for the Taylor expansions to converge, we assumed that the grid was fine enough to produce meaningful solutions. In the formulation of our analysis no special material properties were made, allowing for a wide range of analysis scenarios. Furthermore, in the special case of the Family of Continuous Finite Element Methods, this analysis yields their exact Case-mode structure.

An extension of our scheme to multiple dimensions is worth further research. To the numerical and parallelization advantages of this scheme, we add one: in multiple dimensions it should mitigate the ray effects that discrete ordinates transport approximations produce. The asymptotic solution, which persists faraway from particle

sources, will be constructed by a diffusion solver; therefore, only the local transient problems will present the discrete ordinates shortcoming of ray effects. Our iterative scheme could therefore improve the accuracy of a discrete ordinates solution.

### VII.B. Suggestion for Future Work

The development of a filter to discriminate among transient and asymptotic Case-modes is the main challenge in the extension of our scheme into multiple dimensions. A successful multidimensional filter should differentiate Case-modes belonging to different relaxation lengths and propagating along different mode directions. Currently, our filtering scheme can only differentiate those Case-modes propagating along the same Case-mode direction. We suggest a change in path to derive such a filter. A simpler approach could result from first changing the basis of the Case-mode space and then deriving a filtering scheme under the new basis. An ideal candidate change of basis would expand the angular flux into a linear combination of naturally orthogonal functions that only depends on the streaming direction. The search of a filtering relation would be simplified in such an orthogonal space, and the extension of our iterative scheme to XY geometry resolved.

A Legendre Polynomial expansion of the angle-shape functions seems like an ideal choice. This family of functions is orthogonal, and could allow the separation of the relaxation length, propagation direction and streaming direction variables in the angle-shape function. An expansion of the angle-shape function would take the form:

$$\alpha^k(\hat{\omega} \cdot \hat{\Omega}) = \frac{v^k}{v^k - \hat{\omega} \cdot \hat{\Omega}} = \sum_{l=1}^{\infty} B_l^k P^l(\hat{\omega} \cdot \hat{\Omega}), \quad (414)$$

which can be combined with the Spherical Harmonics Addition Theorem to separate the distribution in streaming direction and propagation direction in the angle-shape function:

$$P^l(\hat{\omega} \cdot \hat{\Omega}) = \frac{4\pi}{2l+1} \sum_{m=-l}^l Y_{lm}^*(\hat{\omega}) Y_{lm}(\hat{\Omega}), \quad (415)$$

$$\alpha^k(\hat{\omega} \cdot \hat{\Omega}) = \sum_{l=1}^{\infty} \frac{4\pi}{2l+1} B_l^k \sum_{m=-l}^l Y_{lm}^*(\hat{\omega}) Y_{lm}(\hat{\Omega}). \quad (416)$$

Such a change in basis would consolidate the infinite set of Case-modes in  $\hat{\omega}$  into a single Case-mode function:

$$\psi_n^k(\vec{r}) = \sum_{l=1}^{\infty} \sum_{m=-l}^l \frac{4\pi}{2l+1} B_l^k Y_{lm}(\hat{\Omega}_n) \int_0^1 d\mu_0 \int_0^\pi d\gamma_0 A^k(\mu_0, \gamma_0, \vec{r}) Y_{lm}^*(\mu_0, \gamma_0), \quad (417)$$

$$\psi_n^k(\vec{r}) = \sum_{l=1}^{\infty} \sum_{m=-l}^l \frac{4\pi}{2l+1} \tilde{B}_l^k(\vec{r}) Y_{lm}(\hat{\Omega}_n), \quad (418)$$

where,

$$\tilde{B}_l^k(\vec{r}) = \int_0^1 d\mu_0 \int_0^\pi d\gamma_0 A^k(\mu_0, \gamma_0) f^k(\vec{r}, \mu_0) \sum_{l=0}^{\infty} B_l^k P_l(\hat{\omega}(\mu_0, \gamma_0) \cdot \hat{\Omega}_n). \quad (419)$$

This could simplify the derivation of the filtering scheme in XY geometry.

An extension to multiple dimension of our iterative scheme appears to be the most pressing challenge. If success is achieved in doing so then, problems with anisotropic scattering and multiple energy groups could be considered. However, slab-geometry description of these more complex problems exists<sup>33</sup> and their extension to multiple dimensions should follow that of problems with one-energy group and isotropic scattering.

## REFERENCES

1. E. E. Lewis and W. F. Miller, Jr. , *Computational Methods of Neutron Transport*, American Nuclear Society, La Grange Park, IL (1993).
2. R. E. Hiromoto and B. R. Wienke, "Parallel Sn Iteration Schemes," *Nucl. Sci. Eng.*, **90**, 116-128 (1985).
3. T. Manteuffel, S. F. McCormick, J. E. Morel, S. Oliveira and G. Yang, "A Fast Multigrid Algorithm for Isotropic Transport Problems I: Pure Scattering," *SIAM J. Sci. Comp.*, **16**, 601-635 (1995).
4. T. Manteuffel, S. F. McCormick, J. E. Morel, S. Oliveira and G. Yang, "A Fast Multigrid Algorithm for Isotropic Transport Problems II: With Absorption," *SIAM J. Sci. Comp.*, **17**, 1449-1474 (1996).
5. M. L. Adams and E. W. Larsen, "Fast Iterative Methods for Discrete-Ordinates Particle Transport Calculations," *Prog. Nucl. Energy*, **40**, 3-159 (2002).
6. J. H. Chang, "Efficient Algorithms for Discrete-Ordinates Transport Iterations in Massively Parallel Computers," Ph.D. Dissertation, Texas A&M University, College Station, Texas (2004).
7. Y. Y. Azmy, "Performance and Performance Modeling of a Parallel Algorithm for Solving the Neutron Transport Equation," *J. Supercomputing*, **6**, 211-235 (1992).
8. A. Haghghat and R. Mattis, "Domain Decomposition of a Two-Dimensional Sn Method," *Nucl. Sci. Eng.*, **111**, 180-196 (1992).
9. A. Haghghat, M. A. Hunter and R. Mattis, "Iterative Schemes for Parallel Sn Algorithms in a Shared-Memory Computer Environment," *Nucl. Sci. Eng.*, **121**, 103-113 (1995).
10. B. Carlson and K. Lathrop, "Numerical Solution of the Boltzmann Transport Equation," *J. Comp. Phys.*, **1**, 173-197 (1966).
11. E. Larsen and M. Yavuz, "Iterative Method for Solving X-Y Geometry Sn Problems on Parallel Architectures Computers," *Nucl. Sci. Eng.*, **112**, 32-42 (1992).
12. R. S. Baker and K. R. Koch, "An Sn Algorithm for Massively Parallel CM-200 Computer," *Nucl. Sci. Eng.*, **128**, 312-320 (1998).

13. M. R. Dorr and C. H. Still, "Concurrent Source Iteration in the Solution of Three-Dimensional, Multigroup Discrete Ordinates Neutron Transport Equations," *Nucl. Sci. Eng.*, **122**, 287-308 (1996).
14. E. Larsen, P. F. Nowak and W. R. Martin, "A Multigrid Method for Sn Calculations in X-Y Geometry", *Trans. Am. Nucl. Soc.*, San Diego, CA, June 12-16, 1988, **56**, 291-292 (1988).
15. K.S. Kim and T. S. Palmer, "Diffusion Synthetic Acceleration for One-Cell Block Inversion in Slab Geometry", *Trans. Am. Nucl. Soc.*, Long Beach, CA, November 14-18, 1999, **81**, 138-140 (1999).
16. R. C. Barros and E. Larsen, "A Numerical Method for One-Group Slab Geometry Transport Problems with no Spatial Truncation Error", *Nucl. Sci. Eng.*, **104**, 199-208, (1990).
17. R. C. Barros and E. Larsen, "A Spectral Nodal Method for One-Group X,Y-Geometry Discrete Ordinates Problems", *Nucl. Sci. Eng.*, **111**, 34-45 (1992).
18. K. M. Case, "Elementary Solutions of the Transport Equation and Their Applications", *Ann. Phys.*, **9**, 1-23 (1960).
19. K. M. Case and P. F. Zweifel, *Linear Transport Theory*, Addison-Wesley, Reading, MA, (1967).
20. E. H. Bareiss and I. K. Abu-Shumays, "On the Structure of Isotropic Transport Operators in Space", *Transport Theory: Proceedings of a Symposium in Applied Mathematics of the American Mathematical Society and the Society for Industrial and Applied Mathematics*, New York, April 5-8 1967, 1, 37-78 (1967).
21. G. C. Pomraning, "(Weakly) Three-Dimensional Caseology", *Ann. Nucl. Energy*, **23**, 4 & 5, 413-427 (1996).
22. B. Davison, "Angular Distribution Due to an Isotropic Point Source and Spherically Symmetrical Eigensolutions for the Transport Equation", *Prog. Nucl. Energy*, **36**, 323-365 (2000).
23. N. G. Van Kampen, "On the Theory of Stationary Waves in Plasmas", *Physica* **21**, 949-963 (1955).
24. P. F. Zweifel, "Transport Theory Revisited (1960 – 1995)", *Transport Th. Statis. Phys.*, **26**, 1&2, 181-193 (1997).

25. E. W. Larsen and G. J. Habetler, "A Functional Analytic Derivation of Case's Full and Half-Range Formulas", *Comm. Pure Appl. Math.*, **26**, 525-537 (1973).
26. R. Hangelbroek, "Linear Analysis and Solution of Neutron Transport Problems", *Transp. Theory Stat. Phys.*, **5**, 1-85 (1976).
27. J. Slawny and P. F. Zweifel, "A Note on the Singular Eigenfunction Method in Transport Theory", *Transp. Theory Stat. Phys.*, **17**, 283-294 (1988).
28. I. K. Abu-Shumays and E. H. Bareiss, "Generating Functions for the Exact Solution of the Transport Equation. I", *J. Math. Phys.*, **9**, 10, 1722-1731 (1968).
29. T. A. Germogenova, "Space Moment Approximations for Transport Problems in Slab", *Preprint of the Keldysh Institute of Applied Mathematics Russian Academy of Science*, paper 39, Moscow, Russia (1997), in Russian.
30. J. R. Mika, "Neutron Transport with Anisotropic Scattering", *Nucl. Sci. Eng.*, **11**, 415-427 (1961).
31. R. L. Bowden, S. Sancakhart and P. F. Zweifel, "Multigroup Neutron Transport. I", *J. Math. Phys.*, **17**, 1, 76-81 (1976).
32. R. L. Bowden, S. Sancakhart and P. F. Zweifel, "Multigroup Neutron Transport. II", *J. Math. Phys.*, **17**, 1, 82-86 (1976).
33. B. D. Ganapol, "Multigroup Caseology in 1D via the Fourier Transform". *Prog. Nucl. Energy*, **50**, 886-907 (2008).
34. E. Larsen and W. F. Miller, "Convergence Rates of Spatial Difference Equations for the Discrete-Ordinates Neutron Transport Equations in Slab Geometry," *Nucl. Sci. Eng.*, **73**, 76-83 (1980).

## APPENDIX A

### DFEM CASE-MODE ANALYSIS EXAMPLE: LINEAR

#### DISCONTINUOUS

##### *Definitions*

We define the left and right node Case-modes to the LD approximate transport solution:

$$\psi_{n,R,i} = f^i b_n z, \psi_{n,L,i} = f^i a_n$$

The LD system of equations is defined by:

$$\mu_n > 0:$$

$$\frac{-\psi_{n,L} + \psi_{n,R}}{2} + \tau_n \frac{\psi_{n,L} + 2\psi_{1,R}}{6} = \tau_n \frac{c}{2} \frac{\phi_L + 2\phi_R}{6}$$

$$\frac{\psi_{n,L} + \psi_{n,R}}{2} + \tau_n \frac{2\psi_{n,L} + \psi_{1,R}}{6} = \tau_n \frac{c}{2} \frac{2\phi_L + \phi_R}{6} + \frac{\psi_{n,R}}{f}$$

$$\mu_n < 0:$$

$$\frac{\psi_{n,L} - \psi_{n,R}}{2} + \tau_n \frac{2\psi_{n,L} + \psi_{n,R}}{6} = \tau_n \frac{c}{2} \frac{2\phi_L + \phi_R}{6}$$

$$\frac{\psi_{n,L} + \psi_{n,R}}{2} + \tau_n \frac{\psi_{n,L} + 2\psi_{n,R}}{6} = \tau_n \frac{c}{2} \frac{\phi_L + 2\phi_R}{6} + f\psi_{n,L}$$

where

$$\tau = \frac{\Delta x \sigma}{|\mu_n|}, \phi = \sum_{n=1}^{N_p} w_n \psi_n, \sum_{n=1}^{N_p} w_n = 2$$

We normalize the angle-shape functions:

$$\sum_{n=1}^{N_p} w_n a_n = \sum_{n=1}^{N_p} w_n b_n = \frac{2}{c}$$

and decompose each unknown as a Power series with respect to the cell thickness:

$$a_n = \sum_{k=0}^{\infty} a_n^{(k)} \Delta x^k, b_n = \sum_{k=0}^{\infty} b_n^{(k)} \Delta x^k, z = \sum_{k=0}^{\infty} z^{(k)} \Delta x^k = \sum_{k=0}^{\infty} \tilde{z}^{(k)} \left( \frac{\Delta x \sigma}{\nu} \right)^k, f = \sum_{k=0}^{\infty} f^{(k)} \Delta x^k = \sum_{k=0}^{\infty} \tilde{f}^{(k)} \left( \frac{\Delta x \sigma}{\nu} \right)^k$$

### Summary of Results

Our analysis yields the following power expansions to each Case-mode component. The single-cell attenuation factor abides to the expansion:

$$f = \tilde{f}^{(0)} + \frac{\tilde{f}^{(1)}}{\nu} (\sigma_t \Delta x) + \frac{1}{2} \frac{\tilde{f}^{(1)} \tilde{f}^{(1)}}{\nu^2} (\sigma_t \Delta x)^2 + \frac{1}{6} \frac{\tilde{f}^{(1)} \tilde{f}^{(1)} \tilde{f}^{(1)}}{\nu^3} (\sigma_t \Delta x)^3 + \sum_{k=4}^{\infty} \tilde{f}^{(k)} \left( \frac{\Delta x \sigma_t}{\nu} \right)^k$$

$$f = 1 - \frac{\sigma_t \Delta x}{\nu} + \frac{1}{2} \left( \frac{\sigma_t \Delta x}{\nu} \right)^2 - \frac{1}{6} \left( \frac{\sigma_t \Delta x}{\nu} \right)^3 + \sum_{k=4}^{\infty} \tilde{f}^{(k)} \left( \frac{\Delta x \sigma_t}{\nu} \right)^k$$

Within-cell attenuation factor:

$$z = \tilde{f}^{(0)} + \frac{\tilde{f}^{(1)}}{\nu} \sigma_t \Delta x + \frac{1}{2} \frac{\tilde{f}^{(1)} \tilde{f}^{(1)}}{\nu^2} (\sigma_t \Delta x)^2 \left[ 1 + \frac{c}{6} \left( \sum_{\mu_n > 0} w_n a_n^{(0)} - \sum_{\mu_n < 0} w_n a_n^{(0)} \right) \right] + \sum_{k=3}^{\infty} \tilde{z}^{(k)} \left( \frac{\Delta x \sigma_t}{\nu} \right)^k$$

$$z = 1 - \frac{\sigma_t \Delta x}{\nu} + \frac{1}{2} \left( \frac{\sigma_t \Delta x}{\nu} \right)^2 \left[ 1 + \frac{c}{6} \left( \sum_{\mu_n > 0} w_n a_n^{(0)} - \sum_{\mu_n < 0} w_n a_n^{(0)} \right) \right] + \sum_{k=3}^{\infty} \tilde{z}^{(k)} \left( \frac{\Delta x \sigma_t}{\nu} \right)^k$$

Left-node angle-shape function:

$$\mu_n > 0: a_n = a_n^{(0)} + a_n^{(2)} \Delta x^2 + \sum_{k=3}^{\infty} a_n^{(k)} \Delta x^k = \frac{\nu}{\tilde{f}^{(1)}} \left[ 1 - \frac{c}{12} \frac{\tilde{f}^{(1)} \tilde{f}^{(1)}}{\nu^2} (\sigma_t \Delta x)^2 \left( \sum_{\mu_n < 0} w_n a_n^{(0)} \right) \right] + \sum_{k=3}^{\infty} a_n^{(k)} \Delta x^k$$

$$a_n = \frac{\nu}{\nu - |\mu_n|} \left[ 1 - \frac{c}{12} \sum_{\mu_n < 0} w_n a_n^{(0)} \left( \frac{\sigma_t \Delta x}{\nu} \right)^2 \right] + \sum_{k=3}^{\infty} a_n^{(k)} \Delta x^k$$

$$\mu_n < 0: a_n = a_n^{(0)} + a_n^{(2)} \Delta x^2 + \sum_{k=3}^{\infty} a_n^{(k)} \Delta x^k$$

$$a_n = \frac{\nu}{\tilde{f}^{(1)}} \left[ 1 + \frac{c}{12} \frac{\tilde{f}^{(1)} \tilde{f}^{(1)}}{\nu^2} (\sigma_t \Delta x)^2 \left( \sum_{\mu_n > 0} w_n a_n^{(0)} \right) \right] + \sum_{k=3}^{\infty} a_n^{(k)} \Delta x^k$$

$$a_n = \frac{\nu}{\nu + |\mu_n|} \left[ 1 + \frac{c}{12} \sum_{\mu_n > 0} w_n a_n^{(0)} \left( \frac{\sigma_t \Delta x}{\nu} \right)^2 \right] + \sum_{k=3}^{\infty} a_n^{(k)} \Delta x^k$$

With the following normalization relations:

$$\sum_{n=1}^{Np} w_n a_n^{(k)} = \begin{cases} \frac{2}{c} : k = 0 \\ 0 : k > 0 \end{cases}$$

Right-node angle-shape function:

$$\mu_n > 0 : b_n = b_n^{(0)} + b_n^{(2)} \Delta x^2 + \sum_{k=3}^{\infty} b_n^{(k)} \Delta x^k$$

$$b_n = a_n^{(0)} + \left[ -\frac{c}{12} \frac{\tilde{f}^{(1)} \tilde{f}^{(1)}}{\nu^2} a_n^{(0)} \sum_{\mu_n > 0} w_n a_n^{(0)} + \frac{1}{6} \frac{\tilde{f}^{(1)}}{\nu} \frac{1 - a_n^{(0)}}{|\mu_n|} \right] (\sigma_t \Delta x)^2 + \sum_{k=3}^{\infty} a_n^{(k)} \Delta x^k$$

$$b_n = a_n^{(0)} + \tilde{f}^{(1)} \tilde{f}^{(1)} \frac{c}{12} \left[ -a_n^{(0)} \sum_{\mu_n > 0} w_n a_n^{(0)} + \frac{2}{c} \frac{\nu}{\tilde{f}^{(1)} |\mu_n|} \frac{\nu - |\mu_n| - \nu}{\nu - |\mu_n|} \right] \left( \frac{\sigma_t \Delta x}{\nu} \right)^2 + \sum_{k=3}^{\infty} a_n^{(k)} \Delta x^k$$

$$b_n = \frac{\nu}{\nu - |\mu_n|} \left\{ 1 - \frac{c}{12} \left[ \sum_{\mu_n > 0} w_n a_n^{(0)} - \sum_{\mu_n > 0} w_n a_n^{(0)} - \sum_{\mu_n < 0} w_n a_n^{(0)} \right] \left( \frac{\sigma_t \Delta x}{\nu} \right)^2 \right\} + \sum_{k=3}^{\infty} a_n^{(k)} \Delta x^k$$

$$b_n = \frac{\nu}{\nu - |\mu_n|} \left\{ 1 + \frac{c}{12} \sum_{\mu_n < 0} w_n a_n^{(0)} \left( \frac{\sigma_t \Delta x}{\nu} \right)^2 \right\} + \sum_{k=3}^{\infty} a_n^{(k)} \Delta x^k$$

$$\mu_n < 0 : b_n = b_n^{(0)} + b_n^{(2)} \Delta x^2 + \sum_{k=3}^{\infty} b_n^{(k)} \Delta x^k$$

$$b_n = a_n^{(0)} + \left[ \frac{c}{12} \frac{\tilde{f}^{(1)} \tilde{f}^{(1)}}{\nu^2} a_n^{(0)} \sum_{\mu_n < 0} w_n a_n^{(0)} + \frac{1}{6} \frac{\tilde{f}^{(1)}}{\nu} \frac{1 - a_n^{(0)}}{|\mu_n|} \right] (\sigma_t \Delta x)^2 + \sum_{k=3}^{\infty} a_n^{(k)} \Delta x^k$$

$$b_n = a_n^{(0)} + \tilde{f}^{(1)} \tilde{f}^{(1)} \frac{c}{12} \left[ a_n^{(0)} \sum_{\mu_n < 0} w_n a_n^{(0)} + \frac{2}{c} \frac{\nu}{\tilde{f}^{(1)} |\mu_n|} \frac{\nu + |\mu_n| - \nu}{\nu + |\mu_n|} \right] \left( \frac{\sigma_t \Delta x}{\nu} \right)^2 + \sum_{k=3}^{\infty} a_n^{(k)} \Delta x^k$$

$$b_n = a_n^{(0)} \left\{ 1 + \frac{c}{12} \left[ \sum_{\mu_n < 0} w_n a_n^{(0)} - \sum_{\mu_n > 0} w_n a_n^{(0)} - \sum_{\mu_n < 0} w_n a_n^{(0)} \right] \left( \frac{\sigma_t \Delta x}{\nu} \right)^2 \right\} + \sum_{k=3}^{\infty} a_n^{(k)} \Delta x^k$$

$$b_n = \frac{\nu}{\nu + |\mu_n|} \left\{ 1 - \frac{c}{12} \sum_{\mu_n > 0} w_n a_n^{(0)} \left( \frac{\sigma_t \Delta x}{\nu} \right)^2 \right\} + \sum_{k=3}^{\infty} a_n^{(k)} \Delta x^k$$

With the following normalization relations:

$$\sum_{n=1}^{Np} w_n b_n^{(k)} = \begin{cases} \frac{2}{c} : k = 0 \\ 0 : k > 0 \end{cases}$$

Analysis

### Zero Order Terms

$\mu_n > 0$ :

$$\left(\frac{-\psi_{n,L} + \psi_{n,R}}{2}\right)^{(0)} = 0 \Rightarrow (1) \boxed{\frac{-a_n^{(0)} f^{(0)} + b_n^{(0)} z^{(0)} f^{(0)}}{2} = 0}$$

$$\left(\frac{\psi_{n,L} + \psi_{n,R}}{2}\right)^{(0)} = \left(\frac{\psi_{n,R}}{f}\right)^{(0)} \Rightarrow (2) \boxed{\frac{a_n^{(0)} f^{(0)} + b_n^{(0)} z^{(0)} f^{(0)}}{2} = b_n^{(0)} z^{(0)}}$$

$\mu_n < 0$ :

$$\left(\frac{\psi_{n,L} - \psi_{n,R}}{2}\right)^{(0)} = 0 \Rightarrow (3) \boxed{\frac{-a_n^{(0)} f^{(0)} + b_n^{(0)} z^{(0)} f^{(0)}}{2} = 0}$$

$$\left(\frac{\psi_{n,L} + \psi_{n,R}}{2}\right)^{(0)} = f(\psi_{n,L})^{(0)} \Rightarrow (4) \boxed{\frac{a_n^{(0)} f^{(0)} + b_n^{(0)} z^{(0)} f^{(0)}}{2} = a_n^{(0)} f^{(0)} f^{(0)}}$$

Add (1)+(3):

$$\frac{-f^{(0)} \sum_{n=1}^{N_p} w_n a_n^{(0)} + z^{(0)} f^{(0)} \sum_{n=1}^{N_p} w_n b_n^{(0)}}{2} = 0$$

$$\Rightarrow \frac{-f^{(0)} + z^{(0)} f^{(0)}}{c} = 0 \Rightarrow f^{(0)} (1 - z^{(0)}) = 0 \Rightarrow z^{(0)} = 1$$

$$\therefore f^{(0)} = 1 \Rightarrow \tilde{f}^{(0)} = 1, z^{(0)} = 1 \Rightarrow \tilde{z}^{(0)} = 1$$

Replace  $z^{(0)}$  into (1),(3):

$$\mu_n > 0: \frac{-a_n^{(0)} f^{(0)} + b_n^{(0)} f^{(0)}}{2} = 0 \Rightarrow a_n^{(0)} = b_n^{(0)}$$

$$\mu_n < 0: \frac{-a_n^{(0)} f^{(0)} + b_n^{(0)} f^{(0)}}{2} = 0 \Rightarrow a_n^{(0)} = b_n^{(0)}$$

Replace  $a_n^{(0)} = b_n^{(0)}$  (for any  $\mu_n$ ),  $z^{(0)} = 1, (2) + (4)$ :

### First Order Terms

$\mu_n > 0$ :

$$\left( \frac{-\psi_{n,L} + \psi_{n,R}}{2} \right)^{(1)} + \tau_n \left( \frac{\psi_{n,L} + 2\psi_{1,R}}{6} \right)^{(0)} = \tau_n \left( \frac{c}{2} \frac{\phi_L + 2\phi_R}{6} \right)^{(0)}$$

$$\left\{ \begin{array}{l} \left[ \frac{-a_n^{(0)} f^{(1)} - a_n^{(1)} f^{(0)} + b_n^{(0)} z^{(0)} f^{(1)}}{2} \right. \\ \left. + \frac{b_n^{(0)} z^{(1)} f^{(0)} + b_n^{(1)} z^{(0)} f^{(0)}}{2} \right] \\ + \frac{\sigma_t}{|\mu|} \left[ \frac{a_n^{(0)} f^{(0)} + 2b_n^{(0)} z^{(0)} f^{(0)}}{6} \right] \end{array} \right\} = \frac{\sigma_t c}{|\mu| 2} \left[ \frac{f^{(0)} \sum_{m=1}^{Np} w_m a_n^{(0)} + 2z^{(0)} f^{(0)} \sum_{m=1}^{Np} w_m b_n^{(0)}}{6} \right]$$

$$\left\{ -a_n^{(1)} \frac{f^{(0)}}{2} + b_n^{(1)} \frac{z^{(0)} f^{(0)}}{2} \right\} = \left\{ \begin{array}{l} a_n^{(0)} \frac{f^{(1)}}{2} - b_n^{(0)} \frac{z^{(0)} f^{(1)} + z^{(1)} f^{(0)}}{2} \\ + \frac{\sigma_t}{|\mu|} \left[ \frac{f^{(0)} (1 - a_n^{(0)}) + 2z^{(0)} f^{(0)} (1 - b_n^{(0)})}{6} \right] \end{array} \right\}$$

Insert the definition of  $z^{(0)}$ ,  $f^{(0)}$ ,  $a_n^{(0)}$ ,  $b_n^{(0)}$ :

$$(1) \quad \boxed{-a_n^{(1)} + b_n^{(1)} = -a_n^{(0)} z^{(1)} + \frac{\sigma_t}{|\mu_n|} (1 - a_n^{(0)})}$$

$$\left( \frac{\psi_{n,L} + \psi_{n,R}}{2} \right)^{(1)} + \tau_n \left( \frac{2\psi_{n,L} + \psi_{1,R}}{6} \right)^{(0)} = \tau_n \left( \frac{c}{2} \frac{2\phi_L + \phi_R}{6} \right)^{(0)} + \left( \frac{\psi_{n,R}}{f} \right)^{(1)}$$

$$\left\{ \begin{array}{l} \left[ \frac{a_n^{(0)} f^{(1)} + a_n^{(1)} f^{(0)}}{2} \right. \\ \left. + \frac{b_n^{(0)} z^{(0)} f^{(1)} + b_n^{(0)} z^{(1)} f^{(0)} + b_n^{(1)} z^{(0)} f^{(0)}}{2} \right] \\ + \frac{\sigma_t}{|\mu_n|} \left[ \frac{2a_n^{(0)} f^{(0)} + b_n^{(0)} z^{(0)} f^{(0)}}{6} \right] \end{array} \right\} = \left\{ \begin{array}{l} \frac{\sigma_t c}{|\mu_n| 2} \left[ \frac{2f^{(0)} \sum_{m=1}^{Np} w_m a_n^{(0)} + z^{(0)} f^{(0)} \sum_{m=1}^{Np} w_m b_n^{(0)}}{6} \right] \\ + \left[ b_n^{(0)} z^{(1)} + b_n^{(1)} z^{(0)} \right] \end{array} \right\}$$

$$\left. \begin{aligned} & \left[ \frac{a_n^{(0)} f^{(1)} + a_n^{(1)} f^{(0)}}{2} \right. \\ & \left. + \frac{\sigma_t}{|\mu_n|} \frac{2a_n^{(0)} f^{(0)} + b_n^{(0)} z^{(0)} f^{(0)}}{6} \right] \\ & = \left. \begin{aligned} & \frac{\sigma_t}{|\mu_n|} \frac{c}{2} \frac{2f^{(0)} \sum_{m=1}^{Np} w_m a_n^{(0)} + z^{(0)} f^{(0)} \sum_{m=1}^{Np} w_m b_n^{(0)}}{6} \right. \\ & \left. + \left[ b_n^{(0)} z^{(1)} + b_n^{(1)} z^{(0)} \right] \right\} \\ & a_n^{(1)} \frac{f^{(0)}}{2} - b_n^{(1)} \frac{z^{(0)} (2 - f^{(0)})}{2} = \left. \begin{aligned} & -a_n^{(0)} \frac{f^{(1)}}{2} + b_n^{(0)} \frac{z^{(1)} (2 - f^{(0)})}{2} - b_n^{(0)} \frac{z^{(0)} f^{(1)}}{2} \right. \\ & \left. + \frac{\sigma_t}{|\mu_n|} \frac{2f^{(0)} (1 - a_n^{(0)}) + z^{(0)} f^{(0)} (1 - b_n^{(0)})}{6} \right\} \end{aligned} \right.
\end{aligned}$$

Insert the definition of  $z^{(0)}$ ,  $f^{(0)}$ ,  $a_n^{(0)}$ ,  $b_n^{(0)}$ :

$$a_n^{(1)} - b_n^{(1)} = \left\{ \begin{aligned} & -2a_n^{(0)} f^{(1)} + a_n^{(0)} z^{(1)} \\ & + \frac{\sigma_t}{|\mu_n|} (1 - a_n^{(0)}) \end{aligned} \right\}$$

$$(2) \quad \boxed{a_n^{(1)} - b_n^{(1)} = -2a_n^{(0)} f^{(1)} + a_n^{(0)} z^{(1)} + \frac{\sigma_t}{|\mu_n|} (1 - a_n^{(0)})}$$

$\mu_n < 0$ :

$$\left( \frac{\psi_{n,L} - \psi_{n,R}}{2} \right)^{(1)} + \tau_n \left( \frac{2\psi_{n,L} + \psi_{n,R}}{6} \right)^{(0)} = \tau_n \left( \frac{c}{2} \frac{2\phi_L + \phi_R}{6} \right)^{(0)}$$

$$\left. \begin{aligned} & \frac{(a_n^{(0)} f^{(1)} + a_n^{(1)} f^{(0)}) - (b_n^{(0)} z^{(0)} f^{(1)} + b_n^{(0)} z^{(1)} f^{(0)} + b_n^{(1)} z^{(0)} f^{(0)})}{2} \right. \\ & \left. + \frac{\sigma}{|\mu_n|} \frac{2(a_n^{(0)} f^{(0)}) + (b_n^{(0)} z^{(0)} f^{(0)})}{6} \right\}
\end{aligned}$$

$$\begin{aligned}
&= \frac{\sigma}{|\mu_n|} \frac{c}{2} \frac{\left\{ 2f^{(0)} \sum_{n=1}^{Np} w_n a_n^{(0)} + z^{(0)} f^{(0)} \sum_{n=1}^{Np} w_n b_n^{(0)} \right\}}{6} \\
(a_n^{(1)} - b_n^{(1)}) \frac{f^{(0)}}{2} &= \left\{ \begin{aligned} & -a_n^{(0)} \frac{f^{(1)}}{2} + b_n^{(0)} \frac{z^{(0)} f^{(1)} + z^{(1)} f^{(0)}}{2} \\ & \frac{\sigma}{|\mu_n|} \left[ 2f^{(0)} \frac{1-a_n^{(0)}}{6} + z^{(0)} f^{(0)} \frac{1-b_n^{(0)}}{6} \right] \end{aligned} \right\}
\end{aligned}$$

Insert the definition of  $z^{(0)}$ ,  $f^{(0)}$ ,  $a_n^{(0)}$ ,  $b_n^{(0)}$ :

$$\begin{aligned}
(3) \quad & \boxed{a_n^{(1)} - b_n^{(1)} = a_n^{(0)} z^{(1)} + \frac{\sigma}{|\mu_n|} (1 - a_n^{(0)})} \\
& \left( \frac{\psi_{n,L} + \psi_{n,R}}{2} \right)^{(1)} + \tau_n \left( \frac{\psi_{n,L} + 2\psi_{n,R}}{6} \right)^{(0)} = \tau_n \left( \frac{c \phi_L + 2\phi_R}{2 \cdot 6} \right)^{(0)} + (f\psi_{n,L})^{(1)} \\
& \left\{ \begin{aligned} & \frac{\left( a_n^{(0)} f^{(1)} + a_n^{(1)} f^{(0)} \right) + \left( b_n^{(0)} z^{(0)} f^{(1)} + b_n^{(0)} z^{(1)} f^{(0)} + b_n^{(1)} z^{(0)} f^{(0)} \right)}{2} \\ & + \frac{\sigma_t a_n^{(0)} f^{(0)} + 2b_n^{(0)} z^{(0)} f^{(0)}}{6} \end{aligned} \right\} \\
& = \left\{ \begin{aligned} & \frac{\sigma_t c}{|\mu_n|} \frac{f^{(0)} \sum_{n=1}^{Np} w_n a_n^{(0)} + 2z^{(0)} f^{(0)} \sum_{n=1}^{Np} w_n b_n^{(0)}}{6} \\ & + 2a_n^{(0)} f^{(0)} f^{(1)} + a_n^{(1)} f^{(0)} f^{(0)} \end{aligned} \right\} \\
a_n^{(1)} \left( \frac{f^{(0)}}{2} - f^{(0)} f^{(0)} \right) + b_n^{(1)} \frac{z^{(0)} f^{(0)}}{2} &= \left\{ \begin{aligned} & a_n^{(0)} f^{(1)} \left( -\frac{1}{2} + 2f^{(0)} \right) - b_n^{(0)} \left( \frac{z^{(0)} f^{(1)} + z^{(1)} f^{(0)}}{2} \right) \\ & + \frac{\sigma_t}{|\mu_n|} \left[ \frac{f^{(0)} (1 - a_n^{(0)}) + 2z^{(0)} f^{(0)} (1 - b_n^{(0)})}{6} \right] \end{aligned} \right\}
\end{aligned}$$

Insert the definition of  $z^{(0)}$ ,  $f^{(0)}$ ,  $a_n^{(0)}$ ,  $b_n^{(0)}$ :

$$(4) \quad \boxed{a_n^{(1)} - b_n^{(1)} = -2a_n^{(0)} f^{(1)} + a_n^{(0)} z^{(1)} - \frac{\sigma_t}{|\mu_n|} (1 - a_n^{(0)})}$$

Add (1)+(3) over all angles:

$$\sum_{n=1}^{Np} w_n \left( -a_n^{(1)} + b_n^{(1)} \right) = -z^{(1)} \sum_{n=1}^{Np} w_n a_n^{(0)} + \sigma_t \left[ \sum_{n=1}^{Np} \frac{w_n}{\mu_n} (1 - a_n^{(0)}) \right]$$

$$\Rightarrow z^{(1)} \sum_{n=1}^{Np} w_n a_n^{(0)} = -\sigma_t \sum_{n=1}^{Np} \frac{w_n}{\mu_n} a_n^{(0)}$$

$$\boxed{z^{(1)} = -\frac{c}{2} \sigma_t \sum_{n=1}^{Np} \frac{w_n}{\mu_n} a_n^{(0)}}$$

Add (2)+(4) over all angles:

$$\sum_{n=1}^{Np} w_n \left( a_n^{(1)} - b_n^{(1)} \right) = -2f^{(1)} \sum_{n=1}^{Np} w_n a_n^{(0)} + z^{(1)} \sum_{n=1}^{Np} w_n a_n^{(0)} + \sigma_t \sum_{n=1}^{Np} \frac{w_n}{\mu_n} (\lambda - a_n^{(0)})$$

$$0 = -2f^{(1)} \sum_{n=1}^{Np} w_n a_n^{(0)} + z^{(1)} \sum_{n=1}^{Np} w_n a_n^{(0)} + \sigma_t \sum_{n=1}^{Np} \frac{w_n}{\mu_n} (\lambda - a_n^{(0)})$$

$$\Rightarrow 2f^{(1)} \frac{2}{c} = z^{(1)} \frac{2}{c} - \sigma_t \sum_{n=1}^{Np} \frac{w_n}{\mu_n} a_n^{(0)} \Rightarrow \boxed{f^{(1)} = -\frac{c}{2} \sigma_t \sum_{n=1}^{Np} \frac{w_n}{\mu_n} a_n^{(0)} = z^{(1)}}$$

(1)+(2):

$$0 = -a_n^{(0)} f^{(1)} + \frac{\sigma_t}{|\mu_n|} (1 - a_n^{(0)}) \Rightarrow a_n^{(0)} \frac{f^{(1)}}{|\mu_n|} \left( |\mu_n| + \frac{\sigma_t}{f^{(1)}} \right) = \frac{\sigma_t}{|\mu_n|}$$

$$\Rightarrow \boxed{a_n^{(0)} = b_n^{(0)} = \frac{\frac{\sigma_t}{f^{(1)}}}{\frac{\sigma_t}{f^{(1)}} + |\mu_n|} \quad \forall \mu_n > 0}$$

$$a_n^{(0)} = b_n^{(0)} = \frac{\frac{\cancel{\sigma_t}}{\tilde{f}^{(1)} \cancel{\sigma_t}}}{\frac{\cancel{\sigma_t}}{\tilde{f}^{(1)} \cancel{\sigma_t}} + |\mu_n|} = \frac{\frac{v}{\tilde{f}^{(1)}}}{\frac{v}{\tilde{f}^{(1)}} + |\mu_n|} \quad \forall \mu_n > 0$$

(3)-(4):

$$a_n^{(0)} f^{(1)} = -\frac{\sigma_t}{|\mu_n|} (1 - a_n^{(0)}) \Rightarrow a_n^{(0)} \left( -\frac{f^{(1)} |\mu_n|}{\sigma_t} + 1 \right) = 1 \Rightarrow a_n^{(0)} = b_n^{(0)} = \frac{\frac{\sigma_t}{f^{(1)}}}{\frac{\sigma_t}{f^{(1)}} - |\mu_n|} \quad \forall \mu_n < 0$$

$$(1) - (2), (3) + (4) \Rightarrow a_n^{(1)} = b_n^{(1)}$$

From which we derive the equivalent dispersion equation:

$$\sum_{n=1}^{Np} \frac{w_n}{\mu_n} a_n^{(0)} = -2 \frac{f^{(1)}}{\sigma_t} \Rightarrow \sum_{\mu_n > 0}^{Np} w_n \frac{\left( \frac{\sigma_t}{f^{(1)}} \right)^2}{\left( \frac{\sigma_t}{f^{(1)}} \right)^2 - |\mu_n|^2} \Rightarrow 1 = \frac{c}{2} \sum_{\mu_n > 0}^{Np} w_n \left[ \frac{\left( \frac{\sigma_t}{f^{(1)}} \right)}{\left( \frac{\sigma_t}{f^{(1)}} \right) - |\mu_n|} + \frac{\left( \frac{\sigma_t}{f^{(1)}} \right)}{\left( \frac{\sigma_t}{f^{(1)}} \right) + |\mu_n|} \right]$$

$$1 = \frac{c}{2} \sum_{n=1}^{Np} w_n a_n^{(0)}$$

## Second Order Terms

$\mu_n > 0$ :

$$\left( \frac{-\psi_{n,L} + \psi_{n,R}}{2} \right)^{(2)} + \tau_n \left( \frac{2\psi_{n,L} + \psi_{n,R}}{6} \right)^{(1)} = \tau_n \left( \frac{c}{2} \frac{\phi_L + 2\phi_R}{6} \right)^{(1)}$$

$$\left( \frac{-\psi_{n,L} + \psi_{n,R}}{2} \right)^{(2)}$$

$$= \Delta x^2 \frac{\left[ -\left( a_n^{(0)} f^{(2)} + a_n^{(1)} f^{(1)} + a_n^{(2)} f^{(0)} \right) + \left( b_n^{(0)} z^{(0)} f^{(2)} + b_n^{(0)} z^{(1)} f^{(1)} + b_n^{(1)} z^{(0)} f^{(1)} \right) + \left( b_n^{(0)} z^{(2)} f^{(0)} + b_n^{(1)} z^{(1)} f^{(0)} + b_n^{(2)} z^{(0)} f^{(0)} \right) \right]}{2}$$

$$\left( \frac{-\psi_{n,L} + \psi_{n,R}}{2} \right)^{(2)}$$

$$= \Delta x^2 \frac{\left[ -\left( a_n^{(0)} f^{(2)} + a_n^{(1)} f^{(1)} + a_n^{(2)} f^{(0)} \right) + \left( a_n^{(0)} f^{(0)} f^{(2)} + a_n^{(0)} f^{(1)} f^{(1)} + a_n^{(1)} f^{(0)} f^{(1)} \right) + \left( a_n^{(0)} z^{(2)} f^{(0)} + a_n^{(1)} f^{(1)} f^{(0)} + b_n^{(2)} f^{(0)} f^{(0)} \right) \right]}{2}$$

$$\begin{aligned}
& \left( \frac{-\psi_{n,L} + \psi_{n,R}}{2} \right)^{(2)} \\
&= \Delta x^2 \frac{\left[ -\left( \cancel{a_n^{(0)} f^{(2)}} + \cancel{a_n^{(1)} f^{(1)}} + a_n^{(2)} \right) + \left( \cancel{a_n^{(0)} f^{(2)}} + a_n^{(0)} f^{(1)} f^{(1)} + \cancel{a_n^{(1)} f^{(1)}} \right) \right]}{2} \\
& \left( \frac{-\psi_{n,L} + \psi_{n,R}}{2} \right)^{(2)} = \Delta x^2 \frac{\left[ \begin{array}{l} -a_n^{(2)} + a_n^{(0)} f^{(1)} f^{(1)} + a_n^{(0)} z^{(2)} f^{(0)} \\ + a_n^{(1)} f^{(1)} + b_n^{(2)} \end{array} \right]}{2} \\
\tau_n \left( \frac{\psi_{n,L} + 2\psi_{n,R}}{6} \right)^{(1)} &= \frac{\Delta x^2 \sigma_t}{|\mu_n|} \left( \frac{a_n^{(0)} f^{(1)} + a_n^{(1)} f^{(0)} + 2b_n^{(0)} z^{(0)} f^{(1)} + 2b_n^{(0)} z^{(1)} f^{(0)} + 2b_n^{(1)} z^{(0)} f^{(0)}}{6} \right) \\
\tau_n \left( \frac{\psi_{n,L} + 2\psi_{n,R}}{6} \right)^{(1)} &= \frac{\Delta x^2 \sigma_t}{|\mu_n|} \left( \frac{a_n^{(0)} f^{(1)} + a_n^{(1)} f^{(0)} + 2a_n^{(0)} f^{(0)} f^{(1)} + 2a_n^{(0)} f^{(1)} f^{(0)} + 2a_n^{(1)} f^{(0)} f^{(0)}}{6} \right) \\
\tau_n \left( \frac{\psi_{n,L} + 2\psi_{n,R}}{6} \right)^{(1)} &= \frac{\Delta x^2 \sigma_t}{|\mu_n|} \left( \frac{5a_n^{(0)} f^{(1)} + 3a_n^{(1)}}{6} \right) \\
\tau_n \left( \frac{c \phi_L + 2\phi_R}{2 \cdot 6} \right)^{(1)} &= \frac{\Delta x^2 \sigma_t}{|\mu_n|} \frac{c}{2} \frac{\left[ \begin{array}{l} f^{(1)} \sum_{n=1}^{Np} w_n a_n^{(0)} + f^{(0)} \sum_{n=1}^{Np} \cancel{w_n a_n^{(1)}} \\ + 2 \left( z^{(0)} f^{(1)} + z^{(1)} f^{(0)} \right) \sum_{n=1}^{Np} w_n b_n^{(0)} + 2z^{(0)} f^{(0)} \sum_{n=1}^{Np} \cancel{w_n b_n^{(1)}} \end{array} \right]}{6} \\
\tau_n \left( \frac{c \phi_L + 2\phi_R}{2 \cdot 6} \right)^{(1)} &= \frac{\Delta x^2 \sigma_t}{|\mu_n|} \frac{c}{2} \frac{f^{(1)} \left( \frac{2}{c} \right) + 2 \left( f^{(0)} f^{(1)} + f^{(1)} f^{(0)} \right) \left( \frac{2}{c} \right)}{6} = \frac{\Delta x^2 \sigma_t}{|\mu_n|} \frac{5}{6} f^{(1)}
\end{aligned}$$

Grouping all terms:

$$\begin{aligned}
& \left[ \frac{-a_n^{(2)} + a_n^{(0)} f^{(1)} f^{(1)} + a_n^{(0)} z^{(2)}}{2} + \frac{\sigma_t}{|\mu_n|} \left( \frac{5}{6} a_n^{(0)} f^{(1)} + \frac{1}{2} a_n^{(1)} \right) = \frac{\sigma_t}{|\mu_n|} \frac{5}{6} f^{(1)} \right. \\
& \left. \left( \frac{\psi_{n,L} + \psi_{n,R}}{2} \right)^{(2)} - \left( \frac{\psi_{n,R}}{f} \right)^{(2)} + \tau_n \left( \frac{2\psi_{n,L} + \psi_{n,R}}{6} \right)^{(1)} = \tau_n \left( \frac{c}{2} \frac{2\phi_L + \phi_R}{6} \right)^{(1)} \right. \\
& \left. \left( \frac{\psi_{n,L} + \psi_{n,R}}{2} \right)^{(2)} - \left( \frac{\psi_{n,R}}{f} \right)^{(2)} = \left\{ \begin{array}{l} \Delta x^2 \left[ \frac{a_n^{(0)} f^{(2)} + a_n^{(1)} f^{(1)} + a_n^{(2)} f^{(0)} + b_n^{(0)} z^{(0)} f^{(2)} + b_n^{(0)} z^{(1)} f^{(1)} + b_n^{(1)} z^{(0)} f^{(1)} + b_n^{(0)} z^{(2)} f^{(0)} + b_n^{(1)} z^{(1)} f^{(0)} + b_n^{(2)} z^{(0)} f^{(0)} \right]}{2} \\ -\Delta x^2 \left( b_n^{(0)} z^{(2)} + b_n^{(1)} z^{(1)} + b_n^{(2)} z^{(0)} \right) \end{array} \right\} \\
& \left( \frac{\psi_{n,L} + \psi_{n,R}}{2} \right)^{(2)} - \left( \frac{\psi_{n,R}}{f} \right)^{(2)} = \left\{ \begin{array}{l} \Delta x^2 \left[ \frac{a_n^{(0)} f^{(2)} + a_n^{(1)} f^{(1)} + a_n^{(2)} f^{(0)} + a_n^{(0)} f^{(0)} f^{(2)} + a_n^{(0)} f^{(1)} f^{(1)} + a_n^{(1)} f^{(0)} f^{(1)} + a_n^{(0)} z^{(2)} f^{(0)} + a_n^{(1)} f^{(1)} f^{(0)} + b_n^{(2)} f^{(0)} f^{(0)} \right]}{2} \\ -\Delta x^2 \left( a_n^{(0)} z^{(2)} + a_n^{(1)} f^{(1)} + b_n^{(2)} f^{(0)} \right) \end{array} \right\} \\
& \left( \frac{\psi_{n,L} + \psi_{n,R}}{2} \right)^{(2)} - \left( \frac{\psi_{n,R}}{f} \right)^{(2)} \\
& \quad = \Delta x^2 \left\{ a_n^{(0)} \left[ \frac{1}{2} f^{(1)} f^{(1)} - \frac{1}{2} z^{(2)} + f^{(2)} \right] + a_n^{(1)} \left[ \frac{1}{2} f^{(1)} \right] + a_n^{(2)} \frac{1}{2} - b_n^{(2)} \frac{1}{2} \right\} \\
& \tau_n \left( \frac{2\psi_{n,L} + \psi_{n,R}}{6} \right)^{(1)} = \frac{\Delta x \sigma_t}{|\mu_n|} \left( \frac{2a_n^{(0)} f^{(1)} + 2a_n^{(1)} f^{(0)} + b_n^{(0)} z^{(0)} f^{(1)} + b_n^{(0)} z^{(1)} f^{(0)} + b_n^{(1)} z^{(0)} f^{(0)} \right) \\
& \tau_n \left( \frac{2\psi_{n,L} + \psi_{n,R}}{6} \right)^{(1)} \\
& \quad = \frac{\Delta x \sigma_t}{|\mu_n|} \left( \frac{2a_n^{(0)} f^{(1)} + 2a_n^{(1)} f^{(0)} + a_n^{(0)} f^{(0)} f^{(1)} + a_n^{(0)} f^{(1)} f^{(0)} + a_n^{(1)} f^{(0)} f^{(0)} \right)
\end{aligned}$$

$$\tau_n \left( \frac{2\psi_{n,L} + \psi_{n,R}}{6} \right)^{(1)} = \frac{\Delta x^2 \sigma_t}{|\mu_n|} \left( \frac{4a_n^{(0)} f^{(1)} + 3a_n^{(1)}}{6} \right)$$

$$\tau_n \left( \frac{c}{2} \frac{2\phi_L + \phi_R}{6} \right)^{(1)} = \frac{\Delta x^2 \sigma_t c}{|\mu_n|} \frac{2}{6} \left[ \begin{array}{l} 2f^{(1)} \sum_{n=1}^{Np} w_n a_n^{(0)} + 2f^{(0)} \sum_{n=1}^{Np} w_n a_n^{(1)} \\ + (z^{(0)} f^{(1)} + z^{(1)} f^{(0)}) \sum_{n=1}^{Np} w_n b_n^{(0)} + z^{(0)} f^{(0)} \sum_{n=1}^{Np} w_n b_n^{(1)} \end{array} \right]$$

$$\tau_n \left( \frac{c}{2} \frac{2\phi_L + \phi_R}{6} \right)^{(1)} = \frac{\Delta x^2 \sigma_t c}{|\mu_n|} \frac{2}{6} \left[ 2f^{(1)} \left( \frac{2}{c} \right) + (f^{(0)} f^{(1)} + f^{(1)} f^{(0)}) \left( \frac{2}{c} \right) \right] = \frac{\Delta x^2 \sigma_t}{|\mu_n|} f^{(1)} \frac{2}{3}$$

Grouping all terms:

$$\left\{ a_n^{(0)} \left[ \frac{1}{2} f^{(1)} f^{(1)} - \frac{1}{2} z^{(2)} + f^{(2)} \right] + a_n^{(1)} \left[ \frac{1}{2} f^{(1)} \right] + a_n^{(2)} \frac{1}{2} - b_n^{(2)} \frac{1}{2} \right\} + \frac{\sigma_t}{|\mu_n|} \left( \frac{4a_n^{(0)} f^{(1)} + 3a_n^{(1)}}{6} \right)$$

$$= \frac{\sigma_t}{|\mu_n|} f^{(1)} \frac{2}{3}$$

$$(2) a_n^{(2)} \frac{1}{2} - b_n^{(2)} \frac{1}{2}$$

$$= \frac{\sigma_t}{|\mu_n|} \left[ \frac{2}{3} f^{(1)} (1 - a_n^{(0)}) - \frac{1}{2} a_n^{(1)} \right] - a_n^{(0)} \left[ \frac{1}{2} f^{(1)} f^{(1)} - \frac{1}{2} z^{(2)} + f^{(2)} \right] - a_n^{(1)} \left[ \frac{1}{2} f^{(1)} \right]$$

$\mu_n > 0$ :

$$\left( \frac{\psi_{n,L} - \psi_{n,R}}{2} \right)^{(2)} + \tau_n \left( \frac{2\psi_{n,L} + \psi_{n,R}}{6} \right)^{(1)} = \tau_n \left( \frac{c}{2} \frac{2\phi_L + \phi_R}{6} \right)^{(1)}$$

$$\left( \frac{\psi_{n,L} - \psi_{n,R}}{2} \right)^{(2)}$$

$$= \Delta x^2 \frac{\left[ \left( a_n^{(0)} f^{(2)} + a_n^{(1)} f^{(1)} + a_n^{(2)} f^{(0)} \right) - \left( b_n^{(0)} z^{(0)} f^{(2)} + b_n^{(0)} z^{(1)} f^{(1)} + b_n^{(1)} z^{(0)} f^{(1)} + b_n^{(0)} z^{(2)} f^{(0)} + b_n^{(1)} z^{(1)} f^{(0)} + b_n^{(2)} z^{(0)} f^{(0)} \right) \right]}{2}$$

$$\left(\frac{\psi_{n,L} - \psi_{n,R}}{2}\right)^{(2)} = \Delta x^2 \frac{\left[ \left( a_n^{(0)} f^{(2)} + a_n^{(1)} f^{(1)} + a_n^{(2)} f^{(0)} \right) - \left( a_n^{(0)} f^{(0)} f^{(2)} + a_n^{(0)} f^{(1)} f^{(1)} + a_n^{(1)} f^{(0)} f^{(1)} + a_n^{(0)} z^{(2)} f^{(0)} + a_n^{(1)} f^{(1)} f^{(0)} + b_n^{(2)} f^{(0)} f^{(0)} \right) \right]}{2}$$

$$\left(\frac{\psi_{n,L} - \psi_{n,R}}{2}\right)^{(2)} = \Delta x^2 \frac{\left[ -a_n^{(0)} \left( f^{(1)} f^{(1)} + z^{(2)} \right) - a_n^{(1)} \left( f^{(1)} \right) + a_n^{(2)} - b_n^{(2)} \right]}{2}$$

Grouping all terms:

$$\frac{\left[ -a_n^{(0)} \left( f^{(1)} f^{(1)} + z^{(2)} \right) - a_n^{(1)} \left( f^{(1)} \right) + a_n^{(2)} - b_n^{(2)} \right]}{2} + \frac{\sigma_t}{|\mu_n|} \left( \frac{4a_n^{(0)} f^{(1)} + 3a_n^{(1)}}{6} \right) = \frac{\sigma_t}{|\mu_n|} f^{(1)} \frac{2}{3}$$

$$(3) \quad \frac{1}{2} a_n^{(2)} - \frac{1}{2} b_n^{(2)} = \frac{\sigma_t}{|\mu_n|} \left[ \frac{2}{3} f^{(1)} \left( 1 - a_n^{(0)} \right) - \frac{1}{2} a_n^{(1)} \right] + \frac{1}{2} a_n^{(0)} \left( f^{(1)} f^{(1)} + z^{(2)} \right) + \frac{1}{2} a_n^{(1)} \left( f^{(1)} \right)$$

$$\left(\frac{\psi_{n,L} + \psi_{n,R}}{2}\right)^{(2)} + \tau_n \left(\frac{\psi_{n,L} + 2\psi_{n,R}}{6}\right)^{(1)} = \tau_n \left(\frac{c \phi_L + 2\phi_R}{2 \cdot 6}\right)^{(1)} + (f\psi_{n,L})^{(2)}$$

$$\left(\frac{\psi_{n,L} + \psi_{n,R}}{2}\right)^{(2)} - (f\psi_{n,L})^{(2)} = \left\{ \begin{array}{l} \Delta x^2 \frac{\left[ \begin{array}{l} a_n^{(0)} f^{(2)} + a_n^{(1)} f^{(1)} + a_n^{(2)} f^{(0)} \\ + a_n^{(0)} f^{(0)} f^{(2)} + a_n^{(0)} f^{(1)} f^{(1)} + a_n^{(1)} f^{(0)} f^{(1)} \\ + a_n^{(0)} z^{(2)} f^{(0)} + a_n^{(1)} f^{(1)} f^{(0)} + b_n^{(2)} f^{(0)} f^{(0)} \end{array} \right]}{2} \\ -\Delta x^2 \left( \begin{array}{l} 2a_n^{(0)} f^{(0)} f^{(2)} + a_n^{(0)} f^{(1)} f^{(1)} \\ + a_n^{(1)} f^{(0)} f^{(1)} + a_n^{(1)} f^{(1)} f^{(0)} \\ + a_n^{(2)} f^{(0)} f^{(0)} \end{array} \right) \end{array} \right\}$$

$$\left(\frac{\Psi_{n,L} + \Psi_{n,R}}{2}\right)^{(2)} - (f\Psi_{n,L})^{(2)} = \left\{ \begin{array}{l} \Delta x^2 \frac{\left[ \begin{array}{l} a_n^{(0)} f^{(2)} + a_n^{(1)} f^{(1)} + a_n^{(2)} f^{(0)} \\ + a_n^{(0)} f^{(0)} f^{(2)} + a_n^{(0)} f^{(1)} f^{(1)} + a_n^{(1)} f^{(0)} f^{(1)} \\ + a_n^{(0)} z^{(2)} f^{(0)} + a_n^{(1)} f^{(1)} f^{(0)} + b_n^{(2)} f^{(0)} f^{(0)} \end{array} \right]}{2} \\ -\Delta x^2 \left( \begin{array}{l} 2a_n^{(0)} f^{(0)} f^{(2)} + a_n^{(0)} f^{(1)} f^{(1)} \\ + 2a_n^{(1)} f^{(0)} f^{(1)} + a_n^{(2)} f^{(0)} f^{(0)} \end{array} \right) \end{array} \right\}$$

$$\left(\frac{\Psi_{n,L} + \Psi_{n,R}}{2}\right)^{(2)} - (f\Psi_{n,L})^{(2)} = \Delta x^2 \left[ a_n^{(0)} \left( -f^{(2)} - \frac{1}{2} f^{(1)} f^{(1)} + \frac{1}{2} z^{(2)} \right) + a_n^{(1)} \left( -\frac{1}{2} f^{(1)} \right) - \frac{1}{2} a_n^{(2)} + \frac{1}{2} b_n^{(2)} \right]$$

Grouping all terms:

$$a_n^{(0)} \left( \frac{-f^{(1)} f^{(1)} + z^{(2)}}{2} - f^{(2)} \right) - a_n^{(1)} \left( \frac{f^{(1)}}{2} \right) - \frac{1}{2} a_n^{(2)} + \frac{1}{2} b_n^{(2)} + \frac{\sigma_t}{|\mu_n|} \left( \frac{5a_n^{(0)} f^{(1)} + 3a_n^{(1)}}{6} \right) = \frac{\sigma_t}{|\mu_n|} \frac{5}{6} f^{(1)}$$

$$(4) - \frac{1}{2} a_n^{(2)} + \frac{1}{2} b_n^{(2)} = \frac{\sigma_t}{|\mu_n|} \left[ \frac{5}{6} f^{(1)} (1 - a_n^{(0)}) - \frac{1}{2} a_n^{(1)} \right] - a_n^{(0)} \left( \frac{-f^{(1)} f^{(1)} + z^{(2)}}{2} - f^{(2)} \right) + a_n^{(1)} \left( \frac{f^{(1)}}{2} \right)$$

(1) + (4) over all angles:

$$(5) \frac{1}{c} z^{(2)} = \left\{ \begin{array}{l} -\frac{1}{2} f^{(1)} f^{(1)} \left( \sum_{\mu_n > 0} w_n a_n^{(0)} - \sum_{\mu_n < 0} w_n a_n^{(0)} \right) + f^{(2)} \sum_{\mu_n < 0} w_n a_n^{(0)} \\ -\frac{f^{(1)}}{2} \left( \sum_{\mu_n > 0} w_n a_n^{(0)} - \sum_{\mu_n < 0} w_n a_n^{(0)} \right) + \sum_{n=1}^{S_n} w_n \frac{\sigma_t}{|\mu_n|} \left[ \frac{5}{6} f^{(1)} (1 - a_n^{(0)}) - \frac{1}{2} a_n^{(1)} \right] \end{array} \right\}$$

(2) + (3) over all angles:

$$(6) - z^{(2)} \frac{1}{c} = \left\{ \begin{array}{l} \sum_{n=1}^{S_n} w_n \frac{\sigma_t}{|\mu_n|} \left[ \frac{2}{3} f^{(1)} (1 - a_n^{(0)}) - \frac{1}{2} a_n^{(1)} \right] - \frac{f^{(1)} f^{(1)}}{2} \left( \sum_{\mu_n > 0} w_n a_n^{(0)} - \sum_{\mu_n < 0} w_n a_n^{(0)} \right) \\ -f^{(2)} \left( \sum_{\mu_n > 0} w_n a_n^{(0)} \right) - \frac{1}{2} f^{(1)} \left( \sum_{\mu_n > 0} w_n a_n^{(1)} - \sum_{\mu_n < 0} w_n a_n^{(1)} \right) \end{array} \right\}$$

$$(5) - (6) : z^{(2)} - f^{(2)} = \frac{c}{12} \sum_{n=1}^{S_n} w_n \frac{\sigma_t}{|\mu_n|} \left[ f^{(1)} (1 - a_n^{(0)}) \right]$$

(5) + (6) :

$$0 = \left\{ \begin{array}{l} \left( -f^{(1)} f^{(1)} - f^{(2)} \right) \left( \sum_{\mu_n > 0} w_n a_n^{(0)} - \sum_{\mu_n < 0} w_n a_n^{(0)} \right) - \frac{1}{2} f^{(1)} \left( \sum_{\mu_n > 0} w_n a_n^{(1)} - \sum_{\mu_n < 0} w_n a_n^{(1)} \right) \\ \sum_{n=1}^{S_n} w_n \frac{\sigma_t}{|\mu_n|} \left[ \frac{4+5}{6} f^{(1)} (1 - a_n^{(0)}) - a_n^{(1)} \right] \end{array} \right\}$$

Solve for  $\sum_{n=1}^{S_n} w_n \frac{\sigma_t}{|\mu_n|} a_n^{(1)}$  :

(1) + (2) :

$$a_n^{(1)} \left[ \frac{\sigma_t}{|\mu_n|} + f^{(1)} \right] = \frac{3}{2} \frac{\sigma_t}{|\mu_n|} f^{(1)} (1 - a_n^{(0)}) - a_n^{(0)} f^{(1)} \left[ f^{(1)} + \frac{f^{(2)}}{f^{(1)}} \right]$$

$$a_n^{(1)} f^{(1)} \left[ \frac{\frac{\sigma_t}{f^{(1)}} + |\mu_n|}{|\mu_n|} \right] = \frac{3}{2} \frac{\sigma_t}{|\mu_n|} f^{(1)} (1 - a_n^{(0)}) - a_n^{(0)} f^{(1)} \left[ f^{(1)} + \frac{f^{(2)}}{f^{(1)}} \right]$$

$$a_n^{(1)} = \frac{3}{2} \frac{\sigma_t}{|\mu_n|} \left( \frac{1}{a_n^{(0)}} - 1 \right) - \left[ f^{(1)} + \frac{f^{(2)}}{f^{(1)}} \right] \Rightarrow \sum_{\mu_n > 0} w_n a_n^{(1)} = \frac{3}{2} f^{(1)} - \left[ f^{(1)} + \frac{f^{(2)}}{f^{(1)}} \right]$$

$$\sum_{\mu_n > 0} w_n \frac{a_n^{(1)}}{|\mu_n|} = \left[ \frac{3}{2} f^{(1)} - \left[ f^{(1)} + \frac{f^{(2)}}{f^{(1)}} \right] \right] \sum_{\mu_n > 0} w_n \frac{1}{|\mu_n|}$$

(3) + (4) :

$$0 = \frac{\sigma_t}{|\mu_n|} \left[ \frac{3}{2} f^{(1)} (1 - a_n^{(0)}) - a_n^{(1)} \right] + a_n^{(0)} (f^{(1)} f^{(1)} + f^{(2)}) + a_n^{(1)} f^{(1)}$$

$$a_n^{(1)} \left[ \frac{\frac{\sigma_t}{f^{(1)}} - |\mu_n|}{|\mu_n|} \right] = \frac{3}{2} \frac{\sigma_t}{|\mu_n|} (1 - a_n^{(0)}) + a_n^{(0)} \left( f^{(1)} + \frac{f^{(2)}}{f^{(1)}} \right)$$

$$a_n^{(1)} = \frac{3}{2} \frac{\sigma_t}{|\mu_n|} \left( \frac{-|\mu_n|}{\frac{\sigma_t}{f^{(1)}}} \right) + \left( f^{(1)} + \frac{f^{(2)}}{f^{(1)}} \right) \Rightarrow \sum_{\mu_n < 0} w_n a_n^{(1)} = -\frac{3}{2} f^{(1)} + \left( f^{(1)} + \frac{f^{(2)}}{f^{(1)}} \right)$$

$$\sum_{\mu_n < 0} w_n \frac{a_n^{(1)}}{|\mu_n|} = \left[ -\frac{3}{2} f^{(1)} + \left( f^{(1)} + \frac{f^{(2)}}{f^{(1)}} \right) \right] \sum_{\mu_n < 0} w_n \frac{1}{|\mu_n|}$$

$$\therefore \left( \sum_{\mu_n > 0} w_n a_n^{(1)} - \sum_{\mu_n < 0} w_n a_n^{(1)} \right) = f^{(1)} - 2 \frac{f^{(2)}}{f^{(1)}}, \sum_{n=1}^{s_n} w_n \frac{a_n^{(1)}}{|\mu_n|} = 0$$

$$z^{(2)} - f^{(2)} = -\frac{c}{6} f^{(1)} \sigma_t \left\{ \sum_{\mu_n > 0} w_n \frac{|\mu_n|}{\left( \frac{\sigma_t}{f^{(1)}} \right)^2 - |\mu_n|^2} \right\}$$

$$z^{(2)} - f^{(2)} = \frac{c}{12} [f^{(1)}]^2 \left\{ -2 \frac{\sigma_t}{f^{(1)}} \sum_{\mu_n > 0} w_n \frac{|\mu_n|}{\left[ \frac{\sigma_t}{f^{(0)}} \right]^2 - |\mu_n|^2} \right\} \quad (5) + (6):$$

$$\Rightarrow \left\{ \sum_{\mu_n > 0} w_n a_n^{(0)} - \sum_{\mu_n < 0} w_n a_n^{(0)} \right\} = \frac{12}{c} \frac{z^{(2)} - f^{(2)}}{[f^{(1)}]^2}$$

$$0 = \left\{ \begin{aligned} & \left( -f^{(1)} f^{(1)} - f^{(2)} \right) \left( \sum_{\mu_n > 0} w_n a_n^{(0)} - \sum_{\mu_n < 0} w_n a_n^{(0)} \right) - \frac{1}{2} f^{(1)} \left( \sum_{\mu_n > 0} w_n a_n^{(1)} - \sum_{\mu_n < 0} w_n a_n^{(1)} \right) \\ & \left[ \sum_{n=1}^{s_n} w_n \frac{\sigma_t}{|\mu_n|} \left[ \frac{4+5}{6} f^{(1)} (1 - a_n^{(0)}) - a_n^{(1)} \right] \right] \end{aligned} \right\}$$

$$\begin{aligned}
0 &= \left\{ \begin{aligned} &\left(-f^{(1)} f^{(1)} - f^{(2)}\right) \left( \frac{12}{c} \frac{z^{(2)} - f^{(2)}}{[f^{(1)}]^2} \right) - \left( \frac{1}{2} f^{(1)} f^{(1)} - f^{(2)} \right) \\ &\sum_{n=1}^{S_n} w_n \frac{\sigma_t}{|\mu_n|} \left[ \frac{4+5}{6} f^{(1)} (1 - a_n^{(0)}) \right] \end{aligned} \right\} \\
0 &= \left\{ \begin{aligned} &\left(-f^{(1)} f^{(1)} - f^{(2)}\right) \left( \frac{12}{c} \frac{z^{(2)} - f^{(2)}}{[f^{(1)}]^2} \right) - \left( \frac{1}{2} f^{(1)} f^{(1)} - f^{(2)} \right) \\ &\frac{3}{2} f^{(1)} \sigma_t \sum_{\mu_n > 0} w_n \left( \frac{1}{\frac{\sigma_t}{f^{(1)}} + |\mu_n|} - \frac{1}{\frac{\sigma_t}{f^{(1)}} - |\mu_n|} \right) \end{aligned} \right\} \\
0 &= \left\{ \begin{aligned} &\left(-f^{(1)} f^{(1)} - f^{(2)}\right) \left( \frac{12}{c} \frac{z^{(2)} - f^{(2)}}{[f^{(1)}]^2} \right) - \left( \frac{1}{2} f^{(1)} f^{(1)} - f^{(2)} \right) \\ &-3 f^{(1)} \sigma_t \sum_{\mu_n > 0} w_n \left( \frac{|\mu_n|}{\left( \frac{\sigma_t}{f^{(1)}} \right)^2 - |\mu_n|^2} \right) \end{aligned} \right\} \\
0 &= \left\{ \begin{aligned} &\left( \frac{-f^{(1)} f^{(1)} - f^{(2)}}{f^{(1)} f^{(1)}} \right) \frac{12}{c} (z^{(2)} - f^{(2)}) - \left( \frac{1}{2} f^{(1)} f^{(1)} - f^{(2)} \right) \\ &+ \frac{18}{c} (z^{(2)} - f^{(2)}) \end{aligned} \right\} \\
0 &= \left( \frac{-2 f^{(1)} f^{(1)} - 2 f^{(2)} + 3 f^{(1)} f^{(1)}}{2 f^{(1)} f^{(1)}} \right) \frac{12}{c} (z^{(2)} - f^{(2)}) - \left( \frac{1}{2} f^{(1)} f^{(1)} - f^{(2)} \right) \\
0 &= \left( \frac{1}{2} f^{(1)} f^{(1)} - f^{(2)} \right) \frac{1}{f^{(1)} f^{(1)}} \frac{12}{c} (z^{(2)} - f^{(2)}) - \left( \frac{1}{2} f^{(1)} f^{(1)} - f^{(2)} \right) \\
0 &= \left( \frac{1}{2} f^{(1)} f^{(1)} - f^{(2)} \right) \left[ \frac{12}{c} (z^{(2)} - f^{(2)}) - f^{(1)} f^{(1)} \right] \left( \frac{1}{f^{(1)} f^{(1)}} \right)
\end{aligned}$$

Two possibilities:

$$f^{(2)} = \frac{1}{2} f^{(1)} f^{(1)}, z^{(2)} - f^{(2)} = \frac{c}{12} f^{(1)} f^{(1)}$$

Assume the second one is correct:

$$(5)-(6): z^{(2)} - f^{(2)} = \frac{c}{12} \sum_{n=1}^{S_n} w_n \frac{\sigma_t}{|\mu_n|} \left[ f^{(1)} (1 - a_n^{(0)}) \right] = \frac{c}{12} f^{(1)} f^{(1)}$$

$$\Rightarrow \sum_{n=1}^{S_n} w_n \frac{\sigma_t}{|\mu_n|} (1 - a_n^{(0)}) \neq f^{(1)}$$

$$\text{Untrue since: } f^{(1)} = -\frac{c}{2} \sigma_t \sum_{n=1}^{N_p} \frac{w_n}{\mu_n} a_n^{(0)} .$$

$$f^{(2)} = \frac{1}{2} f^{(1)} f^{(1)} \therefore \boxed{f^{(2)} = \frac{1}{2} f^{(1)} f^{(1)}}$$

Get  $z^{(2)}$  from (5)-(6):

$$(5)-(6): z^{(2)} = \frac{1}{2} f^{(1)} f^{(1)} + \frac{c}{12} \sum_{n=1}^{S_n} w_n \frac{\sigma_t}{|\mu_n|} \left[ f^{(1)} (1 - a_n^{(0)}) \right]$$

$$z^{(2)} = \frac{1}{2} f^{(1)} f^{(1)} + \frac{c}{12} f^{(1)} \sigma_t \left[ \begin{array}{l} \sum_{\mu_n > 0} w_n \frac{1}{|\mu_n|} \left( \frac{\frac{\sigma_t}{f^{(1)}} - |\mu_n| - \frac{\sigma_t}{f^{(1)}}}{\frac{\sigma_t}{f^{(1)}} - |\mu_n|} \right) \\ + \sum_{\mu_n < 0} w_n \frac{1}{|\mu_n|} \left( \frac{\frac{\sigma_t}{f^{(1)}} + |\mu_n| - \frac{\sigma_t}{f^{(1)}}}{\frac{\sigma_t}{f^{(1)}} + |\mu_n|} \right) \end{array} \right]$$

$$z^{(2)} = \frac{1}{2} f^{(1)} f^{(1)} + \frac{c}{12} f^{(1)} f^{(1)} \left[ - \sum_{\mu_n > 0} w_n \frac{\frac{\sigma_t}{f^{(1)}}}{\frac{\sigma_t}{f^{(1)}} - |\mu_n|} + \sum_{\mu_n < 0} w_n \frac{\frac{\sigma_t}{f^{(1)}}}{\frac{\sigma_t}{f^{(1)}} + |\mu_n|} \right]$$

$$\boxed{z^{(2)} = \frac{1}{2} f^{(1)} f^{(1)} + \frac{c}{12} f^{(1)} f^{(1)} \left[ \sum_{\mu_n > 0} w_n a_n^{(0)} - \sum_{\mu_n < 0} w_n a_n^{(0)} \right]}$$

Solve for  $a_n^{(1)}$ :

$$(1)+(2): a_n^{(1)} \left[ \frac{\sigma_t}{|\mu_n|} + f^{(1)} \right] = \frac{3}{2} \frac{\sigma_t}{|\mu_n|} f^{(1)} (1 - a_n^{(0)}) - a_n^{(0)} f^{(1)} \left[ f^{(1)} + \frac{f^{(2)}}{f^{(1)}} \right]$$

$$a_n^{(1)} = \frac{|\mu_n|}{\left( \frac{\sigma_t}{f^{(1)}} + |\mu_n| \right)^2} \left\{ \frac{1}{2} \sigma_t - \sigma_t \frac{f^{(2)}}{f^{(1)} f^{(1)}} \right\} \Rightarrow a_n^{(1)} = \frac{|\mu_n|}{\left( \frac{\sigma_t}{f^{(1)}} + |\mu_n| \right)^2} \left\{ \frac{1}{2} \sigma_t - \frac{1}{2} \sigma_t \right\}$$

$$\therefore \mu_n > 0: \boxed{a_n^{(1)} = 0}$$

(3)+(4):

$$a_n^{(1)} \left[ \frac{\frac{\sigma_t}{f^{(1)}} - |\mu_n|}{|\mu_n|} \right] = \frac{3}{2} \frac{\sigma_t}{|\mu_n|} (1 - a_n^{(0)}) + a_n^{(0)} \left( f^{(1)} + \frac{f^{(2)}}{f^{(1)}} \right)$$

$$a_n^{(1)} \left[ \frac{\frac{\sigma_t}{f^{(1)}} - |\mu_n|}{|\mu_n|} \right] = \frac{3}{2} \frac{\sigma_t}{|\mu_n|} \left( \frac{-|\mu_n|}{\frac{\sigma_t}{f^{(1)}} - |\mu_n|} \right) + \left( \frac{\frac{\sigma_t}{f^{(1)}}}{\frac{\sigma_t}{f^{(1)}} - |\mu_n|} \right) \left( f^{(1)} + \frac{f^{(2)}}{f^{(1)}} \right)$$

$$a_n^{(1)} = \frac{\sigma_t |\mu_n|}{\left( \frac{\sigma_t}{f^{(1)}} - |\mu_n| \right)^2} \left[ -\frac{3}{2} + 1 + \frac{f^{(2)}}{f^{(1)} f^{(1)}} \right] \Rightarrow a_n^{(1)} = \frac{\sigma_t |\mu_n|}{\left( \frac{\sigma_t}{f^{(1)}} - |\mu_n| \right)^2} \left[ -\frac{1}{2} + \frac{1}{2} \right]$$

$$\therefore \mu_n > 0: \boxed{a_n^{(1)} = 0}$$

(1)-(2):

$$-a_n^{(2)} + b_n^{(2)} = \frac{\sigma_t}{|\mu_n|} \left[ \frac{1}{6} f^{(1)} (1 - a_n^{(0)}) \right] + a_n^{(0)} (f^{(2)} - z^{(2)}) \Rightarrow \boxed{a_n^{(2)} \neq b_n^{(2)}}$$

(3)-(4):

$$-a_n^{(2)} + b_n^{(2)} = \frac{\sigma_t}{|\mu_n|} \left[ \frac{1}{6} f^{(1)} (1 - a_n^{(0)}) \right] + a_n^{(0)} (f^{(2)} - z^{(2)}) \Rightarrow \boxed{a_n^{(2)} \neq b_n^{(2)}}$$

### Third Order Terms

$\mu_n > 0$ :

$$\left(\frac{-\psi_{n,L} + \psi_{n,R}}{2}\right)^{(3)} + \tau_n \left(\frac{\psi_{n,L} + 2\psi_{n,R}}{6}\right)^{(2)} = \tau_n \left(\frac{c\phi_L + 2\phi_R}{2 \cdot 6}\right)^{(2)}$$

$$\left(\frac{-\psi_{n,L} + \psi_{n,R}}{2}\right)^{(3)} = \frac{\left[ \begin{aligned} & -a_n^{(0)} f^{(3)} - a_n^{(1)} f^{(2)} - a_n^{(2)} f^{(1)} - a_n^{(3)} f^{(0)} + b_n^{(0)} z^{(0)} f^{(3)} + b_n^{(0)} z^{(3)} f^{(0)} + b_n^{(3)} z^{(0)} f^{(0)} \\ & + b_n^{(0)} z^{(1)} f^{(2)} + b_n^{(1)} z^{(0)} f^{(2)} + b_n^{(0)} z^{(2)} f^{(1)} + b_n^{(1)} z^{(2)} f^{(0)} + b_n^{(2)} z^{(0)} f^{(1)} + b_n^{(2)} z^{(1)} f^{(0)} \\ & + b_n^{(1)} z^{(1)} f^{(1)} \end{aligned} \right]}{2}$$

$$\left(\frac{-\psi_{n,L} + \psi_{n,R}}{2}\right)^{(3)} = \frac{\left[ \begin{aligned} & -a_n^{(0)} f^{(3)} - a_n^{(1)} f^{(2)} - a_n^{(2)} f^{(1)} - a_n^{(3)} f^{(0)} + a_n^{(0)} f^{(0)} f^{(3)} + a_n^{(0)} z^{(3)} f^{(0)} + b_n^{(3)} f^{(0)} f^{(0)} \\ & + a_n^{(0)} f^{(1)} f^{(2)} + a_n^{(1)} f^{(0)} f^{(2)} + a_n^{(0)} z^{(2)} f^{(1)} + a_n^{(1)} z^{(2)} f^{(0)} + b_n^{(2)} f^{(0)} f^{(1)} + b_n^{(2)} f^{(1)} f^{(0)} \\ & + a_n^{(1)} f^{(1)} f^{(1)} \end{aligned} \right]}{2}$$

$$\left(\frac{-\psi_{n,L} + \psi_{n,R}}{2}\right)^{(3)} = \frac{\left[ \begin{aligned} & -a_n^{(0)} f^{(3)} - a_n^{(2)} f^{(1)} - a_n^{(3)} + a_n^{(0)} f^{(3)} + a_n^{(0)} z^{(3)} + b_n^{(3)} \\ & + a_n^{(0)} f^{(1)} f^{(2)} + a_n^{(0)} z^{(2)} f^{(1)} + b_n^{(2)} f^{(1)} + b_n^{(2)} f^{(1)} \end{aligned} \right]}{2}$$

$$\left(\frac{-\psi_{n,L} + \psi_{n,R}}{2}\right)^{(3)} = \frac{1}{2} a_n^{(0)} \left( z^{(3)} + f^{(1)} f^{(2)} + z^{(2)} f^{(1)} \right) - \frac{1}{2} a_n^{(2)} f^{(1)} - \frac{1}{2} a_n^{(3)} + b_n^{(2)} f^{(1)} + \frac{1}{2} b_n^{(3)}$$

$$\left(\frac{\psi_{n,L} + 2\psi_{n,R}}{6}\right)^{(2)} = \frac{\left[ \begin{aligned} & a_n^{(0)} f^{(2)} + a_n^{(2)} f^{(0)} + a_n^{(1)} f^{(1)} \\ & + 2b_n^{(0)} z^{(0)} f^{(2)} + 2b_n^{(0)} z^{(2)} f^{(0)} + 2b_n^{(2)} z^{(0)} f^{(0)} \\ & + 2b_n^{(0)} z^{(1)} f^{(1)} + 2b_n^{(1)} z^{(0)} f^{(1)} + 2b_n^{(1)} z^{(1)} f^{(0)} \end{aligned} \right]}{6}$$

$$\left(\frac{\psi_{n,L} + 2\psi_{n,R}}{6}\right)^{(2)} = \frac{\begin{bmatrix} a_n^{(0)} f^{(2)} + a_n^{(2)} f^{(0)} + a_n^{(1)} f^{(1)} \\ + 2a_n^{(0)} f^{(0)} f^{(2)} + 2a_n^{(0)} z^{(2)} f^{(0)} + 2b_n^{(2)} z^{(0)} f^{(0)} \\ + 2a_n^{(0)} f^{(1)} f^{(1)} + 2a_n^{(1)} f^{(0)} f^{(1)} + 2a_n^{(1)} f^{(1)} f^{(0)} \end{bmatrix}}{6}$$

$$\left(\frac{\psi_{n,L} + 2\psi_{n,R}}{6}\right)^{(2)} = \frac{3a_n^{(0)} f^{(2)} + a_n^{(2)} + 2a_n^{(0)} z^{(2)} + 2b_n^{(2)} + 2a_n^{(0)} f^{(1)} f^{(1)}}{6}$$

$$\left(\frac{\psi_{n,L} + 2\psi_{n,R}}{6}\right)^{(2)} = \frac{1}{6} a_n^{(0)} \left[ 3f^{(2)} + 2z^{(2)} + 2f^{(1)} f^{(1)} \right] + \frac{1}{6} a_n^{(2)} + \frac{1}{3} b_n^{(2)}$$

$$\left(\frac{c \phi_L + 2\phi_R}{2 \cdot 6}\right)^{(2)} = \frac{c}{2} \frac{\begin{bmatrix} f^{(2)} \sum_{n=1}^{Np} w_n a_n^{(0)} + f^{(0)} \sum_{n=1}^{Np} w_n a_n^{(2)} + f^{(1)} \sum_{n=1}^{Np} w_n a_n^{(1)} \\ + 2z^{(0)} f^{(2)} \sum_{n=1}^{Np} w_n b_n^{(0)} + 2z^{(2)} f^{(0)} \sum_{n=1}^{Np} w_n b_n^{(0)} + 2z^{(0)} f^{(0)} \sum_{n=1}^{Np} w_n b_n^{(2)} \\ + 2z^{(1)} f^{(1)} \sum_{n=1}^{Np} w_n b_n^{(0)} + 2z^{(0)} f^{(1)} \sum_{n=1}^{Np} w_n b_n^{(1)} + 2z^{(1)} f^{(0)} \sum_{n=1}^{Np} w_n b_n^{(1)} \end{bmatrix}}{6}$$

$$\left(\frac{c \phi_L + 2\phi_R}{2 \cdot 6}\right)^{(2)} = \frac{c}{2} \frac{f^{(2)} \frac{2}{c} + 2f^{(0)} f^{(2)} \frac{2}{c} + 2z^{(2)} f^{(0)} \frac{2}{c} + 2f^{(1)} f^{(1)} \frac{2}{c}}{6}$$

$$\left(\frac{c \phi_L + 2\phi_R}{2 \cdot 6}\right)^{(2)} = \frac{3f^{(2)} + 2z^{(2)} + 2f^{(1)} f^{(1)}}{6}$$

Combining the three results:

$$\left\{ \begin{array}{l} \left\{ \frac{1}{2} a_n^{(0)} \left( z^{(3)} + f^{(1)} f^{(2)} + z^{(2)} f^{(1)} \right) \right. \\ \left. - \frac{1}{2} a_n^{(2)} f^{(1)} - \frac{1}{2} a_n^{(3)} + b_n^{(2)} f^{(1)} + \frac{1}{2} b_n^{(3)} \right\} \\ + \frac{\sigma_t}{|\mu_n|} \left\{ \frac{1}{6} a_n^{(0)} \left[ 3f^{(2)} + 2z^{(2)} + 2f^{(1)} f^{(1)} \right] \right. \\ \left. + \frac{1}{6} a_n^{(2)} + \frac{1}{3} b_n^{(2)} \right\} \end{array} \right\} = \frac{\sigma_t}{|\mu_n|} \left\{ \frac{3f^{(2)} + 2z^{(2)} + 2f^{(1)} f^{(1)}}{6} \right\}$$

$$(1) -\frac{1}{2}a_n^{(3)} + \frac{1}{2}b_n^{(3)} = \left\{ \begin{array}{l} \frac{\sigma_t}{|\mu_n|} \left[ \left( \frac{3f^{(2)} + 2z^{(2)} + 2f^{(1)}f^{(1)}}{6} \right) (1 - a_n^{(0)}) \right] \\ -\frac{1}{6}a_n^{(2)} - \frac{1}{3}b_n^{(2)} \\ -\frac{1}{2}a_n^{(0)} (z^{(3)} + f^{(1)}f^{(2)} + z^{(2)}f^{(1)}) + \frac{1}{2}a_n^{(2)}f^{(1)} - b_n^{(2)}f^{(1)} \end{array} \right\}$$

$$\left( \frac{\psi_{n,L} + \psi_{n,R}}{2} \right)^{(3)} - \left( \frac{\psi_{n,R}}{f} \right)^{(3)} + \tau_n \left( \frac{2\psi_{n,L} + \psi_{n,R}}{6} \right)^{(2)} = \tau_n \left( \frac{c}{2} \frac{2\phi_L + \phi_R}{6} \right)^{(2)}$$

$$\left( \frac{\psi_{n,L} + \psi_{n,R}}{2} \right)^{(3)} - \left( \frac{\psi_{n,R}}{f} \right)^{(3)} = \frac{\left[ \begin{array}{l} a_n^{(0)}f^{(3)} + a_n^{(1)}f^{(2)} + a_n^{(2)}f^{(1)} + a_n^{(3)}f^{(0)} \\ + b_n^{(0)}z^{(0)}f^{(3)} + b_n^{(0)}z^{(3)}f^{(0)} + b_n^{(3)}z^{(0)}f^{(0)} \\ + b_n^{(0)}z^{(1)}f^{(2)} + b_n^{(1)}z^{(0)}f^{(2)} + b_n^{(0)}z^{(2)}f^{(1)} \\ + b_n^{(1)}z^{(2)}f^{(0)} + b_n^{(2)}z^{(0)}f^{(1)} + b_n^{(2)}z^{(1)}f^{(0)} \end{array} \right]}{2} - \left[ \begin{array}{l} b_n^{(0)}z^{(3)} + b_n^{(1)}z^{(2)} \\ + b_n^{(2)}z^{(1)} + b_n^{(3)}z^{(0)} \end{array} \right]$$

$$\left( \frac{\psi_{n,L} + \psi_{n,R}}{2} \right)^{(3)} - \left( \frac{\psi_{n,R}}{f} \right)^{(3)} = \left\{ \begin{array}{l} \left[ \begin{array}{l} 2a_n^{(0)}f^{(3)} + a_n^{(2)}f^{(1)} + a_n^{(3)} + a_n^{(0)}z^{(3)} \\ + b_n^{(3)} + a_n^{(0)}f^{(1)}f^{(2)} + a_n^{(0)}z^{(2)}f^{(1)} \\ + 2b_n^{(2)}f^{(1)} \end{array} \right] \\ 2 \\ - \left[ a_n^{(0)}z^{(3)} + b_n^{(2)}f^{(1)} + b_n^{(3)} \right] \end{array} \right\}$$

$$\left( \frac{\psi_{n,L} + \psi_{n,R}}{2} \right)^{(3)} - \left( \frac{\psi_{n,R}}{f} \right)^{(3)} = \left[ \begin{array}{l} \frac{1}{2}a_n^{(0)} (2f^{(3)} - z^{(3)} + f^{(1)}f^{(2)} + z^{(2)}f^{(1)}) \\ + \frac{1}{2}a_n^{(2)}f^{(1)} + \frac{1}{2}a_n^{(3)} - \frac{1}{2}b_n^{(3)} \end{array} \right]$$

$$\left( \frac{2\psi_{n,L} + \psi_{n,R}}{6} \right)^{(2)} = \frac{\left[ \begin{array}{l} 2a_n^{(0)}f^{(2)} + 2a_n^{(2)}f^{(0)} + 2a_n^{(1)}f^{(1)} \\ + b_n^{(0)}z^{(0)}f^{(2)} + b_n^{(0)}z^{(2)}f^{(0)} + b_n^{(2)}z^{(0)}f^{(0)} \\ + b_n^{(0)}z^{(1)}f^{(1)} + b_n^{(1)}z^{(0)}f^{(1)} + b_n^{(1)}z^{(1)}f^{(0)} \end{array} \right]}{6}$$

$$\left(\frac{2\psi_{n,L} + \psi_{n,R}}{6}\right)^{(2)} = \frac{3a_n^{(0)}f^{(2)} + a_n^{(0)}z^{(2)} + a_n^{(0)}f^{(1)}f^{(1)} + 2a_n^{(2)} + b_n^{(2)}}{6}$$

$$\left(\frac{c}{2} \frac{2\phi_L + \phi_R}{6}\right) = \frac{3f^{(2)} + z^{(2)} + f^{(1)}f^{(1)}}{6}$$

Grouping all terms:

$$\left[ \begin{array}{l} \frac{1}{2}a_n^{(0)}(2f^{(3)} - z^{(3)} + f^{(1)}f^{(2)} + z^{(2)}f^{(1)}) \\ + \frac{1}{2}a_n^{(2)}f^{(1)} + \frac{1}{2}a_n^{(3)} - \frac{1}{2}b_n^{(3)} \end{array} \right] = \frac{\sigma_t}{|\mu_n|} \left[ \begin{array}{l} \left(\frac{3f^{(2)} + z^{(2)} + f^{(1)}f^{(1)}}{6}\right)(1 - a_n^{(0)}) \\ - \frac{2a_n^{(2)} + b_n^{(2)}}{6} \end{array} \right]$$

$$(2) \frac{1}{2}a_n^{(3)} - \frac{1}{2}b_n^{(3)} = \left\{ \begin{array}{l} \frac{\sigma_t}{|\mu_n|} \left[ \begin{array}{l} \left(\frac{3f^{(2)} + z^{(2)} + f^{(1)}f^{(1)}}{6}\right)(1 - a_n^{(0)}) \\ - \frac{2a_n^{(2)} + b_n^{(2)}}{6} \end{array} \right] \\ - \frac{1}{2}a_n^{(0)}(2f^{(3)} - z^{(3)} + f^{(1)}f^{(2)} + z^{(2)}f^{(1)}) - \frac{1}{2}a_n^{(2)}f^{(1)} \end{array} \right\}$$

$\mu_n < 0$ :

$$\left(\frac{\psi_{n,L} - \psi_{n,R}}{2}\right)^{(3)} + \tau_n \left(\frac{2\psi_{n,L} + \psi_{n,R}}{6}\right)^{(2)} = \tau_n \left(\frac{c}{2} \frac{2\phi_L + \phi_R}{6}\right)^{(2)}$$

$$\left(\frac{\psi_{n,L} - \psi_{n,R}}{2}\right)^{(3)}$$

$$= \frac{\left[ \begin{array}{l} a_n^{(0)}f^{(3)} + a_n^{(1)}f^{(2)} + a_n^{(2)}f^{(1)} + a_n^{(3)}f^{(0)} - b_n^{(0)}z^{(0)}f^{(3)} - b_n^{(0)}z^{(3)}f^{(0)} - b_n^{(3)}z^{(0)}f^{(0)} \\ - b_n^{(0)}z^{(1)}f^{(2)} - b_n^{(1)}z^{(0)}f^{(2)} - b_n^{(0)}z^{(2)}f^{(1)} - b_n^{(1)}z^{(2)}f^{(0)} - b_n^{(2)}z^{(0)}f^{(1)} - b_n^{(2)}z^{(1)}f^{(0)} \\ - b_n^{(1)}z^{(1)}f^{(1)} \end{array} \right]}{2}$$

$$\left(\frac{\psi_{n,L} - \psi_{n,R}}{2}\right)^{(3)}$$

$$\begin{aligned}
& \left[ \begin{array}{l} a_n^{(0)} f^{(3)} + a_n^{(1)} f^{(2)} + a_n^{(2)} f^{(1)} + a_n^{(3)} f^{(0)} - a_n^{(0)} f^{(0)} f^{(3)} - a_n^{(0)} z^{(3)} f^{(0)} - b_n^{(3)} f^{(0)} f^{(0)} \\ -a_n^{(0)} f^{(1)} f^{(2)} - a_n^{(1)} f^{(0)} f^{(2)} - a_n^{(0)} z^{(2)} f^{(1)} - a_n^{(1)} z^{(2)} f^{(0)} - b_n^{(2)} f^{(0)} f^{(1)} - b_n^{(2)} f^{(1)} f^{(0)} \\ -a_n^{(1)} f^{(1)} f^{(1)} \end{array} \right] \\
& = \frac{\quad}{2} \\
& \left( \frac{\psi_{n,L} - \psi_{n,R}}{2} \right)^{(3)} = \frac{\left[ \begin{array}{l} a_n^{(0)} f^{(3)} + a_n^{(2)} f^{(1)} + a_n^{(3)} - a_n^{(0)} f^{(3)} - a_n^{(0)} z^{(3)} - b_n^{(3)} \\ -a_n^{(0)} f^{(1)} f^{(2)} - a_n^{(0)} z^{(2)} f^{(1)} - b_n^{(2)} f^{(1)} - b_n^{(2)} f^{(1)} \end{array} \right]}{2} \\
& \left( \frac{\psi_{n,L} - \psi_{n,R}}{2} \right)^{(3)} = \left\{ \begin{array}{l} \frac{1}{2} a_n^{(0)} \left( -z^{(3)} - f^{(1)} f^{(2)} - z^{(2)} f^{(1)} \right) \\ + \frac{1}{2} a_n^{(2)} f^{(1)} + \frac{1}{2} a_n^{(3)} - b_n^{(2)} f^{(1)} - \frac{1}{2} b_n^{(3)} \end{array} \right\}
\end{aligned}$$

Grouping all terms:

$$(3) \frac{1}{2} a_n^{(3)} - \frac{1}{2} b_n^{(3)} = \left\{ \begin{array}{l} \frac{\sigma_t}{|\mu_n|} \left[ \frac{3f^{(2)} + z^{(2)} + f^{(1)} f^{(1)}}{6} \right] (1 - a_n^{(0)}) \\ -\frac{1}{3} a_n^{(2)} - \frac{1}{6} b_n^{(2)} \\ -\frac{1}{2} a_n^{(0)} \left( -z^{(3)} - f^{(1)} f^{(2)} - z^{(2)} f^{(1)} \right) - \frac{1}{2} a_n^{(2)} f^{(1)} + b_n^{(2)} f^{(1)} \end{array} \right\}$$

$$\left( \frac{\psi_{n,L} + \psi_{n,R}}{2} \right)^{(3)} + \tau_n \left( \frac{\psi_{n,L} + 2\psi_{n,R}}{6} \right)^{(2)} = \tau_n \left( \frac{c \phi_L + 2\phi_R}{2 \cdot 6} \right)^{(2)} + (f\psi_{n,L})^{(3)}$$

$$\left( \frac{\psi_{n,L} + \psi_{n,R}}{2} \right)^{(3)} - (f\psi_{n,L})^{(3)}$$

$$\begin{aligned}
& \left[ \begin{array}{l} a_n^{(0)} f^{(3)} + a_n^{(1)} f^{(2)} + a_n^{(2)} f^{(1)} + a_n^{(3)} f^{(0)} \\ + b_n^{(0)} z^{(0)} f^{(3)} + b_n^{(0)} z^{(3)} f^{(0)} + b_n^{(3)} z^{(0)} f^{(0)} \\ + b_n^{(0)} z^{(1)} f^{(2)} + b_n^{(1)} z^{(0)} f^{(2)} + b_n^{(0)} z^{(2)} f^{(1)} \\ + b_n^{(1)} z^{(2)} f^{(0)} + b_n^{(2)} z^{(0)} f^{(1)} + b_n^{(2)} z^{(1)} f^{(0)} \end{array} \right] \\
& = \frac{\quad}{2} - \left[ \begin{array}{l} 2a_n^{(0)} f^{(0)} f^{(3)} + a_n^{(3)} f^{(0)} f^{(0)} \\ + 2a_n^{(0)} f^{(1)} f^{(2)} + 2a_n^{(1)} f^{(0)} f^{(2)} \\ + 2a_n^{(2)} f^{(0)} f^{(1)} \end{array} \right]
\end{aligned}$$

$$\begin{aligned}
& \left( \frac{\Psi_{n,L} + \Psi_{n,R}}{2} \right)^{(3)} - (f\Psi_{n,L})^{(3)} \\
&= \frac{\begin{bmatrix} a_n^{(0)} f^{(3)} + a_n^{(1)} f^{(2)} + a_n^{(2)} f^{(1)} + a_n^{(3)} f^{(0)} \\ + a_n^{(0)} f^{(0)} f^{(3)} + a_n^{(0)} z^{(3)} f^{(0)} + b_n^{(3)} f^{(0)} f^{(0)} \\ + a_n^{(0)} f^{(1)} f^{(2)} + a_n^{(1)} z^{(0)} f^{(2)} + a_n^{(0)} z^{(2)} f^{(1)} \\ + a_n^{(1)} z^{(2)} f^{(0)} + b_n^{(2)} f^{(0)} f^{(1)} + b_n^{(2)} f^{(1)} f^{(0)} \end{bmatrix}}{2} - \begin{bmatrix} 2a_n^{(0)} f^{(0)} f^{(3)} + a_n^{(3)} f^{(0)} f^{(0)} \\ + 2a_n^{(0)} f^{(1)} f^{(2)} + 2a_n^{(1)} f^{(0)} f^{(2)} \\ + 2a_n^{(2)} f^{(0)} f^{(1)} \end{bmatrix} \\
& \left( \frac{\Psi_{n,L} + \Psi_{n,R}}{2} \right)^{(3)} - (f\Psi_{n,L})^{(3)} = \frac{\begin{bmatrix} a_n^{(0)} f^{(3)} + a_n^{(2)} f^{(1)} + a_n^{(3)} \\ + a_n^{(0)} f^{(3)} + a_n^{(0)} z^{(3)} + b_n^{(3)} \\ + a_n^{(0)} f^{(1)} f^{(2)} + a_n^{(0)} z^{(2)} f^{(1)} \\ + b_n^{(2)} f^{(1)} + b_n^{(2)} f^{(1)} \end{bmatrix}}{2} - \begin{bmatrix} 2a_n^{(0)} f^{(3)} + a_n^{(3)} \\ + 2a_n^{(0)} f^{(1)} f^{(2)} + 2a_n^{(2)} f^{(1)} \end{bmatrix} \\
& \left( \frac{\Psi_{n,L} + \Psi_{n,R}}{2} \right)^{(3)} - (f\Psi_{n,L})^{(3)} = \left\{ \begin{array}{l} \frac{1}{2} a_n^{(0)} \left( -2f^{(3)} - 3f^{(1)} f^{(2)} + z^{(2)} f^{(1)} + z^{(3)} \right) \\ -\frac{3}{2} a_n^{(2)} f^{(1)} - \frac{1}{2} a_n^{(3)} + b_n^{(2)} f^{(1)} + \frac{1}{2} b_n^{(3)} \end{array} \right\}
\end{aligned}$$

Grouping all the terms:

$$\left\{ \begin{array}{l} \frac{1}{2} a_n^{(0)} \left( -2f^{(3)} - 3f^{(1)} f^{(2)} + z^{(2)} f^{(1)} + z^{(3)} \right) \\ -\frac{3}{2} a_n^{(2)} f^{(1)} - \frac{1}{2} a_n^{(3)} + b_n^{(2)} f^{(1)} + \frac{1}{2} b_n^{(3)} \end{array} \right\} = \left\{ \begin{array}{l} \frac{\sigma_t}{|\mu_n|} \left[ \left( \frac{3f^{(2)} + 2z^{(2)} + 2f^{(1)} f^{(1)}}{6} \right) (1 - a_n^{(0)}) \right] \\ -\frac{1}{6} a_n^{(2)} - \frac{1}{3} b_n^{(2)} \end{array} \right\}$$

$$(4) \quad -\frac{1}{2} a_n^{(3)} + \frac{1}{2} b_n^{(3)} = \left\{ \begin{array}{l} \frac{\sigma_t}{|\mu_n|} \left[ \left( \frac{3f^{(2)} + 2z^{(2)} + 2f^{(1)} f^{(1)}}{6} \right) (1 - a_n^{(0)}) \right] \\ -\frac{1}{6} a_n^{(2)} - \frac{1}{3} b_n^{(2)} \\ -\frac{1}{2} a_n^{(0)} \left( -2f^{(3)} - 3f^{(1)} f^{(2)} + z^{(2)} f^{(1)} + z^{(3)} \right) + \frac{3}{2} a_n^{(2)} f^{(1)} - b_n^{(2)} f^{(1)} \end{array} \right\}$$

(1)+(2):

$$0 = \left\{ \begin{array}{l} \frac{\sigma_t}{|\mu_n|} \left[ \left( \frac{2f^{(2)} + z^{(2)} + f^{(1)}f^{(1)}}{2} \right) (1 - a_n^{(0)}) \right] - \frac{1}{2} a_n^{(0)} (2f^{(3)} + 2f^{(1)}f^{(2)} + 2z^{(2)}f^{(1)}) \\ -\frac{1}{2} a_n^{(2)} - \frac{1}{2} b_n^{(2)} \\ -b_n^{(2)} f^{(1)} \end{array} \right\}$$

$$\mu_n > 0: \boxed{b_n^{(2)} \left( f^{(1)} + \frac{1}{2} \frac{\sigma_t}{|\mu_n|} \right) + a_n^{(2)} \frac{1}{2} \frac{\sigma_t}{|\mu_n|} = \left\{ \begin{array}{l} \frac{\sigma_t}{|\mu_n|} \left( \frac{2f^{(2)} + z^{(2)} + f^{(1)}f^{(1)}}{2} \right) (1 - a_n^{(0)}) \\ -a_n^{(0)} (f^{(3)} + f^{(1)}f^{(2)} + z^{(2)}f^{(1)}) \end{array} \right\}}$$

From  $k = 2$ :

$$b_n^{(2)} = a_n^{(2)} + \frac{\sigma_t}{|\mu_n|} \left[ \frac{1}{6} f^{(1)} (1 - a_n^{(0)}) \right] + a_n^{(0)} (f^{(2)} - z^{(2)})$$

$$\left\{ \begin{array}{l} \left[ a_n^{(2)} + \frac{\sigma_t}{|\mu_n|} \left[ \frac{1}{6} f^{(1)} (1 - a_n^{(0)}) \right] \right] \left( f^{(1)} + \frac{1}{2} \frac{\sigma_t}{|\mu_n|} \right) \\ + a_n^{(0)} (f^{(2)} - z^{(2)}) \\ + a_n^{(2)} \frac{1}{2} \frac{\sigma_t}{|\mu_n|} \end{array} \right\} = \left\{ \begin{array}{l} \frac{\sigma_t}{|\mu_n|} \left( \frac{2f^{(2)} + z^{(2)} + f^{(1)}f^{(1)}}{2} \right) (1 - a_n^{(0)}) \\ -a_n^{(0)} (f^{(3)} + f^{(1)}f^{(2)} + z^{(2)}f^{(1)}) \end{array} \right\}$$

$$a_n^{(2)} f^{(1)} \left( \frac{\sigma_t}{f^{(1)} |\mu_n|} - |\mu_n| \right) = \left\{ \begin{array}{l} -a_n^{(0)} (-f^{(3)} - 2f^{(1)}f^{(2)} + z^{(2)}f^{(1)}) \\ + \frac{\sigma_t}{|\mu_n|} \left( \frac{2f^{(2)} + z^{(2)} + f^{(1)}f^{(1)}}{2} \right) (1 - a_n^{(0)}) \\ - \frac{1}{12} \frac{\sigma_t^2}{|\mu_n|^2} f^{(1)} (1 - a_n^{(0)}) - \frac{1}{2} \frac{\sigma_t}{|\mu_n|} a_n^{(0)} (f^{(2)} - z^{(2)}) \end{array} \right\}$$

$$a_n^{(2)} \left( f^{(1)} + \frac{\sigma_t}{|\mu_n|} \right) = \left\{ \begin{array}{l} \frac{\sigma_t}{|\mu_n|} \left( \frac{6f^{(2)} + 3z^{(2)} + 3f^{(1)}f^{(1)} - f^{(1)}f^{(1)}}{6} \right) (1 - a_n^{(0)}) \\ -\frac{1}{12} \frac{\sigma_t^2}{|\mu_n|^2} f^{(1)} (1 - a_n^{(0)}) \\ -a_n^{(0)} (f^{(3)} + f^{(1)}f^{(2)} + z^{(2)}f^{(1)} + f^{(2)}f^{(1)} - z^{(2)}f^{(1)}) \\ -\frac{1}{2} \frac{\sigma_t}{|\mu_n|} a_n^{(0)} (f^{(2)} - z^{(2)}) \end{array} \right\}$$

$$a_n^{(2)} \left( f^{(1)} + \frac{\sigma_t}{|\mu_n|} \right) = \left\{ \begin{array}{l} \frac{\sigma_t}{|\mu_n|} \left( \frac{6f^{(2)} + 3z^{(2)} + 2f^{(1)}f^{(1)}}{6} \right) (1 - a_n^{(0)}) \\ -\frac{1}{12} \frac{\sigma_t^2}{|\mu_n|^2} f^{(1)} (1 - a_n^{(0)}) - a_n^{(0)} (f^{(3)} + 2f^{(2)}f^{(1)}) \\ -\frac{1}{2} \frac{\sigma_t}{|\mu_n|} a_n^{(0)} (f^{(2)} - z^{(2)}) \end{array} \right\}$$

From  $k=1$ :

$$a_n^{(0)} = \frac{\frac{\sigma_t}{f^{(1)}}}{\frac{\sigma_t}{f^{(1)}} + |\mu_n|} \Rightarrow 1 - a_n^{(0)} = \frac{|\mu_n|}{\frac{\sigma_t}{f^{(1)}} + |\mu_n|}$$

$$a_n^{(2)} f^{(1)} \left( \frac{|\mu_n| + \frac{\sigma_t}{f^{(1)}}}{|\mu_n|} \right) = \left\{ \begin{array}{l} \frac{\sigma_t}{|\mu_n|} \left( \frac{6f^{(2)} + 3z^{(2)} + 2f^{(1)}f^{(1)}}{6} \right) \left( \frac{|\mu_n|}{\frac{\sigma_t}{f^{(1)}} + |\mu_n|} \right) \\ -\frac{1}{12} \frac{\sigma_t^2}{|\mu_n|^2} f^{(1)} \left( \frac{|\mu_n|}{\frac{\sigma_t}{f^{(1)}} + |\mu_n|} \right) - (f^{(3)} + 2f^{(2)}f^{(1)}) \left( \frac{\frac{\sigma_t}{f^{(1)}}}{\frac{\sigma_t}{f^{(1)}} + |\mu_n|} \right) \\ -\frac{1}{2} \frac{\sigma_t}{|\mu_n|} (f^{(2)} - z^{(2)}) \left( \frac{\frac{\sigma_t}{f^{(1)}}}{\frac{\sigma_t}{f^{(1)}} + |\mu_n|} \right) \end{array} \right\}$$

$$a_n^{(2)} = \left\{ \begin{array}{l} \frac{|\mu_n|}{\sigma_t} \left( \frac{6f^{(2)}f^{(1)} + 3z^{(2)}f^{(1)} + 2f^{(1)}f^{(1)}f^{(1)} - 6f^{(3)} - 12f^{(2)}f^{(1)}}{6} \right) \\ -\frac{1}{12}f^{(1)}f^{(1)} - \frac{1}{2}(f^{(2)} - z^{(2)}) \end{array} \right\} \left( \frac{\frac{\sigma_t}{f^{(1)}}}{\frac{\sigma_t}{f^{(1)}} + |\mu_n|} \right)^2$$

From  $k = 2$ :

$$\frac{f^{(2)}}{f^{(1)}} = \frac{1}{2}f^{(1)}, \quad \frac{z^{(2)}}{f^{(1)}} = \frac{1}{2}f^{(1)} + \frac{c}{12}f^{(1)} \left[ \sum_{\mu_n > 0} w_n a_n^{(0)} - \sum_{\mu_n < 0} w_n a_n^{(0)} \right]$$

$$a_n^{(2)} = \left\{ \begin{array}{l} \frac{|\mu_n|}{\sigma_t} \left( \frac{-2f^{(2)}f^{(1)} + 3z^{(2)}f^{(1)} - 6f^{(3)}}{6} \right) \\ -\left( \frac{4f^{(2)} - 3z^{(2)}}{6} \right) \end{array} \right\} \left( \frac{\frac{\sigma_t}{f^{(1)}}}{\frac{\sigma_t}{f^{(1)}} + |\mu_n|} \right)^2$$

$$\therefore \mu_n > 0: a_n^{(2)} = \left\{ \begin{array}{l} \frac{|\mu_n|}{\sigma_t} \left( \frac{-2f^{(2)}f^{(1)} + 3z^{(2)}f^{(1)} - 6f^{(3)}}{6} \right) \\ -\left( \frac{4f^{(2)} - 3z^{(2)}}{6} \right) \end{array} \right\} \left[ a_n^{(0)} \right]^2$$

$$\Rightarrow a_n^{(2)} = \left\{ \begin{array}{l} \frac{\mu_n}{\sigma_t} \left( \frac{-2f^{(3)} + z^{(2)}f^{(1)}}{2} \right) \\ + \frac{-2f^{(2)} + 3z^{(2)}}{6} - \frac{f^{(2)}}{3} \left( 1 + \frac{\mu_n}{\sigma_t} f^{(1)} \right) \end{array} \right\} \left[ a_n^{(0)} \right]^2$$

$$\frac{b_n^{(2)}}{|\mu_n|} = \frac{a_n^{(2)}}{|\mu_n|} + \frac{\sigma_t}{|\mu_n|^2} \left[ \frac{1}{6}f^{(1)}(1 - a_n^{(0)}) \right] + \frac{a_n^{(0)}}{|\mu_n|} (f^{(2)} - z^{(2)})$$

$$\frac{b_n^{(2)}}{|\mu_n|} = \left\{ \begin{array}{l} \frac{\left[ a_n^{(0)} \right]^2}{\sigma_t} \frac{12f^{(2)}f^{(1)} + 3z^{(2)}f^{(1)} - f^{(3)}}{6} \\ -\frac{\left[ a_n^{(0)} \right]^2}{|\mu_n|} \frac{f^{(2)}}{6} \end{array} \right\}$$

$$+ \frac{\sigma_t}{|\mu_n|^2} \left[ \frac{1}{6}f^{(1)}(1 - a_n^{(0)}) \right] + \frac{a_n^{(0)}}{|\mu_n|} (f^{(2)} - z^{(2)}) \left( 1 - \frac{1}{2}a_n^{(0)} \right)$$

(3)+(4):

$$\mu_n < 0: \left. a_n^{(2)} \left( \frac{1}{2} \frac{\sigma_t}{|\mu_n|} - f^{(1)} \right) + \frac{1}{2} b_n^{(2)} \frac{\sigma_t}{|\mu_n|} = \left\{ \begin{array}{l} a_n^{(0)} \left( f^{(3)} + 2f^{(1)} f^{(2)} \right) \\ + \frac{\sigma_t}{|\mu_n|} \left( \frac{2f^{(2)} + z^{(2)} + f^{(1)} f^{(1)}}{2} \right) (1 - a_n^{(0)}) \end{array} \right\}$$

From  $k = 2$ :

$$b_n^{(2)} = a_n^{(2)} + \frac{\sigma_t}{|\mu_n|} \left[ \frac{1}{6} f^{(1)} (1 - a_n^{(0)}) \right] + a_n^{(0)} (f^{(2)} - z^{(2)})$$

$$a_n^{(2)} f^{(1)} \left( \frac{\frac{\sigma_t}{f^{(1)}} - |\mu_n|}{|\mu_n|} \right) = \left\{ \begin{array}{l} a_n^{(0)} \left( f^{(3)} + 2f^{(1)} f^{(2)} \right) \\ + \frac{\sigma_t}{|\mu_n|} \left( \frac{2f^{(2)} + z^{(2)} + f^{(1)} f^{(1)}}{2} \right) (1 - a_n^{(0)}) \\ - \frac{1}{12} \frac{\sigma_t^2}{|\mu_n|^2} f^{(1)} (1 - a_n^{(0)}) - \frac{1}{2} \frac{\sigma_t}{|\mu_n|} a_n^{(0)} (f^{(2)} - z^{(2)}) \end{array} \right\}$$

From  $k = 1$ :

$$a_n^{(0)} = \frac{\frac{\sigma_t}{f^{(1)}}}{\frac{\sigma_t}{f^{(1)}} - |\mu_n|} \Rightarrow 1 - a_n^{(0)} = -\frac{|\mu_n|}{\frac{\sigma_t}{f^{(1)}} - |\mu_n|}$$

$$a_n^{(2)} f^{(1)} \left( \frac{\frac{\sigma_t}{f^{(1)}} - |\mu_n|}{|\mu_n|} \right) = \left\{ \begin{array}{l} \left( f^{(3)} + 2f^{(1)} f^{(2)} \right) \left( \frac{\frac{\sigma_t}{f^{(1)}}}{\frac{\sigma_t}{f^{(1)}} - |\mu_n|} \right) \\ - \frac{\sigma_t}{|\mu_n|} \left( \frac{2f^{(2)} + z^{(2)} + f^{(1)} f^{(1)}}{2} \right) \left( \frac{|\mu_n|}{\frac{\sigma_t}{f^{(1)}} - |\mu_n|} \right) \\ + \frac{1}{12} \frac{\sigma_t^2}{|\mu_n|^2} f^{(1)} \left( \frac{|\mu_n|}{\frac{\sigma_t}{f^{(1)}} - |\mu_n|} \right) \\ - \frac{1}{2} \frac{\sigma_t}{|\mu_n|} \left( f^{(2)} - z^{(2)} \right) \left( \frac{\frac{\sigma_t}{f^{(1)}}}{\frac{\sigma_t}{f^{(1)}} - |\mu_n|} \right) \end{array} \right\}$$

$$a_n^{(2)} = \left\{ \begin{array}{l} \frac{|\mu_n|}{\sigma_t} \left( f^{(3)} + 2f^{(1)} f^{(2)} \right) \\ - \frac{|\mu_n|}{\sigma_t} \left( \frac{2f^{(2)} f^{(1)} + z^{(2)} f^{(1)} + f^{(1)} f^{(1)} f^{(1)}}{2} \right) \\ + \frac{1}{12} f^{(1)} f^{(1)} - \frac{1}{2} \left( f^{(2)} - z^{(2)} \right) \end{array} \right\} \left( \frac{\frac{\sigma_t}{f^{(1)}}}{\frac{\sigma_t}{f^{(1)}} - |\mu_n|} \right)^2$$

From  $k = 2$ :

$$\frac{f^{(2)}}{f^{(1)}} = \frac{1}{2} f^{(1)}, \quad \frac{z^{(2)}}{f^{(1)}} = \frac{1}{2} f^{(1)} + \frac{c}{12} f^{(1)} \left[ \sum_{\mu_n > 0} w_n a_n^{(0)} - \sum_{\mu_n < 0} w_n a_n^{(0)} \right]$$

$$\mu_n < 0: a_n^{(2)} = \left\{ \begin{array}{l} \frac{\mu_n}{\sigma_t} \left( \frac{-2f^{(3)} + z^{(2)} f^{(1)}}{2} \right) \\ + \frac{-2f^{(2)} + 3z^{(2)}}{6} \end{array} \right\} \left[ a_n^{(0)} \right]^2 \Rightarrow \frac{a_n^{(2)}}{|\mu_n|} = \left\{ \begin{array}{l} \frac{1}{\sigma_t} \left( \frac{2f^{(3)} - z^{(2)} f^{(1)}}{2} \right) \\ + \frac{1}{|\mu_n|} \frac{-2f^{(2)} + 3z^{(2)}}{6} \end{array} \right\} \left[ a_n^{(0)} \right]^2$$

Summing  $a_n^{(2)}$  over all directions:

$$\begin{aligned}
 0 &= \left\{ \begin{aligned} &\frac{\sum_{n=1}^{Np} w_n \mu_n [a_n^{(0)}]^2}{\sigma_t} \left( \frac{-2f^{(3)} + z^{(2)} f^{(1)}}{2} \right) \\ &+ \frac{-2f^{(2)} + 3z^{(2)}}{6} \sum_{n=1}^{Np} w_n [a_n^{(0)}]^2 - \frac{f^{(2)}}{3} \sum_{\mu_n > 0} w_n [a_n^{(0)}]^2 \left( 1 + \frac{\mu_n}{\sigma_t} f^{(1)} \right) \end{aligned} \right\} \\
 \frac{f^{(3)}}{\sigma_t} \sum_{n=1}^{Np} w_n \mu_n [a_n^{(0)}]^2 &= \left\{ \begin{aligned} &\frac{z^{(2)}}{2} \left( \frac{f^{(1)}}{\sigma_t} \sum_{n=1}^{Np} w_n \mu_n [a_n^{(0)}]^2 + \sum_{n=1}^{Np} w_n [a_n^{(0)}]^2 \right) \\ &- \frac{f^{(2)}}{3} \sum_{n=1}^{Np} w_n [a_n^{(0)}]^2 \\ &+ \frac{f^{(2)}}{3} \left( \frac{f^{(1)}}{\sigma_t} \sum_{\mu_n > 0} w_n \mu_n [a_n^{(0)}]^2 - \sum_{\mu_n > 0} w_n [a_n^{(0)}]^2 \right) \end{aligned} \right\} \\
 \sum_{n=1}^{Np} w_n \mu_n [a_n^{(0)}]^2 &= \left( \frac{\sigma_t}{f^{(1)}} \right)^2 \sum_{\mu_n > 0} w_n \mu_n \left[ \frac{1}{\left( \frac{\sigma_t}{f^{(1)}} + |\mu_n| \right)^2} - \frac{1}{\left( \frac{\sigma_t}{f^{(1)}} - |\mu_n| \right)^2} \right] \\
 \sum_{n=1}^{Np} w_n \mu_n [a_n^{(0)}]^2 &= \left( \frac{\sigma_t}{f^{(1)}} \right)^2 \sum_{\mu_n > 0} w_n \mu_n \frac{\cancel{\left( \frac{\sigma_t}{f^{(1)}} \right)^2} - 2|\mu_n| \frac{\sigma_t}{f^{(1)}} + \cancel{|\mu_n|^2} - \cancel{\left( \frac{\sigma_t}{f^{(1)}} \right)^2} - 2|\mu_n| \frac{\sigma_t}{f^{(1)}} - \cancel{|\mu_n|^2}}{\left[ \left( \frac{\sigma_t}{f^{(1)}} \right)^2 - |\mu_n|^2 \right]^2} \\
 \sum_{n=1}^{Np} w_n \mu_n [a_n^{(0)}]^2 &= \left( \frac{\sigma_t}{f^{(1)}} \right)^3 \sum_{\mu_n > 0} w_n \frac{-4|\mu_n|^2}{\left[ \left( \frac{\sigma_t}{f^{(1)}} \right)^2 - |\mu_n|^2 \right]^2}
 \end{aligned}$$

$$\sum_{n=1}^{Np} w_n [a_n^{(0)}]^2 = \left( \frac{\sigma_t}{f^{(1)}} \right)^2 \sum_{\mu_n > 0} w_n \left[ \frac{1}{\left( \frac{\sigma_t}{f^{(1)}} + |\mu_n| \right)^2} + \frac{1}{\left( \frac{\sigma_t}{f^{(1)}} - |\mu_n| \right)^2} \right]$$

$$\sum_{n=1}^{Np} w_n [a_n^{(0)}]^2 = \left( \frac{\sigma_t}{f^{(1)}} \right)^2 \sum_{\mu_n > 0} w_n \frac{\left( \frac{\sigma_t}{f^{(1)}} - |\mu_n| \right)^2 + \left( \frac{\sigma_t}{f^{(1)}} + |\mu_n| \right)^2}{\left[ \left( \frac{\sigma_t}{f^{(1)}} \right)^2 - |\mu_n|^2 \right]^2}$$

$$\sum_{n=1}^{Np} w_n [a_n^{(0)}]^2 = \left( \frac{\sigma_t}{f^{(1)}} \right)^2 \sum_{\mu_n > 0} 2w_n \frac{\left( \frac{\sigma_t}{f^{(1)}} \right)^2 + |\mu_n|^2}{\left[ \left( \frac{\sigma_t}{f^{(1)}} \right)^2 - |\mu_n|^2 \right]^2}$$

$$\frac{f^{(1)}}{\sigma_t} \sum_{n=1}^{Np} w_n \mu_n [a_n^{(0)}]^2 + \sum_{n=1}^{Np} w_n [a_n^{(0)}]^2 = \left( \frac{\sigma_t}{f^{(1)}} \right)^2 \sum_{\mu_n > 0} w_n \frac{\cancel{4|\mu_n|^2} + 2 \left( \frac{\sigma_t}{f^{(1)}} \right)^2 + \cancel{2|\mu_n|^2}}{\left[ \left( \frac{\sigma_t}{f^{(1)}} \right)^2 - |\mu_n|^2 \right]^2}$$

$$\frac{f^{(1)}}{\sigma_t} \sum_{n=1}^{Np} w_n \mu_n [a_n^{(0)}]^2 + \sum_{n=1}^{Np} w_n [a_n^{(0)}]^2 = \sum_{\mu_n > 0} w_n \frac{2 \left( \frac{\sigma_t}{f^{(1)}} \right)^2}{\left( \frac{\sigma_t}{f^{(1)}} \right)^2 - |\mu_n|^2}$$

$$\frac{f^{(1)}}{\sigma_t} \sum_{n=1}^{Np} w_n \mu_n [a_n^{(0)}]^2 + \sum_{n=1}^{Np} w_n [a_n^{(0)}]^2 = \sum_{\mu_n > 0} w_n \frac{\left( \frac{\sigma_t}{f^{(1)}} \right)^2 + \left( \frac{\sigma_t}{f^{(1)}} \right) |\mu_n| + \left( \frac{\sigma_t}{f^{(1)}} \right)^2 - \left( \frac{\sigma_t}{f^{(1)}} \right) |\mu_n|}{\left( \frac{\sigma_t}{f^{(1)}} \right)^2 - |\mu_n|^2}$$

$$\frac{f^{(1)}}{\sigma_t} \sum_{n=1}^{Np} w_n \mu_n [a_n^{(0)}]^2 + \sum_{n=1}^{Np} w_n [a_n^{(0)}]^2 = \sum_{\mu_n > 0} w_n \frac{\left(\frac{\sigma_t}{f^{(1)}}\right)}{\left(\frac{\sigma_t}{f^{(1)}}\right) + |\mu_n|} + \frac{\left(\frac{\sigma_t}{f^{(1)}}\right)}{\left(\frac{\sigma_t}{f^{(1)}}\right) - |\mu_n|} = \sum_{n=1}^{Np} w_n a_n^{(0)}$$

$$\boxed{\frac{f^{(1)}}{\sigma_t} \sum_{n=1}^{Np} w_n \mu_n [a_n^{(0)}]^2 + \sum_{n=1}^{Np} w_n [a_n^{(0)}]^2 = \frac{2}{c}}$$

$$\frac{f^{(1)}}{\sigma_t} \sum_{\mu_n > 0} w_n \mu_n [a_n^{(0)}]^2 + \sum_{\mu_n > 0} w_n [a_n^{(0)}]^2 = \sum_{\mu_n > 0} w_n \frac{\left(\frac{\sigma_t}{f^{(1)}}\right)^2 \left(\frac{f^{(1)}}{\sigma_t} |\mu_n| + 1\right)}{\left[\left(\frac{\sigma_t}{f^{(1)}}\right) + |\mu_n|\right]^2}$$

$$\frac{f^{(1)}}{\sigma_t} \sum_{\mu_n > 0} w_n \mu_n [a_n^{(0)}]^2 + \sum_{\mu_n > 0} w_n [a_n^{(0)}]^2 = \frac{\sigma_t}{f^{(1)}} \sum_{\mu_n > 0} w_n \frac{|\mu_n| + \frac{\sigma_t}{f^{(1)}}}{\left[\left(\frac{\sigma_t}{f^{(1)}}\right) + |\mu_n|\right]^2}$$

$$\frac{f^{(3)}}{\sigma_t} \sum_{n=1}^{Np} w_n \mu_n [a_n^{(0)}]^2 = \left\{ \begin{array}{l} \frac{z^{(2)}}{c} - \frac{f^{(2)}}{3} \sum_{n=1}^{Np} w_n [a_n^{(0)}]^2 \\ - \frac{f^{(2)}}{3} \frac{\sigma_t}{f^{(1)}} \sum_{\mu_n > 0} w_n \frac{|\mu_n| + \frac{\sigma_t}{f^{(1)}}}{\left[\left(\frac{\sigma_t}{f^{(1)}}\right) + |\mu_n|\right]^2} \end{array} \right\}$$

From  $k = 2$ :

$$\begin{aligned} \frac{z^{(2)}}{c} &= \frac{1}{c} f^{(2)} + \frac{1}{12} \sum_{n=1}^{S_n} w_n \frac{\sigma_t}{|\mu_n|} [f^{(1)} (1 - a_n^{(0)})] \\ \Rightarrow \frac{z^{(2)}}{c} &= \frac{1}{c} f^{(2)} + \frac{1}{6} \frac{f^{(1)} f^{(1)}}{2} \left[ \sum_{\mu_n > 0} w_n a_n^{(0)} - \sum_{\mu_n < 0} w_n a_n^{(0)} \right] \\ \frac{z^{(2)}}{c} &= \frac{1}{c} f^{(2)} + \frac{1}{6} f^{(2)} \left[ \sum_{\mu_n > 0} w_n a_n^{(0)} - \sum_{\mu_n < 0} w_n a_n^{(0)} \right] \end{aligned}$$

$$\frac{f^{(3)}}{\sigma_t} \sum_{n=1}^{Np} w_n \mu_n [a_n^{(0)}]^2 = f^{(2)} \left\{ \begin{array}{l} \frac{1}{2} \left[ \sum_{\mu_n > 0} w_n a_n^{(0)} + \sum_{\mu_n < 0} w_n a_n^{(0)} \right] + \frac{1}{6} \left[ \sum_{\mu_n > 0} w_n a_n^{(0)} - \sum_{\mu_n < 0} w_n a_n^{(0)} \right] \\ - \frac{1}{3} \sum_{n=1}^{Np} w_n [a_n^{(0)}]^2 - \frac{1}{3} \frac{\sigma_t}{f^{(1)}} \sum_{\mu_n > 0} w_n \frac{|\mu_n| + \frac{\sigma_t}{f^{(1)}}}{\left[ \left( \frac{\sigma_t}{f^{(1)}} \right) + |\mu_n| \right]^2} \end{array} \right\}$$

$$\frac{f^{(3)}}{\sigma_t} \sum_{n=1}^{Np} w_n \mu_n [a_n^{(0)}]^2 = f^{(2)} \left\{ \begin{array}{l} \sum_{\mu_n > 0} w_n a_n^{(0)} \left[ \frac{1}{2} + \frac{1}{6} - \frac{1}{3} \frac{\frac{\sigma_t}{f^{(1)}}}{\frac{\sigma_t}{f^{(1)}} + |\mu_n|} \right] \\ + \sum_{\mu_n < 0} w_n a_n^{(0)} \left[ \frac{1}{2} - \frac{1}{6} - \frac{1}{3} \frac{\frac{\sigma_t}{f^{(1)}}}{\frac{\sigma_t}{f^{(1)}} - |\mu_n|} \right] \\ - \frac{1}{3} \frac{\sigma_t}{f^{(1)}} \sum_{\mu_n > 0} w_n \frac{|\mu_n| + \frac{\sigma_t}{f^{(1)}}}{\left[ \left( \frac{\sigma_t}{f^{(1)}} \right) + |\mu_n| \right]^2} \end{array} \right\}$$

$$\frac{f^{(3)}}{\sigma_t} \sum_{n=1}^{Np} w_n \mu_n [a_n^{(0)}]^2 = f^{(2)} \left\{ \begin{array}{l} \sum_{\mu_n > 0} w_n a_n^{(0)} \frac{3 \frac{\sigma_t}{f^{(1)}} + 3|\mu_n| + \frac{\sigma_t}{f^{(1)}} + |\mu_n| - 2 \frac{\sigma_t}{f^{(1)}}}{6 \left( \frac{\sigma_t}{f^{(1)}} + |\mu_n| \right)} \\ + \sum_{\mu_n < 0} w_n a_n^{(0)} \frac{3 \frac{\sigma_t}{f^{(1)}} - 3|\mu_n| - \frac{\sigma_t}{f^{(1)}} + |\mu_n| - 2 \frac{\sigma_t}{f^{(1)}}}{6 \left( \frac{\sigma_t}{f^{(1)}} - |\mu_n| \right)} \\ - \frac{1}{3} \frac{\sigma_t}{f^{(1)}} \sum_{\mu_n > 0} w_n \frac{|\mu_n| + \frac{\sigma_t}{f^{(1)}}}{\left[ \left( \frac{\sigma_t}{f^{(1)}} \right) + |\mu_n| \right]^2} \end{array} \right\}$$

$$\begin{aligned}
\frac{f^{(3)}}{\sigma_t} \sum_{n=1}^{Np} w_n \mu_n [a_n^{(0)}]^2 = f^{(2)} & \left\{ \begin{aligned} & \frac{\sigma_t}{f^{(1)}} \frac{1}{3} \sum_{\mu_n > 0} w_n \frac{\frac{\sigma_t}{f^{(1)}} + 2|\mu_n|}{\left(\frac{\sigma_t}{f^{(1)}} + |\mu_n|\right)^2} + \frac{\sigma_t}{f^{(1)}} \sum_{\mu_n > 0} w_n \frac{-2|\mu_n|}{6\left(\frac{\sigma_t}{f^{(1)}} - |\mu_n|\right)^2} \\ & - \frac{1}{3} \frac{\sigma_t}{f^{(1)}} \sum_{\mu_n > 0} w_n \frac{|\mu_n| + \frac{\sigma_t}{f^{(1)}}}{\left[\left(\frac{\sigma_t}{f^{(1)}}\right) + |\mu_n|\right]^2} \end{aligned} \right\} \\
\frac{f^{(3)}}{\sigma_t} \sum_{n=1}^{Np} w_n \mu_n [a_n^{(0)}]^2 = \frac{1}{3} f^{(2)} & \left\{ \begin{aligned} & \sum_{\mu_n > 0} w_n \frac{\left(\frac{\sigma_t}{f^{(1)}}\right) + 2|\mu_n| \left(\frac{\sigma_t}{f^{(1)}}\right) - |\mu_n| \left(\frac{\sigma_t}{f^{(1)}}\right) - \left(\frac{\sigma_t}{f^{(1)}}\right)}{\left(\frac{\sigma_t}{f^{(1)}} + |\mu_n|\right)^2} \\ & - \frac{\sigma_t}{f^{(1)}} \sum_{\mu_n > 0} w_n \frac{|\mu_n|}{\left(\frac{\sigma_t}{f^{(1)}} - |\mu_n|\right)^2} \end{aligned} \right\} \\
\frac{f^{(3)}}{\sigma_t} \sum_{n=1}^{Np} w_n \mu_n [a_n^{(0)}]^2 = \frac{1}{3} f^{(2)} \sum_{\mu_n > 0} w_n & \frac{|\mu_n| \left(\frac{\sigma_t}{f^{(1)}}\right) \left(\frac{\sigma_t}{f^{(1)}} - |\mu_n|\right)^2 - |\mu_n| \left(\frac{\sigma_t}{f^{(1)}}\right) \left(\frac{\sigma_t}{f^{(1)}} + |\mu_n|\right)^2}{\left[\left(\frac{\sigma_t}{f^{(1)}}\right)^2 - |\mu_n|^2\right]^2} \\
\frac{f^{(3)}}{\sigma_t} \sum_{n=1}^{Np} w_n \mu_n [a_n^{(0)}]^2 = \frac{1}{3} f^{(2)} \sum_{\mu_n > 0} w_n & \frac{\left[ |\mu_n| \left(\frac{\sigma_t}{f^{(1)}}\right) \left[ \left(\frac{\sigma_t}{f^{(1)}}\right) - 2|\mu_n| \left(\frac{\sigma_t}{f^{(1)}}\right) + |\mu_n| \right] \right.}{\left. - |\mu_n| \left(\frac{\sigma_t}{f^{(1)}}\right) \left[ \left(\frac{\sigma_t}{f^{(1)}}\right) + 2|\mu_n| \left(\frac{\sigma_t}{f^{(1)}}\right) + |\mu_n| \right] \right]}{\left[\left(\frac{\sigma_t}{f^{(1)}}\right)^2 - |\mu_n|^2\right]^2}
\end{aligned}$$

$$\frac{f^{(3)} \left( \frac{\sigma_t}{f^{(1)}} \right)^{\cancel{\delta}}}{\sigma_t} \sum_{\mu_n > 0} w_n \frac{\cancel{-4|\mu_n|^2}}{\left[ \left( \frac{\cancel{\sigma_t}}{f^{(1)}} \right)^2 - |\mu_n|^2 \right]^2} = \frac{1}{3} f^{(2)} \left( \frac{\cancel{\sigma_t}}{f^{(1)}} \right)^{\cancel{2}} \sum_{\mu_n > 0} w_n \frac{\cancel{-4|\mu_n|^2}}{\left[ \left( \frac{\cancel{\sigma_t}}{f^{(1)}} \right)^2 - |\mu_n|^2 \right]^2}$$

$$\boxed{f^{(3)} = \frac{1}{3} f^{(2)} f^{(1)} = \frac{1}{6} f^{(1)} f^{(1)} f^{(1)}}$$

Solving for  $a_n^{(2)}$  based on  $f^{(3)}$  :

$$a_n^{(2)} = \left\{ \begin{aligned} & f^{(3)} \left( -\frac{\mu_n}{\sigma_t} \right) - \frac{1}{3} f^{(2)} \left( 2 + \frac{\mu_n}{\sigma_t} f^{(1)} \right) \\ & + \frac{1}{2} \left( \frac{1}{2} f^{(1)} f^{(1)} + \frac{c}{12} f^{(1)} f^{(1)} \left[ \sum_{\mu_n > 0} w_n a_n^{(0)} - \sum_{\mu_n < 0} w_n a_n^{(0)} \right] \right) \left( 1 + \frac{\mu_n}{\sigma_t} f^{(1)} \right) \end{aligned} \right\} [a_n^{(0)}]^2$$

$$a_n^{(2)} = \left\{ \begin{aligned} & \frac{1}{6} f^{(1)} f^{(1)} f^{(1)} \left( -\frac{2\mu_n}{\sigma_t} - \frac{2}{f^{(1)}} \right) + \frac{1}{4} f^{(1)} f^{(1)} f^{(1)} \left( \frac{1}{f^{(1)}} + \frac{\mu_n}{\sigma_t} \right) \\ & + \frac{c}{24} f^{(1)} f^{(1)} f^{(1)} \left[ \sum_{\mu_n > 0} w_n a_n^{(0)} - \sum_{\mu_n < 0} w_n a_n^{(0)} \right] \left( \frac{1}{f^{(1)}} + \frac{\mu_n}{\sigma_t} \right) \end{aligned} \right\} [a_n^{(0)}]^2$$

$$a_n^{(2)} = \frac{f^{(1)} f^{(1)} f^{(1)}}{12} \left\{ \begin{aligned} & -\frac{4\mu_n}{\cancel{\sigma_t}} - \frac{4}{\cancel{f^{(1)}}} + \frac{3}{\cancel{f^{(1)}}} + \frac{3\mu_n}{\cancel{\sigma_t}} \\ & + \frac{c}{2} \left[ \sum_{\mu_n > 0} w_n a_n^{(0)} - \sum_{\mu_n < 0} w_n a_n^{(0)} \right] \left( \frac{1}{f^{(1)}} + \frac{\mu_n}{\sigma_t} \right) \end{aligned} \right\} [a_n^{(0)}]^2$$

$$a_n^{(2)} = \frac{f^{(1)} f^{(1)}}{12} \left\{ -1 + \frac{c}{2} \left[ \sum_{\mu_n > 0} w_n a_n^{(0)} - \sum_{\mu_n < 0} w_n a_n^{(0)} \right] \right\} \left[ \frac{\cancel{\frac{\sigma_t}{f^{(1)}} + \mu_n}}{\cancel{\frac{\sigma_t}{f^{(1)}}}} \right] [a_n^{(0)}]^{\cancel{2}}$$

$$a_n^{(2)} = -\frac{f^{(1)} f^{(1)}}{12} \frac{c}{2} \left\{ \sum_{\cancel{\mu_n > 0}} \cancel{w_n a_n^{(0)}} + \sum_{\mu_n < 0} w_n a_n^{(0)} - \sum_{\cancel{\mu_n > 0}} \cancel{w_n a_n^{(0)}} + \sum_{\mu_n < 0} w_n a_n^{(0)} \right\} [a_n^{(0)}]$$

$$\mu_n > 0: \boxed{a_n^{(2)} = -\frac{c}{12} f^{(1)} f^{(1)} a_n^{(0)} \left[ \sum_{\mu_n < 0} w_n a_n^{(0)} \right]}$$

$$\mu_n < 0 : a_n^{(2)} = \left\{ \begin{array}{l} \frac{\mu_n \left( \frac{-2f^{(3)} + z^{(2)} f^{(1)}}{2} \right)}{\sigma_t} \\ + \frac{-2f^{(2)} + 3z^{(2)}}{6} \end{array} \right\} [a_n^{(0)}]^2$$

$$a_n^{(2)} = \left\{ \begin{array}{l} \frac{\mu_n}{\sigma_t} f^{(1)} \left( \frac{-2f^{(2)} + 3z^{(2)}}{6} \right) \\ + \frac{-2f^{(2)} + 3z^{(2)}}{6} \end{array} \right\} [a_n^{(0)}]^2 \Rightarrow a_n^{(2)} = \left( \frac{-2f^{(2)} + 3z^{(2)}}{6} \right) \left[ \begin{array}{l} \mu_n + \frac{\sigma_t}{f^{(1)}} \\ \frac{\sigma_t}{f^{(1)}} \end{array} \right] [a_n^{(0)}]^2$$

$$a_n^{(2)} = -\frac{1}{12} (4f^{(2)} - 6z^{(2)}) a_n^{(0)}$$

$$a_n^{(2)} = -\frac{1}{12} \left\{ 2f^{(1)} f^{(1)} - 3f^{(1)} f^{(1)} - \frac{c}{2} f^{(1)} f^{(1)} \left[ \sum_{\mu_n > 0} w_n a_n^{(0)} - \sum_{\mu_n < 0} w_n a_n^{(0)} \right] \right\} a_n^{(0)}$$

$$a_n^{(2)} = \frac{1}{12} f^{(1)} f^{(1)} \left\{ 1 + \frac{c}{2} \left[ \sum_{\mu_n > 0} w_n a_n^{(0)} - \sum_{\mu_n < 0} w_n a_n^{(0)} \right] \right\} a_n^{(0)}$$

$$a_n^{(2)} = \frac{1}{12} f^{(1)} f^{(1)} \frac{c}{2} \left\{ \sum_{\mu_n > 0} w_n a_n^{(0)} + \sum_{\mu_n < 0} w_n a_n^{(0)} + \sum_{\mu_n > 0} w_n a_n^{(0)} - \sum_{\mu_n < 0} w_n a_n^{(0)} \right\} a_n^{(0)}$$

$$\mu_n < 0 : a_n^{(2)} = \frac{c}{12} f^{(1)} f^{(1)} a_n^{(0)} \left[ \sum_{\mu_n > 0} w_n a_n^{(0)} \right]$$

Some dummy checks. First, compare the results to the S2 results:

$$\mu_n > 0 : a_1^{(2)} = -\frac{c}{12} f^{(1)} f^{(1)} a_1^{(0)} \left[ \sum_{\mu_n < 0} w_n a_n^{(0)} \right]$$

$$a_1^{(2)} = -\frac{c}{12} \cancel{f^{(1)} f^{(1)}} \frac{\frac{\sigma_t}{\cancel{f^{(1)}}}}{\frac{\sigma_t}{f^{(1)}} + |\mu|} \frac{\frac{\sigma_t}{\cancel{f^{(1)}}}}{\frac{\sigma_t}{f^{(1)}} - |\mu|}$$

$$\Rightarrow a_1^{(2)} = -\frac{c}{12} \frac{\sigma_t^2}{\left(\frac{\sigma_t}{f^{(1)}}\right)^2 - |\mu|^2} \Rightarrow a_1^{(2)} = -\frac{c}{12} \frac{\sigma_t^2}{v^2 - |\mu|^2}$$

$$a_1^{(2)} = -\frac{c}{12} \frac{\sigma_t^2}{\frac{|\mu|^2}{1-c} - |\mu|^2} \Rightarrow a_1^{(2)} = -\frac{\cancel{c} \sigma_t^2}{12 |\mu|^2} \frac{1}{\cancel{1} + \cancel{c}} = -\frac{1}{12} \frac{\sigma_t^2}{v^2}$$

$$\mu_n < 0: a_2^{(2)} = \frac{c}{12} f^{(1)} f^{(1)} a_2^{(0)} \left[ \sum_{\mu_n > 0} w_n a_n^{(0)} \right]$$

$$a_2^{(2)} = \frac{c}{12} \cancel{f^{(1)}} \cancel{f^{(1)}} \frac{\frac{\sigma_t}{\cancel{f^{(1)}}}}{\frac{\sigma_t}{f^{(1)}} + |\mu|} \frac{\frac{\sigma_t}{\cancel{f^{(1)}}}}{\frac{\sigma_t}{f^{(1)}} - |\mu|} \Rightarrow a_1^{(2)} = \frac{c}{12} \frac{\sigma_t^2}{\left(\frac{\sigma_t}{f^{(1)}}\right)^2 - |\mu|^2} \Rightarrow a_1^{(2)} = \frac{c}{12} \frac{\sigma_t^2}{v^2 - |\mu|^2}$$

$$a_2^{(2)} = \frac{c}{12} \frac{\sigma_t^2}{\frac{|\mu|^2}{1-c} - |\mu|^2} \Rightarrow a_2^{(2)} = \frac{\cancel{c} \sigma_t^2}{12 |\mu|^2} \frac{1}{\cancel{1} + \cancel{c}} = \frac{1}{12} \frac{\sigma_t^2}{v^2}$$

Second, sum over all angle to guarantee normalization:

$$\sum_{n=1}^{Np} w_n a_n^{(2)} = \frac{c}{12} f^{(1)} f^{(1)} \sum_{\mu_n > 0} w_n \left\{ -\frac{\frac{\sigma_t}{f^{(1)}}}{\frac{\sigma_t}{f^{(1)}} + |\mu_n|} \left[ \sum_{\mu_m < 0} w_m a_m^{(0)} \right] + \frac{\frac{\sigma_t}{f^{(1)}}}{\frac{\sigma_t}{f^{(1)}} - |\mu_n|} \left[ \sum_{\mu_m > 0} w_m a_m^{(0)} \right] \right\}$$

$$\sum_{n=1}^{Np} w_n a_n^{(2)} = \frac{c}{12} f^{(1)} f^{(1)} \sum_{\mu_n > 0} w_n \sum_{\mu_m > 0} w_m \frac{\sigma_t}{f^{(1)}} \frac{\sigma_t}{f^{(1)}} \left\{ \begin{array}{l} -\frac{1}{\frac{\sigma_t}{f^{(1)}} + |\mu_n|} \frac{1}{\frac{\sigma_t}{f^{(1)}} - |\mu_m|} \\ + \frac{1}{\frac{\sigma_t}{f^{(1)}} - |\mu_n|} \frac{1}{\frac{\sigma_t}{f^{(1)}} + |\mu_m|} \end{array} \right\}$$

$$\sum_{n=1}^{Np} w_n a_n^{(2)} = \frac{c}{12} \sigma_t^2 \sum_{\mu_n > 0} w_n \sum_{\mu_m > 0} w_m \left\{ \begin{array}{l} -\left(\frac{\sigma_t}{f^{(1)}}\right) + \frac{\sigma_t}{f^{(1)}} (-|\mu_m| + |\mu_n|) + \cancel{|\mu_n||\mu_m|} \\ +\left(\frac{\sigma_t}{f^{(1)}}\right) + \frac{\sigma_t}{f^{(1)}} (-|\mu_m| + |\mu_n|) - \cancel{|\mu_n||\mu_m|} \\ \left[\left(\frac{\sigma_t}{f^{(1)}}\right)^2 - |\mu_n|^2\right] \left[\left(\frac{\sigma_t}{f^{(1)}}\right)^2 - |\mu_m|^2\right] \end{array} \right\}$$

$$\sum_{n=1}^{Np} w_n a_n^{(2)} = \frac{c}{6} \sigma_t^2 \frac{\sigma_t}{f^{(1)}} \left\{ \begin{array}{l} -\sum_{\mu_n > 0} w_n \frac{1}{\left(\frac{\sigma_t}{f^{(1)}}\right)^2 - |\mu_n|^2} \sum_{\mu_m > 0} w_m \frac{|\mu_m|}{\left(\frac{\sigma_t}{f^{(1)}}\right)^2 - |\mu_m|^2} \\ + \sum_{\mu_m > 0} w_m \frac{1}{\left(\frac{\sigma_t}{f^{(1)}}\right)^2 - |\mu_m|^2} \sum_{\mu_n > 0} w_n \frac{|\mu_n|}{\left(\frac{\sigma_t}{f^{(1)}}\right)^2 - |\mu_n|^2} \end{array} \right\} = 0$$

$b_n^{(2)}$ :

$$\mu_n > 0 : b_n^{(2)} = a_n^{(2)} + \frac{\sigma_t}{|\mu_n|} \left[ \frac{1}{6} f^{(1)} (1 - a_n^{(0)}) \right] + a_n^{(0)} (f^{(2)} - z^{(2)})$$

$$b_n^{(2)} = \left\{ \begin{array}{l} -\frac{c}{12} f^{(1)} f^{(1)} a_n^{(0)} \left[ \sum_{\mu_n < 0} w_n a_n^{(0)} \right] + \frac{\sigma_t}{|\mu_n|} \left[ \frac{1}{6} f^{(1)} (1 - a_n^{(0)}) \right] \\ + a_n^{(0)} \left( \frac{1}{2} f^{(1)} f^{(1)} - \frac{1}{2} f^{(1)} f^{(1)} - \frac{c}{12} f^{(1)} f^{(1)} \left[ \sum_{\mu_n > 0} w_n a_n^{(0)} - \sum_{\mu_n < 0} w_n a_n^{(0)} \right] \right) \end{array} \right\}$$

$$\mu_n > 0 : b_n^{(2)} = -\frac{c}{12} f^{(1)} f^{(1)} a_n^{(0)} \sum_{\mu_n > 0} w_n a_n^{(0)} + \frac{1}{6} \frac{\sigma_t}{|\mu_n|} f^{(1)} (1 - a_n^{(0)})$$

$$\mu_n < 0 : b_n^{(2)} = a_n^{(2)} + \frac{\sigma_t}{|\mu_n|} \left[ \frac{1}{6} f^{(1)} (1 - a_n^{(0)}) \right] + a_n^{(0)} (f^{(2)} - z^{(2)})$$

$$b_n^{(2)} = \left\{ \begin{array}{l} \frac{c}{12} f^{(1)} f^{(1)} a_n^{(0)} \left[ \sum_{\mu_n > 0} w_n a_n^{(0)} \right] + \frac{\sigma_t}{|\mu_n|} \left[ \frac{1}{6} f^{(1)} (1 - a_n^{(0)}) \right] \\ + a_n^{(0)} \left( \frac{1}{2} f^{(1)} f^{(1)} - \frac{1}{2} f^{(1)} f^{(1)} - \frac{c}{12} f^{(1)} f^{(1)} \left[ \sum_{\mu_n < 0} w_n a_n^{(0)} - \sum_{\mu_n < 0} w_n a_n^{(0)} \right] \right) \end{array} \right\}$$

$$\mu_n < 0: \boxed{b_n^{(2)} = \frac{c}{12} f^{(1)} f^{(1)} a_n^{(0)} \sum_{\mu_n < 0} w_n a_n^{(0)} + \frac{1}{6} \frac{\sigma_t}{|\mu_n|} f^{(1)} (1 - a_n^{(0)})}$$

Compare  $b_n^{(2)}$  to the S2 results:

$$b_1^{(2)} = -\frac{c}{12} f^{(1)} f^{(1)} [a_1^{(0)}]^2 + \frac{1}{6} \frac{\sigma_t}{|\mu|} f^{(1)} (1 - a_1^{(0)})$$

$$b_1^{(2)} = -\frac{c}{12} \sigma_t^2 \frac{1}{[\nu + |\mu|]^2} + \frac{1}{6} \frac{\sigma_t}{|\mu|} f^{(1)} \frac{|\mu|}{\frac{\sigma_t}{f^{(1)}} + |\mu|}$$

$$b_1^{(2)} = -\frac{c}{12} \sigma_t^2 \frac{1}{[\nu + |\mu|]^2} + \frac{1}{6} \frac{\sigma_t^2}{\nu} \frac{1}{\nu + |\mu|} \Rightarrow b_1^{(2)} = \frac{\sigma_t^2}{12} \left\{ \frac{-c \frac{|\mu|}{\sqrt{1-c}} + 2 \frac{|\mu|}{\sqrt{1-c}} + 2|\mu|}{|\mu|^z \left[ \frac{1}{\sqrt{1-c}} + 1 \right]^2} \right\}$$

$$b_1^{(2)} = \frac{\sigma_t^2}{12} \frac{\frac{1+2\sqrt{1-c}+(1-c)}{\sqrt{1-c}}}{|\mu| \frac{[1+\sqrt{1-c}]^2}{1-c}} \Rightarrow \boxed{b_1^{(2)} = \frac{1}{12} \frac{\sigma_t^2}{\nu}}$$

$$b_2^{(2)} = \frac{c}{12} f^{(1)} f^{(1)} [a_2^{(0)}]^2 + \frac{1}{6} \frac{\sigma_t}{|\mu|} f^{(1)} (1 - a_2^{(0)})$$

$$b_2^{(2)} = \frac{c}{12} \frac{\sigma_t^2}{\left( \frac{\sigma_t}{f^{(1)}} - |\mu| \right)^2} + \frac{1}{6} \frac{\sigma_t}{|\mu|} f^{(1)} \left( 1 - \frac{\frac{\sigma_t}{f^{(1)}}}{\frac{\sigma_t}{f^{(1)}} - |\mu|} \right)$$

$$\begin{aligned}
b_2^{(2)} &= \frac{c}{12} \frac{\sigma_t^2}{\left(\frac{\sigma_t}{f^{(1)}} - |\mu|\right)^2} + \frac{1}{6} \frac{\sigma_t}{|\mu|} f^{(1)} \left( \frac{\frac{\sigma}{f^{(1)}} - |\mu| - \frac{\sigma}{f^{(1)}}}{\frac{\sigma_t}{f^{(1)}} - |\mu|} \right) \\
\Rightarrow b_2^{(2)} &= \frac{c}{12} \frac{\sigma_t^2}{(\nu - |\mu|)^2} - \frac{1}{6} \frac{\sigma_t^2}{\nu} \frac{1}{\nu - |\mu|} \\
b_2^{(2)} &= \frac{\sigma_t^2}{12 \nu} \left[ \frac{\nu c - 2\nu + 2|\mu|}{(\nu - |\mu|)^2} \right] \Rightarrow b_2^{(2)} = \frac{\sigma_t^2}{12 \nu} \left[ \frac{\frac{|\mu|c - 2|\mu|}{\sqrt{1-c}} + |\mu|}{|\mu|^2 \left( \frac{1}{\sqrt{1-c}} - 1 \right)^2} \right] \\
b_2^{(2)} &= -\frac{\sigma_t^2}{12 \nu} \left[ \frac{\frac{1 - 2\sqrt{1-c} + (1-c)}{\sqrt{1-c}}}{\frac{|\mu| \frac{(1 - \sqrt{1-c})^2}{1-c}}{1-c}} \right] \Rightarrow \boxed{b_2^{(2)} = -\frac{1}{12} \frac{\sigma_t^2}{\nu^2}}
\end{aligned}$$

Second, sum over all angles to guarantee normalization:

$$\sum_{n=1}^{N_p} w_n b_n^{(2)} = \sum_{\mu_n > 0} w_n \left[ -\frac{c}{12} f^{(1)} f^{(1)} \frac{\frac{\sigma_t}{f^{(1)}}}{\frac{\sigma_t}{f^{(1)}} + |\mu_n|} \sum_{\mu_m > 0} w_m a_m^{(0)} + \frac{1}{6} \frac{\sigma_t}{|\mu_n|} f^{(1)} \left( 1 - \frac{\frac{\sigma_t}{f^{(1)}}}{\frac{\sigma_t}{f^{(1)}} + |\mu_n|} \right) \right] \\
+ \sum_{\mu_n < 0} w_n \left[ \frac{c}{12} f^{(1)} f^{(1)} \frac{\frac{\sigma_t}{f^{(1)}}}{\frac{\sigma_t}{f^{(1)}} - |\mu_n|} \sum_{\mu_m < 0} w_m a_m^{(0)} + \frac{1}{6} \frac{\sigma_t}{|\mu_n|} f^{(1)} \left( 1 - \frac{\frac{\sigma_t}{f^{(1)}}}{\frac{\sigma_t}{f^{(1)}} - |\mu_n|} \right) \right]$$

$$\begin{aligned}
\sum_{n=1}^{N_p} w_n b_n^{(2)} = & \left\{ \frac{c}{12} f^{(1)} f^{(1)} \sum_{\mu_n > 0} w_n \frac{\frac{\sigma_t}{f^{(1)}}}{\frac{\sigma_t}{f^{(1)}} + |\mu_n|} \left[ \begin{aligned} & - \sum_{\mu_m > 0} \left( w_m \frac{\frac{\sigma_t}{f^{(1)}}}{\frac{\sigma_t}{f^{(1)}} + |\mu_m|} \right) \\ & + \frac{\frac{\sigma_t}{f^{(1)}} + |\mu_n|}{\frac{\sigma_t}{f^{(1)}} - |\mu_n|} \sum_{\mu_m < 0} \left( w_m \frac{\frac{\sigma_t}{f^{(1)}}}{\frac{\sigma_t}{f^{(1)}} - |\mu_m|} \right) \end{aligned} \right] \right\} \\
& + \frac{1}{6} \sigma_t f^{(1)} \sum_{\mu_n > 0} w_n \frac{1/|\mu_n|}{\frac{\frac{\sigma_t}{f^{(1)}} + |\mu_n|}{\frac{\sigma_t}{f^{(1)}} + |\mu_n|} + \frac{\frac{\sigma_t}{f^{(1)}} - |\mu_n|}{\frac{\sigma_t}{f^{(1)}} - |\mu_n|}} \\
\sum_{n=1}^{N_p} w_n b_n^{(2)} = & \left\{ \frac{c}{12} f^{(1)} f^{(1)} \sum_{\mu_n > 0} w_n \frac{\frac{\sigma_t}{f^{(1)}}}{\frac{\sigma_t}{f^{(1)}} + |\mu_n|} \frac{\frac{\sigma_t}{f^{(1)}}}{\frac{\sigma_t}{f^{(1)}} - |\mu_n|} \left[ \begin{aligned} & \sum_{\mu_m > 0} \left( w_m \frac{\frac{\sigma_t}{f^{(1)}}}{\frac{\sigma_t}{f^{(1)}} + |\mu_m|} \right) \\ & + \frac{\frac{\sigma_t}{f^{(1)}}}{\frac{\sigma_t}{f^{(1)}} - |\mu_m|} \end{aligned} \right] \right\} \\
& + |\mu_n| \frac{f^{(1)}}{\sigma_t} \sum_{\mu_m > 0} \left( w_m \frac{\frac{\sigma_t}{f^{(1)}}}{\frac{\sigma_t}{f^{(1)}} + |\mu_m|} + \frac{\frac{\sigma_t}{f^{(1)}}}{\frac{\sigma_t}{f^{(1)}} - |\mu_m|} \right) \\
& + \frac{1}{6} \sigma_t f^{(1)} \sum_{\mu_n > 0} w_n \left[ \frac{1}{\frac{\sigma_t}{f^{(1)}} + |\mu_n|} - \frac{1}{\frac{\sigma_t}{f^{(1)}} - |\mu_n|} \right]
\end{aligned}$$

$$\sum_{n=1}^{Np} w_n b_n^{(2)} = \left\{ \begin{aligned} & \frac{c}{12} f^{(1)} f^{(1)} \sum_{\mu_n > 0} w_n \frac{\frac{\sigma_t}{f^{(1)}}}{\frac{\sigma_t}{f^{(1)}} + |\mu_n|} \frac{\frac{\sigma_t}{f^{(1)}}}{\frac{\sigma_t}{f^{(1)}} - |\mu_n|} \left[ - \left( \sum_{\mu_m > 0} w_m a_n^{(0)} - \sum_{\mu_m < 0} w_m a_n^{(0)} \right) \right. \\ & \left. + |\mu_n| \frac{f^{(1)}}{\sigma_t} \frac{2}{c} \right] \\ & + \frac{1}{6} f^{(1)} f^{(1)} \sum_{\mu_n > 0} w_n \left[ \frac{\frac{\sigma_t}{f^{(1)}}}{\frac{\sigma_t}{f^{(1)}} + |\mu_n|} - \frac{\frac{\sigma_t}{f^{(1)}}}{\frac{\sigma_t}{f^{(1)}} - |\mu_n|} \right] \end{aligned} \right\}$$

$$\sum_{n=1}^{Np} w_n b_n^{(2)} = \left\{ \begin{aligned} & \frac{c}{12} f^{(1)} \sigma_t \left[ - \left( \sum_{\mu_m > 0} w_m a_n^{(0)} - \sum_{\mu_m < 0} w_m a_n^{(0)} \right) \frac{1}{2} \sum_{\mu_n > 0} w_n \frac{2 \frac{\sigma_t}{f^{(1)}}}{\left( \frac{\sigma_t}{f^{(1)}} + |\mu_n| \right) \left( \frac{\sigma_t}{f^{(1)}} - |\mu_n| \right)} \right. \\ & \left. + \frac{2}{c} \sum_{\mu_n > 0} w_n \frac{|\mu_n|}{\left( \frac{\sigma_t}{f^{(1)}} + |\mu_n| \right) \left( \frac{\sigma_t}{f^{(1)}} - |\mu_n| \right)} \right] \\ & + \frac{1}{6} f^{(1)} f^{(1)} \left( \sum_{\mu_m > 0} w_m a_n^{(0)} - \sum_{\mu_m < 0} w_m a_n^{(0)} \right) \end{aligned} \right\}$$

$$\sum_{n=1}^{Np} w_n b_n^{(2)} = \left\{ \begin{array}{l} \frac{c}{12} f^{(1)} \sigma_t \left[ - \left( \sum_{\mu_m > 0} w_m a_n^{(0)} - \sum_{\mu_m < 0} w_m a_n^{(0)} \right) \frac{1}{2} \frac{f^{(1)}}{\sigma_t} \sum_{\mu_n > 0} w_n \left[ \frac{\frac{\sigma_t}{f^{(1)}}}{\left( \frac{\sigma_t}{f^{(1)}} + |\mu_n| \right)} + \frac{\frac{\sigma_t}{f^{(1)}}}{\left( \frac{\sigma_t}{f^{(1)}} - |\mu_n| \right)} \right] \right. \\ \left. + \frac{1}{c} \frac{f^{(1)}}{\sigma_t} \sum_{\mu_n > 0} w_n \left[ - \frac{\frac{\sigma_t}{f^{(1)}}}{\left( \frac{\sigma_t}{f^{(1)}} + |\mu_n| \right)} + \frac{\frac{\sigma_t}{f^{(1)}}}{\left( \frac{\sigma_t}{f^{(1)}} - |\mu_n| \right)} \right] \right] \\ + \frac{1}{6} f^{(1)} f^{(1)} \left( \sum_{\mu_m > 0} w_m a_n^{(0)} - \sum_{\mu_m < 0} w_m a_n^{(0)} \right) \end{array} \right\}$$

$$\sum_{n=1}^{Np} w_n b_n^{(2)} = \left\{ \begin{array}{l} \frac{c}{12} f^{(1)} \sigma_t \left[ - \left( \sum_{\mu_m > 0} w_m a_n^{(0)} - \sum_{\mu_m < 0} w_m a_n^{(0)} \right) \frac{f^{(1)}}{\sigma_t} \frac{1}{c} \right] \\ - \frac{1}{c} \frac{f^{(1)}}{\sigma_t} \left( \sum_{\mu_m > 0} w_m a_n^{(0)} - \sum_{\mu_m < 0} w_m a_n^{(0)} \right) \\ + \frac{1}{6} f^{(1)} f^{(1)} \left( \sum_{\mu_m > 0} w_m a_n^{(0)} - \sum_{\mu_m < 0} w_m a_n^{(0)} \right) \end{array} \right\}$$

$$\sum_{n=1}^{Np} w_n b_n^{(2)} = \left\{ \begin{array}{l} - \frac{1}{6} f^{(1)} f^{(1)} \left( \sum_{\mu_m > 0} w_m a_n^{(0)} - \sum_{\mu_m < 0} w_m a_n^{(0)} \right) \\ + \frac{1}{6} f^{(1)} f^{(1)} \left( \sum_{\mu_m > 0} w_m a_n^{(0)} - \sum_{\mu_m < 0} w_m a_n^{(0)} \right) \end{array} \right\} = 0$$

$$\begin{aligned}
\mu_n > 0 : a_n^{(2)} &= -\frac{c}{12} f^{(1)} f^{(1)} a_n^{(0)} \left[ \sum_{\mu_n < 0} w_n a_n^{(0)} \right] \\
\mu_n < 0 : b_n^{(2)} &= \frac{c}{12} f^{(1)} f^{(1)} a_n^{(0)} \sum_{\mu_n < 0} w_n a_n^{(0)} + \frac{1}{6} \frac{\sigma_t}{|\mu_n|} f^{(1)} (1 - a_n^{(0)}) \\
a_n^{(2)} - b_m^{(2)} &= -\frac{c}{12} f^{(1)} f^{(1)} a_n^{(0)} \sum_{\mu_n < 0} w_n a_n^{(0)} - \frac{c}{12} f^{(1)} f^{(1)} a_m^{(0)} \sum_{\mu_n < 0} w_n a_n^{(0)} - \frac{1}{6} \frac{\sigma_t}{|\mu_n|} f^{(1)} (1 - a_m^{(0)}) \\
a_n^{(2)} - b_m^{(2)} &= -\frac{c}{6} \sigma_t \sigma_t \frac{1}{\left( \frac{\sigma_t}{f^{(1)}} \right)^2 - |\mu_n|^2} \sum_{\mu_n < 0} w_n a_n^{(0)} + \frac{1}{6} \sigma_t f^{(1)} \frac{1}{\frac{\sigma_t}{f^{(1)}} - |\mu_n|} \\
a_n^{(2)} - b_m^{(2)} &= \left\{ \begin{array}{l} -\frac{c}{6} \sigma_t \sigma_t \frac{1}{\left( \frac{\sigma_t}{f^{(1)}} \right)^2 - |\mu_n|^2} \sum_{\mu_n < 0} w_n a_n^{(0)} \\ + \frac{c}{6} \frac{\sigma_t f^{(1)}}{2} \frac{1}{\frac{\sigma_t}{f^{(1)}} - |\mu_n|} \left[ \sum_{\mu_n < 0} w_n a_n^{(0)} + \sum_{\mu_n > 0} w_n a_n^{(0)} \right] \end{array} \right\}
\end{aligned}$$

**VITA**

Name: Alexander E. Maslowski Olivares

Address: Department of Nuclear Engineering  
3133 TAMU  
College Station, TX 77843-3133

Email Address: alexmas@ne.tamu.edu  
Alternate: alexmas@gmail.com

Education: Ph.D. in Nuclear Engineering, Texas A&M University,  
College Station Texas, 2008

B.S. in Nuclear Engineering, Texas A&M University,  
College Station Texas, 2003